DISSERTATION

SEARCH FOR AN ANOMALOUS EXCESS OF CHARGED-CURRENT ELECTRON NEUTRINO INTERACTIONS WITH THE MICROBOONE DETECTOR

Submitted by

Ivan Caro Terrazas

Department of Physics

In partial fulfillment of the requirements

For the Degree of Doctor of Philosophy

Colorado State University

Fort Collins, Colorado

Fall 2022

Doctoral Committee:

Advisor: Michael R. Mooney

Robert J. Wilson
Norm Buchanan
Michael Kirby

ABSTRACT

SEARCH FOR AN ANOMALOUS EXCESS OF CHARGED-CURRENT ELECTRON NEUTRINO INTERACTIONS WITH THE MICROBOONE DETECTOR

MicroBooNE is a liquid argon time projection chamber detector designed to address the excess of low-energy electromagnetic events observed by the MiniBooNE detector. Electron neutrinos can create a wide variety of topologies when interacting with liquid argon; this analysis measures events without pions, both with ($1e\mathrm{N}p0\pi$) and without ($1e0p0\pi$) visible protons. This thesis presents a first measurement of pionless charged-current electron neutrino interactions from the Booster Neutrino Beam at Fermilab in the MicroBooNE detector. A model based on the MiniBooNE result is used to quantify the strength of the electron neutrino excess. The analysis suggests that if an excess is present, it is not consistent with a simple scaling of the electron-neutrino contribution to the flux. Combined, the $1e\mathrm{N}p0\pi$ and $1e0p0\pi$ channels do not give a conclusive indication of the tested model, but separately they both disfavor the low-energy excess model at $> 90\%$ CL. The observation in the most sensitive $1e\mathrm{N}p0\pi$ channel is below the prediction and is consistent with no excess. In the less sensitive $1e0p0\pi$ channel the observation at low energy is above the prediction, while overall there is agreement over the full energy spectrum.

DEDICATION

To my friends and family, thank you for all your support.

TABLE OF CONTENTS

LIST OF FIGURES

Chapter 1

Introduction

The neutrino was proposed as an impractical solution to the problematic beta decay energy spectrum, where the ad hoc addition of an electrically neutral spin 1/2 fermion would solve the energy conservation problem. Three decades after the neutrino was proposed, it was first detected by Fred Reines and George Cowan, and since then the neutrino has continued to motivate scientists to find out everything possible about this fundamental particle. According to the Standard Model, neutrinos are massless particles that only interact via the weak and gravitational forces and come in three flavors: electron, muon, and tau. However, neutrinos display physics beyond the Standard Model in that neutrinos propagate as mass eigenstates which are superpositions of the flavor eigenstates. This gives an oscillatory nature to the neutrino, which requires it to have mass, contradicting the Standard Model. Even after nearly 70 years since their discovery, neutrinos continue to open up more questions about the nature of our universe. Why is there a matter/antimatter asymmetry in the universe? Do additional (sterile) neutrinos exist? What is the correct ordering of the neutrino masses?

The necessity of characterizing these elusive particles has led scientists to build increasingly large and sensitive neutrino detectors. One of the leading neutrino detector technologies is the liquid argon time projection chamber (LArTPC), which has been chosen to perform important physics measurements because of its ability to image complicated neutrino interactions, leading to precise reconstruction of spatial and calorimetric information. This makes LArTPCs a powerful type of detector, allowing one to discriminate between neutrino interaction signal events of different flavors as well as background events. The design behind LArTPCs is based on a multiwire-plane anode and a cathode plane separated by a long drift distance to create an electric field in a large volume of liquid argon. Impinging charged particles leads to ionization

of argon, and the ionization electrons are subsequently picked up by the anode-plane sensing wires. Events are then reconstructed by taking two dimensions from the location of detected ionization on the wire planes and a third from the time the drifting electrons produce a signal on the wires. This design choice makes LArTPCs high-resolution tracking calorimeters that allow for detailed reconstruction of charged-particle trajectories and energy deposition. These characteristics make LArTPCs the high-performing technology for current and future neutrino experiments.

The Micro Booster Neutrino Experiment (MicroBooNE) consists of a large 170-ton LArTPC detector located on the Booster Neutrino Beamline (BNB) at Fermilab. It was built as the successor to the MiniBooNE experiment with the main goal of understanding the nature of the observed excess of low-energy electromagnetic events. This excess is consistent with an anomalous number of electron neutrino interactions and could be attributed to some sterile neutrino oscillations. The MicroBooNE detector will search for low-energy electron neutrino signatures using the advantages brought on by LArTPC technology.

This thesis will focus on one of the analyses carried out by the MicroBooNE collaboration to address the MiniBooNE low-energy excess (LEE) by searching for charged-current electron neutrino interactions without pions in the final state. Chapter 2 will provide background information on neutrino physics and relevant physics to understand neutrino interactions. Chapter 3 explores the historical context of experimental neutrino physics and the current phenomenological understanding of the MiniBooNE LEE. Chapter 4 will introduce the inner workings of the LArTPC detector and will also provide a case study of a LArTPC with the ICEBERG test stand. Chapter 5 describes the MicroBooNE detector in detail, including its physics motivations and neutrino beam. Chapter 6 introduces the main analysis of this thesis, describing the signal model and giving a brief overview of the analysis. Chapter 7 presents the MicroBooNE simulation and reconstruction algorithms used to perform this analysis. Chapter 8 describes the selections of neutrino events and the requirements used to separate well-reconstructed neutrino events from background events. Chapter 9 describes the sources of uncertainty in the analysis

along with the constraint procedure used to reduce such uncertainties. Chapter 10 discusses the statistical methods to quantify the observation and presents the results of this analysis. The last chapter, Chapter 11, will recapitulate the results and give a brief conclusion.

Chapter 2

Neutrino Physics

This chapter provides the theoretical overview along with some historical context of neutrino physics. Section 2.1 provides some historical overview the neutrino and leads into the role neutrinos play in the Standard Model. Section 2.2 discusses the interactions modes observed with neutrinos and Section 2.3 gives a brief overview of neutrino oscillations. Finally, Section 2.4 discusses the search for a sterile neutrino in the 3+1 model.

2.1 Neutrinos in the Standard Model

In 1930, Wolfgang Pauli proposed [26] the unthinkable at the time, a particle that could not be detected – or so he thought. In a letter directed to his "radioactive" audience, he laid out the properties that this particle should have based upon the problem observed in the beta decay spectrum of the N-14 and Li-6 nuclei. The mystery particle should be electrically neutral, spin 1/2 and obey the Pauli exclusion principle. In addition, this particle should be extremely light with a mass on the same order of magnitude as the electron. Pauli did not know it at the time, but the particle he was proposing is very much possible to detect (albeit hard) and would be later named the neutrino.

Fast forward to the present, and our knowledge on the neutrino has expanded and we now know that its a part of a family of particles that are considered fundamental, meaning that as far as we know, this particle is not composed out of any other particles. The theoretical framework that describes elementary particles and the fundamental forces that govern them is called the Standard Model (SM) of particle physics. The fundamental forces or interactions – the strong nuclear, the weak nuclear and the electromagnetic force – are mediated by the gauge bosons. Bosons are characterized by having an integer spin and obeying Bose-Eisntein statistics. Pho-

tons mediate the electromagnetic force, gluons are the force carriers to strong nuclear force and the weak nuclear force is mediated by both the Z and $W^{\pm}$ bosons. Though not listed, the gravitational force is also fundamental interaction and its believed to be carried by a hypothetical gauge boson called the graviton. The last boson listed in the SM is the Higgs boson; though not a force carrier like the other bosons, the field associated with this particle is responsible for particle masses via the Higgs mechanism [27]. Figure 2.1 shows an image of all particles contained in the SM.

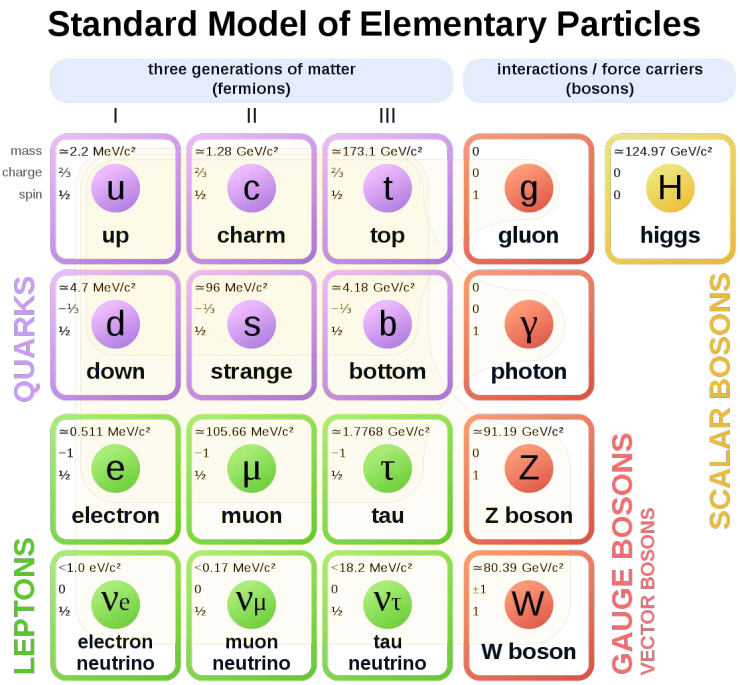

Figure 2.1: The Standard Model of particle physics.

Matter is composed of particles the fermion sector of the SM. These particles are characterized by having spin 1/2 and obeying Fermi-Dirac statistics. Two types of particles can be found in this sector, the quarks and leptons. These classes are split further into three generations of matter. For quarks, the up (u) and down (d) quarks make up the first generation, the charm (c) and strange (s) quarks make up the second generation and the third generation of quarks is formed by the top (t) and bottom (b) quarks. In the lepton sector we have the electron (e),

muon (μ) and tau (τ) particle making up each of the three generation respectively, along with its corresponding neutrino, the ν_e, ν_μ and ν_τ.

The neutrino is an elusive particle as it only interacts via the weak nuclear force, meaning that for practical purposes they can cover an enormous amount of distance without ever interacting. For scale, a single neutrino can travel through a lightyear of lead and will most likely not interact at all. However, although difficult to observe, physicists have made great efforts to advance the field of neutrino detection since the first (anti)neutrino was detected in 1956 by Cowan and Reines [28] and the first observation of a neutrino interaction in 1970 at Argonne (Figure 2.2).

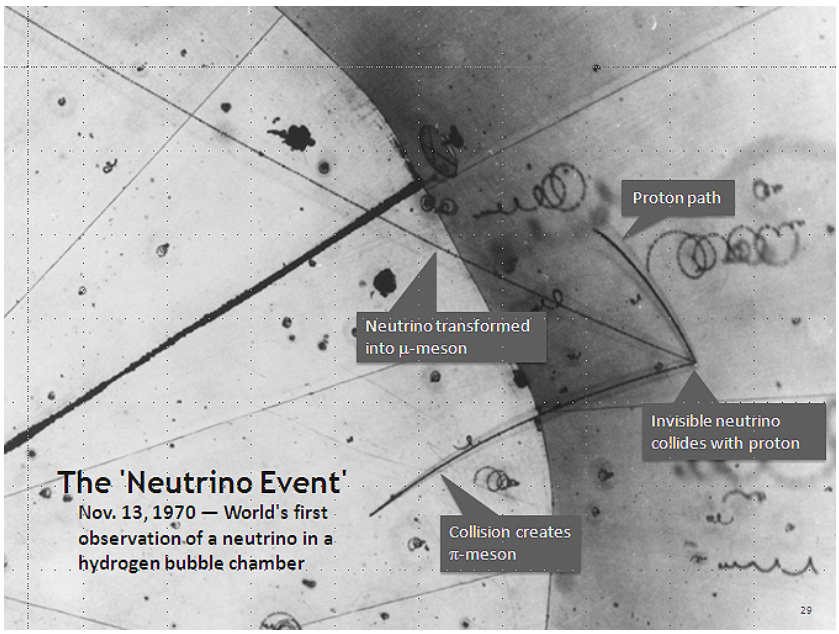

Figure 2.2: The first observation of a neutrino in a hydrogen bubble chamber taken with the Argonne 12-foot chamber.

Although the SM is incredibly accurate in its description of particles and their interactions, it is not without limitations, specifically when dealing with neutrinos. In the SM, neutrinos are assumed to conserve individual lepton number and are also assumed to be massless. The conservation of individual lepton number is supported by the absence of decays that would indicate such a violation. The MEGA experiment has performed searches for muon and electron

number-violating decays such as $\mu^{\pm} \rightarrow e^{\pm} + \gamma$, but only an upper limit branching ratio has been computed [29]. As a result of these assumptions, the right-handed component of the neutrino field is missing in the SM because the weak force only interacts with the left-handed components.

Despite these assumptions working within the SM framework, recent discoveries in the field of neutrino physics have shown evidence that the neutrino has mass. The search for a direct mass measurement has bounded the neutrino mass to be 1.1 eV [30]. Furthermore, the phenomenon of neutrino oscillations, in which a neutrino changes flavor as a function of time, has been linked to the existence of a massive neutrino.

2.2 Neutrino Interactions

Neutrinos only interact via two fundamental forces: weak and gravitational interactions. The latter of these forces is negligible given the tiny mass of the neutrino ($m_{\nu} < 1$ eV). This opens up only the weak interaction as our main mode of neutrino detection.

Weak interactions are mediated by the W and Z bosons. Neutrino interactions fall into two categories, those mediated by the $W^{\pm}$ boson which are known as charged current (CC) interactions, and those mediated by the Z boson which are known as neutral current (NC) interactions. CC processes are characterized by an outgoing lepton. Figure 2.3a shows a ν_e-neutron CC process where we expect an electron in the final state, along with a proton which is the result of the W boson changing the flavor from down quarks to up quarks in the neutron. The NC process is obtained by changing the mediator particle to the neutral Z boson, which produces an outgoing neutrino instead of a charged lepton (Figure 2.3b). In general, when a neutrino is interacting with a nucleon, the CC and NC interactions take the form of:

$$\nu_{\ell} + A \rightarrow \ell^{-} + X \quad \text{(CC)}, \quad \nu_{\ell} + A \rightarrow \nu_{\ell} + X \quad \text{(NC)} \tag{2.1}$$

where $\ell = e, \mu, \tau$ represents the lepton and the leptonic flavor in the case of the neutrino, A is the nucleon, and X are any number of final-state particles resulting from the interaction.

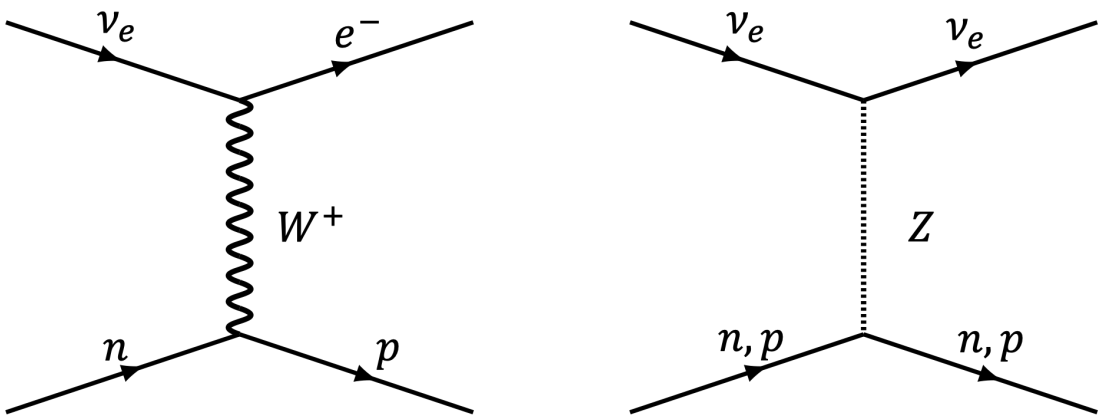

(a) Charged Current **(b)** Neutral Current

Figure 2.3: Feynman diagrams of standard neutrino-nucleon interactions for charged-current and neutral-current processes.

Moreover, neutrino interactions can be classified by the incident neutrino energy and its interaction with hadrons (i.e. a target nucleus). The major categories by which one can classify neutrino interactions in this way are quasielastic scattering (QE), resonant production (RES), and deep inelastic scattering (DIS). Figure 2.4 shows a breakdown of possible interaction modes as a function of energy.

2.2.1 Quasielastic Scattering

Quasielastic scattering is dominant at neutrino energies below 1 GeV. This process involves a neutrino being scattered off a nucleon and often freeing it from the target atom. In the CCQE process, the incoming neutrino modifies the flavor of one of the constituent quarks of the target nucleons. An example Feynman diagram of this process is shown in Figure 2.5a. This process is represented by the following:

$$\nu_\ell + n \rightarrow \ell^- + p \tag{2.2}$$

with n and p representing the neutron and proton respectively.

2.2.2 Resonant Interactions

Resonant interactions occur when the incoming neutrino excites one of the target nucleons into a resonant state, e.g. a delta baryon Δ. The excited nucleon then decays into some final state

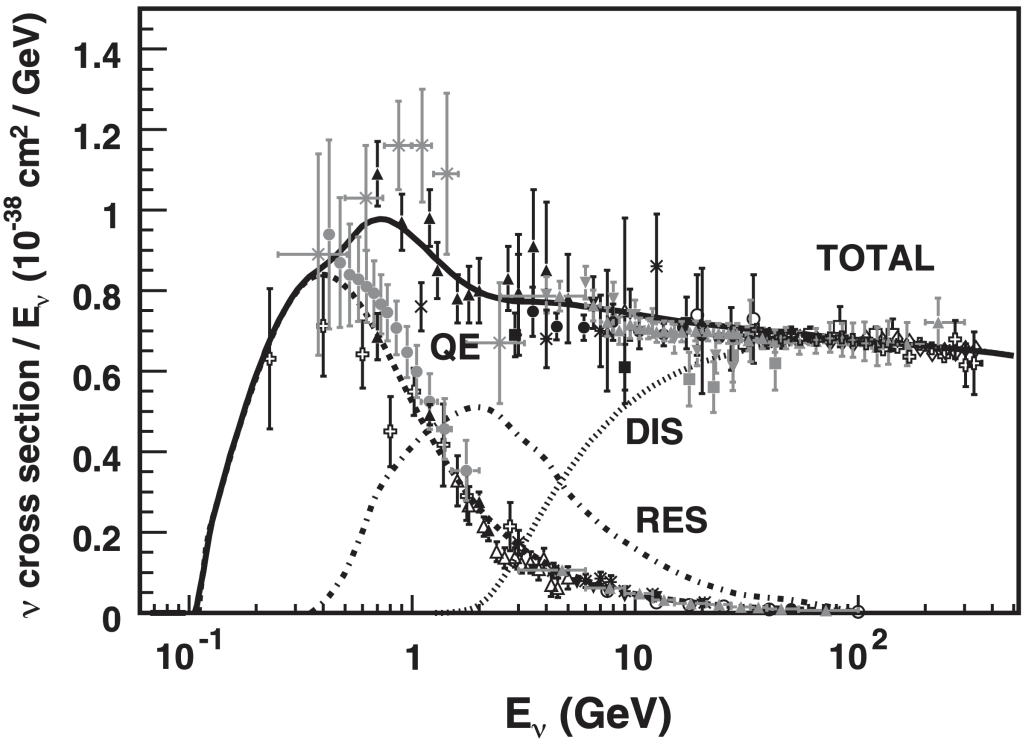

Figure 2.4: Predicted ν_μ CC cross sections as a function of neutrino energy for QE, RES and DIS processes with overlayed data from several neutrino experiments. Figure taken from [4].

that is most often into a nucleon and a single pion. Figure 2.5b shows an example Feynman diagram for this type of interaction. This process is active for neutrino energies greater than ~ 0.5 GeV and has a major contribution in the range of 1-4 GeV.

2.2.3 Deep Inelastic Scattering

Neutrinos with an energy above 4 GeV tend to go deep into the target nucleus and scatter off the constituent quarks. This scattered quark causes a slew of other interactions within the nucleus resulting in multiple final-state particles and a corresponding charged lepton. Figure 2.5c shows an example Feynman diagram for this type of interaction.

2.3 Neutrino Oscillations

Bruno Pontecorvo first predicted neutrino oscillations in 1959 [31], specifically oscillations between ν_e and ν_μ, showing that individual lepton number is not conserved. Neutrino oscilla-

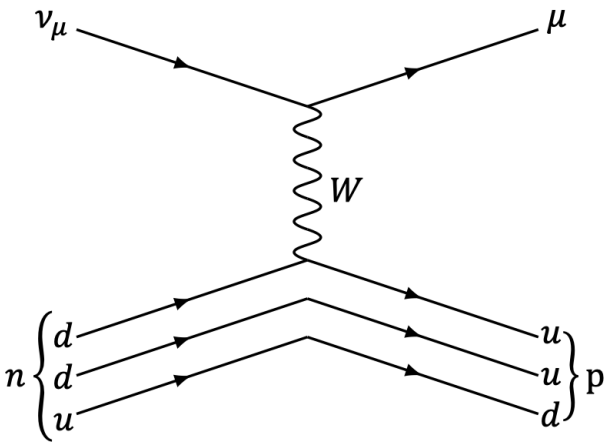

(a) CCQE

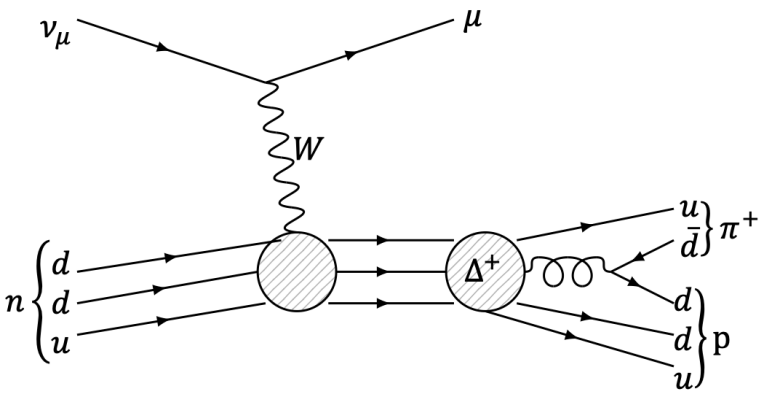

(b) Resonant Interaction

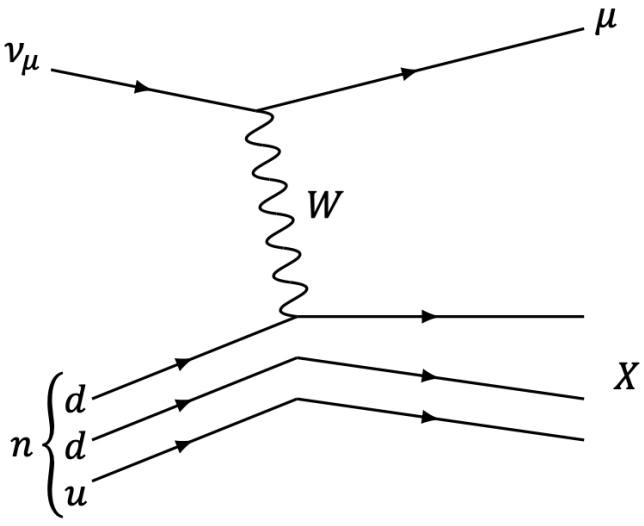

(c) Deep Inelastic Scattering

Figure 2.5: Feynman diagrams of neutrino interaction modes at the GeV energy scale.

tions were first observed by Ray Davis in the 1960s in the Homestake experiment [32] where a discrepancy was found between the predicted and measured solar neutrino flux. It would not be until the late 1990s and early 2000s that the Super-Kamiokande collaboration [33] and the Sudbury Neutrino Observatory [34] collaboration would confirm that the discrepancy found by Ray Davis was due to neutrino flavor oscillations. Neutrino flavor oscillations are a quantum mechanical effect, products of the non-orthogonality of mass eigenstates of the Hamiltonian and the flavor eigenstates produced by weak interactions – meaning that when a reaction that produces a neutrino occurs, we can know its flavor state, but the mass state will be a superposition of all possible mass states.

Neutrinos are produced in three distinct flavors, ν_e, ν_μ, and ν_τ, each flavor state being a superposition of three mass eigenstates. One can also represent this flavor basis as a superposition of mass eignestates. The change in basis can be described as a unitary transformation and can be written as

$$|\nu_k\rangle = \sum_\alpha U_{\alpha k} |\nu_\alpha\rangle\,, \quad |\nu_\alpha\rangle = \sum_k (U^\dagger)_{k\alpha} |\nu_k\rangle = \sum_k U^*_{\alpha k} |\nu_k\rangle \tag{2.3}$$

where ν_k are the mass eignestates ($k = 1,2,3$), ν_α are the flavor eignestates ($\alpha = e,\mu,\tau$) and U is a unitary matrix that relates the flavor and mass eigenstates.

We can derive the formalism for neutrino oscillations starting with a two-flavor hypothesis. The derivations used here are largely taken from the reference [35]. We assume that two mass states $|\nu_1\rangle$ and $|\nu_2\rangle$ and two flavor states $|\nu_\alpha\rangle$ and $\left|\nu_\beta\right\rangle$ are complete sets. Then, we can write both bases as a unitary transformation of one another in the following way:

$$\begin{pmatrix} |\nu_\alpha\rangle \\ \left|\nu_\beta\right\rangle \end{pmatrix} = \begin{pmatrix} \cos(\theta) & \sin(\theta) \\ -\sin(\theta) & \cos(\theta) \end{pmatrix} \begin{pmatrix} |\nu_1\rangle \\ |\nu_2\rangle \end{pmatrix} \tag{2.4}$$

Note that the matrix used here is unitary and depends only on a mixing angle θ.

Treating the neutrino as a free particle propagating in a vacuum, we can use the free particle solutions to the time-dependent Schrödinger equation to model the evolution of the flavor eigenstates. A neutrino initially produced in the flavor eigenstate $|\nu_\alpha\rangle$ will propagate as

$$|\nu_\alpha(t,x)\rangle = \cos(\theta)e^{-i(p_1 x)}|\nu_1\rangle + \sin(\theta)e^{-i(p_2 x)}|\nu_2\rangle \tag{2.5}$$

where $|\nu_k\rangle$ are the unevolved mass states at $t=0$ and $p_k x = E_k t - \vec{p}_k \cdot \vec{x}$ are the Lorentz-invariant phases with E_k as energy and $\vec{p}_k$ as the three-momentum vector of the neutrino mass eigenstates.

We can assume that our neutrino has traveled a distance L along a single direction x. Furthermore, most neutrinos produced in a beam for experimental detection are ultra-relativistic, meaning that $\left|\vec{p}_k\right| \equiv p_k \gg m_k$ and $t \sim L$. Given these approximations, the momentum and phase factors can be written as follows:

$$p_k = (E_k^2 - m_k^2)^{1/2} \approx E_k - \frac{m_k^2}{2E_k} \tag{2.6}$$

$$p_k \cdot x = E_k t - \vec{p}_k \cdot \vec{x} \approx (E_k - p_k)L = \frac{m_k^2}{2E_k}L \tag{2.7}$$

We note the use of natural units, i.e. $c = \hbar = 1$. Similarly, $E_k - p_k = (E_i^2 - \left|\vec{p}\right|^2)/(E_k + p_k) \approx m_k^2/2E_k \approx m_k^2/2E$ where $E_1 \approx E_2 \approx E$. Combining the momentum and phase factor approximations in Equations 2.6 and 2.7, Equation 2.5 turns into:

$$|\nu_\alpha(x)\rangle = \cos(\theta)e^{-i\frac{m_1^2}{2E}L}|\nu_1\rangle + \sin(\theta)e^{-i\frac{m_2^2}{2E}L}|\nu_2\rangle \tag{2.8}$$

Given the results in Equation 2.8, one can calculate the probability of detecting a neutrino that started in the α flavor, oscillated into another flavor mid-flight, and oscillated back into the

α flavor at the moment of detection.

$$\begin{aligned}
P_{\alpha\to\alpha} &= |\langle \nu_\alpha | \nu_\alpha(L)\rangle|^2 \\
&= \left| (\langle \nu_1|\cos(\theta) + \langle \nu_2|\sin(\theta)) \left(\cos(\theta) e^{-i\frac{m_1^2}{2E}L} |\nu_1\rangle + \sin(\theta) e^{-i\frac{m_2^2}{2E}L} |\nu_2\rangle \right) \right|^2 \\
&= \left| \left(\cos^2(\theta) e^{-i\frac{m_1^2}{2E}L} + \sin^2(\theta) e^{-i\frac{m_2^2}{2E}L} \right) \right|^2 \\
&= \cos^4(\theta) + \sin^4(\theta) + \left(e^{-i\frac{(m_2^2-m_1^2)}{2E}L} + e^{i\frac{(m_2^2-m_1^2)}{2E}L} \right) \cos^2\theta \sin^2\theta \\
&= \cos^4(\theta) + \sin^4(\theta) + 2\cos^2\theta\sin^2\theta \cdot \cos\left(\frac{(m_1^2 - m_2^2)}{2} \frac{L}{E} \right)
\end{aligned} \tag{2.9}$$

Setting $\Delta m_{12}^2 \equiv (m_1^2 - m_2^2)$ and using several trigonometric identities, we can reduce Equation 2.9 to:

$$P_{\alpha\to\alpha} = 1 - \sin^2(2\theta)\sin^2\left(\frac{\Delta m_{12}^2}{4} \frac{L}{E} \right) \tag{2.10}$$

Starting from Equation 2.10, it is easy to obtain the probability of detecting a neutrino that oscillates between the flavors α and β since:

$$P_{\alpha\to\beta} = 1 - P_{\alpha\to\alpha} = \sin^2(2\theta)\sin^2\left(\frac{\Delta m_{12}^2}{4} \frac{L}{E} \right) \tag{2.11}$$

This simple two-flavor neutrino model reveals several aspects of the flavor mixing phenomena. The probabilities calculated in Equations 2.10 and 2.11 are dependent on two parameters set by nature: the mixing angle θ which controls the probability amplitude through the $\sin^2(2\theta)$ term and Δm_{12}^2, which is the splitting of the mass between the two states of the neutrino mass and contributes to the frequency term. Its important to note that for any oscillations to occur $\Delta m_{12}^2 \neq 0$, meaning that either m_1^2 or m_2^2 are not both equal and only one can be allowed to be zero. At the same time, if $\theta \neq 0$ or $\pi/2$ and $\Delta m_{12}^2 \neq 0$, the neutrino probability changes as a function of L/E and has a maximum for $L = (2n+1)L_{osc}/2$ with $n = 1, 2, \ldots$ where L_{osc} is the neutrino

oscillation length defined by:

$$\pi\frac{L}{L_{osc}} \equiv \frac{\Delta m^2_{12} L}{4E} \approx 1.27 \times \left(\frac{L}{\text{km}}\right)\left(\frac{\Delta m^2_{12}}{\text{eV}^2}\right)\left(\frac{\text{GeV}}{E}\right) \tag{2.12}$$

The phase responsible for the oscillations is given in terms of the mass splitting, which is known to be on the order of $1 \times 10^{-4}\text{eV}^2$, the oscillation distance L is on the order of kilometers, and the neutrino energy is typically given in GeV (sometimes in MeV).

In general, there is no bound on the number of flavor or mass eigenstates one can have. Equations 2.10 and 2.11 can be generalized to N, the number of neutrino eigenstates. The generalized probability for neutrino oscillations is given by:

$$\begin{aligned} P_{\alpha\to\beta} = \delta_{\alpha\beta} - 4\sum_{k>j}\text{Re}\left(U^*_{\alpha k}U_{\beta k}U_{\alpha j}U^*_{\beta j}\right)\sin^2\left(\left[\frac{1.27\text{GeV}}{\text{eV}^2\text{km}}\right]\frac{\Delta m^2_{kj}L}{E}\right) \\ + 2\sum_{k>j}\text{Im}\left(U^*_{\alpha k}U_{\beta k}U_{\alpha j}U^*_{\beta j}\right)\sin\left(\left[\frac{2.54\text{GeV}}{\text{eV}^2\text{km}}\right]\frac{\Delta m^2_{kj}L}{E}\right) \end{aligned} \tag{2.13}$$

where U is the N-dimensional neutrino mixing unitary matrix, $\Delta m^2_{jk} = m^2_j - m^2_k$ is the neutrino mass splitting, and E is the neutrino energy. Its also important to note that oscillations do not allow for absolute mass measurements; oscillations are sensitive only to the mass splitting terms Δm^2.

The current accepted neutrino model allows for three massive neutrinos leading to two different mass splittings, Δm^2_{21} and Δm^2_{32}. The unitary transformation for this system is given by a 3×3 matrix called the Pontecorvo-Maki-Nakagawa-Sakata (PMNS) matrix [36] [37]. The PMNS matrix is a unitary matrix and is used to relate the flavor and mass eigenstates as a unitary transformation. In the case where $\alpha = e,\mu,\tau$ and $k = 1,2,3$, the transformation takes the form of:

$$\begin{pmatrix} \nu_\text{e} \\ \nu_\mu \\ \nu_\tau \end{pmatrix} = \begin{pmatrix} U_{\text{e}1} & U_{\text{e}2} & U_{\text{e}3} \\ U_{\mu 1} & U_{\mu 2} & U_{\mu 3} \\ U_{\tau 1} & U_{\tau 2} & U_{\tau 3} \end{pmatrix} \begin{pmatrix} \nu_1 \\ \nu_2 \\ \nu_3 \end{pmatrix} \tag{2.14}$$

Any 3×3 unitary matrix allows nine degrees of freedom, but in the case of the PMNS matrix, five of these parameters can be absorbed as phases of the lepton fields. In this case, the PMNS matrix can be described by four free parameters, three flavor mixing angles θ_{12}, θ_{23}, and θ_{13}, and a charge-parity (CP) violating phase, δ_{CP}. With these parameters in mind, the matrix in 2.14 can be rewritten as:

$$U = \begin{pmatrix} c_{12}c_{13} & s_{12}c_{13} & s_{13}e^{-i\delta_{CP}} \\ -s_{12}c_{23} - c_{12}s_{23}s_{13}e^{i\delta_{CP}} & c_{12}c_{23} - s_{12}s_{23}s_{13}e^{i\delta_{CP}} & s_{23}c_{13} \\ s_{12}s_{23} - c_{12}c_{23}s_{13}e^{i\delta_{CP}} & -c_{12}s_{23} - s_{12}c_{23}s_{13}e^{i\delta_{CP}} & c_{23}c_{13} \end{pmatrix} \tag{2.15}$$

With $c_{ij} = \cos(\theta_{ij})$ and $s_{ij} = \sin(\theta_{ij})$. Careful measurements must be made to calculate the mixing parameters. Experimental calculations and methods will be explored in Chapter 3.

2.4 Sterile Neutrinos

Up to this point we have only discussed oscillations in terms of the three neutrino generation hypothesis but in principle, Equation 2.13 is unbounded in the number of neutrinos that can exist. The number of light active neutrino flavor states, that is, those which undergo electroweak interactions, has been determined to be three by measuring Z boson decays in the Large Electron-Proton Collider (LEP) [38] as shown in Figure 2.6. From this, additional neutrinos added to the theory should not interact via the electroweak interaction – so-called "sterile neutrinos" (ν_s).

Although three neutrino oscillation experiments show a good fit to the three-light active neutrino hypothesis, there have been some anomalies that cannot be explained by this model. Short-baseline anomalies (to be explored in more detail in Chapter 3) are defined by discrepancies in the number of neutrinos expected from one flavor oscillating to another, basically violating the results of Equation 2.13 for the case of three neutrinos. These anomalies could point to the existence of a new (sterile) neutrino with a mass of around 1 eV [39].

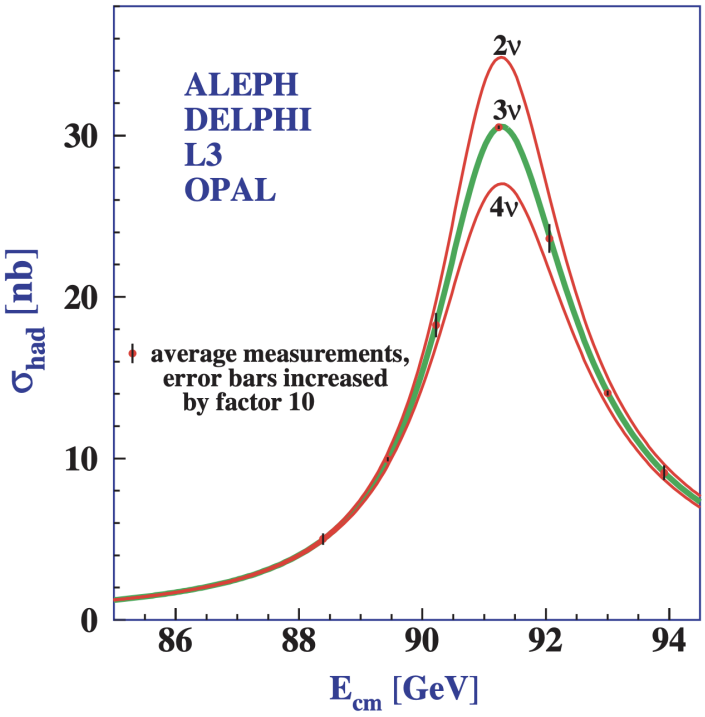

Figure 2.6: The measurement of the hadron cross section around the Z resonance as a function of energy. Each line represents the prediction given an expected number of neutrinos the Z boson can decay into. The data (red points) agree with the three neutrino prediction.

A natural extension of the current neutrino oscillation framework is the $3+1$ model [40]. In this model, we add one additional neutrino flavor state to the light neutrino model, introducing a third mass splitting. Moreover, the mixing matrix in Equation 2.14 gets an additional seven terms, turning the PMNS matrix into a 4×4 matrix with the form of

$$U = \begin{pmatrix} U_{e1} & U_{e2} & U_{e3} & U_{e4} \\ U_{\mu1} & U_{\mu2} & U_{\mu3} & U_{\mu4} \\ U_{\tau1} & U_{\tau2} & U_{\tau3} & U_{\tau4} \\ U_{s1} & U_{s2} & U_{s3} & U_{s4} \end{pmatrix} \tag{2.16}$$

where s corresponds to the sterile neutrino eigenstate. These additional terms $(U_{s1},...,U_{s4})$ cannot be constrained by through direct measurements due to the non-interacting nature of the

added sterile neutrino. This new PMNS matrix is assumed to be unitary and can be parametrized by introducing three new neutrino mixing angles θ_{i4} and two new CP-violating phases.

Noting that our PMNS matrix has changed, this alters the oscillation probability calculated in Equation 2.13 which now takes the following form:

$$P_{\alpha\to\beta} = \delta_{\alpha\beta} - 4(\delta_{\alpha\beta} - U_{\alpha4}U^*_{\beta4})U^*_{\alpha4}U_{\beta4}\sin^2\left(\left[\frac{1.27\text{GeV}}{\text{eV}^2\text{km}}\right]\frac{\Delta m^2_{41}L}{E}\right) \tag{2.17}$$

This equation is valid for $E/L \gtrsim \Delta m^2_{41}$ and $m^2_{41} >> m^2_{21}, m^2_{32}$. This approximation starts to break down for longer baselines or lower energies.

The search for these types of neutrino oscillations can be done using neutrinos produced from accelerators or nuclear reactors. One can further constrain the flavor outcomes taking into account that the tau particles are not produced in these types of experiments due to their high rest mass (1.8 GeV). This allows us to work with sources of ν_e and ν_μ to parameterize the probability of sterile oscillations (Equation 2.17) in terms of U_{e4}, $U_{\mu4}$ and Δm^2_{41}. The three available channels are thus:

$$P_{\nu_e\to\nu_e} = 1 - 4(1-|U_{e4}|^2)|U_{e4}|^2\sin^2\left(\frac{1.27\text{GeV}}{\text{eV}^2\text{km}}\Delta m^2_{41}\frac{L}{E}\right) \tag{2.18}$$

$$P_{\nu_\mu\to\nu_\mu} = 1 - 4(1-\left|U_{\mu4}\right|^2)\left|U_{\mu4}\right|^2\sin^2\left(\frac{1.27\text{GeV}}{\text{eV}^2\text{km}}\Delta m^2_{41}\frac{L}{E}\right) \tag{2.19}$$

$$P_{\nu_e\to\nu_\mu} = 4|U_{e4}|^2\left|U_{\mu4}\right|^2\sin^2\left(\frac{1.27\text{GeV}}{\text{eV}^2\text{km}}\Delta m^2_{41}\frac{L}{E}\right) \tag{2.20}$$

The probabilities calculated above give way to two methods for searching for sterile neutrinos, with Equations 2.18 and 2.19 giving the disappearance channels and Equation 2.20 giving the appearance channel.

Chapter 3

Neutrino Experiments

There exists a wide variety of neutrino sources. Some examples include: β decays during fission in nuclear reactors, fusion of hydrogen into helium in the inner workings of the Sun, cascading particle showers when a cosmic ray hits our atmosphere and from a proton beam hitting a fixed target in particle accelerators.

Sections 3.1 - 3.4 will briefly discuss the experiments carried out with each neutrino source and their contributions to the measurement of neutrino mixing parameters (Equation 2.14). The best-fit values of neutrino mixing parameters are summarized in publications by the Particle Data Group (PDG) [41].

In Section 3.5 we will discuss recent results measuring an excess in the predicted number of events. These anomalous excesses could point to the existence of new physics such as the existence of a sterile neutrino. The discussion will focus on the MiniBooNE low-energy excess, which is the main motivation for the MicroBooNE experiment.

3.1 Solar Neutrino Experiments

Neutrinos are produced in the Sun as products of two forms of nuclear fusion reactions that turn hydrogen into helium, the p-p chain (proton-proton) and the CNO cycle (carbon-nitrogen-oxigen). The p-p chain dominates in a star the size of our Sun producing 99% of solar neutrinos, with the CNO cycle making up the rest of neutrino production. Each stage of both reactions produces neutrinos of different energies and at particular rates. A breakdown of the different stages in the p-p chain and the CNO cycle is shown in Figure 3.1 and the corresponding neutrino flux as a function of energies is shown in Figure 3.2. Neutrinos produced in the first stage of the

p-p chain are around 400 keV; however, neutrinos produced in later parts of the chain have energies of $\mathcal{O}$(10 MeV).

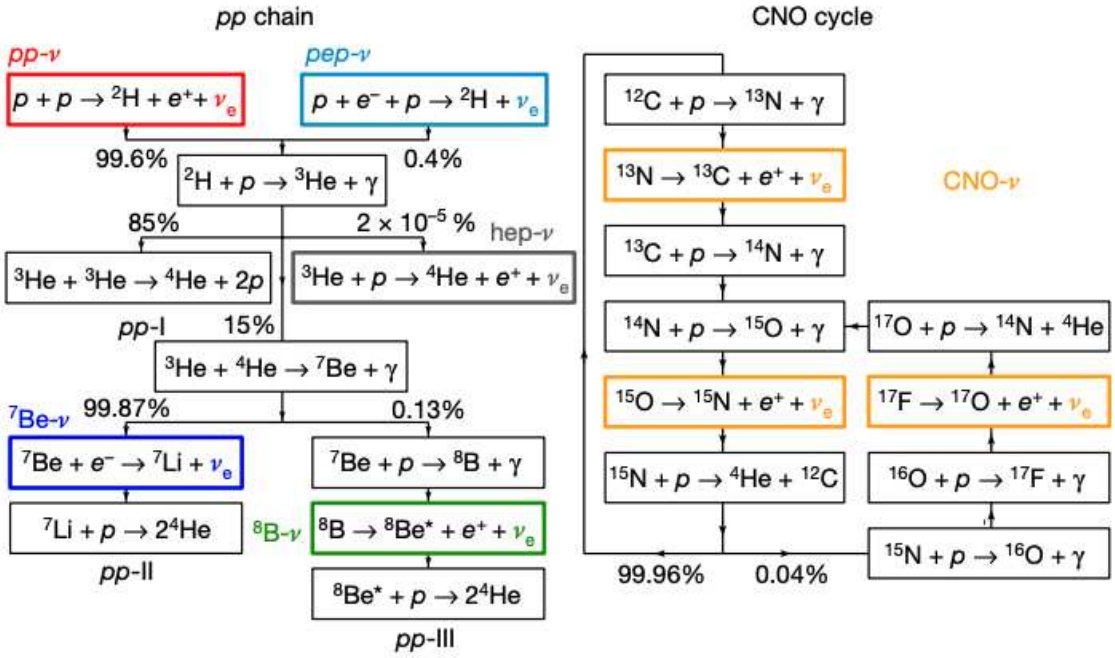

Figure 3.1: Solar neutrino production chains for the p-p chain (left) and the CNO cycle (right) [5].

Solar neutrino experiments were the first to observe neutrino oscillations, with the Homestake experiment making the first measurements in the late 1960s. This experiment measured the number of ^{37}Ar atoms that come from the capture of neutrinos in the following reaction: $\nu_e + {}^{37}\text{Cl} \rightarrow {}^{37}\text{Ar} + e^-$. The unexpected conclusion (at that time) was that the Homestake experiment had measured a third of the predicted number of neutrinos coming from the Sun. Later radiochemical experiments, such as Gallex, GNO, and SAGE, would bring about the same problem. It would not be at the end of the twentieth century that SNO would realize their measurements of the solar neutrino flux and its ν_e content and solve the solar neutrino problem.

Solar neutrinos are the best candidates to measure θ_{12} and Δm_{12} mass splitting. Measurements of these parameters have been performed by neutrino experiments such as the Homestake, GALLEX, SAGE, Borexino, Super-Kamiokande, and SNO experiments. The nuclear reactor experiment, KamLAND, is also sensitive to Δm_{12} due to its long baseline of 180 km. Recent

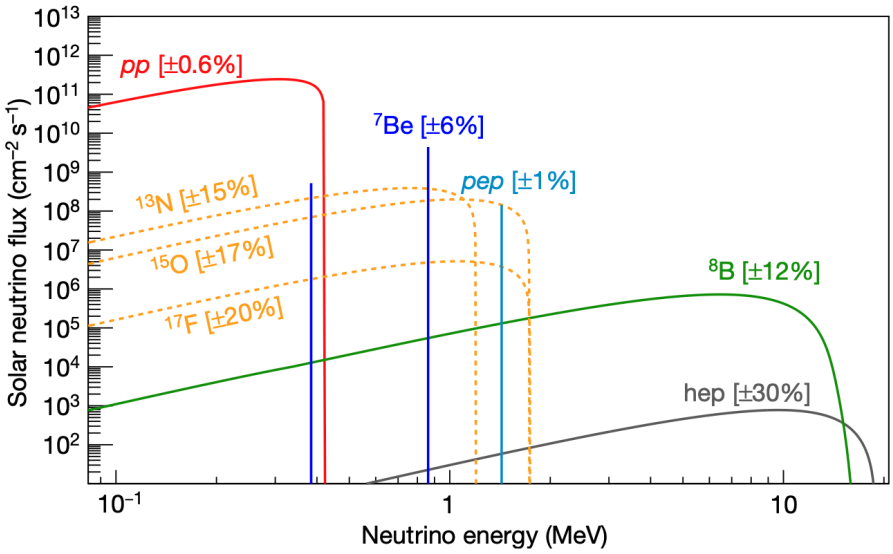

Figure 3.2: Breakdown of the solar neutrino spectrum [5]. The different colored curves correspond to different stages at which the neutrino was produced (see Figure 3.1).

global fit analyses give current 1σ best fit values for these parameters as $\theta_{12} = 34.0 \pm 1.0$ degrees and $\Delta m^2_{12} = (7.50^{+0.22}_{-0.20}) \times 10^{-5}$ eV^2.

3.2 Atmospheric Neutrino Experiments

Heavy particles are constantly hitting Earth's atmosphere, producing a large number of neutrinos. These particles —typically high-energy protons and atomic nuclei—travel through outer space close to light speed and produce hadronic showers somewhere around 15 km above the Earth's surface. These hadronic showers are most commonly composed of charged pions that decay into muons and their respective neutrinos. Furthermore, muons also decay, producing electrons, electron neutrinos, and muon neutrinos (see Figure 3.3). The neutrino energies observed in underground detectors range from about 100 MeV to more than 10 TeV.

In 1998, the Super-Kamiokande Collaboration was among the first to announce experimental evidence for the existence of neutrino oscillations [6]. They measured the atmospheric rate of electron and muon neutrinos using a large Cherenkov detector. What they found was a discrepancy between upward-going neutrinos (those being generated on the other side of the

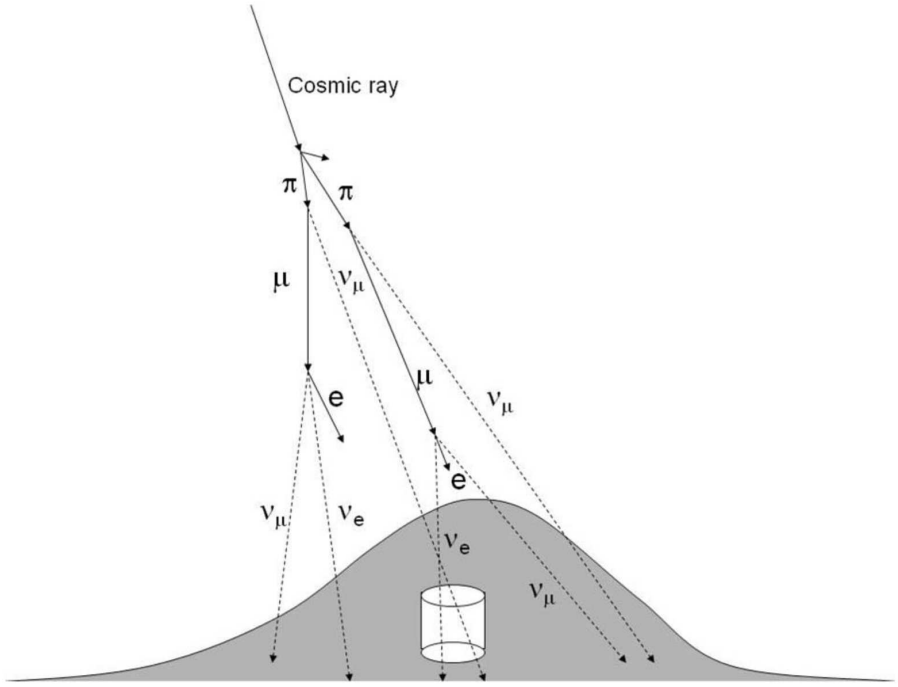

Figure 3.3: Diagram of atmospheric neutrino production [6].

Earth) and downward-going neutrinos coming from the atmosphere. Figure 3.4 shows the results. The explanation for this discrepancy came in the form of neutrino oscillations.

Global fits to atmospheric neutrino data use Super-Kamiokande [42], IceCube [43], and the IceCube DeepCore upgrade [44]. The current 1 σ best-fit value for the atmospheric mixing angle is $\theta_{23} = 49.26 \pm 0.79$ degrees for the normal neutrino mass ordering and $\theta_{23} = 49.46^{+0.60}_{-0.97}$ degrees for the inverted neutrino mass ordering.

3.3 Reactor-Based Neutrino Experiments

Nuclear reactors are an excellent source of neutrinos, or more precisely, antineutrinos. Unstable isotopes such as ^{235}U, ^{238}U, ^{239}Pu, and ^{241}U undergo beta decay and produce antineutrinos with energies of $\mathcal{O}$(1 MeV) [7]. Figure 3.5 shows the neutrino energy spectrum for a given isotope. Compared to other sources of neutrinos, reactor neutrinos come in only one flavor, antielectron neutrinos. These are then detected via inverse beta decays, producing prompt light via e^+e^- annihilation followed another delayed light signal from neutron capture.

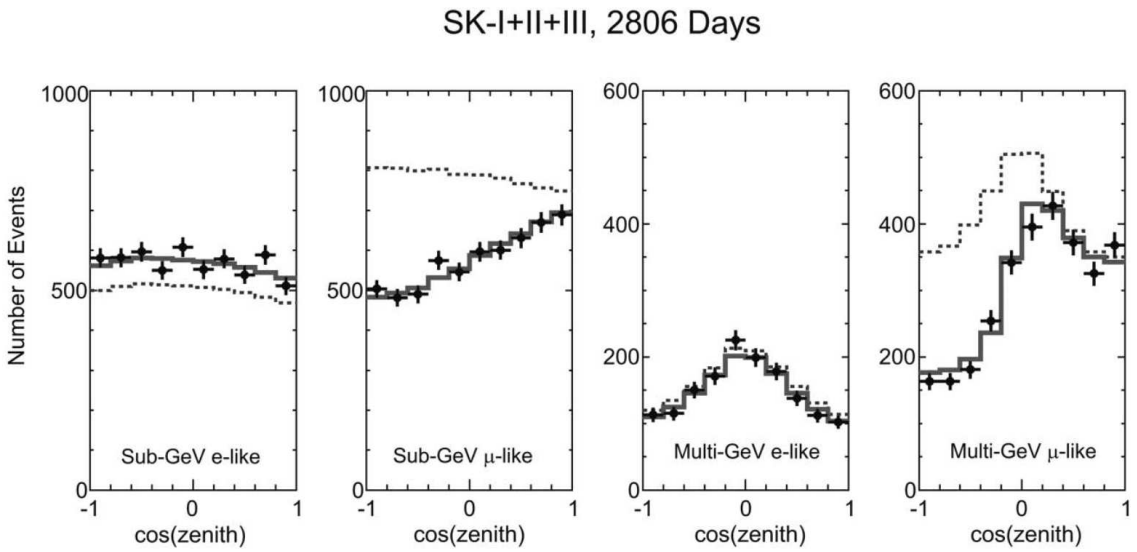

Figure 3.4: Zenith angle distribution of neutrino interaction events at the Super-Kamiokande experiment. Solid and dotted histograms show the unoscillated and oscillated predictions, respectively. The data, represented by the points, clearly favor the neutrino oscillation model [6].

Reactor-based neutrino experiments are sensitive to θ_{13} and Δm^2_{13}. Neutrino experiments such as RENO, Daya Bay, and Double Chooz have contributed to the measurement of these paramaters. The current 1σ global fits for these parameters come to $\theta_{13} = 8.53^{+0.13}_{-0.12}$ degrees and $\Delta m^2_{13} = 2.55^{+0.02}_{-0.03} \times 10^{-3}\text{eV}^2$ in the normal neutrino mass ordering and $\theta_{13} = 8.58^{+0.12}_{-0.14}$ degrees and $\Delta m^2_{13} = 2.45^{+0.02}_{-0.03} \times 10^{-3}\text{eV}^2$ in the inverse neutrino mass ordering.

An open question in reactor neutrino detection is the so-called Reactor Antineutrino Anomaly (RAA). This RAA pertains to a lower $\bar{\nu}_e$ flux measured compared to the prediction. In 2011, both Huber [45] and Muller [46] introduced higher-order corrections to the β decay spectrum used in the prediction of antineutrino spectra. Their findings show a +3% shift in energy-averaged antineutrino fluxes along with shape differences. RAA has been quantified by an observed to predicted ratio of 0.943 ± 0.023 with a deviation from unity at the 98.6% confidence level (CL) [47]. Furthermore, the RAA can be studied in light of a 3+1 model. Figure 3.6 shows the data for all reactor neutrino experiments (up to 2013) and compares them with a light neutrino model and a 3+1 model [8]. A clear preference for the 3+1 neutrino hypothesis is shown.

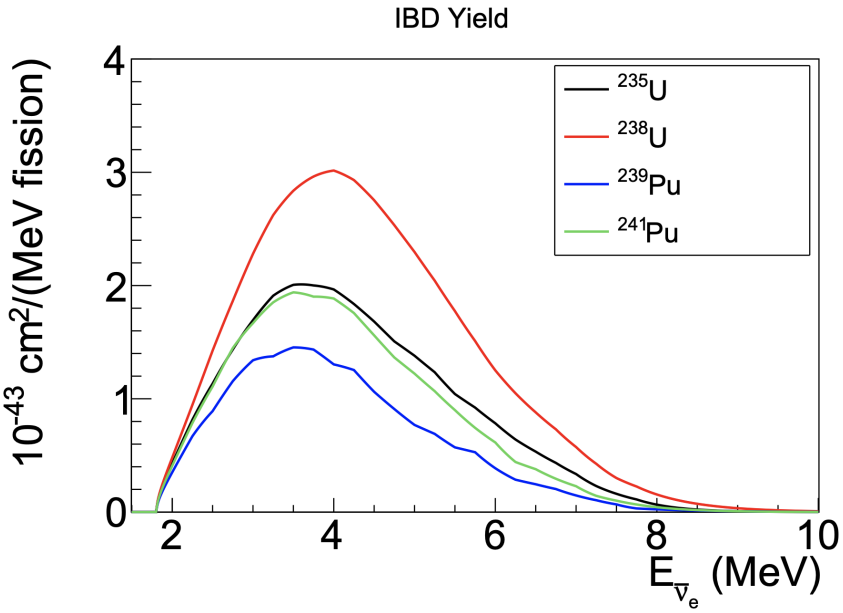

Figure 3.5: Inverse beta decay energy spectra for various nuclear reactor by-products. Figure taken from [7].

3.4 Accelerator-Based Neutrino Experiments

The last type of neutrino production explored and the main focus of this thesis are those produced at a particle accelerator facility. The idea of generating neutrinos comes from Pontecorvo's theory on neutrino production via pion decays [31] and Schwartz's calculations of protons striking a target to produce a collimated neutrino beam [48]. In 1962, the Alternating Gradient Synchrotron at Brookhaven National Laboratory was commissioned, and the first neutrino beam experiment was carried out. The results of this experiment found the existence of two types of neutrinos, ν_e and ν_μ [49]. This result earned Leon M. Lederman, Melvin Schwartz, and Jack Steinberger the Nobel Prize in Physics *"for the neutrino beam method and the demonstration of the doublet structure of the leptons through the discovery of the muon neutrino."*

To produce neutrinos with a particle accelerator, one has to strike protons onto a dense material. Protons are obtained by stripping them from a gas (usually hydrogen) which are subsequently accelerated to near-light speeds creating a proton beam. The proton beam is then forced to collide with a dense material target to produce pions and kaons. The target is inserted into a magnetic focusing horn which helps select the charge of the outgoing mesons depending

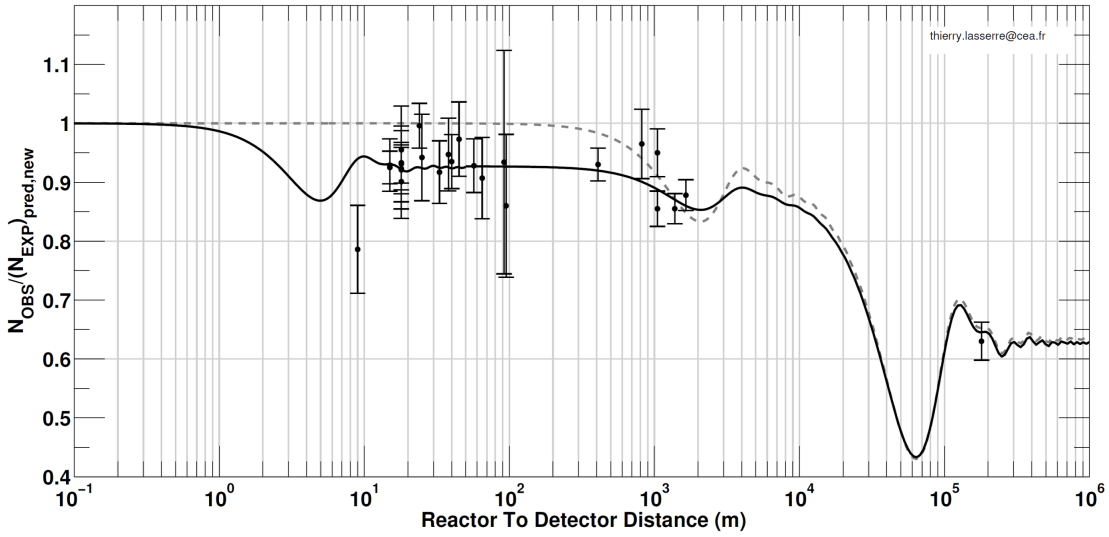

Figure 3.6: Plot of the reactor antineutrino anomaly. The graph shows the ratio of observed and expected events as a function of the detector distance from the reactor for all reactor experiments. Solid and dashed lines represent the three neutrino oscillation model and the 3+1 oscillation model, respectively. Figure from [8].

on the polarity of the magnetic field. This determines whether the resulting beam will be made up of neutrinos or antineutrinos ($\pi^+ \to \mu^+ + \nu_\mu$ or $\pi^- \to \mu^- + \bar{\nu}_\mu$ for example). The pions and kaons then enter the decay region, where long-lived mesons can decay. Finally, following the decay pipe, there is a dump of iron and/or rock that is used to absorb residual hadrons, electrons, and muons. The resulting neutrino energy varies depending on the energy of the proton beam with neutrino energies ranging from $\mathcal{O}$(100 MeV) to $\mathcal{O}$(100 GeV).

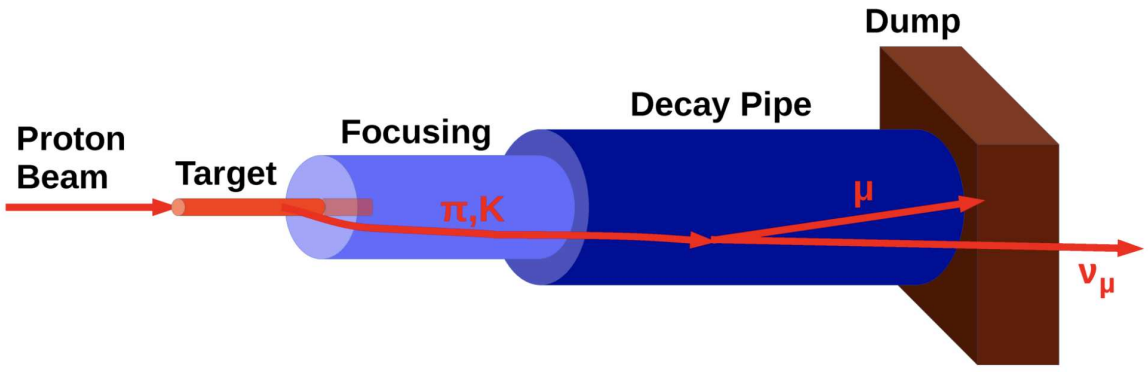

Figure 3.7: Neutrino-beam production process.

To carry out a neutrino oscillation experiment, one needs to know the neutrino energy, flavor, and baseline. Shown in section 2.3, the neutrino oscillation probability $P(\nu_\alpha \rightarrow \nu_\beta)$ (Equation 2.13) depends on two tunable parameters, the distance the neutrinos travel or the baseline L and the neutrino energy E. Accelerator neutrino experiments are generally subdivided into two categories: *long-baseline* and *short-baseline* experiments, depending on the relative ratio of L/E. The goal of short-baseline experiments is to measure minimal neutrino oscillations of the three Standard Model neutrinos. With a detector placed at $\mathcal{O}(1km)$ distance from the neutrino source, L/E is approximately 0, making short-baseline experiments well suited for neutrino modeling and non-standard neutrino oscillations or massive (eV-scale) sterile neutrino searches. Long-baseline experiments, on the other hand, place their detectors where L/E give maximal neutrino oscillations with the aim of measuring the mass splitting and mixing parameters. Both short-baseline and long-baseline neutrino experiments use multiple detectors to minimize systematic uncertainties associated with the neutrino flux and neutrino-nucleus interactions. This two detector scheme allows for the observation of neutrino flavor appearance and disappearance.

3.4.1 Long-Baseline Accelerator Neutrino Experiments

In recent years, several long-baseline accelerator neutrino experiments have offered world-leading complementary results. Experiments of this type are sensitive to $\Delta m^2_{31}, \theta_{23}, \theta_{13}$, the CP-violating phase δ_{CP}, and the neutrino mass ordering.

The Main Injector Neutrino Oscillation Search (MINOS) experiment consisted of two steel scintillator sampling calorimeters, one located at the Fermi National Accelerator Laboratory (Fermilab) and serving as the near detector, and the far detector located 735 km away at the Soudan Mine in northern Minnesota. The neutrino beamline used by MINOS was the NuMI (Neutrinos at the Main Injector) beam, originating at Fermilab. The most recent mass splitting measurements from the MINOS Collaboration report a $\left|\Delta m^2_{32}\right| = [2.28 - 2.46] \times 10^{-3}$ eV^2 (68% CL) and $\sin^2(\theta_{23}) = 0.35 - 0.65$ (90% CL) for normal mass ordering, and $\left|\Delta m^2_{32}\right| = [2.32 - 2.53] \times 10^{-3}$ eV^2 (68% CL) and $\sin^2(\theta_{23}) = 0.34 - 0.67$ (90% CL) for inverted mass ordering [50].

NOvA (NuMI Off-Axis ν_e Appearance) and T2K (Tokai-to-Kamioka) are two current-generation neutrino oscillation experiments, both having the primary goal of measuring θ_{13} by looking at ν_e appearance in a ν_μ beam. NOvA, like MINOS, uses the NuMI beamline and both experiments share the same near- and far-detector sites having a baseline of 810 km. The T2K experiment is based in Japan, the near detector is housed at the J-PARC facility in Tokai on the east coast of Japan, and the far detector is the Super-Kamiokande detector with a 295 km baseline. Both T2K and NOvA are 'off-axis', meaning that the far detector is around 2° from the axis of the beamline. This produces a more monochromatic neutrino energy spectrum to maximize neutrino oscillations and allows for more precise measurements in specific phase spaces. Recent combined results from NOvA and T2K show maximum θ_{23} (which determines the ν_μ and ν_τ components of ν_3) mixing at more than 90% CL and a reduction in sensitivity in the CP violating phase (δ_{CP}) in normal mass ordering [51] with recent results showing a tension at more than 90% CL for 2 degrees of freedom in the determination of δ_{CP} [52]. Future joint analysis efforts are underway, allowing these experiments to make significant measurements before the next generation of neutrino experiments.

The future of long-baseline neutrino experiments looks to have larger far detectors and higher power neutrino beams. Hyper-Kamiokande [53], which will be an upgrade to the T2K experiment, will use the same Cherenkov water technology as its predecessor, but with an active fiducial volume 25 times larger than the current iteration. In the US, the Deep Underground Neutrino Experiment (DUNE) [54] will use liquid argon time projection technology for its neutrino detection paradigm. The latter technology will be explored in Chapter 4 as it is the same technology employed in the main analysis of this thesis.

3.5 Short-Baseline Anomalies

Up to this point, we have focused on the results for the three active neutrino oscillation hypothesis. However, there has been some excitement in the neutrino field produced by anomalous observations that appear to be in tension with the three-flavor neutrino model. Such anoma-

Table 3.1: Global data measured three flavor oscillation parameters up to the 1σ Best-Fit (BF) and the 3σ range. Note that $\Delta m^2_{3\ell} \equiv \Delta m^2_{31} > 0$ for normal hierarchy and $\Delta m^2_{3\ell} \equiv \Delta m^2_{32} < 0$ for inverted hierarchy. Values taken from [1].

	Normal Mass Ordering		Inverted Mass Ordering	
Parameter	1σ BF	3σ range	1σ BF	3σ range
$\theta_{12}(^\circ)$	$33.44^{+0.77}_{-0.74}$	$31.27 \rightarrow 35.86$	$33.45^{+0.78}_{-0.75}$	$31.27 \rightarrow 35.87$
$\theta_{23}(^\circ)$	$49.2^{+0.9}_{-1.2}$	$40.1 \rightarrow 51.7$	$49.3^{+0.9}_{-1.1}$	$40.3 \rightarrow 51.8$
$\theta_{13}(^\circ)$	$8.57^{+0.12}_{-0.12}$	$8.20 \rightarrow 8.93$	$8.6^{+0.12}_{-0.12}$	$8.24 \rightarrow 8.96$
$\delta_{CP}(^\circ)$	197^{+27}_{-24}	$120 \rightarrow 369$	282^{+26}_{-30}	$193 \rightarrow 352$
$\Delta m^2_{21}(10^{-5}\text{eV}^2)$	$7.42^{+0.21}_{-0.2}$	$6.82 \rightarrow 8.04$	$7.42^{+0.21}_{-0.2}$	$6.82 \rightarrow 8.04$
$\Delta m^2_{3\ell}(10^{-3}\text{eV}^2)$	$+2.517^{+0.026}_{-0.027}$	$+2.435 \rightarrow +2.598$	$-2.498^{+0.028}_{-0.028}$	$-2.414 \rightarrow -2.518$

lies may indicate some mismodeled or unknown background or, more excitingly, an additional nonactive (sterile) neutrino. Although the experimental evidence in favor of the sterile neutrino hypothesis has been mixed, anomalies measured by short-baseline experiments have fueled this interpretation in the last 30 years [55]. This section will cover the LSND and MiniBooNE anomalous measurements in the low-energy region, key observations motivating the MicroBooNE experiment.

3.5.1 LSND

The Liquid Scintillator Neutrino Detector (LSND) was an experiment that ran from 1993 to 1998. It was located at Los Alamos National Laboratory with the aim of measuring neutrino oscillations by looking at the byproducts of inverse beta decay produced from accelerator neutrinos:

$$\bar{\nu}_\mu \xrightarrow{\text{oscillation}} \bar{\nu}_e + p \rightarrow e^+ + n \tag{3.1}$$

The neutrino beam was produced by firing 0.8 GeV protons onto a target to produce a muon antineutrino source with a $0-53$ MeV energy spectrum. The liquid scintillator detector was placed 31 meters from the target. In 2001, the LSND Collaboration reported a significant excess of $\bar{\nu}_e$ events [56] as shown in Figure 3.8b. The data points are overlayed over a series of predictions, with the blue histogram representing the contribution of an additional oscillation.

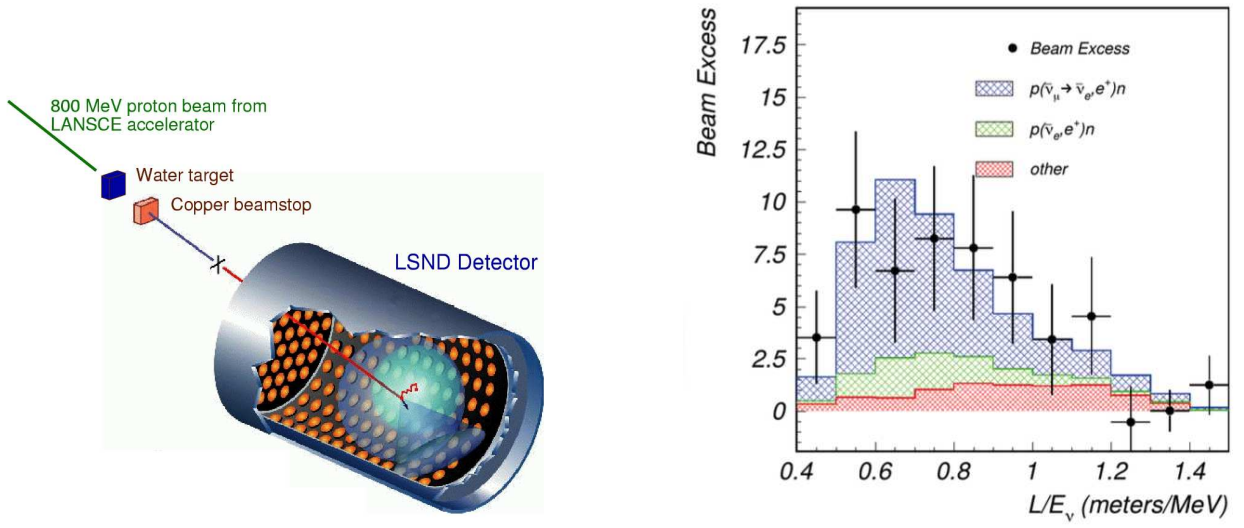

(a) LSND detector schematic

(b) LSND excess

Figure 3.8: Schematic of the LSND detector (left) and a plot of antineutrino events measured in terms of L/E. The red and green histograms represent the expected backgrounds while the blue histogram assumes an oscillation with a mass splitting of $\Delta m^2 \sim 1\text{eV}^2$ (right).

The implication of this oscillation could be the result of a new mass splitting of $\Delta m^2 \sim 1$ eV^2, significantly higher than previously measured (see Table 3.1).

3.5.2 MiniBooNE

Following the surprising results of LSND, the MiniBooNE experiment was proposed to determine the validity of the observed anomaly in Los Alamos. MiniBooNE consisted of a large Cherenkov mineral oil detector built on the Booster Neutrino Beamline (BNB) at Fermilab. A schematic of the detector is shown in Figure 3.9a. The BNB could be run in both neutrino and anti-nuetrino mode with an energy peak of around 800 MeV. The detector was 541 meters from the beam source, and although its L differs from that of LSND, the ratio L/E is still comparable.

The body of the detector is a 12 m radius sphere filled with 10 million liters of mineral oil. It was instrumented with 1280 8-inch photomultiplier tubes (PMTs) with an additional 240 PMTs in its outer shell, which was used as a veto region for cosmic rejection. The main mode of signal production is through Cherenkov radiation, that is, the light produced by a charged particle when it travels faster than the speed of light in a given medium. Cherenkov radiation is emitted

in the form of a light cone and is detected by the signal region PMTs, manifesting as a signal ring. The kinetic energy threshold for Cherenkov radiation production is dependent on the mass of the particle; this makes Cherenkov detectors insensitive to more massive particles such as protons and neutrons, favoring lighter particles such as electrons/positrons and muons.

The anomalous channels that were studied at MiniBooNE were as follows.

$$\nu_\mu \xrightarrow{\text{oscillation}} \nu_e + n \rightarrow e^- + p \tag{3.2}$$

$$\bar{\nu}_\mu \xrightarrow{\text{oscillation}} \bar{\nu}_e + p \rightarrow e^+ + n \tag{3.3}$$

Here, the final-state leptons are the key indicators of the neutrino interaction. Muon production is indicative of a ν_μ interaction, while electromagnetic activity can be attributed to ν_e or π^0 events. Muons travel in long straight paths and give off a sharp Cherenkov ring signature. Final-state electrons from CC neutrino scattering, on the other hand, are observed as "fuzzy" and less-defined rings because of the cascade of particles involved in the production of elec-

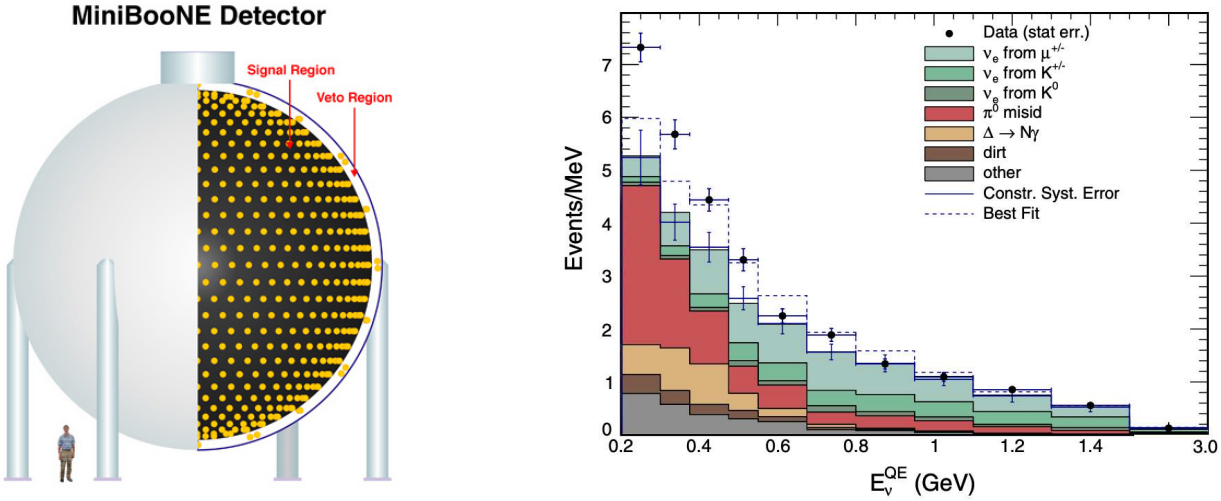

(a) MiniBooNE detector schematic

(b) MiniBooNE low-energy excess [57]

Figure 3.9: Schematic of the MiniBooNE detector (left) and a plot of neutrino-like events measured as a function of the neutrino energy spectrum (right). A clear excess is observed at lower energies. The different colored histograms represent the expected backgrounds with flux and cross section constrained systematic uncertainties represented by the vertical lines on the histograms. The best-fit 3+1 sterile neutrino model is represented by the dashed line.

tromagnetic showers. Electromagnetic showers are also produced by π^0 decays ($\pi^0 \rightarrow \gamma\gamma$) and subsequent γ pair production, where $e^- e+$ pair production will create two fuzzy rings of light, which can overlap and be confused as a single-electron shower event. Similarly, one of the showers can exit the detector leaving only the other shower to be detected, resulting in a ring identical to an electron shower. Processes like these can make it difficult for Cherenkov detectors to discriminate between photons and electrons. Therefore, it is possible for the excess to be an underestimated background involving photons or electrons.

Although MiniBooNE was designed to explain the excess observed by LSND, it also measured an excess of ν_e-like events. Recent results show a excess of events in the $E_{\nu_e} \leq 600$ MeV region with a 4.8σ significance. Figure 3.9b shows the data significantly higher than the expected backgrounds represented by the histograms and is also higher than the best-fit prediction for the 3+1 sterile neutrino model given by the dashed line. A joint analysis using LSND and MiniBooNE data reports consistency in the energy and magnitude of the events and shows a significance of 6.0σ for the two combined experiments [58].

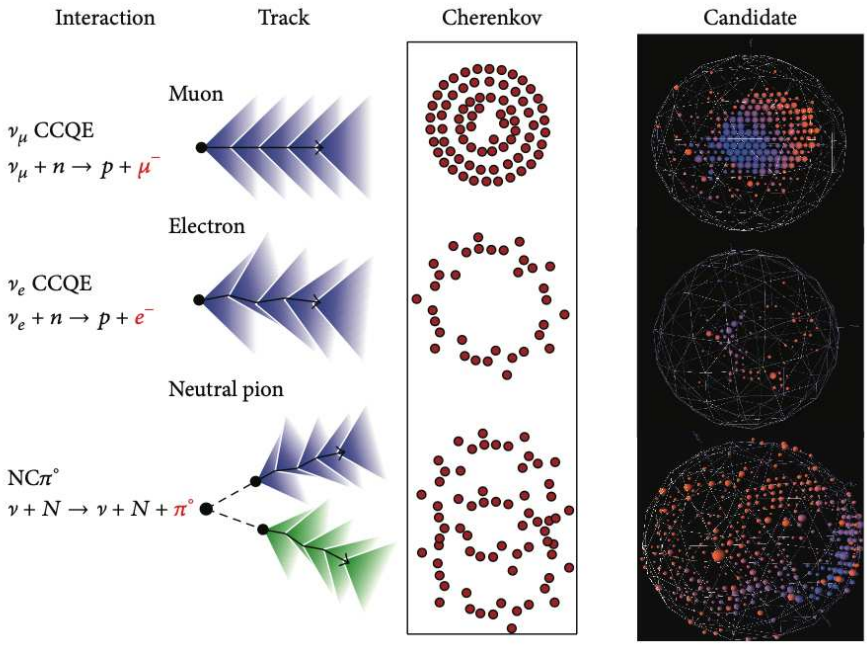

Figure 3.10: MiniBooNE signal formation. Taken from [9].

Three background categories can manifest themselves as the culprits for the MiniBooNE LEE: intrisic ν_e, misidentified π^0, and/or misidentified $\Delta \rightarrow N\gamma$ events. The intrinsic ν_e content of the beam is an irreducible background that makes it impossible to distinguish between ν_μ and ν_e oscillations. Oscillations of the type $\nu_\mu \rightarrow \nu_s \rightarrow \nu_e$ could be an explanation for the LEE. The misidentified π^0 content is the largest background. Although these types of events present a challenge to reconstruct, the MiniBooNE collaboration has constrained their contribution by reconstructing the π^0 invariant mass [59]. Misidentified $\Delta \rightarrow N\gamma$ events are those produced by a Δ resonance that electromagnetically decays into a neutron or proton and emits a photon. This channel is constrained by the NC π^0 measurement with a 12.2% uncertainty [59].

Investigations into these background sources are needed to determine if the MiniBooNE LEE is photon-like or electron-like. The MicroBooNE experiment was constructed to investigate the LEE by using liquid argon time projection (LArTPC) technology. This type of neutrino detector is key for distinguishing between photon-like and electron-like hypothesis for the LEE. The LArTPC technology will be covered in the next chapter.

Chapter 4

The Liquid Argon Time Projection Chamber

Liquid Argon Time Projection Chambers (LArTPCs) are a principal technology of choice for modern neutrino detectors by offering excellent calorimetric and topological measurements of charged particles passing through its liquid argon medium. LArTPCs are a modern update to David Nygren's original gas-filled time projection chamber by using a denser medium in liquid argon which allows for a greater number of interactions [60]. They are a key piece in the United State's neutrino program with MicroBooNE being the longest running LArTPC neutrino experiment and with the upcoming DUNE experiment making use of the largest LArTPC ever to be constructed. This chapter presents the general working principle for LArTPCs, as well a case study of ICEBERG, a small LArTPC used as an electronics test stand for DUNE.

Section 4.1 will provide the general working principle of LArTPC technology, and subsections 4.1.1 and 4.1.2 will give more details of the light and ionization signals expected at LArTPCs, respectively. Section 4.2 will describe the ICEBERG detector (section 4.2.1), the cold electronic prototypes being tested (section 4.2.2), crosstalk measurements (section 4.2.3), detector operations (section 4.2.4) and electron lifetime measurements (section 4.2.5).

4.1 The LArTPC Technology

In 1974, William Willis and Veljko Radeka proposed the idea of using liquid argon (LAr) ionization chambers as a total absorption calorimeter. LAr is easy to ionize and also provides scintillation light, making it a good candidate for recording electromagnetic activity incoming from particle interactions. Ionizing particles crossing the LAr medium also produce scintillation light, which can be used for trigger and timing purposes. Two years later, Nygren proposed the concept of a time projection chamber (TPC), which allowed for three-dimensional reconstruction

of charged particle activity in a fully active volume. In 1977, Carlo Rubbia proposed a new idea for neutrino detection using LAr as a medium in a TPC, making the LArTPC a reality.

The use of LArTPCs offers novel methods to answer open questions in neutrino physics. Given their fine spatial granularity and excellent charge resolution, LArTPC detectors allow one to discriminate between different neutrino flavor interactions as well as provide handles to identify backgrounds. The design behind LArTPCs is based on a multiwire-plane anode and a cathode plane separated by a long drift distance to create an electric field in a large volume of LAr. The main components of a generic LArTPC are: the anode plane, a cathode plane, a field cage (FC), and a photon detection system (PDS). A cartoon drawing a LArTPC and its components is shown in Figure 4.1. The FC is held at both ends by the anode plane and the cathode plane. These two planes create a uniform electric field making the volume between the planes active for charged particles. These three components comprise the TPC and are placed inside a cryostat that is filled with LAr and kept at cryogenic temperatures. Impinging charged particles leads to ionization of argon, and the ionization electrons are subsequently picked up by the anode-plane sensing wires. Events are then reconstructed by taking two dimensions from the location of detected ionization on the wire planes and a third from the time the drifting electrons produce a signal on the wires. Scintillation light produced from due to the ionization particles and the LAr and collected by the PDS for the purposes of event triggering and timing of the event. This design choice makes LArTPCs high-resolution tracking calorimeters allowing for detailed reconstruction of charged particle trajectories and energy deposition.

4.1.1 Light Production

An attractive quality about LAr is that it is transparent to light and, more importantly, it is transparent to its own scintillation light. Scintillation light inside a LArTPC is produced by the deexcitation of argon dimers, which are produced in the argon because of its interaction with charged particles. The number of photons released by minimum-ionizing particles (muons, pions, etc.) is roughly 40,000 photons per MeV at zero electric field [61] and decreases by a factor of two at

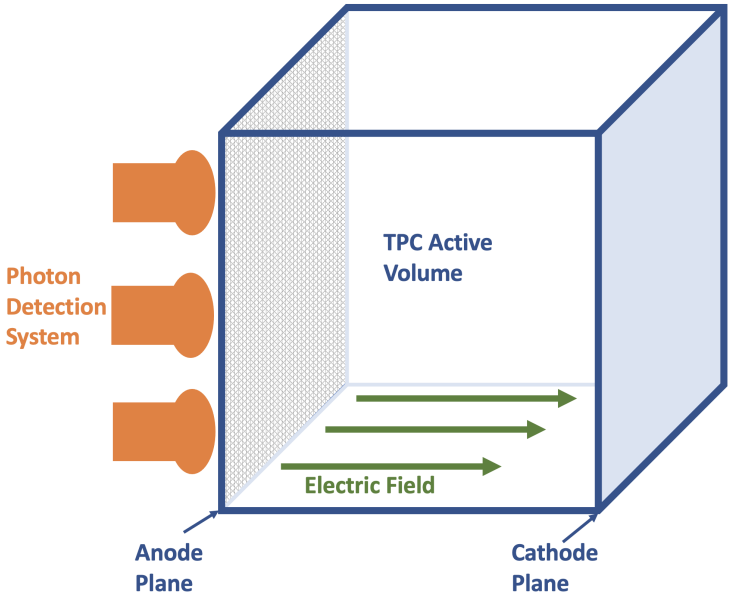

Figure 4.1: A cartoon of a generic LArTPC detector. The anode and cathode are placed opposite of each other. The anode is made out of several planes of sensing wires oriented at different angles while the cathode is made out of conductive material. An electric field is created between the anode and cathode planes. A photon detection systems can be placed behind the anode plane wires.

an electric field of $\mathcal{O}(100 V/cm)$. Scintillation light is produced via two methods:

$$Ar \rightarrow Ar^* \rightarrow Ar_2^* \rightarrow 2Ar + \gamma \tag{4.1}$$

$$Ar \rightarrow Ar^+ \rightarrow Ar_2^+ + e^- \rightarrow Ar_2^* \rightarrow 2Ar + \gamma \tag{4.2}$$

Self-trapped exciton luminescence (Equation 4.1) occurs when an argon atom becomes electromagnetically excited by an ionizing particle, which then is trapped by another similarly excited argon atom producing an excited dimer, which then de-excites by photon emission. Scintillation light from recombination luminescence is described by Equation 4.2 and occurs when argon ions combine to form an ionized argon molecule (Ar_2^+), which then combines with a free electron to form an excited argon dimer (Ar_2^*). In both cases, the excited argon dimer then decays to two ground-state argon atoms and a photon in the ultraviolet spectrum with a wavelength of 128 nm.

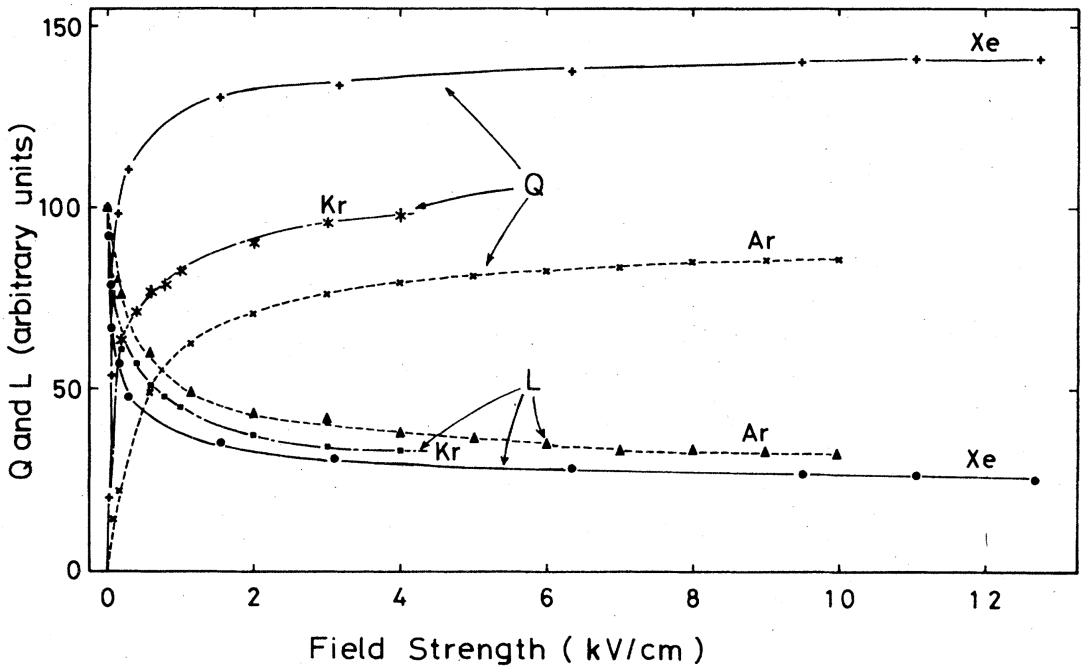

Figure 4.2: Anti-correlation of light and charge yields for different noble elements in the liquid state at increasing electric field strength values. The operation of the typical LArTPC lies around the 500 V/m electric field in order to obtain similar amounts of light and charge from each event [10]

.

The recombination and excitation light production processes are dependant on the magnitude of the applied electric field. Figure 4.2 shows the relationship between the electric field strength and the amount of charge (Q) and light (L) produced for three noble gases (xenon, krypton and argon). A larger field reduces the recombination process and, therefore, reduces the amount of light produced for an event but increases the amount of ionization electrons produced, while a smaller field increases light production but minimizes the ionization signal received at the wire planes. An electric field of 500 V/cm is often chosen for LArTPC neutrino experiments to obtain a balance of both charge and light production.

4.1.2 Ionization Signal

Inside the LArTPC, charged particles traveling through the detector will produce ionization electrons and scintillation light through ionization and excitation of argon atoms. The resulting ionization electrons are created within an electric field and are guided towards the anode

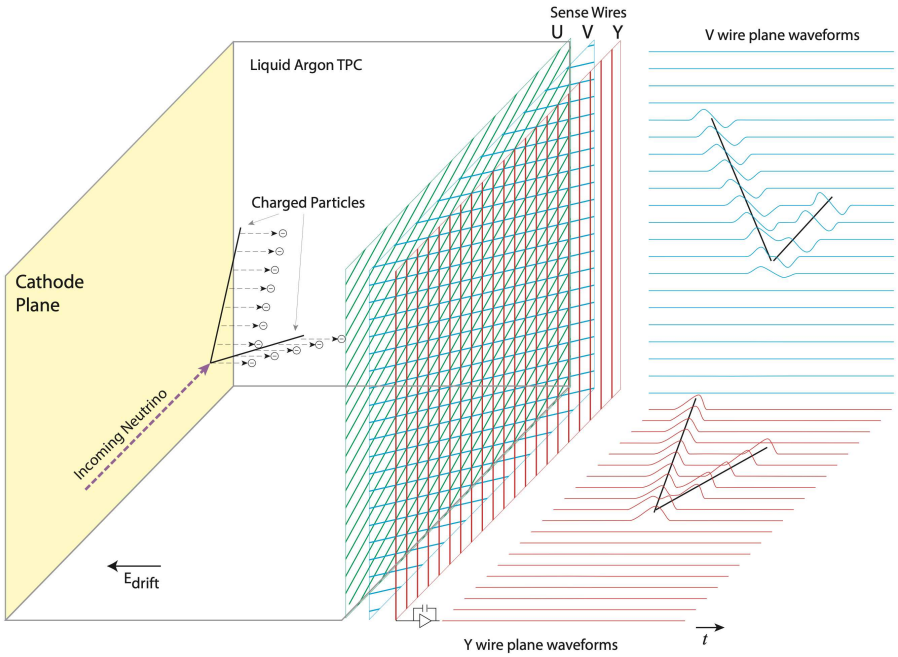

Figure 4.3: Diagram of LArTPC neutrino detection. Impinging charged particles produce ionization electrons within the LAr. These electrons are then drifted towards the readout wire planes by the electric field. The signals produced are then used to reconstruct the neutrino event.

plane. The anode plane consists of wire planes placed in different orientations to facilitate the reconstruction of neutrino events in three dimensions. Wire planes consist of one or more "induction" planes and a "collection" plane, which is the outermost wire plane where all of the ionization charge is captured. Figure 4.3 shows the operation of a typical LArTPC neutrino detector with three wire planes.

The induction planes are held at different voltages from the collection plane such that the electric field lines end at the latter, thus creating a local electric field that promotes the ionization charge to move towards the collection plane. As the ionization cloud drifts past each of the wire planes, a current is induced on the wires, appearing as a bipolar pulse on the induction wires and a unipolar pulse on the collection wires. An image of the response signals for a LArTPC is shown in Figure 4.4. A two-dimensional image is formed by the signal produced on each wire plane over time. An image of a typical LArTPC neutrino event can be seen in Figure 4.5. An additional plane, called the "grid plane", may also be included as an additional wire

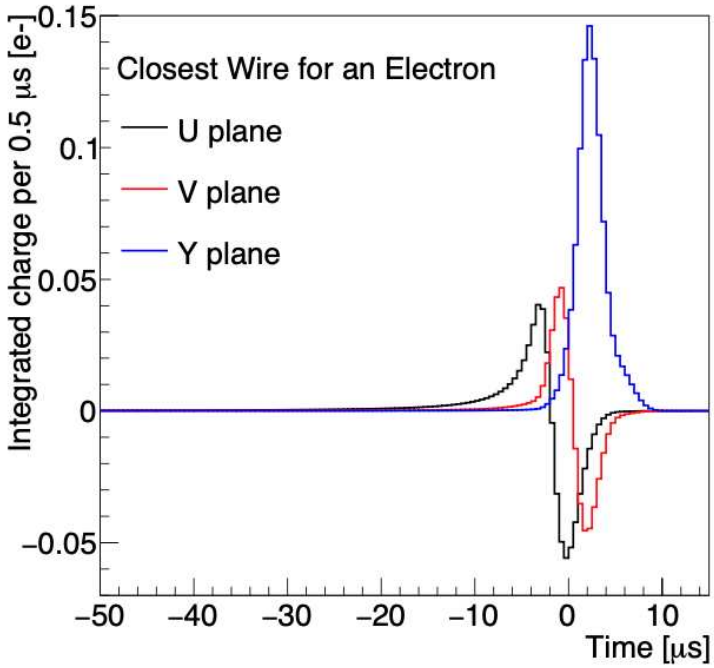

Figure 4.4: Average time-domain response signal for induction planes (red and black) and the collection plane (blue) [11]

plane to shield the signal wire planes from distant drifting electrons, which can cause distortions in the signal on the first induction plane, giving an asymmetric bipolar pulse [62].

About 4×10^4 electrons are released for every MeV of energy deposited in an interaction. The liberated electrons continuously drift towards the wire anode planes, preserving the topological and calorimetric information from the interacting charged particle. Two effects inside the TPC can prevent electrons from reaching the wire readout: electron-ion recombination and attachment of ionization electrons to electronegative impurities in the detector.

Ion recombination occurs when drifting electrons are captured by neighboring argon ions and recombine into neutral argon atoms. Drifting electrons are thermalized by interactions with the neighboring medium. Recombination depends on the electric field strength and the local ion density. Larger electric fields allow for ionization electrons and argon atoms to separate and reduce the chance of recombining.

Argon is characterized as being non-reactive to free drifting electrons, making it ideal for minimizing attenuation of the ionization signal. However, small impurities in the LAr, mostly

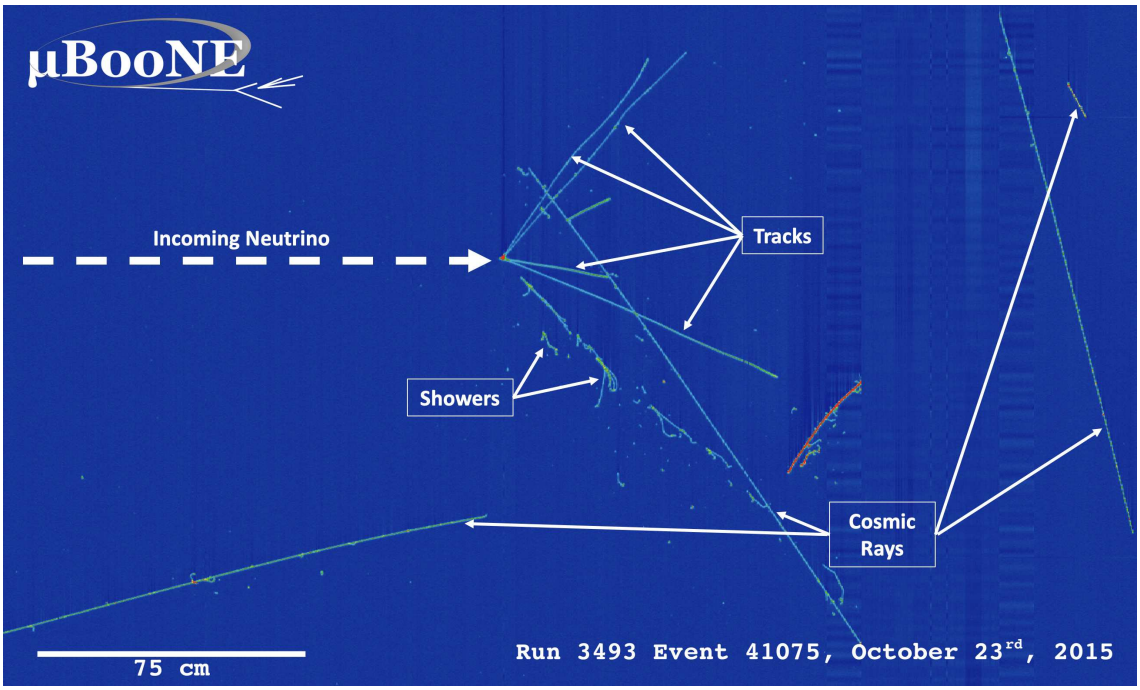

Figure 4.5: Image of a neutrino interaction in the MicroBooNE detector where several tracks and a couple of showers are produced. The color indicates the amount of charge deposited by the ionizing particles.

oxygen and water can attenuate the signal by absorbing the drifting electrons. Impurities can effectively reduce the amount of charge drifting towards the anode plane, which hinders calorimetric and topological reconstruction of the event. A useful metric to determine the purity inside a LArTPC is that of the electron lifetime, which is defined as the average time it takes for a drifting ionization electron to be captured by a contaminant.

4.2 LArTPC Case Study: The ICEBERG Test Stand

LArTPC technology has been instrumental in the advancement of neutrino physics. The R&D work by current and past LArTPC neutrino experiments has advanced the maturity of the technology and further increased the understanding of LArTPCs to the neutrino community. Pioneering experiments such as ICARUS and MicroBooNE are successfully using LArTPCs to take data for analysis and have paved the road to building what is going to be the largest LArTPC experiment ever built to date, the Deep Underground Neutrino Experiment (DUNE).

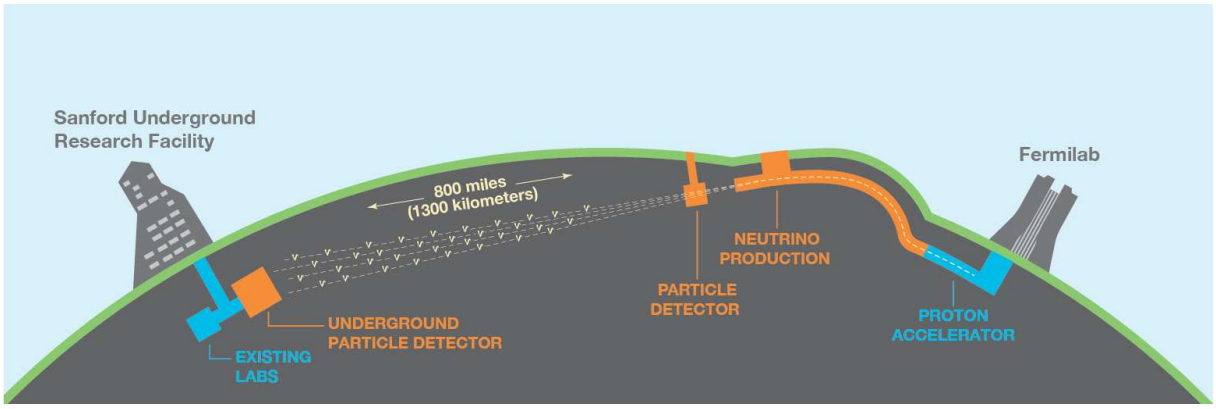

Figure 4.6: Cartoon showing the configuration of the Deep Underground Neutrino Experiment. Neutrinos produced at Fermilab will be sent 1300 km to SURF where the far detector will be located.

DUNE will consist of a neutrino beam and two neutrino detectors, a near detector located close to the neutrino beam at Fermilab and a far detector located 1.5 km underground at the Sanford Underground Research Facility (SURF) in Lead, South Dakota. The two detectors will observe neutrinos originating at Fermilab with the far detector being 1300 km away from the neutrino source along the beamline. It is critical for the DUNE far detector to maximize the signal-to-noise ratio in order to select events of interest and carry out physics measurements. Events of interest include (but are not limited to) beam neutrino interaction events, candidate proton decay events, and potential supernova burst neutrinos from stellar core-collapse supernovae. A high signal-to-noise ratio enables these measurements to be made possible by providing lower thresholds for charged particle detection and by improving the charge resolution, and thus the energy resolution of reconstructed particles in the detector. One key feature of the DUNE far detector design is the use of cryogenic electronics mounted on the TPC wire planes, which allows for very low noise levels in the charge readout and correspondingly high signal-to-noise ratio for signal events of interest in the LArTPC.

Part of the DUNE far detector development program involves prototyping smaller versions of the far detector. Each far detector module will consist of a TPC, cold electronics (CE), and a photon detection system (PDS) all submerged in LAr within a shielded and grounded cryostat; ProtoDUNE, a smaller version of the DUNE far detector located at CERN, has provided a test

run (in a charged particle beam) for the detector components that are to be used at the DUNE far detector [63]. However, in the case of cryogenic electronics, research and development efforts continue in order to increase the performance and reliability beyond that of the cryogenic electronics being used at ProtoDUNE. The Integrated Cryostat and Electronics Built for Experimental Research Goals or ICEBERG serves as a fully instrumented TPC in which to test new cryogenic electronics designs, providing a realistic wire load in a grounded and shielded cryostat exposing the prototype electronics to operating detector conditions expected at DUNE.

4.2.1 The Experimental Setup

ICEBERG is a test LArTPC set-up that involves equipment and facilities available at Fermilab, including a cryostat, feedthroughs, and infrastructure to house the cryostat. ICEBERG provides a LAr detector R&D environment for the purpose of testing CE prototypes. The cryostat allows for a rapid turnaround in testing new CE configurations. The testing procedure consists of draining the LAr in the ICEBERG detector, installing new CE, filling the cryostat again with LAr, and beginning taking cosmic data again once the system satisfies basic checks of wellness.

ICEBERG is installed in the Proton Assembly Building at Fermilab. The cryostat, shown in Figure 4.7, consists of a large circular cylinder capable of holding a volume of 35,000 liters of LAr. The ICEBERG TPC is 115 cm tall, 100 cm wide, and has a width of 60 cm with the FC constructed from printed circuit board. It houses 1,280 sensing wires on a DUNE anode plane assembly (APA) with two drift volumes of 30 cm, one on each side of the APA. The dimensions of the APA are those of $1/10^{\text{th}}$ of a DUNE APA (Figure 4.8 shows a full-sized DUNE APA). The APA frame sensing wires are laid in three planes oriented at different angles: The two induction planes (U and V planes) are located at at $\pm 35.7^{\circ}$ respectively and the collection plane (X plane) wires run vertically. An additional wire plane, the grid plane G, is located in front of the first induction plane. The G plane is not used for signal recollection but rather to improve signal shape on the U plane. The signals induced on the wire planes are transferred to the front-end (FE) readout of the CE mounted on the APA in the LAr.

Figure 4.7: The ICEBERG cryostat.

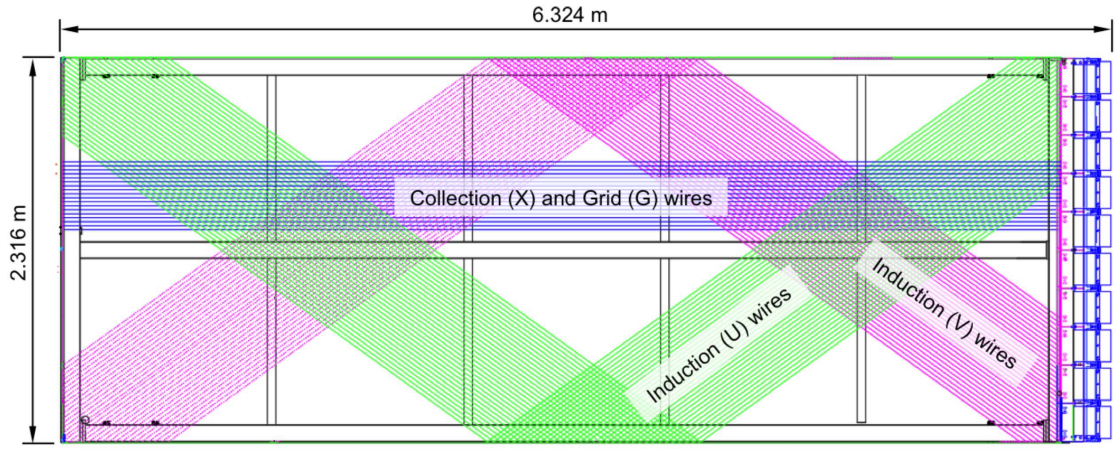

Figure 4.8: The DUNE single-phase far detector APA wire wrapping configuration showing an example using portions of the wires from the three signal planes (U, V, Y) and the grid plane. The TPC electronics sit atop the APA (blue boxes on the right) [12].

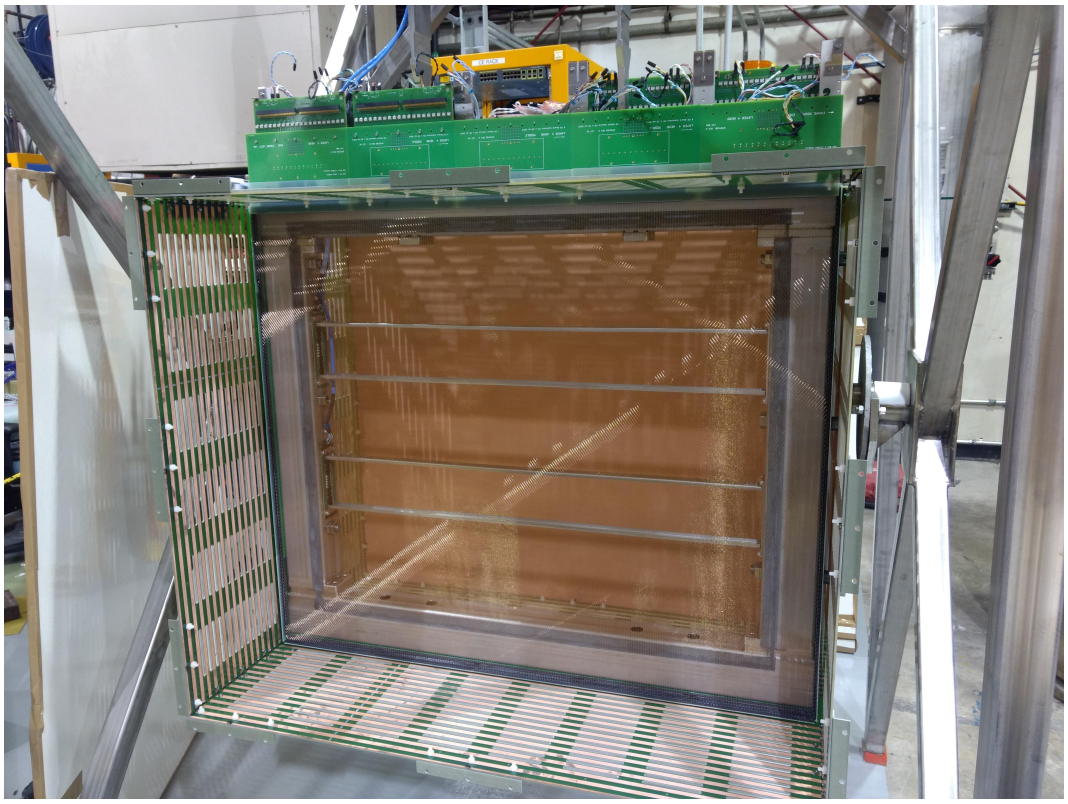

Figure 4.9: The ICEBERG field cage.

The ICEBERG FC, shown in Figure 4.9, is made of printed circuit board material and provides 30 cm of drift length on both sides of the APA. On the opposite sides of the APA are the cathode planes, which consists of circuit boards coated with copper. The cathode planes are powered to -15 kV and a series of 1 GΩ resisters creates a constant voltage gradient inside the TPC that ends with -1 kV near each sides of the APA.

Grounding and shielding play a critical role in reducing the amount of noise allowed in the detector. This involves minimizing the amount of noise on the readout of the APA wire planes. To achieve this, sources of noise inside the cryostat are kept at a minimum through the careful monitoring of ground connections and throughout the readout chain of other detector components, such as the PDS, the high-voltage system, and the cryogenic instrumentation. The cryostat encases the components in the detector and creates a nearly perfect Faraday cage, minimizing noise on the sensing wire planes. The currents used to operate the components inside the detector are controlled to avoid unwanted disturbances that would result in detector noise.

ICEBERG uses the same grounding and shielding principles applied in ProtoDUNE, including the power system that supplies power to the detector; all of its components are connected to an isolated ground separate to the building via a 480 V transformer. The impedance between the detector and the building grounds is continuously monitored.

4.2.2 Cold Electronics

Cold electronics (CE) are responsible for reading out the digitized waveforms from the APA wires. Front-end motherboards (FEMBs) contain the front-end readout electronics. The main components of the FEMBs that handle signal processing are a series of application-specific integrated circuits (ASICs). The signals from the wires are handled by three ASICs: the FE ASIC, the ADC ASIC, and the COLDATA ASIC. The FE ASIC (also known as LArASIC) is a 16-channel chip that is responsible for pulse shaping and amplification. The signal is then digitized by a 16-channel, 12-bit analog-to-digital converter (ADC) ASIC (also known as ColdADC). At the end of the processing chain, the COLDATA ASIC handles the data merging, communication, and streaming of the digitized signal to the warm interface boards (WIBs) located on the feedthrough flange outside of the LAr environment. FE ASICs can operate at one of four gain settings (4.7 mV/fC, 7.8 mV/fC, 14 mV/fC or 25 mV/fC), four shaping time settings (0.5 μs, 1.0 μs, 2.0 μs or 3.0 μs) and two baseline settings (200 mV or 900 mV). The gain setting impacts the signal pulse heights, the shaping time controls the pulse width, and the baseline controls the offset voltage.

The ICEBERG APA is instrumented with 10 FEMBs. The FEMBs plug into the top of the FC, making a connection with the wire planes. Each FEMB reads out signals from 128 channels: 40 from the U plane wires, 40 from the V plane wires, and 48 from the X plane wires. During the ICEBERG commissioning stage, spare ProtoDUNE FEMBs were used. The design for these FEMBs contain eight 16-channel LArASIC chips, eight 16-channel ColdADC ASICs, and two COLDATA control and communication ASICs. A schematic of a ProtoDUNE FEMB is shown in Figure 4.10.

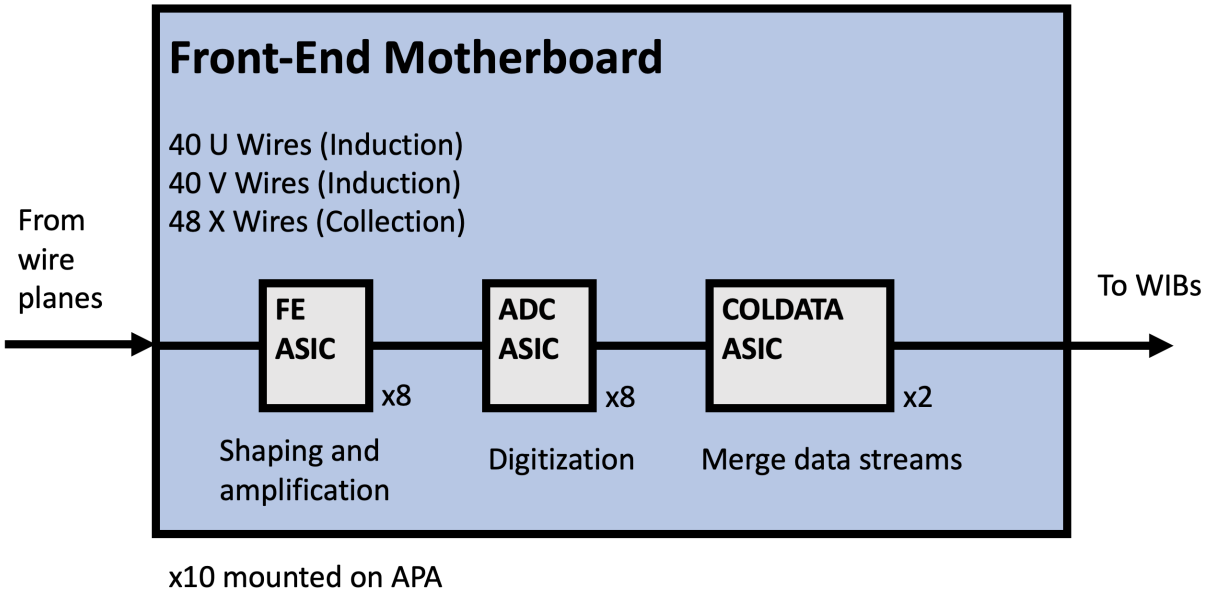

Figure 4.10: Block diagram of the readout electronics for the three-ASIC test at ICEBERG.

ICEBERG was designed to test electronics prototypes in a LAr environment. Alternatives to the ColdADC chip have been explored, with the SBND (Short Baseline Neutrino Experiment) collaboration planning on using commercial off-the-shelf (COTS) ADCs as part of their TPC readout electronics [64]. Another configuration being tested is the three-ASIC scheme, where the functions of the COLDATA ASIC are to be handled by a field programmable gate array (FPGA). The reduction in part count may improve FEMB reliability, reduce power consumption, and reduce cost in production and testing.

4.2.3 Crosstalk Studies for COTS ADC FEMBs

Given the proximity of receiving signal channels, some of the signals from one channel could have the undesirable effect of inducing a signal on neighboring channels, thus distorting the calorimetry in the event reconstruction. The crosstalk between channels was studied using a COTS ADC FEMB on a test bench. The COTS ADC FEMB is equipped with an internal FE ASIC pulser that sends a pulse to each individual channel. The procedure consisted of inducing a pulse signal on each channel using the internal calibration pulser system on the FEMBs and measuring the response on the rest of the channels. Signals from the pulser to the FE ASIC

are treated through a charge amplifier that uses a 5^{th} order semi-Gaussian shaper as an anti-aliasing filter for the TPC signals. The configuration of the FE ASIC is then set: the gain being configured to 7.8 mV/fC, the shaping time set to 1 μs and the baseline is set to 200 mV for all the channels. The pulser is equipped with an injection capacitor of 183 fF, and allows injection of a voltage pulse of 18.75 mV steps in size. The voltage change related to charge signals (Q_s) on channels is calculated as:

$$Q_s = C \times V_p = 3.43\text{fC} = 21.4\text{ke}^- \tag{4.3}$$

with the modulated pulse amplitude for 20 available settings:

$$Q = A \times Q_s \tag{4.4}$$

where $A \in \{1, 2, ..., 20\}$ and Q is the output charge. The pulser settings used for this study are noted in Table 4.1.

Table 4.1: Pulser settings on the FEMB for crosstalk studies.

Setting	Value
Gain	7.8 mV/fC
Shaping Time	1 μs
Baseline	200 mV
Pulser Setting	A = 20
Pulse Amplitude	428 ke^-

The analysis procedure consists of pulsing one channel at a frequency of ~2.8 kHz and recording the resulting waveforms on the rest of the channels, repeating the process for all 128 channels in the FEMB. The data are prepared for analysis by first establishing a common baseline by finding the median ADC value and subtracting it from each waveform. After this step, a peak finding algorithm is used to find the positive peak associated with the bipolar signal in the waveforms for the pulsed channel. For each peak, a window of 500 time ticks, 250 time ticks before and after the peak, is used in order to capture the pulse. The waveform windows are then

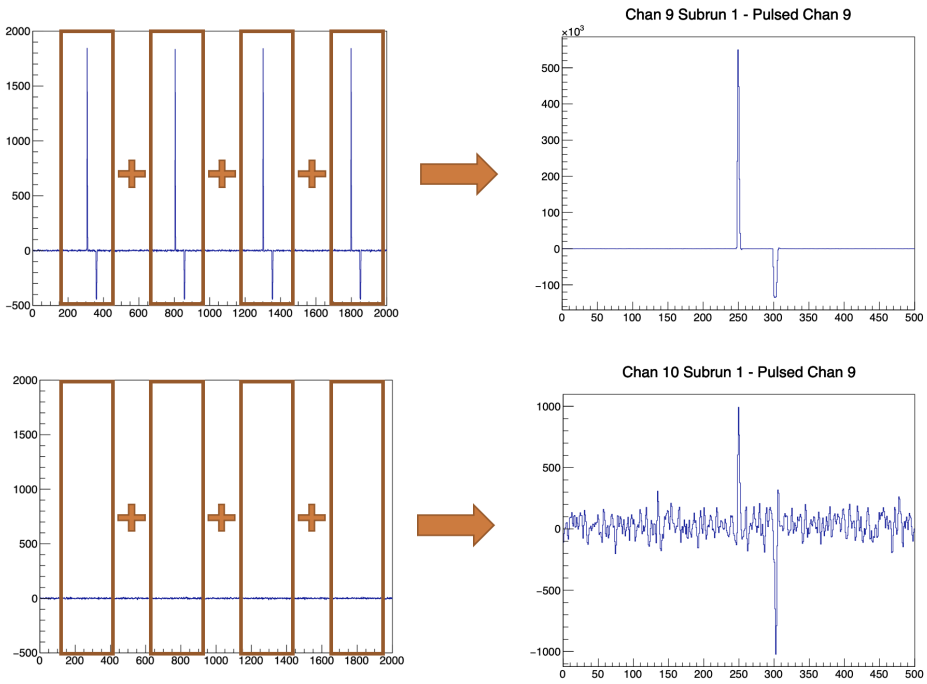

Figure 4.11: Crosstalk data preparation procedure. Top plots show the individual waveforms produced by pulser on the right and the resulting waveform from adding all waveforms over the time the pulser was active. The peak finder algorithm locates the time of the positive peak and the same procedure is applied over the unpulsed channels, shown on the bottom pannels.

added to enhance the signal for the pulsed channel. Similarly, time tick windows in the same time position and size are added up for non-pulsed channels in order to enhance any crosstalk signal. An example of this procedure is shown in Figure 4.11.

We then take the added pulse windows and normalize them to the pulsed channel maximum pulse height. This allows us to compare the pulsed channel height with the available crosstalk in the rest of the channels. This procedure is also applied to the control sample with the pulser off. Comparisons of crosstalk signal peaks are found to be $\mathcal{O}(0.1\%)$ for the pulser on setting and lower when the pulser is off. Figure 4.12 shows the result for one channel with the pulser on and off. The intrinsic noise of the electronics could be contributing to the noise seen with the pulser off.

Each of the eight FE ASICs is responsible for shaping and amplification of the wire signals coming from 16 channels. The pulse height distribution for each FE ASIC, shown in Figure 4.13,

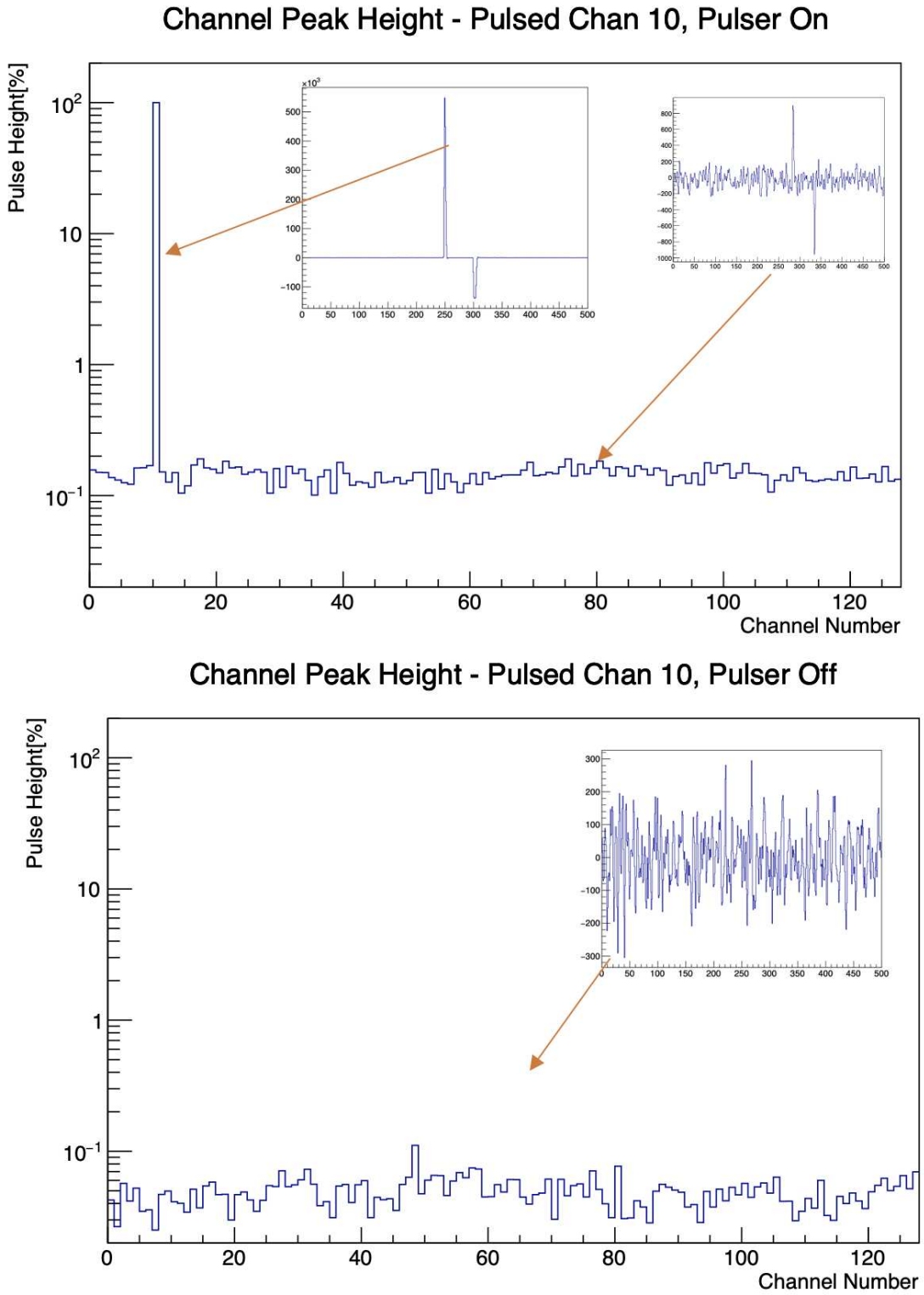

Figure 4.12: Crosstalk measurements for pulsed and unpulsed runs are shown. A pulsed channel, at 100% pulse height, is used as a reference for crosstalk signal comparison over unpulsed channels (top). Pulser off run used for comparison to intrinsic electronics noise (bottom).

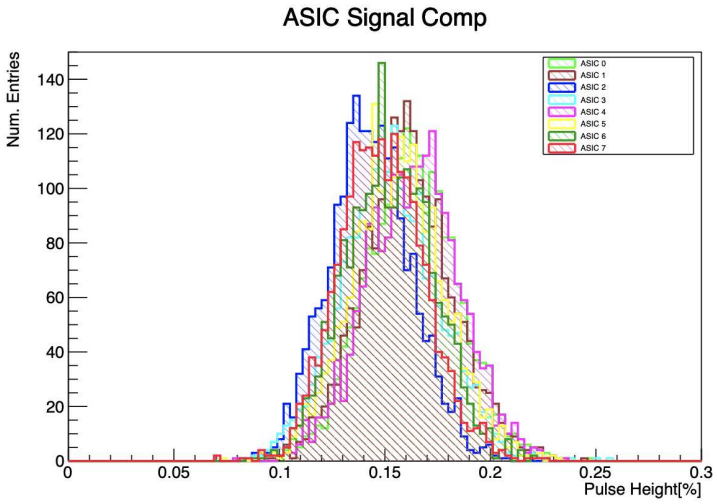

Figure 4.13: Crosstalk for each of the eight FE ASICs is shown. The distribution of pulse heights below 0.25% suggest minimal crosstalk across the various FE ASIC channels.

shows the level of crosstalk limited to levels below $\mathcal{O}(0.25\%)$. The immediate neighbor channels of the pulsed channel were also considered and there was no significant difference between the rest of the channels (Figure 4.14).

Pulse height data with pulser on and off were compared and the same window procedure was employed. For the pulser off data, peak maximums are due to intrinsic noise. Comparisons are shown in Figure 4.15. The average crosstalk for the channels was found to be $\mathcal{O}(0.15\%)$ with the pulser on while for the pulser off, levels of $\mathcal{O}(0.05\%)$ were found. Even though crosstalk levels can be characterized as being above noise levels, the amount of crosstalk noted found is still significantly small and would not impact signal formation.

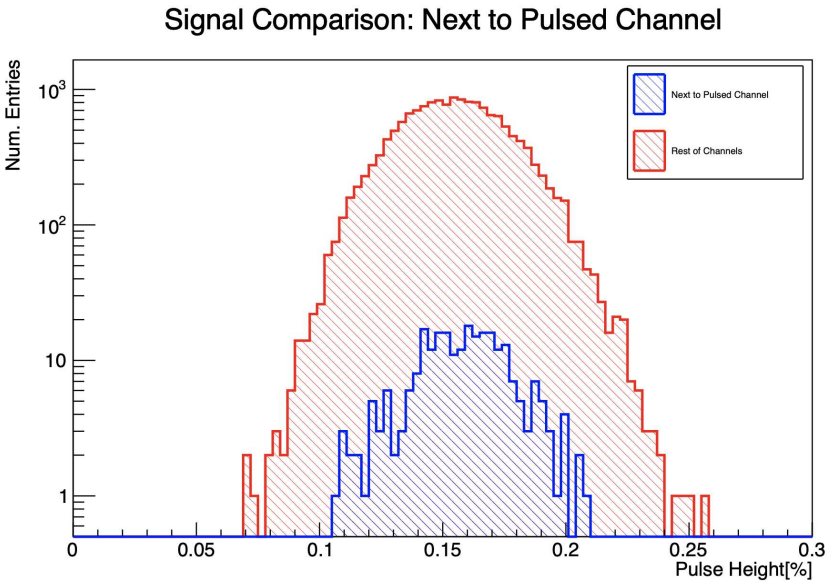

Figure 4.14: Unpulsed channels directly next to pulsed channels where individually analyzed. For channels not immediately next to the pulsed channel (labeled as "Rest of Channels" in red) the crosstalk seems uniform. Across the FEMB, pulse heights below 0.25% suggest neighboring channels are minimally affected by crosstalk processes.

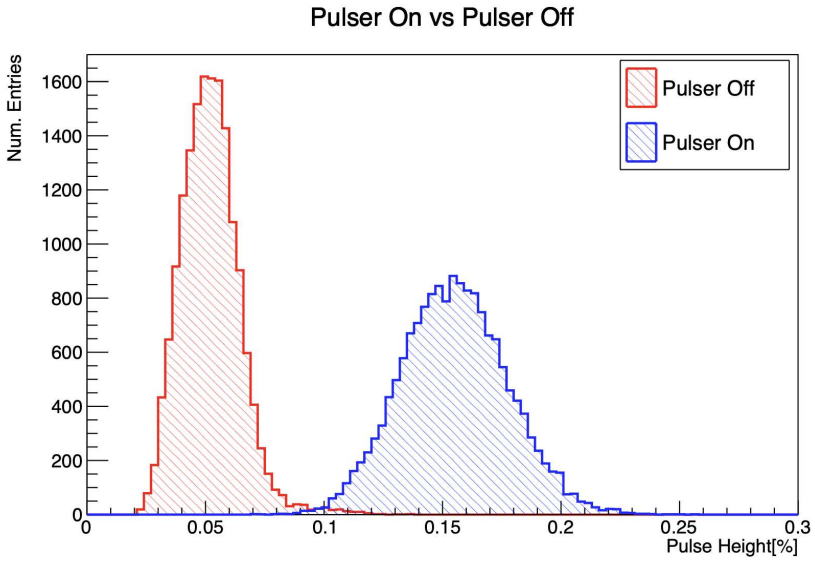

Figure 4.15: Pulse height distributions were compared with pulser on and off. Electronics noise accounts for pulser off measurements (red) and a clear distinction can be made when the pulser is on (blue). High noise channels can be observed at 0.1% pulse height level and account for overlapping pulser off events with pulser on events.

4.2.4 Data-taking with ICEBERG TPC

ICEBERG detector operations are planned around the CE prototype availability for testing purposes and upgrades or fixes needed to keep the detector running in a healthy fashion. The detector operation is separated into distinct data-taking runs, with each run lasting $\mathcal{O}(1)$ months allowing for fast turn-around of CE testing.

The ICEBERG cryostat was filled for the first time in March 2019, with the ProtoDUNE FEMBs installed on the TPC for the commissioning phase. Run 1 was cut short after current instabilities during the cathode HV ramp-up were detected. Following the cathode current fluctuation, 30 channels on the FEMBs were lost. Furthermore, it was found that around 400 additional channels became unresponsive once they were tested at room temperature. Two correlated events are thought to be the cause of this: a 10 second, ~2.5 psi pressure fluctuation in the cryostat and a ~ 14 μA current spike on the collection plane. LAr temperatures within the cryostat vary with the pressure in the argon gas that has evaporated above the liquid level. Therefore, a precise measurement of the pressure allows better understanding of the temperature within within the cryostat.

Upgrades in the FC and cryogenics were initiated by incidents from the first run. The construction of the FC was revisited and was found to have faulty connections between the copper strips of the walls and the top and bottom of the FC. Further investigations also showed short circuits between the copper strips on the walls of the FC. This fault was due to the usage of POGO connections, which caused current spikes between the pieces of the FC. The fix involved replacing the POGO connectors and soldering the side walls to the top and bottom of the FC. Upgrades to the condenser were made to minimize pressure fluctuations within the cryostat. An in-line LAr purification system was also installed in order to achieve a higher purity argon. To further protect the CE, a power inhibitor was installed that helps protect the FEMBs when the wire bias voltage is turned on.

As of the writing of this thesis, four kinds of CE have been tested at ICEBERG: the ProtoDUNE-SP FEMBs, the SBND COTS ADC, the three-ASIC FEMBs and the SLAC CRYO FEMBs. The CRYO

chip differs from the three-chip design introduced for the ProtoDUNE CE by combining the functions of the analog preamplifier, ADC, and data serialization along with transmission for 64 wire channels into a single chip [12]. Using the CRYO chips only requires two ASICs on each FEMB compared to the 18 needed for the ProtoDUNE-SP design.

4.2.5 Electron Lifetime Studies

A critical performance point for the success of LArTPC-based experiments is the need to have high LAr purity during operations. Drift electrons can easily attach to electronegative impurities such as oxygen and water molecules in the LAr. If the impurity level within the detector is high enough, the induced signal will become attenuated, potentially impacting the calorimetric reconstruction of the event. The attenuation effects are more significant for those electrons drifting from further away of the anode planes; given that their drift time is longer, per the following formula:

$$n = n_0 \cdot exp(-t/\tau) \tag{4.5}$$

where n_0 is the number of original electrons, n is the number of electrons that arrive at the anode, and τ and t are the lifetime and drift time of the drift electrons, respectively.

The electron drift lifetime measurement consisted of recording cosmic muon interactions within the cryostat. Cosmic ray reconstruction is done via the TrajCluster technique [65]. Only spatial information associated with the track trajectory is used for the selection, while the electron lifetime measurement uses the reconstructed charge along the track. The selection takes advantage of specific criteria to ensure the cosmic muon tracks pass through both the anode and a cathode, including requirements on track length and track angle. The topology of the track passing through both the anode and a cathode enables precise knowledge of the drift coordinate along the extent of the cosmic muon track. To account for poorly reconstructed tracks, the largest 12.5% and smallest 12.5% dQ/dx measurements are removed (using a similar method used at ICARUS [66]) producing a dQ/dx distribution centered on the most probable dQ/dx value.

Once this selection is made, we can measure the ionization electron survival distribution:

$$dQ/dx = dQ_C/dx \cdot exp(-t/\tau) \tag{4.6}$$

where dQ_C/dx represents the amount of charge per unit length at the cathode, dQ/dx represents the charge per unit length at an arbitrary drift time t in the TPC, and t and τ are the same as in Equation 4.5. We then fit an exponential function to the distribution and obtain τ from the fit. The electron lifetime was measured using the three prototype FEMBS available at the time: the ProtoDUNE-SP FEMBs, the COTS ADC FEMBs, and three-ASIC FEMBs. Figure 4.16 shows the distribution of dQ/dx in terms of the hit peak time for each of the data-taking runs where different FEMB options were tested. The electron lifetime measurement for the ProtoDUNE-SP FEMBs data-taking run was 123.5 μs $\pm$ 1.8 μs, for the COTS run was 906.6 μs $\pm$ 32.4 μs and for the three-ASIC run was 1338.5 μs $\pm$ 32.9 μs.

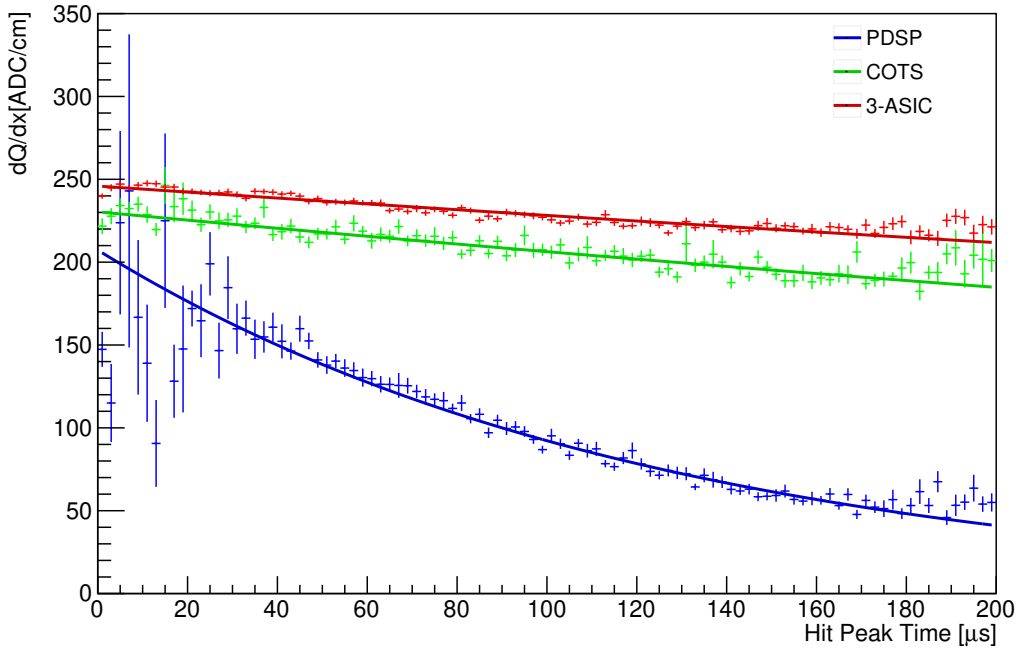

Figure 4.16: dQ/dx distribution for each run of prototype CE. The solid lines show the fit used to estimate the electron lifetime for each data-taking run that a given CE prototype was tested at ICEBERG, with the ProtoDUNE-SP FEMBs (PDSP) in blue, the FEMBs with the COTS ADCs in green and the three-ASIC FEMBs in red.

Chapter 5

MicroBooNE

The Micro Booster Neutrino Experiment, or MicroBooNE for short, was proposed as a follow-up experiment to MiniBooNE to resolve the to address its observation of an excess of low-energy electromagnetic events. It utilizes the liquid argon time projection chamber (LArTPC) as its detector technology, which has proven to be key in making physics measurements because of its ability to image complicated neutrino interactions, leading to precise reconstruction of spatial and calorimetric information. The detector sits roughly 70 meters away from MiniBooNE on the Fermilab campus, giving it a similar L/E. It also utilizes the same beamline, the Booster Neutrino Beamline (BNB), making both experiments share the same systematic uncertainties related to the flux simulation.

This chapter provides an overview of the MicroBooNE detector, its subsystems, and the infrastructure required to perform neutrino measurements. Section 5.1 gives a brief overview of the physics motivations and goals of MicroBooNE. Section 5.2 describes the BNB which is the primary source of neutrinos for both MicroBooNE and MiniBooNE. The LArTPC detector, the light collection system and signal processing are described in Section 5.3. Section 5.4 discusses the operation of the cosmic ray tagger. Section 5.5 focuses on the triggers used to efficiently collect data. Lastly, Section 5.6 briefly describes the detector operations up to MicroBooNE's shutdown in 2020.

5.1 Physics Motivations

MicroBooNE is the first large LArTPC neutrino experiment to run in the United States and the first LArTPC in the world to have automated event reconstruction tools. This opens up the possibility of exploring new physics measurements. MicroBooNE also plays an important role in

the United States neutrino program, as it not only serves to make new measurements, but also provides plentiful research and development for larger and more ambitious experiments such as DUNE. The physics goals of MicroBooNE are threefold: investigate the low-energy excess of electromagnetic events found by MiniBooNE, make precise cross section measurements of ν_μ-Ar interactions, and explore astroparticle and exotic physics.

5.1.1 Investigation of the MiniBooNE Low Energy Excess

MicroBooNE was built to investigate the short baseline anomaly observed by MiniBooNE, introduced in Section 3.5. Built on the same beamline and around the same baseline, MicroBooNE is poised to validate or refute the excess of low-energy electromagnetic events observed at MiniBooNE. One crucial difference that MicroBooNE brings is its LArTPC, a key piece of technology that allows them to differentiate between electrons and photons, which the MiniBooNE detector was unable to do.

5.1.2 Cross Section Measurements

MicroBooNE has the largest number of neutrino-argon interactions in the world. Neutrinos produced by the BNB have a wide variety of interactions; thus, MicroBooNE is well positioned to investigate a large number of these interactions. MicroBooNE has published results looking at ν_μ inclusive channels measuring both single- [67] and double-differential [68] cross sections and results from ν_μ exclusive channels:

- charged-particle multiplicity [69]
- ν_μ CCQE-like scattering [70]
- ν_μ CC0πNp ($N \geq 1$) scattering [71]
- ν_μ CCπ^0 production [72]
- ν_μ CC kaon production [73]
- ν_μ NC 1p production [74]

The results of these cross section analyses have played an important role in the analysis presented in this thesis, specifically the measurement of ν_μ interactions which are used to reduce the modeling uncertainties for intrinsic ν_e events.

5.1.3 Astroparticle and Exotic Physics

MicroBooNE is also involved in studying a variety of neutrino and non-neutrino physics, along with models beyond the Standard Model of particle physics. Some examples include:

- a detection scheme for supernova neutrinos for LArTPCs [75];
- search for heavy neutral leptons [76];
- search for a Higgs portal scalars [77];
- studies of ^{39}Ar beta decays in LArTPCs [78];

5.2 Booster Neutrino Beam

The BNB is a single-horn focused neutrino beam with a peak energy of around 800 MeV [2]. To produce neutrinos of that energy, protons extracted from hydrogen molecules are first accelerated through the Fermilab Linear Accelerator (Linac) to kinetic energies around 400 MeV. The protons are then passed on to the Booster, a 474-meter-circumference synchrotron which further increases the protons kinetic energy to around 8 GeV. Beam spills of $\sim 4 \times 10^{12}$ protons are then sent to the target hall, with each beam spill lasting 1.6 μs.

The protons are then transported through a lattice of focusing and defocusing quadrupoles and bending dipole magnets to either the BNB or the Main Injector to provide neutrinos to the NuMI beamline. At the BNB, protons are then focused onto the beryllium target. The proton-berylium collisions produce a slew of mesons such as $\pi^\pm$, $K^\pm$, and K^0, which are focused by an electromagnetic horn. The horn (see schematic in Figure 5.2) is an aluminum alloy toroidal electromagnet with a pulsed current $\pm$170 kA driving the magnetic field used to focus the secondary charged particles onto the beamline. Two neutrino modes are produced, depending on

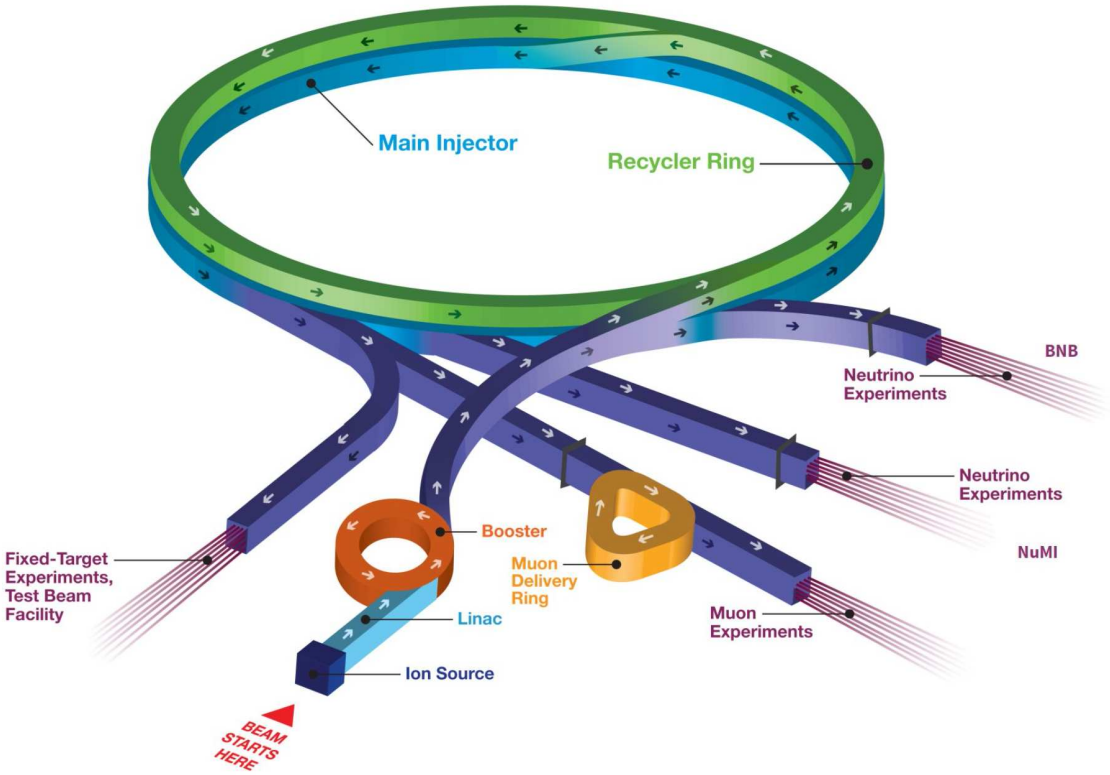

Figure 5.1: Fermilab accelerator complex. Image credit: Fermilab Accelerator Division.

the polarity of the horn current: a positive current produces a beam composed of mostly neutrinos ("neutrino mode") and a negative current gives a beam of mostly antineutrinos ("antineutrino mode"). It is noteworthy to point out that the BNB was operating in neutrino mode for the entirety of MicroBooNE operations. In the case of neutrino mode, a positive current would flow along the inner conductor in the beam direction and folds back onto the outer conductor of the horn (reversed in antineutrino mode). The magnetic field produced is perpendicular to the beamline, which focuses positively charged particles and weeds out negatively charged particles. Focused particles then travel through a 50 m decay pipe, where they eventually decay into neutrinos and other mesons. The dominant process for neutrino production is $\pi^+ \rightarrow \mu^+ + \nu_\mu$, which has a branching ratio of ~99.98%. The muons and remaining mesons are stopped either by a concrete wall at the end of the decay pipe (called the "beam dump") or by the dirt between the detector and the beam dump.

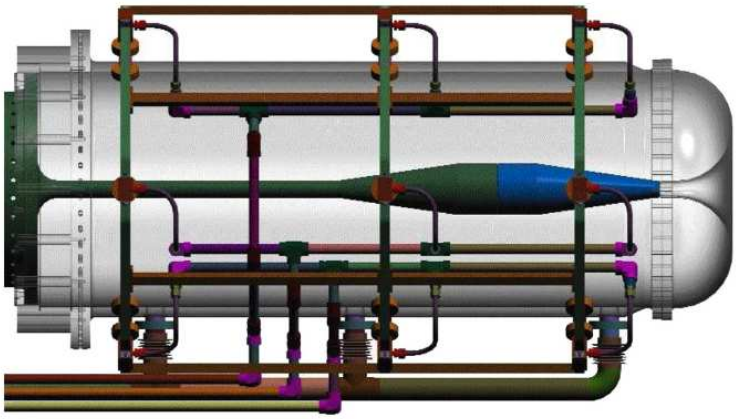

Figure 5.2: Diagram of the BNB electromagnetic focusing horn. In neutrino mode, the current flows from left to right along the inner walls of the aluminum conductor, then from right to left on the outer walls of the conductor. Image taken from [2]

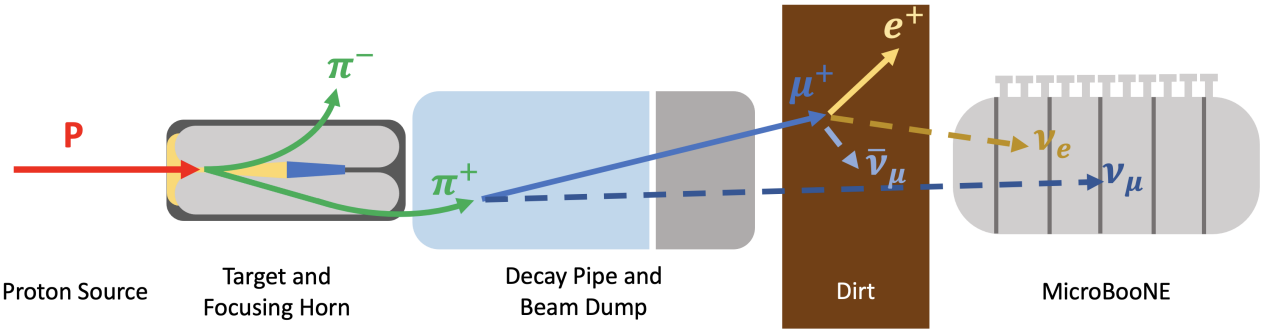

Figure 5.3: Diagram of the BNB neutrino generating chain.

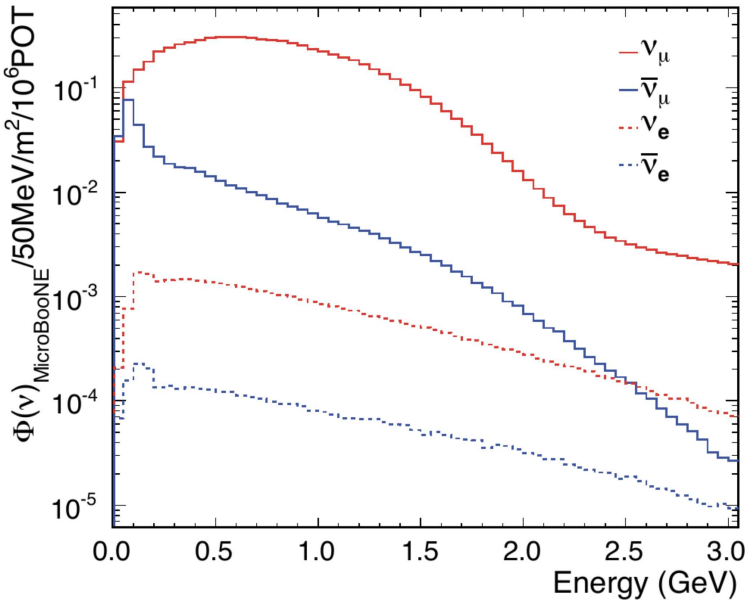

Figure 5.4: Predicted BNB neutrino content received by MicroBooNE. [13]

Table 5.1: Predicted neutrino fluxes at the MicroBooNE detector with the BNB running in neutrino mode. The two most important parental mesons are included [2].

	ν_μ	$\bar{\nu}_\mu$	ν_e	$\bar{\nu}_e$
Flux (ν/cm^2/POT)	5.2×10^{-10}	3.3×10^{-11}	2.9×10^{-12}	3.0×10^{-13}
Fraction	93.6%	5.86 %	0.52%	0.05%
Composition	π^+: 96.7% K^+: 2.7% Other: 0.6%	π^-: 89.7% $\pi^+ \to \mu^+$: 4.5% Other: 5.8%	$\pi^+ \to \mu^+$: 51.6% K^+: 37.7% Other: 11.1%	K^0_L: 70.7% $\pi^- \to \mu^-$: 19.3% Other: 10.0%

The neutrino composition of the BNB running in neutrino mode is shown in Figure 5.4, with the largest component of the flux being the ν_μ contribution predicted at 93.6%. Although most decays produce muon neutrinos, some other neutrino flavors are also produced: with 5.86% $\bar{\nu}_\mu$, 0.52% ν_e and 0.05% $\bar{\nu}_e$. The muons produced from the decay of pions contribute to neutrino production through muon decay ($\mu^+ \to e^+ + \nu_e + \bar{\nu}_\mu$), producing the main source of intrinsic ν_e contamination in the beam. Highly energetic forward-moving negative pions are harder to filter out by the horn and end up contributing to $\bar{\nu}_\mu$ contamination in the beam. Finally, the decays of K^0_L contribute the largest portion of $\bar{\nu}_e$. Table 5.1 shows the breakdown of neutrinos/antineutrinos by flavor in the BNB when running in neutrino mode.

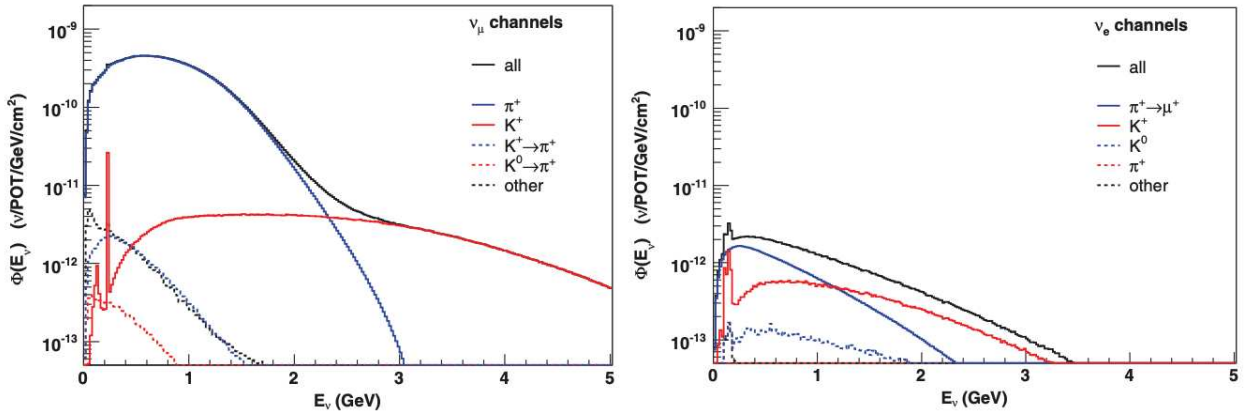

(a) BNB ν_μ content in neutrino mode

(b) BNB ν_e content in neutrino mode

Figure 5.5: Predicted ν_μ and ν_e fluxes at the MicroBooNE detector broken down by parent meson with BNB in neutrino mode. The solid black line indicates the total predicted flux, while all the sub components apart from the dashed black are from nucleon-induced meson production of the indicated decay chains. The dashed black histogram includes all other contributions, primarily from meson decay chains initiated by meson-nucleus interactions. Figure from [2].

5.3 MicroBooNE Detector

The MicroBooNE detector is located downstream of the BNB, around 470 meters north of the beam target. Close by, at around 540 m downstream of the BNB lies MicroBooNE's predecessor, MiniBooNE. Figure 5.6 shows an aerial view of the BNB with both detector locations.

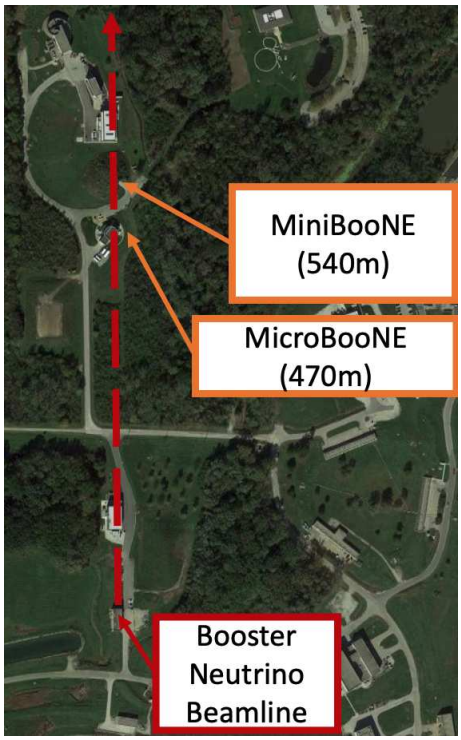

Figure 5.6: Bird's eye view of the BNB with MicroBooNE's and MiniBooNE's detectors positions. Aerial view courtesy of Google Maps.

5.3.1 Cryostat

The cryostat is the cylindrical vessel that contains the neutrino target medium (liquid argon). The body of the cryostat is 17,000 kg of stainless steel. It has a length of 12.2 m and an inner diameter of 3.81 m with a wall thickness of 11.1 mm. A layer of foam surrounds the cryostat to reduce heating from the environment. The cryostat was designed to be a hermetically sealed environment in order to prevent external contaminants, such as water or oxygen, from contaminating the LAr. Additionally, LAr is pumped outside of the vessel to the purification system, which filters out impurities and pumps the clean LAr back into the cryostat. Finally, two liquid

Figure 5.7: MicroBooNE cryostat. Photo courtesy of Fermilab.

nitrogen condensers are used to maintain stable temperatures and pressures within the cryostat to enable electronic systems and pumps to work properly. A photo of the cryostat being moved to the detector hall is shown in Figure 5.7. The temperature within the cryostat is kept steady at 89 K and at a constant pressure of 1.24 bar, slightly above atmospheric pressure in order to minimize contaminants leaking into the cryostat at the cryostat penetrations.

5.3.2 Time Projection Chamber

Inside of the cryostat lies the MicroBooNE TPC. The dimensions of the TPC are 10.4 m along the beam direction (z), 2.3 m tall (vertical coordinate, y) and 2.6 m across (drift direction, x). A total of 170 tons of LAr are contained within the cryostat, and 87 tons are considered the active volume within the TPC volume. A schematic of the TPC sitting inside of the cryostat is shown in Figure 5.8.

At opposite ends of the drift direction lie the anode wire planes and the cathode, which create an electric field (E-field) within the TPC. The cathode plane is kept at -70 kV, which creates a 273 V/cm E-field. Given the E-field strength, an electron takes a maximum of 2.3 ms of drift time to the anode planes with a drift velocity of 0.1098 cm/ms [79]. The field cage is held together by

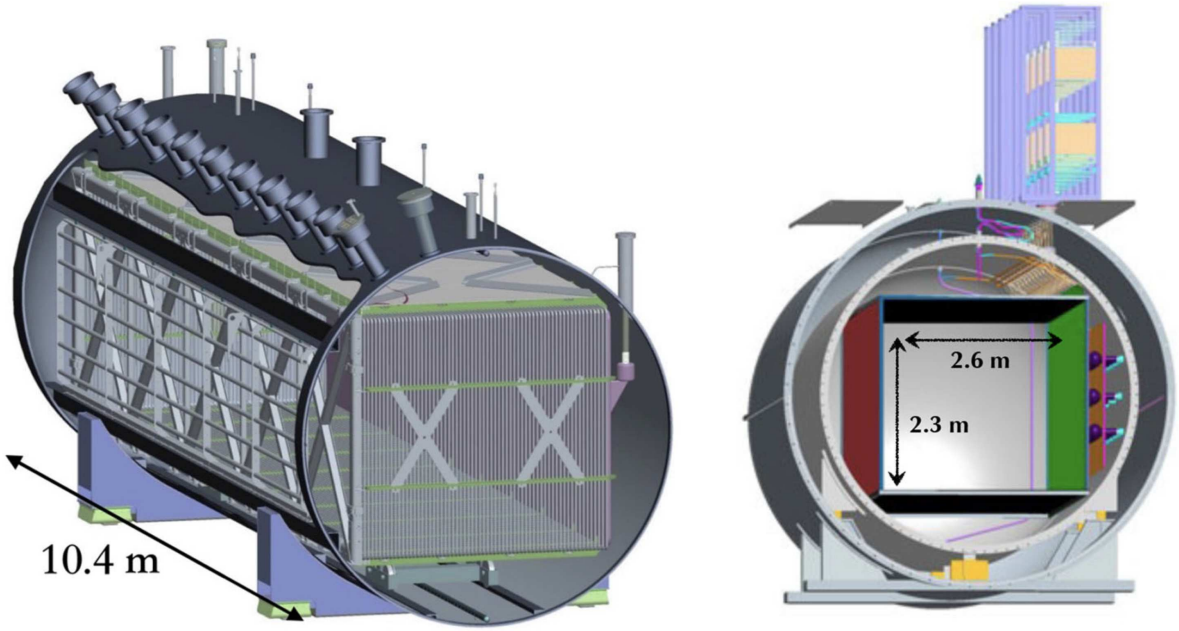

Figure 5.8: MicroBooNE TPC schematic with the TPC dimensions. Image taken from [14].

64 stainless steel poles linked with 250 MΩ resistors between them that uniformly decrease the voltage between the cathode and anode planes in 1 kV increments.

The anode is made up of three wire planes: the two induction planes U and V and one collection plane Y. The spacing between each wire plane is 3 mm, with each wire having a pitch of 3 mm. The wires used are made of copper beryllium and have a diameter of 150 μm. The two induction planes are oriented at $\pm 60^{\circ}$ relative to the vertical, while the collection plane runs parallel to the vertical. To achieve a transparency condition for the drifting charge, the U and V induction planes are biased at -110 V and 0 V, respectively, while the collection plane Y is biased at 230 V. The TPC counts with a total of 8256 wires split among the wire planes: 2400 for each of the induction planes and 3456 wires used in the collection plane. The PMTs lie behind the collection plane with a grounded metal mesh placed between them, which shields against field distortions and prevents stray electrons from drifting behind the anode planes.

5.3.2.1 TPC Readout Electronics

Signals produced in the wire planes due to the ionization charge are amplified, shaped, and digitized before being stored on disk. At MicroBooNE, these processes are split into cold and warm electronics, where the signal is amplified and shaped by cold electronics and then passed to the warm electronics to be digitized. Similarly to ICEBERG (Section 4.2.2), an FE ASIC mounted on an FEMB performs the signal amplification and shaping in the LAr. Furthermore, cryogenic temperatures, along with proximity to the wire planes, reduce the impact of electronic noise.

The FE ASICs used at MicroBooNE have the same settings for the gain and shaping time described in Section 4.2.2. The nominal gain setting of 14 mV/fC was chosen for MicroBooNE to provide a high signal-to-noise ratio from small signals coming from minimally ionizing particles (mostly from cosmic muons) while at the same time avoiding saturation from highly ionizing sources (such as protons). The choice of shaping time is related to the ADC sampling rate, as optimization of both reduces the amount of noise seen on the signal. MicroBooNE's sampling frequency is 2 MHz, so intuitively the shortest shaping time setting that can provide an accurate measurement of the charge deposited is 1 μs. However, due to the chosen E-field at MicroBooNE, a shaping time of 2 μs was chosen to attenuate higher-frequency pick-up noise.

The signals are then passed through ' "cold" twisted-pair cables' in gaseous argon and transmitted to the warm flange, which is at room temperature. At this stage, signal losses have to be mitigated due to the rise in temperatures, so the signal is transferred through an intermediate amplifier line driver before being carried to the data acquisition (DAQ) machines. At the DAQ machines, the signal is digitized at a rate of 2 MHz using ADCs; the sampling rate is set at 0.5 μs for one time "tick". The read-out window at MicroBooNE is 9600 ticks (or 4.8 ms), roughly twice the maximum electron drift time. To ensure that a neutrino event is fully captured, the DAQ readout window is centered around the event trigger (see Section 5.5) in the range of [-1.6, +3.2] ms. Once the signals have been digitized, they are handed over to an FPGA for data processing and reduction. A schematic of the MicroBooNE readout electronics chain is shown in Figure 5.9.

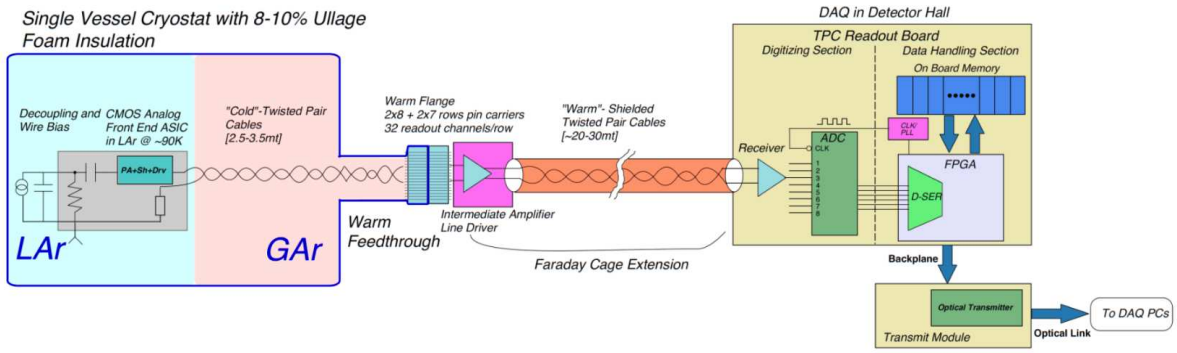

Figure 5.9: Readout electronics schematic at MicroBooNE. Image taken from [15].

5.3.2.2 Unresponsive Wire Channels

After filling the MicroBooNE cryostat and installing all electronics, the status of the TPC readout channels was determined. Around 10% of the channels were found to be misconfigured, shorted, or unresponsive. The U plane contains 224 channels where the FE ASICs are configured with the factory default settings for the gain and shaping times, 4.7 mV/fC and 1 μs, respectively. With these settings, the misconfigured channels have a signal-to-noise ratio lower than the nominal settings. Although these channels have a higher noise content compared to the rest, they are still used with the aid of an offline noise filter.

There are two sectors in the detector that have become unusable for the physics done at MicroBooNE. The first sector involves a group of wires in the U-plane that have been shorted. The likely culprit for this occurrence is the contact of several U-plane wires with one of the grounded V-plane wires. In this region of the detector, the U-plane wires act as another collection plane, thus reducing the signal amplitude in the Y-plane. The second unresponsive region is a group of shorted wires in the Y plane. These wires were shorted by current leakage to a bias-voltage power supply. In this region, drifting electrons are almost entirely collected on the V-plane.

5.3.3 Light Collection System

Liquid argon produced around $\mathcal{O}(10^4)$ photons per MeV of deposited energy for the E-field at MicroBooNE, making LAr a fairly bright scintillator. Furthermore, LAr is transparent to its own scintillation, making the light signals useful alongside the charge information from the TPC. As

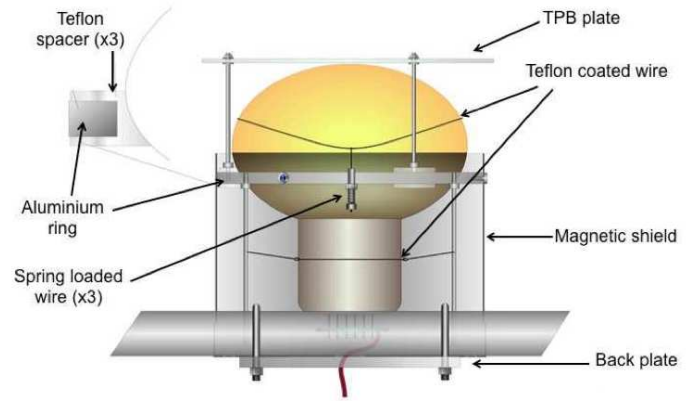

(a) MicroBooNE PMT Schematic

(b) PMT Array

Figure 5.10: Schematic of a MicroBooNE PMT (left) and a photograph of the PMT array mounted inside of the cryostat. [2]

light information is prompt $\mathcal{O}(ns)$ compared to charge information $\mathcal{O}(ms)$, light signals are an efficient way to determine the precise time an event occurred within the detector, denoted t_0.

The light collection system used in MicroBooNE consists of an array of 32 8" Hamamatsu R5912-02mod cryogenic PMTs located behind the anode planes. A schematic of a PMT is shown in Figure 5.10a on the right with a photo of the PMT placements on the detector on the left. LAr ionization light is produced in the vacuum ultraviolet spectrum at 128 nm; however, the PMTs are only sensitive to light in the wavelengths of 350 to 450 nm. The solution used at MicroBooNE was to place tetraphenylbutadine (TPB) wavelength-shifting acrylic plates in front of the PMTs, which shift the light's wavelength to a spectrum peaking at 425 nm. The PMTs are mounted behind the TPC wire planes in a matrix as seen in Figure 5.11.

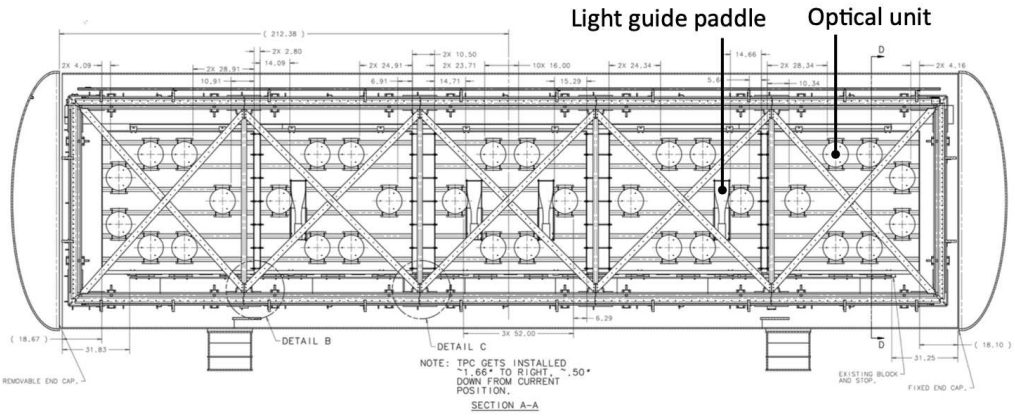

Figure 5.11: Schematic MicroBooNE light collection system. PMTs are shown in circles shaped rosettes along the beam direction. Light guide panels are also shown but are not used in MicroBooNE's standard analyses. [2]

5.4 Cosmic Ray Tagger

MicroBooNE is located on the surface and thus is constantly bombarded with cosmic rays. Around 20 cosmic muons are expected to enter the detector per every 4.8 ms readout window. Cosmic ray muons are a background source that mimics ν_μ interactions and can be misidentified as signal event. Furthermore, cosmic muons also produce Michel electrons and delta rays which can mimic ν_e events. To mitigate the impact of cosmic rays, MicroBooNE installed a series of Cosmic Ray Tagger (CRT) planes that cover the top, bottom and sides of the detector. The CRT planes are made from a series of CRT modules, each made from 16 10.8 cm wide and 2 cm thick plastic scintillating strips. When a muon crosses one of the scintillating strips, the scintillating light produced is guided along optical fibers to the end of the CRT panels to be readout by the silicon photo multipliers. The signal is then read out and digitized by custom front-end boards. A schematic of the CRT plane configuration is shown on the right side of Figure 5.12 along with a simulation of cosmic muons crossing the CRT planes on the left.

The CRT was installed in March 2017, two years after the MicroBooNE detector was commissioned, meaning that some of the data lack the cosmic-rejection capabilities the CRT could provide. The installation of the CRT panels encountered to some limitations due to space restrictions at the Liquid Argon Testing Facility where MicroBooNE is located. Panels were not

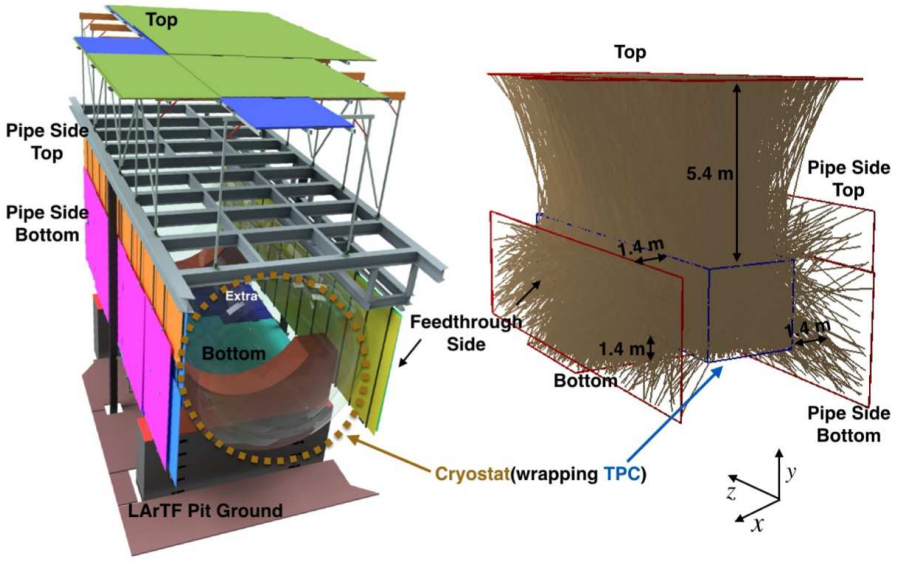

Figure 5.12: Schematic of MicroBooNE CRT array. Four panels are visible at the top, bottom and sides of the cryostat (left). A simulation of cosmic rays crossing all four planes and entering the detector is shown on the right. [16]

installed on the upstream and downstream faces of the detector, and the top panel is located 5.4 m above the cryostat to accommodate the detector electronics racks. With these constraints, the CRT achieves a maximum solid-angle coverage of 85%.

5.5 Event Triggering

MicroBooNE produces a wealth of information, but the experiment is limited in the amount of data storage space available to the experiment. Having a continuous readout or even acquiring every event while the BNB is on would result in $\mathcal{O}(TB)$ of data being stored daily. MicroBooNE employs several triggering schemes that require a certain amount of signals from the PMTs to decide if the event is stored or not, along with a signal given by the BNB operations. Two trigger modes are used: *on-beam* where an event is stored if the beam is on and the PMTs are triggered, and *beam-off* where the beam is off, but there is sufficient optical activity to merit the event being stored. The BNB trigger is called the hardware trigger and the PMT trigger is called the software trigger for reasons that will be made clear in this section.

5.5.1 Hardware Trigger

In order to start MicroBooNE's readout chain, a signal must be received to tell the detector to read out an event. The signal can be produced either by the BNB clock or internally via pulses generated by a function generator on the trigger rack. In either case, MicroBooNE starts reading out data and saves the 4.8 ms read-out window described in Section 5.3.2.1, while the PMT stream opens up a 23.4 μs readout. After applying the hardware trigger, it is 99.8% likely that a neutrino interaction will be recorded for 1 in every 600 beam spills.

The pulse generator or external trigger is used to input a signal to capture cosmic activity while the beam is off, and hence the labels "EXT" or off-beam are often associated with them. These events are useful for studying the cosmogenic backgrounds that one expects from a surface detector. These data sets are treated with the software trigger (see the next section) for storage and reconstruction consideration.

5.5.2 Software Trigger

Following the hardware trigger, a software trigger is applied. The software trigger acts upon the amount of light measured by the PMTs coincident with the beam-spill. This trigger is comprised of two consecutive stages, the online and offline trigger, with a photoelectron (PE) threshold from the PMT hit reconstruction determining at which stage the event should be processed.

As its name suggests, the online trigger runs using the TPC and PMT streams to decide whether to record the data on disk. To activate this trigger, the sum of all PMT activity must be equal to or greater than 6.5 PE. Additionally, only PMTs measuring at least half a PE above the baseline are taken into account. If the threshold is met in a 100 ns time window during the BNB beam-spill gate, the event is considered for beam interaction activity. About 95% of empty events are rejected using this trigger.

An event passing the online trigger will be stored onto tape, but will not be considered for event reconstruction until after passing the offline trigger. The offline trigger runs once the event has been recorded and not in the data-taking stage. The online trigger threshold is 6.5 PE while the offline trigger threshold is set to 20 PE. This threshold was found to minimize

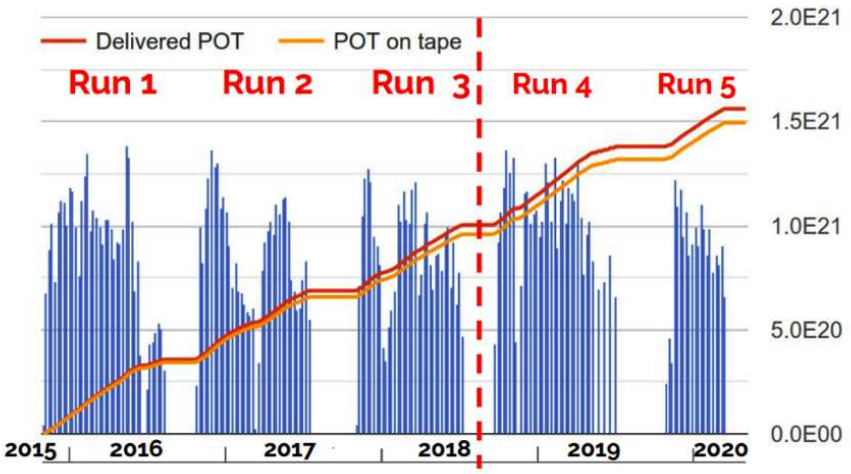

Figure 5.13: BNB POT delivered to MicroBooNE since the beginning of data taking in late 2015. Blue histograms represent the amount of POT delivered during each week, while the red and yellow lines indicate the cumulative POT delivered and recorded onto tape, respectively. Divisions were added showing the POT delivered during each Run period.

the amount of storage needed for recording data sets while maximizing the amount of useful events for low-energy neutrino interactions. About 97% of spills are rejected by software triggers, which increases the signal-to-background ratio to approximately 1 in 6.

5.6 Timeline of Detector Operations

The MicroBooNE detector data collection started in August 2015, taking five datasets (called "Runs") over a period of 5 years. Up to its shutdown in March 2020, MicroBooNE collected more than 1.3×10^{21} protons-on-target (POT) of data. The software trigger described in Section 5.5.2 was implemented in February 2016, so data taken before then are generally not used for analysis. The analysis presented in this thesis uses data collected from February 2016 to September 2018, called Runs 1 to 3, which corresponds to approximately 7×10^{20} POT. Runs 4 and 5 are expected to be ready for analysis in the coming years and bring the total POT for all five runs to about 11×10^{20} POT. Figure 5.13 shows the POT collected during the lifetime of MicroBooNE and also denotes the time periods that correspond to each Run.

Chapter 6

Low-Energy Excess Search

The following chapters will describe an analysis investigating the anomalous excess of low-energy events found by MiniBooNE using the MicroBooNE detector. This particular analysis focuses on charged-current (CC) ν_e interactions that produce single-electron events without any pions in the final state, dividing the analysis into two complementary searches one with and one without visible protons. This signal definition will test whether MiniBooNE observed an excess due to ν_e CC events. The analysis presented in this thesis can be found in the following publication [18].

This search is not the only one carried out by MicroBooNE but is one of four complementary analyses aimed at addressing the MiniBooNE low-energy excess (LEE), with three looking for electron-like signals and the fourth looking for a photon-like signal. The other two ν_e analysis includes an exclusive search of ν_e CC quasielastic interactions with only one electron and one proton in the final state ($1e1p$) and an inclusive search for ν_e CC events with any hadronic activity in the final state. The results of the three ν_e searches, including the one in this thesis, are summarized in [25]. Finally, there is the search for neutral-current Δ resonance events where the Δ decays into a nucleon and a photon in the final state (NC $\Delta \rightarrow \mathrm{N}\gamma$). Although these analyses are interesting on their own, this thesis will focus on the search for the $1e\mathrm{X}p0\pi$ signal.

This chapter will introduce the analysis and describe the motivation behind this search. Section 6.1 describes the low-energy signal model tested by the analysis. Section 6.2 will define the signal that will be the basis of this search. Lastly, Section 6.3 will give a brief overview of the strategy for this analysis.

6.1 Low-Energy Signal Model

The goal of this analysis is the search for an excess of ν_e events over the intrinsic ν_e interaction rate. To benchmark the excess, this analysis uses a phenomenological model constructed from the MiniBooNE observation to obtain a prediction of a ν_e-like excess in the MicroBooNE detector. Many models have been proposed to explain the LEE as an excess of ν_e interactions, but there is no consensus on a definitive theory-based interpretation. Although the chosen model is not based on any single interpretation of the LEE, it does serve several purposes. First, it guides the reconstruction and selection of events to optimize for maximum sensitivity to a signal. Second, it allows this analysis to quantitatively assess the sensitivity of the LEE signal and to measure the significance of the existence of such a signal. While a signal model is a useful tool, it is important to note that any model carries with it a set of assumptions and caveats that may or may not explain the LEE. The goal of the analysis presented in this thesis is to measure the rate of ν_e interactions coming from the BNB while using the LEE as a benchmark compatibility of MicroBooNE's data with a possible ν_e excess at low energies, acknowledging the model assumptions when presenting such a result.

The signal model tested at MicroBooNE is derived by unfolding the MiniBooNE observation. This model assumes that all excess events observed by MiniBooNE are due to an excess of ν_e interactions from the BNB with their true energies obtained by unfolding the reconstructed CCQE energy of the MiniBooNE data events. In the rest of this work, this model will be called "eLEE". It should be noted that the MiniBooNE input data set used in the unfolding procedure was published on 2018 [80], and not the most recent result published in 2021 [57]. The resulting true neutrino energy distribution is shown in Figure 6.1. Although the unfolding procedure gives an estimate of the true signal by removing effects from the MiniBooNE detector and reconstruction, it is not without caveats. The unfolding process is neither uniquely defined nor a well-behaved computation, since the "folding" process usually entails loss of information. Other limitations are associated with the assumptions made when generating the model. These include a reliance on MiniBooNE's simulation to unfold reconstructed to true neutrino energy.

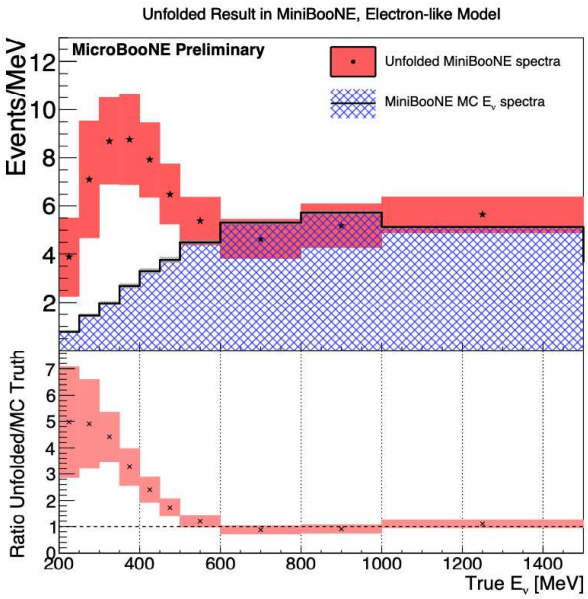

Figure 6.1: Unfolded LEE signal model extracted from MiniBooNE's results [17].

Additional technical limitations include those associated with a binned measurement, rather than a parameterized or analytical prediction of the expected ν_e spectrum, and that the model does not account for events with true energy below 200 MeV. Moreover, the model strongly favors neutrino interactions in the 200-400 MeV energy range, limiting the sensitivity to events within this energy range.

This analysis considers the eLEE signal model as a benchmark that can be scaled depending on the eLEE signal strength. The signal strength is characterized by the parameter μ, where $\mu = 0$ indicates that there is no eLEE signal present and $\mu = 1$ represents the nominal eLEE model. A range of values for μ are considered when calculating the signal strength. This test considers the factor by which the eLEE is present, under the assumption that the signal has the same shape as in Figure 6.1. More details about the signal strength are provided in Chapter 10.

6.2 Signal Definition

This analysis focuses on measuring the rate of CC ν_e interactions in the MicroBooNE detector. CC ν_e interactions within the detector produce visible electrons in the form of electromagnetic showers, together with possible hadronic activity in the form of protons and pions. The chosen

signal definition for this analysis is that of an electron with any number of protons and no visible pions in the final state ($1e\text{X}p0\pi$, with $X \geq 0$). The main motivation for choosing the $1e\text{X}p0\pi$ channel is its similarity to the single-electron topology observed at MiniBooNE. Recall that the MiniBooNE principle handle for detecting ν_e interactions was through the "fuzzy" ring formation characteristic of electron interactions in Cherenkov detectors (see Section 3.5.2). Only electrons are visible by MiniBooNE, but any outgoing protons or neutrons would not be detected. MiniBooNE's signal lies in the CCQE domain, so additional hadronic production, such as pions, is mitigated.

This analysis breaks down the $1e\text{X}p0\pi$ into two orthogonal and mutually exclusive channels based on the proton content. The $1e\text{N}p0\pi$ channel where $N > 0$ indicates the presence of visible protons and the $1e0p0\pi$ channel where no protons are present. Event displays for both channels are shown in Figure 6.2. In the case of the $1e\text{N}p0\pi$ channel, visible protons provide an additional handle for event selection. Furthermore, the $1e0p0\pi$ channel opens the door to a wide range of models that could explain the LEE [81–83] while at the same time mitigating ν_e migration effects due to proton mis-reconstruction, multiplicity, and kinematics.

6.3 Analysis Overview

The goal of this analysis is to measure the CC ν_e interactions with $1e0p0\pi$ and $1e\text{N}p0\pi$ in the final state using the MicroBooNE detector, and to test whether the observation is consistent with the observation provided by MiniBooNE according to the eLEE model described above. This section will provide an overview of the analysis and the steps that are taken to achieve the measurement goals.

The analysis starts with the signal processing and event reconstruction, and is described in Chapter 7. At this stage, the raw waveform signals were collected from the detector and digitized. A series of noise mitigation and deconvolution algorithms are then used on the waveforms to retrieve useful information about the neutrino interaction candidate. This information is then converted to two-dimensional images and read by the Pandora reconstruction al-

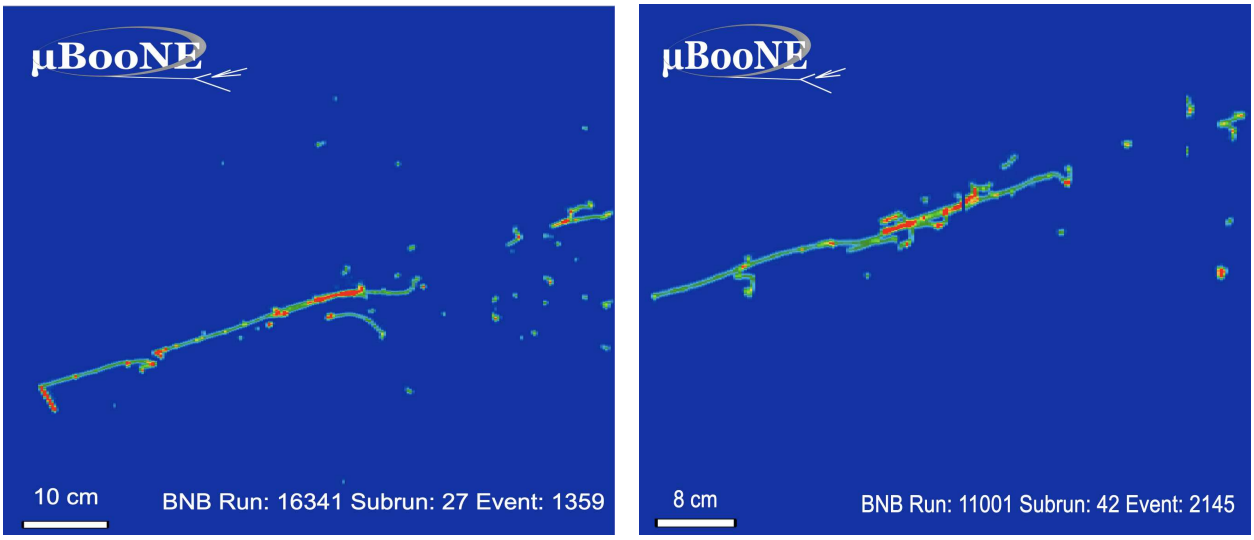

(a) $1e\mathrm{N}p0\pi$ candidate event

(b) $1e0p0\pi$ candidate event

Figure 6.2: Event displays of selected electron-neutrino candidate data events. The horizontal axis corresponds to the wire number, the vertical axis corresponds to the time of the recorded charge, and the color scale corresponds to the deposited charge. The $1e\mathrm{N}p0\pi$ event shown (6.2a) has a long electron shower and a short proton track attached to the vertex with a large amount of deposited energy. The $1e0p0\pi$ event shown (6.2b) consists of a single electron shower [18].

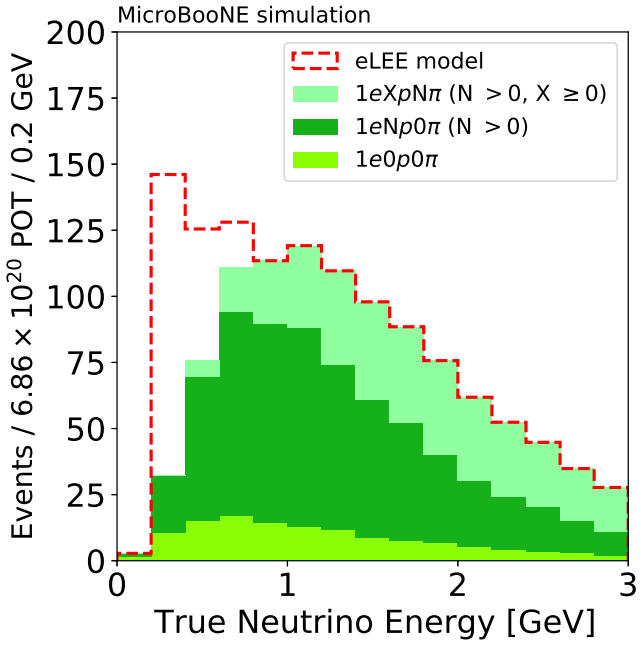

Figure 6.3: Expected ν_e rate in MicroBooNE for 10.1E20 POT subdivided by event topology ($1e\mathrm{N}p0\pi$, $1e0p0\pi$ and $1e\mathrm{X}p\mathrm{N}\pi$), and highlights the low energy region with the unfolded eLEE signal prediction in the red dashed histogram.

gorithm [20]. This stage provides methods for cosmic-ray rejection from neutrino interactions, tools for particle identification, and neutrino energy calculations.

The reconstructed information is then used for the selection of neutrino candidates using the tools described in Chapter 8. The main signal samples are CC ν_e interactions with the channel topology $1e0p0\pi$ or $1e\mathrm{N}p0\pi$, where two independent selection schemes were developed to select each channel. Furthermore, the analysis has developed sideband samples in the two-shower and NuMI sidebands used for shower reconstruction and ν_e modeling validation. Lastly, a ν_μ selection is also developed for the purpose of reducing flux and cross section uncertainties for backgrounds and intrinsic ν_e events.

Chapter 9 gives details on the flux, cross section, and detector response uncertainties. These uncertainties in the prediction allow for a quantitative evaluation with the observation and a constraint procedure is used using the ν_μ selection to reduce flux and cross section uncertainties. Furthermore, evaluating the correlations between the selections of electron and muon neutrino events is crucial when applying the constraint. Details on how the uncertainties are evaluated and the results are shown.

Finally, Chapter 10 presents the results for the ν_e analysis which include the final neutrino energy distributions for the ν_e selections and the results from a series of statistical tests used to assess the agreement between the data and the eLEE model. Three main statistical tests are used: a goodness of fit test between observation and prediction, a simple hypothesis test that gauges the agreement between a prediction without an eLEE present and a prediction with an eLEE present, and a signal strength test that measures the parameter μ. The test statistic for the three tests is the combined Neyman-Pearson (CNP) χ^2_{CNP} [84].

MicroBooNE has taken a "blind" analysis approach for its first measurements of the LEE. This approach means that the ν_e selections had to be developed and "frozen" before they were applied to the MicroBooNE data. This helps prevent bias in the results based on what is observed in the data.

Chapter 7

The MicroBooNE Simulation, Signal Processing and Reconstruction

This chapter describes the simulation, signal processing, and reconstruction algorithms used in MicroBooNE along with the validation of reconstruction and application of energy scale calibrations. These algorithms are implemented in the Liquid Argon Software (LArSoft) framework, a common software package used among all LArTPC neutrino experiments. Section 7.1 describes the simulation of particle production, neutrino-nucleus interactions, and their propagation through the liquid argon in the detector. Section 7.2 describes the techniques applied in the signal processing stage. Section 7.3 explains the algorithms that take the processed waveforms and reconstruct neutrino interactions, while Section 7.4 discusses the calibration of the energy scale for the data and simulations. Section 7.5 touches on the particle identification tools used in this analysis. Finally, Section 7.6 gives details on the energy reconstruction for particle objects, as well as the methods used to calculate the reconstructed neutrino energies.

7.1 The MicroBooNE Simulation

The MicroBooNE simulation is a Monte Carlo simulation aimed at imitating neutrinos and neutrino-induced particles along with their interactions inside the LArTPC. The purpose of the simulation is to serve as a prediction for comparing to data collected from the BNB. Several steps are involved to generate the simulated events. First, the beam flux simulation produces the expected number and energy of neutrinos from the BNB. Next, a neutrino-argon interaction simulation is run and the expected final-state particles and their kinematics are obtained. These particles are then propagated through the liquid argon medium. The detector simulation

then gauges the expected TPC and PMT signals from the neutrino-induced particles. Finally, the signals from the simulation are mixed with signals from the off-beam data (sometimes labeled as EXT), which adds detector noise and cosmic-ray interactions to the simulation. Each of these steps is described in detail below.

7.1.1 Beam Flux Simulation

The beam flux simulation was adapted for MicroBooNE from that used by MiniBooNE [3, 85]. The neutrino flux prediction is based on the GEANT4 framework with appropriate dimensions, detector medium, and beamline location for MicroBooNE [85]. GEANT4 is used to generate both proton-target interactions and secondary particle decay as they travel through the decay pipe. A set of histograms is then created for each neutrino flavor containing its true energy, momentum, and spatial position. The next step then samples these results to generate neutrinos for the detector interaction phase of the simulation.

7.1.2 Neutrino Interaction Simulation

This stage of the simulation handles the interaction between neutrinos and argon nuclei. Neutrino events in the MicroBooNE detector are simulated by the GENIE event generator [86, 87], which employs a combination of phenomelogical models, ab initio calculations, and ad hoc additions for neutrino interactions $\mathcal{O}(1\ \text{GeV})$. The specific version of GENIE adopted for this analysis is GENIE version v3.0.6 [88] with the `G18_10a_02_11a` model configuration [89], which has been well tested to reproduce the results obtained for other experiments such as MiniBooNE, T2K, Minerνa and Noνa. GENIE v3 includes the Valencia group's charged-current quasi elastic (CCQE) interactions and charged-current "two particle, two hole" (CC 2p2h) processes [90–92], considered the best neutrino interaction models at the moment of writing this thesis. Furthermore, MicroBooNE tunes these models using a data sample of CC π^0 from T2K [93], which uses neutrino beam energies similar to the BNB. GENIE treats the argon nucleons as a non-interacting Fermi gas, which is known as the local Fermi gas model [94], and depending on the neutrino kinematics, it uses a particular model to simulate the interaction. The Valencia CCQE

Table 7.1: Interaction models used in GENIE v3.

Interaction	Model
Nuclear Model	Local Fermi Gas
Quasielastic Scattering	Nieves
CC MEC	Nieves
NC MEC	Empirical
NC Elastic	Ahrens
Resonance	Berger Sehgal
Coherent Pion Scattering	Berger Sehgal
Deep Inelastic Scattering	Bodek-Yang
Hadronization	AGKY
Final-state Interactions	hA2018

model [91] accounts for long-range nucleon-nucleon correlations within the nucleus using the random phase approximation (RPA) [93]. This "RPA effect" is used to suppress the CCQE cross section at low Q^2. The strength of the RPA effect is tuned for MicroBooNE. The Nieves model is used for quasi-elastic interactions and the meson exchange current channel (MEC), which accounts for correlated nucleon pairs. The Berger and Sehgal model [95] is used to model RES and coherent pion production, while deep inelastic scattering (DIS) is described by the Bodek-Yang model [96]. The resulting final-state particles and kinematics are then passed on to the detector response simulation.

7.1.3 Detector Response Simulation

The simulated particles generated by GENIE are propagated through a GEANT4-based simulation of the geometry of the MicroBooNE detector [97]. This part of the simulation is handled by the LArSoft framework which uses a suite of tailored algorithms to produce simulated TPC and PMT signals for the amount of simulated neutrino energy. The PMT simulation uses the energy and position of the interaction to estimate the number of photoelectrons that would be generated on each PMT. The TPC simulation is more complex and involves several steps. First, the trajectory of the neutrino-induced particle is broken down into discrete steps, and the amount of energy deposited is found at each point. This deposited energy is then translated into discrete electron depositions that form the ionization cloud. The initial amount of electrons liberated is

dictated by the electron-ion recombination model, which is an effect quantified by the modified Box model [98] that reduces the number of electrons per MeV deposited in the liquid argon. The amount of drifting electrons that will arrive at the anode is calculated as a function of time and folds in multiple drift-dependent detector effects. Space-charge effects (SCE) can change the apparent position of the electrons because of nonuniformities in the electric field [79, 99, 100]. Attenuation and diffusion effects are also considered [101]. Finally, the drifted electron cloud is used to simulate the expected wire waveform signal followed by the shaping, amplification, and digitization of the signal [19, 102].

7.1.4 Cosmic Event Overlay

After generating a neutrino event, the simulation then overlays comic data taken from the off-beam data stream (see Section 5.5.1). This step not only adds cosmic-ray interactions to the simulation but also reproduces detector noise in a data-driven way. The overlay also has the advantage of gauging the channel status (for example, detecting noisy channels) and can apply this information to the simulated channels. The final product of the overlay process is the addition of the raw digitized waveforms for each of the PMT and TPC channels from the detector simulation stage and the off-beam event from collected data. The information from the simulation is then passed to the signal processing and reconstruction steps described in the next sections.

7.2 Signal Processing

Event processing at MicroBooNE begins by taking in the raw detector output and transforms them into information that can be used to reconstruct the neutrino event. This process involves removing excess noise and then processing the voltages registered through a deconvolution process, which removes detector effects in order to obtain an accurate number of drifting electrons as a function of time.

The signal processing inputs are the waveforms formed by clouds of electrons inducing a charge on the sensing wires, whether it be a simulated event described in the last section (Sec-

tion 7.1) or from the MicroBooNE TPC described in Section 5.3.2. Although the wire planes record a voltage over the TPC readout window, more work must be done to extract the number of ionization electrons that reached the wire. MicroBooNE uses the Wire Cell (WC) framework in order to unfold the "true" signal from the measured signal. WC takes into account effects related to event topology, electric field response describing the induced current on the wires due to the drifting electrons, and the electronics response describing the resulting signal waveforms. Before the original signal is unfolded, noise-removing algorithms are employed to address sources of noise within the detector.

Several sources of noise have been identified within the MicroBooNE detector [15]. These sources exceed the low level of excess noise inherent in the readout electronics. The sources of excess noise can be categorized into three types, listed here in the order of greatest impact:

- Noise from the low-voltage regulators: this noise comes from the low-voltage regulators that power the ASICs. It is coherent across all channels with a regulator in common. A correction is applied to the raw waveforms, computed from a set of 48 channels that share the same regulator.

- Noise from the cathode high-voltage power supply: ripples from the cathode HV power supply induce voltage fluctuations via capacitive coupling between the cathode and/or field cage and sense wires and is seen on the signal waveforms. The two highest peaks can be seen at 36 kHz and 108 kHz, which correspond to the ripple frequency of the HV power supply. This noise source has a larger effect on the first induction plane (U) compared to the other planes. The affected frequencies are masked to remove this noise source.

- Burst noise: the source of this noise id due to a ground loop caused by an inadvertent connection between the building ground and detector ground through the electronics rack for the UV laser system. Its been observed at frequencies around 900 kHz. Though no mitigation scheme is developed to remove this source of noise, it is naturally attenuated by the pre-amplifier and the shaper in the ASICs.

The results of the noise removal algorithm can be observed in Figure 7.1.

Once identified noise sources have been subtracted from the waveforms, a deconvolution method is employed to extract the drift electron distribution. This procedure is described in detail in [19, 102]. A brief overview is provided here.

The measured signal $M(t')$ is modeled as a convolution of the original signal $S(t)$ and the detector response function $R(t'-t)$, which represents the instantaneous portion of the measured signal at t' due to an element of the original signal at time t. The convolution takes the form of:

$$M(t') = \int_{-\infty}^{\infty} R(t'-t)S(t)\,dt \tag{7.1}$$

The "full" detector response $R(t'-t)$ carries folded within the function both the wire field response and the electronics response. Using a Fourier transform on Equation 7.1, one can find the original signal form in the frequency domain, ω. However, the solution must be extended to account for additional contributions of detector and electronics noise using a low-pass filter function $F(\omega)$. The original signal function in the frequency domain then takes the form of:

$$S(\omega) = \frac{M(\omega)}{R(\omega)} \cdot F(\omega) \tag{7.2}$$

One can obtain the original signal using an inverse Fourier transform on Equation 7.2.

The deconvolution of Equation 7.2 assumes that the induced current in each of the channels is independent of the topology of the charge distribution across the neighboring wires. However, this is not the case, as the induced current on the sense wire is affected by topology-dependent contributions from the drifting of the ionization charge past neighboring wires during signal formation. To account for these effects to the signal, a more realistic model is given by

$$M_i(t_0) = \int_{-\infty}^{\infty} (... + R_1(t_0-t)\cdot S_{i-1} + R_0(t_0-t)\cdot S_i + R_1(t_0-t)\cdot S_{i+1} + ...)\cdot dt, \tag{7.3}$$

where M_i represents the measured signal from the i-th wire, S_i is the original signal within the boundaries of the i^{th} wire, and R_k is the average response function of the ionization of charge

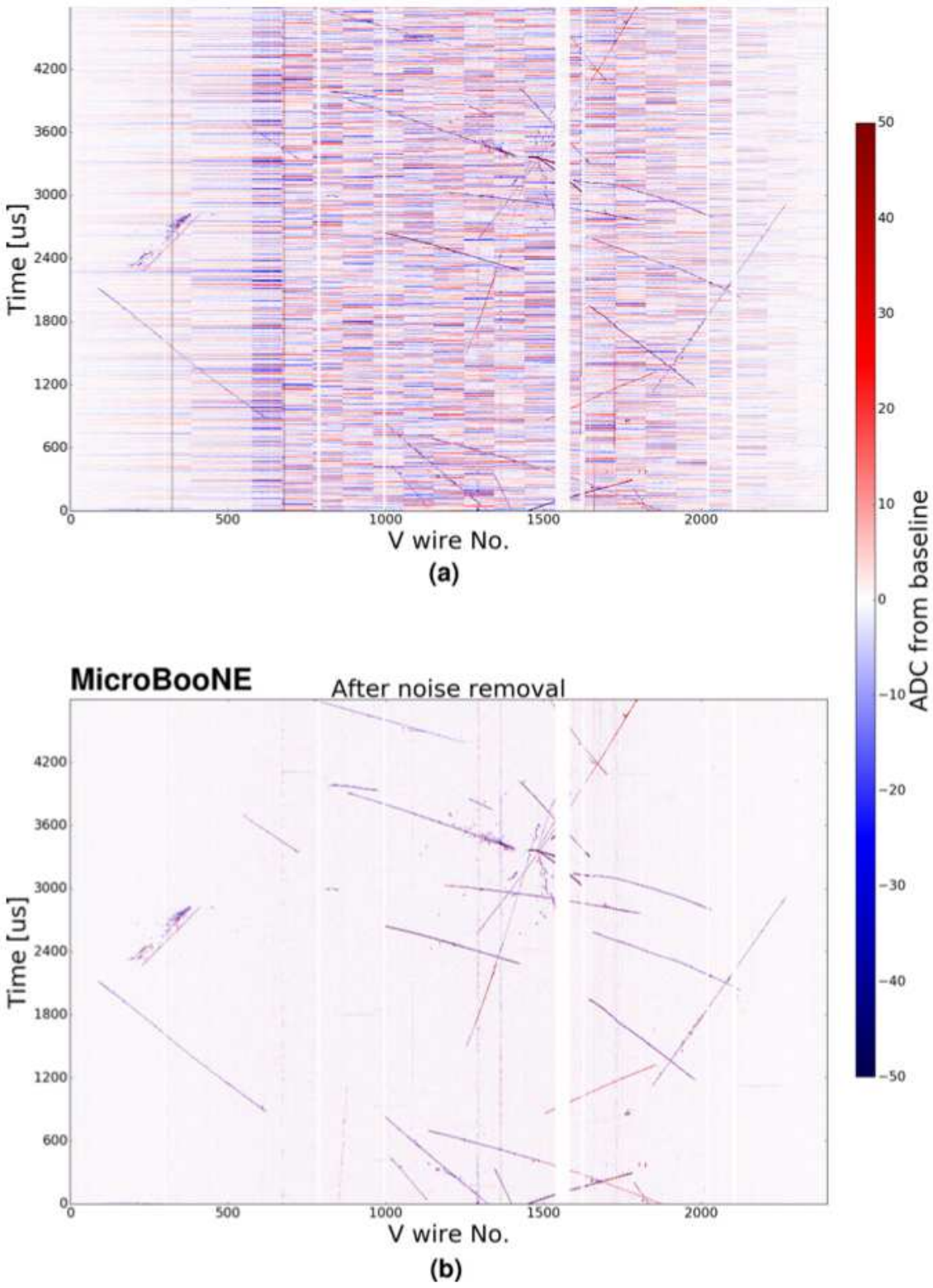

Figure 7.1: A 2D event display of the V plane before (a) and after (b) the offline noise filtering has been applied. The event after noise removal shows a clear and crisp image once all noise sources are subtracted. Figure from [15]

.

passing through the k^{th} wire away from the wire of interest. Note that the response function in Equation 7.3 is assumed to be translationally invariant (i.e. R is independent of the actual location of the wire). Figure 7.2 shows examples of the response function for each wire.

Converting Equation 7.3 into the frequency domain using a Fourier transform yields the following:

$$M_i(\omega) = ... + R_1(\omega) \cdot S_{i-1}(\omega) + R_0(\omega) \cdot S_i(\omega) + R_1(\omega) \cdot S_{i+1}(\omega) + ... \tag{7.4}$$

or, written in matrix notation,

$$\begin{pmatrix} M_1(\omega) \\ M_2(\omega) \\ \vdots \\ M_{n-1}(\omega) \\ M_n(\omega) \end{pmatrix} = \begin{pmatrix} R_0(\omega) & R_1(\omega) & \cdots & R_{n-2}(\omega) & R_{n-1}(\omega) \\ R_1(\omega) & R_0(\omega) & \cdots & R_{n-3}(\omega) & R_{n-2}(\omega) \\ \vdots & \vdots & \ddots & \vdots & \vdots \\ R_{n-2}(\omega) & R_{n-3}(\omega) & \cdots & R_0(\omega) & R_1(\omega) \\ R_{n-1}(\omega) & R_{n-2}(\omega) & \cdots & R_1(\omega) & R_0(\omega) \end{pmatrix} \begin{pmatrix} S_1(\omega) \\ S_2(\omega) \\ \vdots \\ S_{n-1}(\omega) \\ S_n(\omega) \end{pmatrix} \tag{7.5}$$

One can apply Fast Fourier Transform (FFT) methods to invert matrix R and determine the original signal vector S. The signal processing at MicroBooNE utilizes this 2D deconvolution technique, which involves both the time and wire dimensions, and extracts the original signal induced by the electron ionization distribution. A response function used in Equation 7.5 is calculated for the central wire and 10 adjacent wires on either side. The individual wire response is averaged over six equidistant drift paths within 1.5 mm of the wire. Filters to attenuate high-frequency noise are applied in both dimensions.

While the 2D deconvolution procedure described above performs well on the collection plane, the performance suffers on the two induction planes. The low-frequency suppression on the induction planes, a feature of bipolar signals, amplifies low-frequency noise when the 2D deconvolution is applied. To remove such noise, signal regions of interest (ROIs) are designated, where only the signal on the wire waveforms is considered. The portion of the waveform inside the ROI is baseline subtracted, then deconvolved, while the rest of the waveform is discarded. This procedure is applied in both the induction and collection planes for consistency.

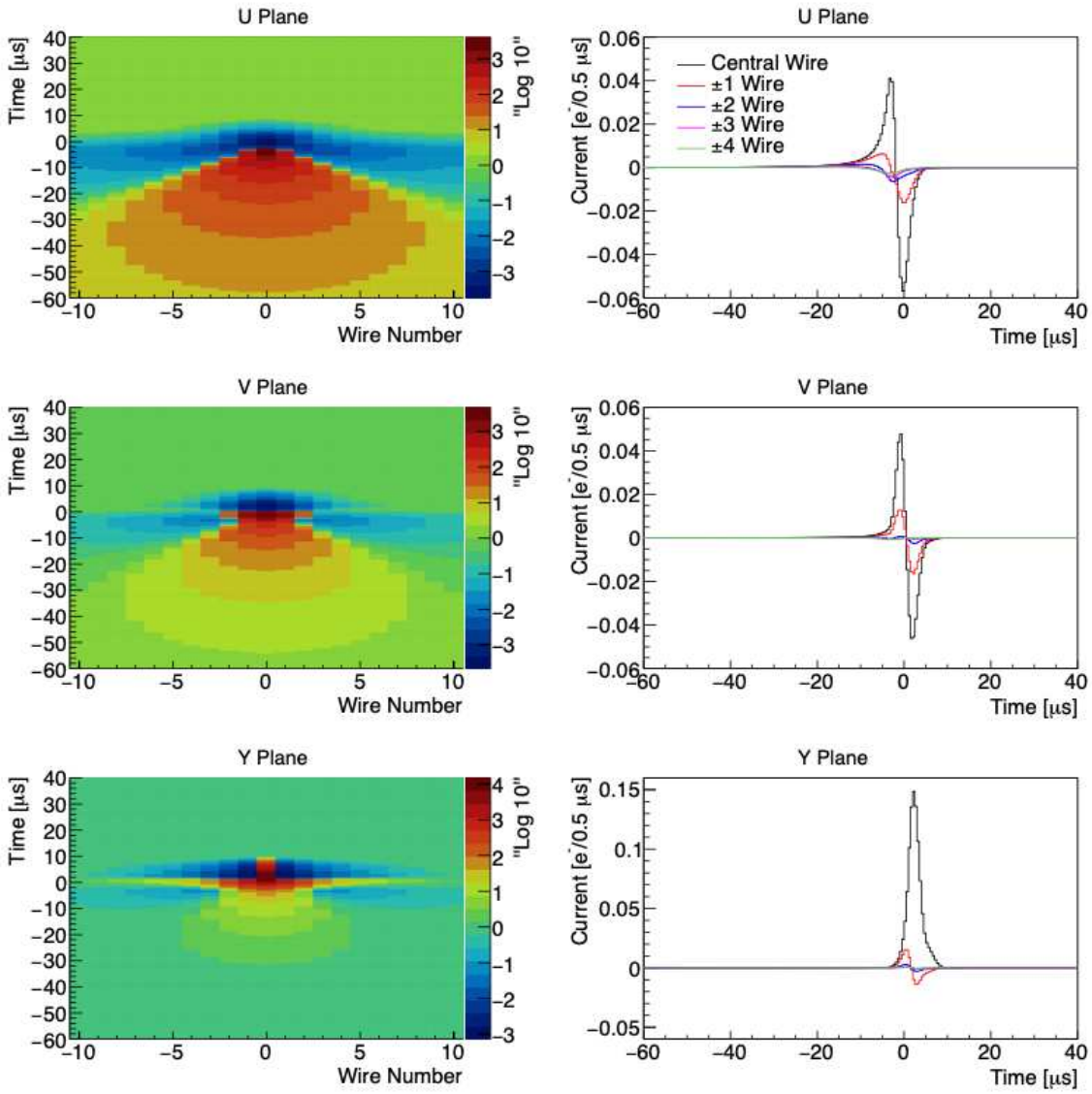

Figure 7.2: The average response functions after convolving the field response function and the electronics response function. The plots in the left column show the response function for a central wire and ±10 wires as a function of time and wire number in a Log_{10} scale. The plots in the right column show the response function in a linear scale for a central wire with ±4 wires as a function of time on a linear scale. Figure from [19]

.

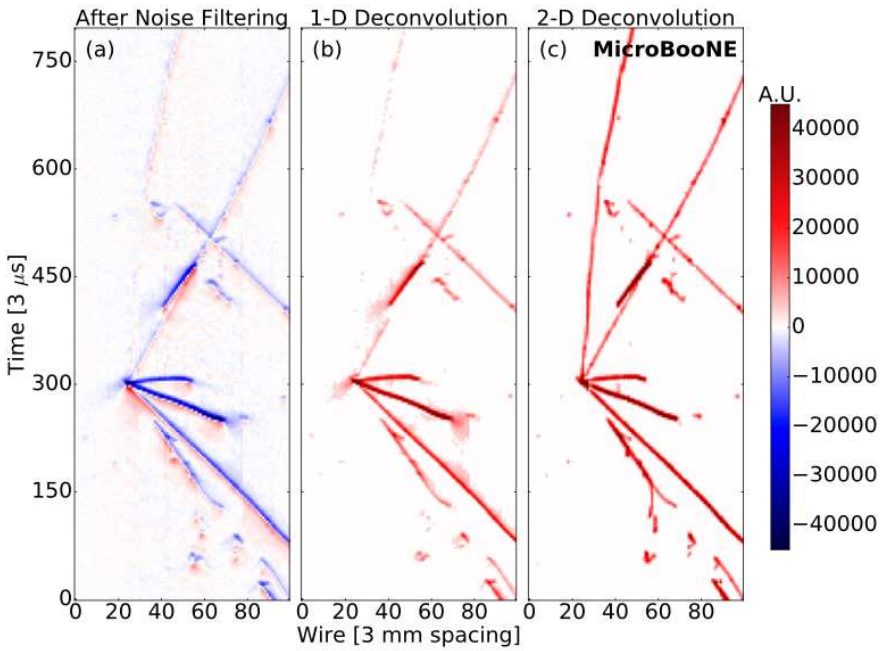

Figure 7.3: Event display from a neutrino candidate (event 41075, run 3493) on the U-plane at different stages of the signal processing. (a) shows the raw waveforms after running the noise filtering algorithms in units of ADC scaled by 250 per 3 μs; (b) and (c) show the charge spectrum in units of electrons per 3 μs after signal processing with 1D and 2D deconvolution respectively. Figure from [19].

The results of the described signal processing chain are deconvolved wire waveforms. The post-deconvolution signal waveforms have a Gaussian shape due to the Gaussian filter function used in the signal processing. This is convenient for the reconstruction and for calculating the amount of charge that drifted past the wire planes. The results of the deconvolution can be observed in Figure 7.3.

7.3 Event Reconstruction at MicroBooNE

MicroBooNE has adopted several reconstruction paradigms, each taking the output of the signal processing from the previous section. The three main reconstruction techniques that have been adopted at MicroBooNE for neutrino searches are the following: Pandora pattern recognition software [20], Wire Cell reconstruction toolkit [103, 104], and deep learning-based reconstruction [105]. Wire Cell Toolkit is a tomographic reconstruction technique that uses charge matching across the wire planes to form a 3D image. The deep learning technique breaks

down the 2D images from the wire planes into pixels, which are then tagged as a certain particle species using a convolutional neural network. Although both the Wire Cell and the deep learning techniques have produced interesting results for MicroBooNE, the Pandora pattern recognition software will be the reconstruction technique used for the analysis presented in this thesis.

7.3.1 Light Signal Reconstruction

After signals are collected by the PMTs (Section 5.3.3), the raw waveforms are used as input for light signal reconstruction is gathered and combined into the "flash". The raw waveforms collected are first examined for optical activity, which is defined as the waveform amplitude exceeding a certain threshold. After determining if optical activity is present, a baseline is calculated using a rolling mean on the parts of the waveform with no signal activity. The baseline is then subtracted from the full waveform. The resulting object is then classified as an optical hit. A flash is then formed from a group of optical hits that are coincident in time. These flashes are then used as input to the flash-matching algorithm, which uses flash timing to identify neutrino events. Each PMT records a certain amount of optical activity, which is then compared to that predicted for a certain event in the TPC. If both the prediction and the measured optical activity closely match the expectation (using a χ^2 test), then the optical activity matches the reconstructed flash. The results of the flash-matching technique significantly reduces the amount of cosmic background by an order of magnitude and improve MicroBooNE's ability to correctly identify neutrino interactions [106].

7.3.2 The Pandora Multi-Algorithm Pattern Recognition Software

After the signal processing is performed on the wire waveforms (described in Section 7.2), the deconvolved waveforms are fitted to a Gaussian and are reconstructed as hit objects or, simply, hits. Hits are then characterized by their peak time and area under the Gaussian fit (integral), which is proportional to the charge registered by the hit. A 2D map is then formed by all the hits

of a plane using the wire coordinates and the arrival time of the ionization electrons. This map serves as the input for the Pandora event reconstruction framework.

The Pandora framework is a suite of algorithms, each designed to address a specific task for a particular event topology and, as a whole, takes a multi-algorithmic approach to pattern recognition. Pandora takes reconstructed hits as input and produces Particle Flow Objects (PFOs), which in turn produces Particle Flow Particles (PFPs) as output. PFOs are linked to other reconstructed objects in a hierarchy of parent and daughter particles. The main reconstruction objects resulting from the Pandora chain are *tracks* and *showers*. Tracks manifest themselves as relatively straight and narrow lines crossing the TPC volume, a signature of cosmic muons and protons. Showers show up as cascades of charge depositions in a conical shape, usually produced by primary electrons or by pair production.

The Pandora reconstruction chain consists of two phases. The first phase is *PandoraCosmic* and targets the reconstruction in a track-oriented approach to unambiguously label them. Daughter delta rays can also be captured and are classified as showers and added as daughter particles of the main track. Cosmic activity is characterized as being downward going, so cosmic muon reconstruction can be easily tagged. Other cases such as muons entering and exiting the TPC or entering the detector outside of the beam timing window are also tagged by PandoraCosmic. At the end of this phase, a cosmic-removed hit collection is created, and the remaining hits are used in the neutrino candidate pattern recognition.

The second phase is *PandoraNu* and aims to identify the neutrino interaction point, known as the vertex, along with all resulting particles. It does this by first reconstructing all tracks and showers and interpolating backward in the beam direction to find the vertex position. Then a neutrino parent particle is made, and all subsequent particles emerging from the interaction are reconstructed as daughter particles. A diagram of the Pandora output data product showing the parent/daughter link for PFPs is shown in Figure 7.4.

At this point, Pandora has classified all 2D hits as containing cosmic activity by *PandoraCosmic* or belonging to a neutrino interaction by *PandoraNu*. Collections containing reconstructed

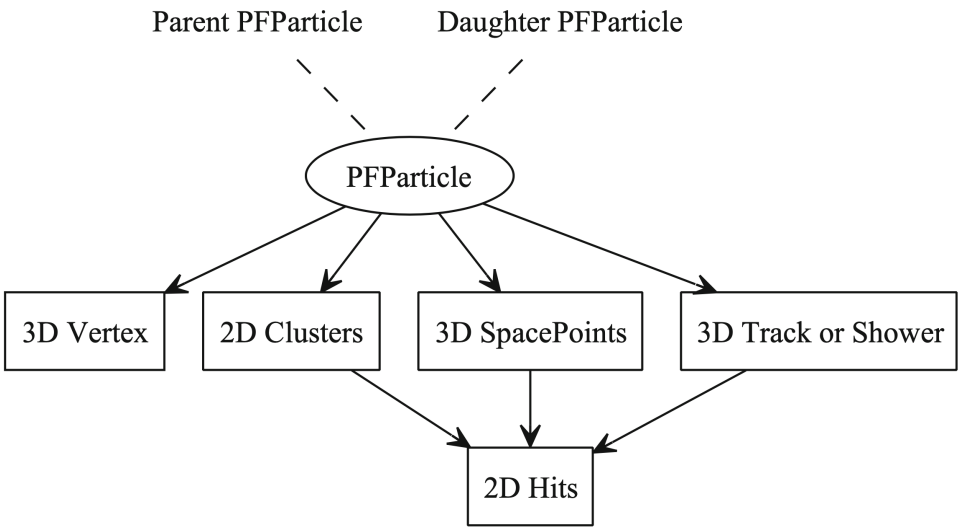

Figure 7.4: The Pandora output data products. The reconstructed particle hierarchy is shown by the dashed lines while the arrows point to the associated data members of a PFP. Figure from [20].

particles of the same interaction are created and called *slices*. The 2D hits within each of the slices tested under both the cosmic hypothesis and the neutrino hypothesis. Each slice is then reconstructed under both a cosmic hypothesis and the neutrino hypothesis assigning a neutrino slice score, where a higher score indicates a neutrino-like interaction, while a lower score indicates a cosmic-like interaction.

To reconstruct neutrino activity in 3D, Pandora starts by matching timing information from at least two wire planes with coincident activity. It then creates a number of 3D candidate vertices, which then project down to each of the 2D clusters. The vertex candidates are then scored using a support vector machine (SVM), declaring the candidate with the highest score as the true vertex. After the vertex has been found, another clustering algorithm is deployed to further improve the matching accross the planes.

The objects resulting from the reconstruction are PFPs, shown in Figure 7.4. PFPs are constructed from the 2D clusters of each of the wire planes. Three-dimensional information for these objects is also available in the form of *SpacePoints*, which are the 3D projection of the 2D clusters. SpacePoints are also associated with charge information from 2D Hits. Additionally, a

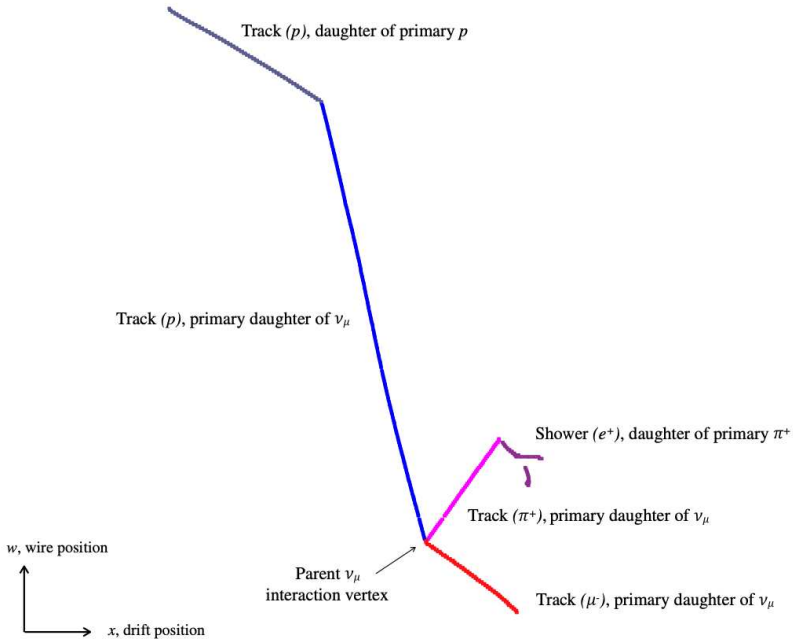

Figure 7.5: Reconstructed CC ν_μ event from simulation. The hierarchy of particles is shown with the parent neutrino at the interaction vertex and primary and secondary daughter particles resulting from the interaction. Figure from [20].

3D vertex is also calculated for PFPs. Furthermore, PFPs have a place in a hierarchical structure, where a parent-daughter relationship is established for particle interactions and decays.

Each PFP is classified as track-like or shower-like according to a continuous score. This score is determined by an SVM that takes into account topological information from the hits. The score runs from 0 to 1 where lower scores indicate shower-like objects and higher scores indicate track-like objects. Shower- or track-like data products are created depending on this score.

For track-like objects, a sliding linear fit procedure is used to find the 3D position and direction at each point along the track. The charge per unit length, dQ/dx, is calculated at each point along the track. Charge deposition (dQ) is calculated taking into account position- and field-dependent charge calibrations (see Section 7.4). The dx includes corrections due to impacts from space charge effects [79, 100]. Obtaining the deposited energy per unit length (dE/dx) from the charge (dQ/dx) is performed applying the inverse modified Box model, which takes into account the non-linearity of local ionization densities on the electron-ion recombination.

For shower reconstruction, the particle is reconstructed as a 3D cone containing the SpacePoint collection. This object has several quantities associated with it such as a defined length, opening angle, and a 3D direction. It should be noted that in MicroBooNE the shower reconstruction was validated using a sample of π^0 events [107]. Similar to tracks, a shower's dE/dx profile can also be measured and can serve as a powerful tool in performing electron-photon separation. The result is a dE/dx measurement (see Section 7.6), which is an important value for the main analysis in this thesis.

7.4 Energy Scale Calibration

Once reconstructed particles have been generated, it is important to calibrate the detector and take into account the accuracy of the reconstructed quantities. The main goal of the detector calibration is to obtain a uniform detector response across the three wire planes, and to accurately reconstruct a particle's deposited energy from the ADC counts read out from the TPC. In particular, being able to predict the dQ/dx and dE/dx is crucial for any analysis making use of data collected from a LArTPC detector; dE/dx is an important handle to distinguish between photons and electrons showers. A photon decaying inside the detector produces a e^-/e^+ pair that deposits twice as much energy compared to a single electron; thus, the dE/dx measurement for a photon would be double that of an electron.

Reconstructing dE/dx in a LArTPC detector involves the extraction of charge information from the signals on the anode plane wires. After signal processing (Section 7.2) and particle reconstruction (Section 7.3) a calculated dE/dx is available, although it is not accurate. Many known detector effects can affect the drifting electron clouds towards the anode, such as electric field distortions caused by space charge effects, electron attachment to impurities, diffusion, and recombination. There is also a set of misconfigured, shorted, or unresponsive TPC channels (see Section 5.3.2.2) that affect the final charge measurement. The calibrations are intended to obtain a uniform detector response and are used to recover misconfigured channels [21]. Recall that a set of U-plane channels have been configured with the factory default set-

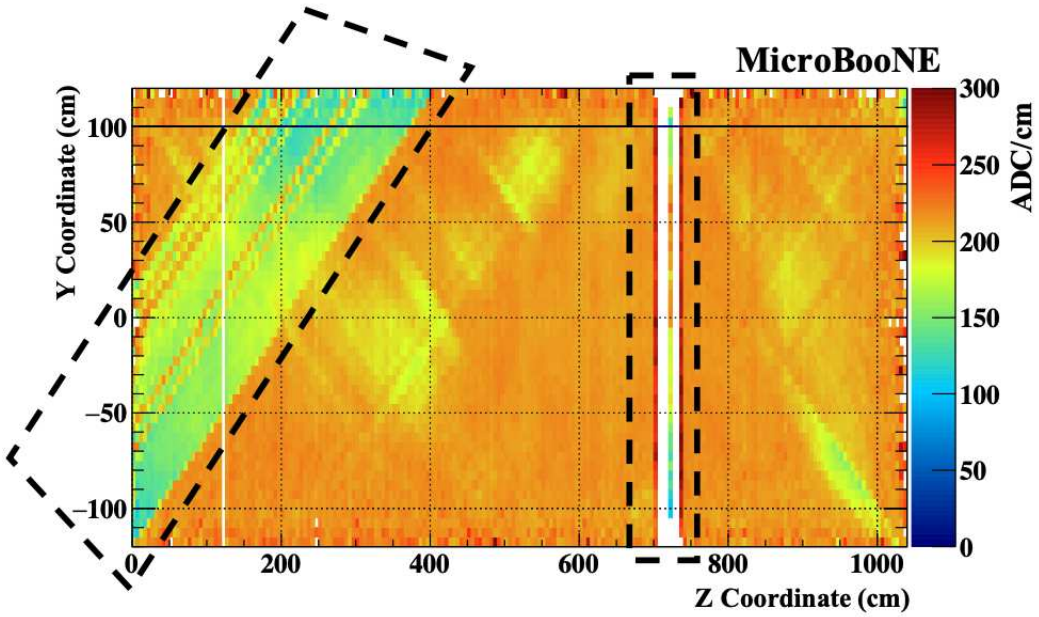

Figure 7.6: Distribution of dQ/dx in the collection plane along the vertical (Y) and beamline (Z) coordinates in data. The highlighted region on the left shows the effect of the cross-connected U-plane channels, while the region on the right shows the unresponsive channels on the collection plane. Figure from [21].

tings for the gain and shaping times. A deconvolution with the nominal gain and shaping time results in channels having higher noise levels, though a signal can still be measured. Figure 7.6 shows the dQ/dx distribution on the collection plane along the plane coordinates, where Y is vertical and Z runs along the beam direction. The highlighted region on the left is the "shorted-U" region, and the vertical region on the right is the "shorted-Y" region. Other nonuniformities are in the drift direction and primarily cause electron attenuation and electron diffusion. The motivation of dQ/dx calibration is to account for these non-uniformities in the detector. Once a calibrated charge response is found, the next step is to obtain the calibrated energy. The calibration chain follows:

$$\frac{dQ}{dx} \xrightarrow[\text{correction}]{\text{uniformity}} \left(\frac{dQ}{dx}\right)_{cal} \xrightarrow[\text{correction}]{\text{recombination}} \left(\frac{dE}{dx}\right)_{cal} \tag{7.6}$$

The calibration of the MicroBooNE detector dQ/dx uses a sample of cosmic muon tracks that cross the detector. The cosmic muons in this sample cross both the cathode and the anode

and are nearly uniformly-ionizing. Furthermore, the start and end positions of the muon tracks are well defined, making their precise arrival time, t_0 in the detector well known. These properties make crossing muons a good standard candle for calibration. The dQ/dx calibration is done in two parts:

- ZY spatial correction: this part aims to remove the effects of space charge, cross-connected TPC channels, and transverse diffusion. The dQ/dx is mapped along the ZY plane in 5×5 cm bins and a median dQ/dx is calculated. The ratio of the local dQ/dx and the global dQ/dx is then used as the correction factor.

- Drift (X-coordinate) correction: this part aims to remove effects of electron attachment to impurities, space charge, and longitudinal diffusion. Electron lifetime measurements (the same method used as in Section 4.2.5) are taken day by day and stored in a database. These values then serve as the drift-dependent correction factor.

After the dQ/dx calibration process is complete, $(dQ/dx)_{cal}$ is found and an absolute energy loss per unit length dE/dx can be determined. The dE/dx is then calculated using a modified Box model [98] for recombination:

$$\left(\frac{dE}{dx}\right)_{cal} = \frac{\exp\left[\frac{\left(\frac{dQ}{dx}\right)_{cal}}{C_{cal}} \cdot \frac{\beta W_{ion}}{\rho \epsilon}\right] - \alpha}{\frac{\beta}{\rho \epsilon}} \tag{7.7}$$

where:

- C_{cal} is a calibration constant used to convert ADC values to the number of electrons,

- W_{ion} is the work function of argon (23.6 MeV/electron),

- ϵ is the MicroBooNE nominal drift electric field (0.273 kV/cm),

- ρ is the density of liquid argon at a pressure of 124.106 kPa (1.38 g/cm^3),

- $\beta = 0.212$ (kV/cm)(g/cm^2/MeV),

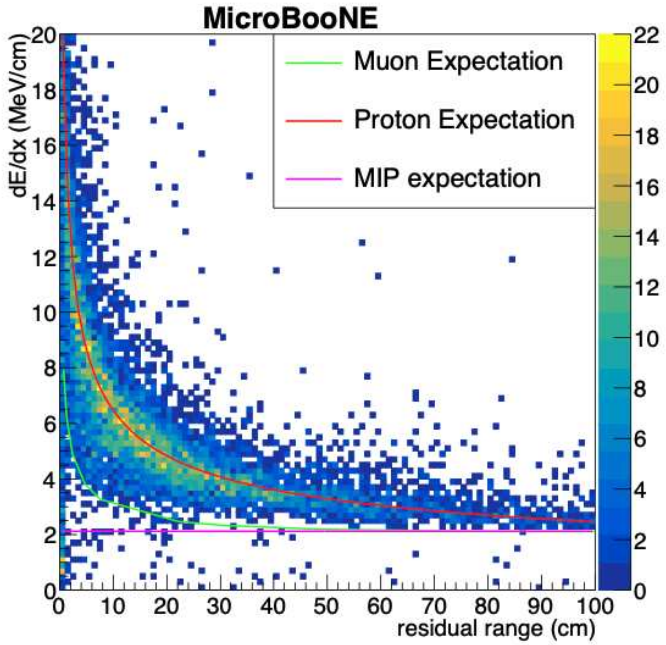

Figure 7.7: Distribution of dE/dx as a function of residual range for CC ν_μ-induced muons. The solid lines indicate the Bethe-Bloch predictions for several particle types. Figure from [21].

- $\alpha = 0.93$

The constants α and β are parameters determined by the ArgoNeuT experiment [98]. To obtain the absolute energy scale, the calibration constant C_{cal} must be measured. This is done by fitting a Landau function convolved with a Gaussian function to dE/dx as a function of the residual range (distance from the end of the track). The most probable value of C_{cal} is the extracted [21].

Another way to verify the calibration is to measure the dE/dx of muons from BNB-induced CC ν_μ interactions [21], specifically looking at the track dE/dx as a function of the residual range. Figure 7.7 shows this result along with the prediction of the Bethe-Bloch formula for muons, protons, and minimum ionizing particles (MIPs). For this analysis, dE/dx information is an important input for the identification of particles in the formulation of a test statistic that quantifies the likelihood that a particle is of a particular species.

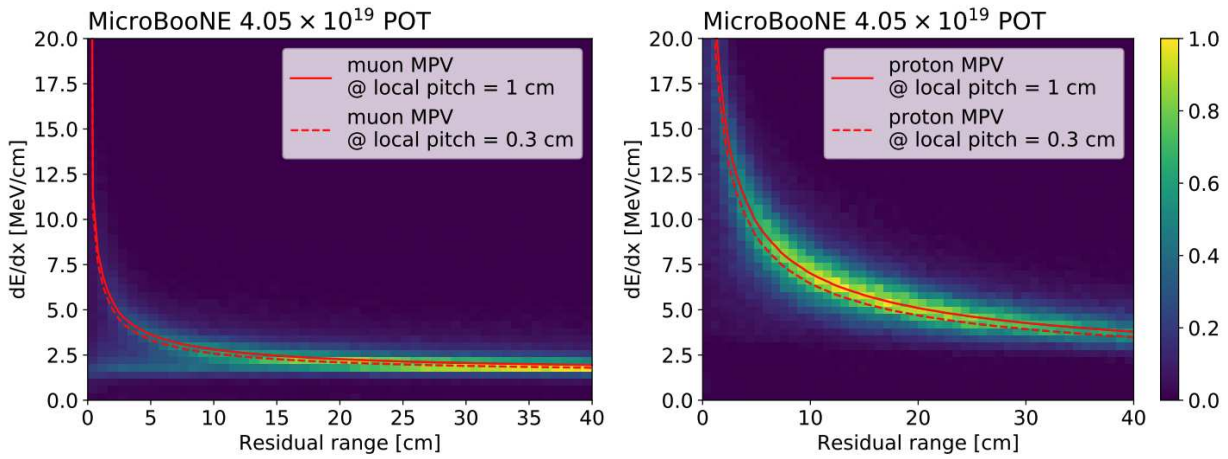

Figure 7.8: Deposited energy per unit length (dE/dx) vs residual range profile for reconstructed and contained tracks in data, for muon (left) and proton (right) candidates, with plots sharing color scales. The theoretical predictions for the extremes of the range of local pitch (red lines) are compared to the underlying profiles [22].

7.5 Particle Identification

Particle identification (PID) in this analysis focuses on μ/p separation for tracks, and e/γ separation for showers. Although the PID methods developed by the analysis rely on the same underlying calorimetric information obtained from track-fitted dE/dx information, PID is performed with different tools depending on whether the particle is selected as a track or shower candidate. For a particle selected as a track-like object, a log-likelihood ratio PID (LLRPID) is performed. The LLRPID tool leverages the differences in the dE/dx vs. residual range profiles of highly-ionizing proton tracks from minimally-ionizing muons; see Figure 7.8. This method builds probability density functions to model dE/dx given a particle type (muon or proton in this case), wire plane, residual range and pitch of the track with respect to the wire plane. The tool then combines the measured dE/dx along the trajectory of the tracks and the probability density functions and performs a likelihood ratio test to perform the classification. The results of the LLRPID tool can be seen in Figure 7.9. The performance of this tool gives a 90% relative efficiency for proton selection with a 5% misidentification rate. Track PID is used to identify muon candidates produced by CC ν_μ interactions, isolate protons, and remove pion candidates. A more detailed description of this tool can be found in [22].

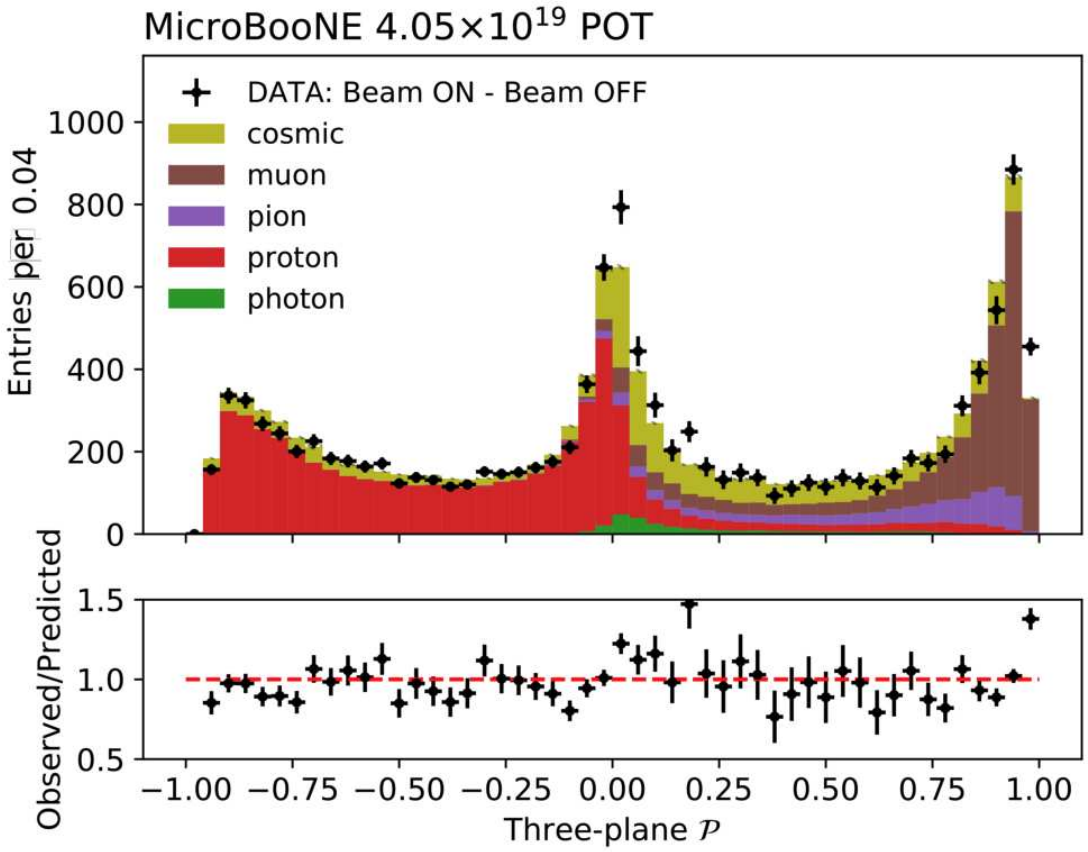

Figure 7.9: Distribution of the log-likelihood-ratio PID variable across the three planes for neutrino-induced tracks contained in the fiducial volume [22].

For shower-like objects, the goal of the PID is to distinguish ν_e-induced electromagnetic showers from photon-induced electromagnetic showers, a crucial step in determining the origin of the LEE. Most of the photonic backgrounds in the ν_e measurements come in the form of $\pi^0 \rightarrow \gamma\gamma$, which are one of the final-state products of neutrino interactions and are larger than the ν_e event rate by approximately one order of magnitude. Three key features are used to separate photon showers from ν_e interactions: the presence of two final-state electromagnetic showers, the distance between the shower and the proton start position from the primary neutrino vertex, and the calorimetric measurement of dE/dx.

The most straightforward way of distinguishing an electron from a photon shower is by counting the number of showers that the interaction produces. Figure 7.10a shows the discrimination of π^0 events from ν_e events based on the number of showers at high energies. The highly boosted π^0 can cause a failure mode in which the reconstruction detects only one shower event in the event of a low energetic second shower where there are two overlapping showers or the second shower can be missed if it is not energetic enough to produce enough hits to be reconstructed. Photons may also go undetected, especially at lower energies (below 100 MeV) or because they escape the detector.

Hadronic activity in a ν_e interaction is another important handle to distinguish photons from electrons, especially to eliminate background in the $1e\mathrm{N}p0\pi$ selection. For these events, a clear gap is present between the neutrino/proton vertex and the shower start point. The performance of this method depends on the ability to detect protons and other hadronic activity at the vertex, and the accuracy of the reconstructed shower start position. Figure 7.10b shows the separation power based on the displacement of the vertex at high energies.

Most of the photons at MicroBooNE are products of π^0 decay and manifest themselves as e^+/e^- pairs. These pairs may be produced as highly-aligned, overlapping showers leading to doubly-ionizing charge segments compared to electron showers. To measure this, reconstructed showers are treated through a Kalman filter procedure, which fits the main trunk of a shower to a track-like object. This excludes all hits outside of the main track [108] and calcu-

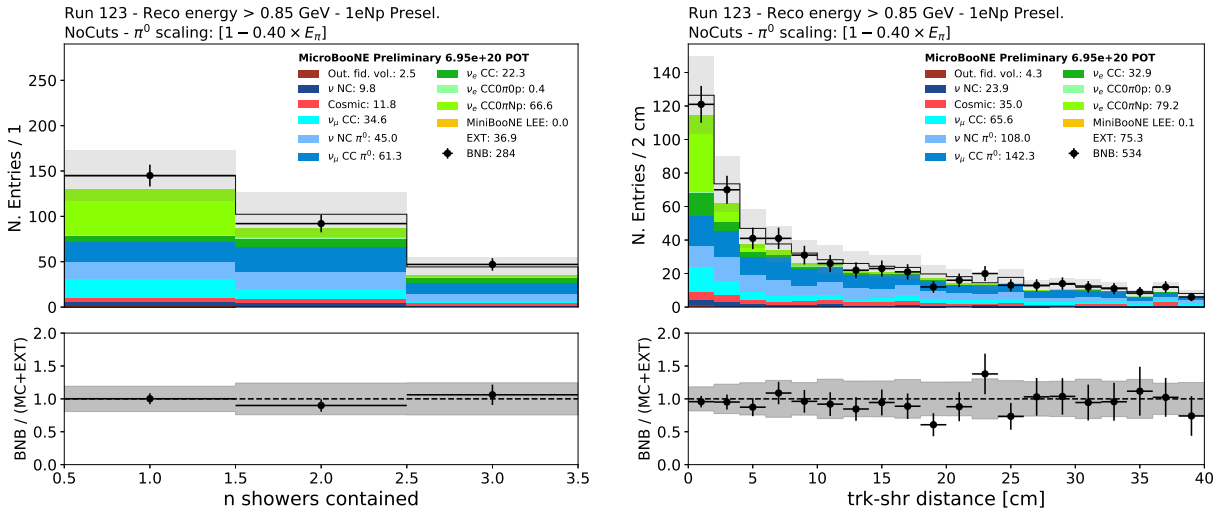

(a) Number of Contained Showers

(b) 3D vertex displacement

Figure 7.10: Performance of electron-photon separation variables for high-energy reconstructed neutrino energy (< 0.85 GeV). The figure on the left shows the number of contained showers with a large amount of ν_e events accumulating on the single shower bin with an underlying amount of misreconstructed π^0 backgrounds. The figure on the right shows the distance distance between the neutrino/hadron vertex and shower start, with most ν_e interactions found at smaller distances.

lates a median dE/dx for a certain portion of the shower. The measured dE/dx distribution is a powerful tool for distinguishing photons from electrons; see Figure 7.11. The result is a significant separation between electrons, which are found around 2 MeV/cm, and photons, where the e^+/e^- pairs produced tend to accumulate around a dE/dx of 4 MeV/cm.

7.6 Energy Reconstruction

Energy reconstruction is based on measurements of the particle range for tracks and calorimetry for electromagnetic showers. For both contained and uncontained muons, energy estimations are also performed using multiple Coulomb scattering (MCS). The reconstruction of the shower energy is measured by integrating the deposited energy (E_{calo}). Table 7.2 shows the energy resolution obtained for several particles, where the numbers are obtained by fitting a Gaussian plus one-sided exponential to $[E_{\text{reco}} - E_{\text{true}}]/E_{\text{true}}$ and extracting the Gaussian standard deviation width σ from the fit. More information on each particle's energy resolution is reported in Figure 7.12 where the reconstructed vs. true energy distribution (in log-scale) is

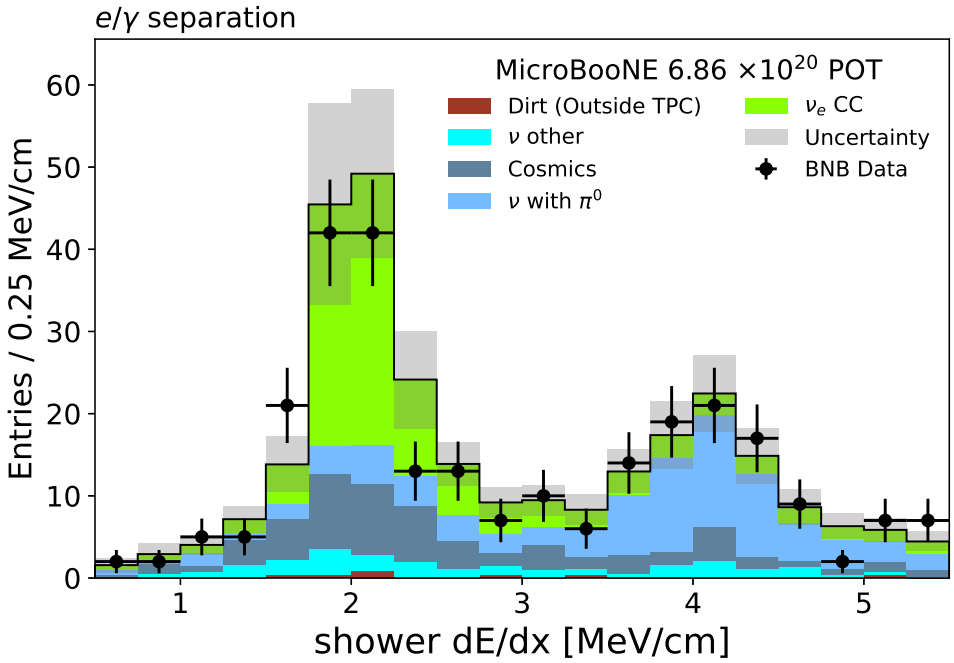

Figure 7.11: Distribution of dE/dx from main shower for neutrino candidates broken down by particle type in the MicroBooNE detector. Showers from electron production peak at 2 MeV/cm while photonic showers peak at 4 MeV/cm.

Table 7.2: Energy resolution for different reconstructed particle species.

Particle	**Kinetic Energy Resolution**
Proton	4% at 100 MeV, 1% at 200 MeV
Muon (range)	3%
Muon (MCS)	25% at 100 MeV, <10% above 400 MeV
Electron	15%

shown on the left, next to a plot of energy resolution vs. true energy on the right. Although this method works well with tracks, calorimetric energy reconstruction for showers presents a significant non-Gaussian component. Figure 7.13 shows the energy resolution for several true electron energy ranges with an applied fit to a Gaussian plus a one-sided exponential function. A residual bias of 3-8% (depending on the energy bin) is reported after applying the 20% energy correction(see following discussion).

The shower energy reconstruction in MicroBooNE is significantly lower than the true shower energy because of reconstruction effects associated with the underclustering of charge and

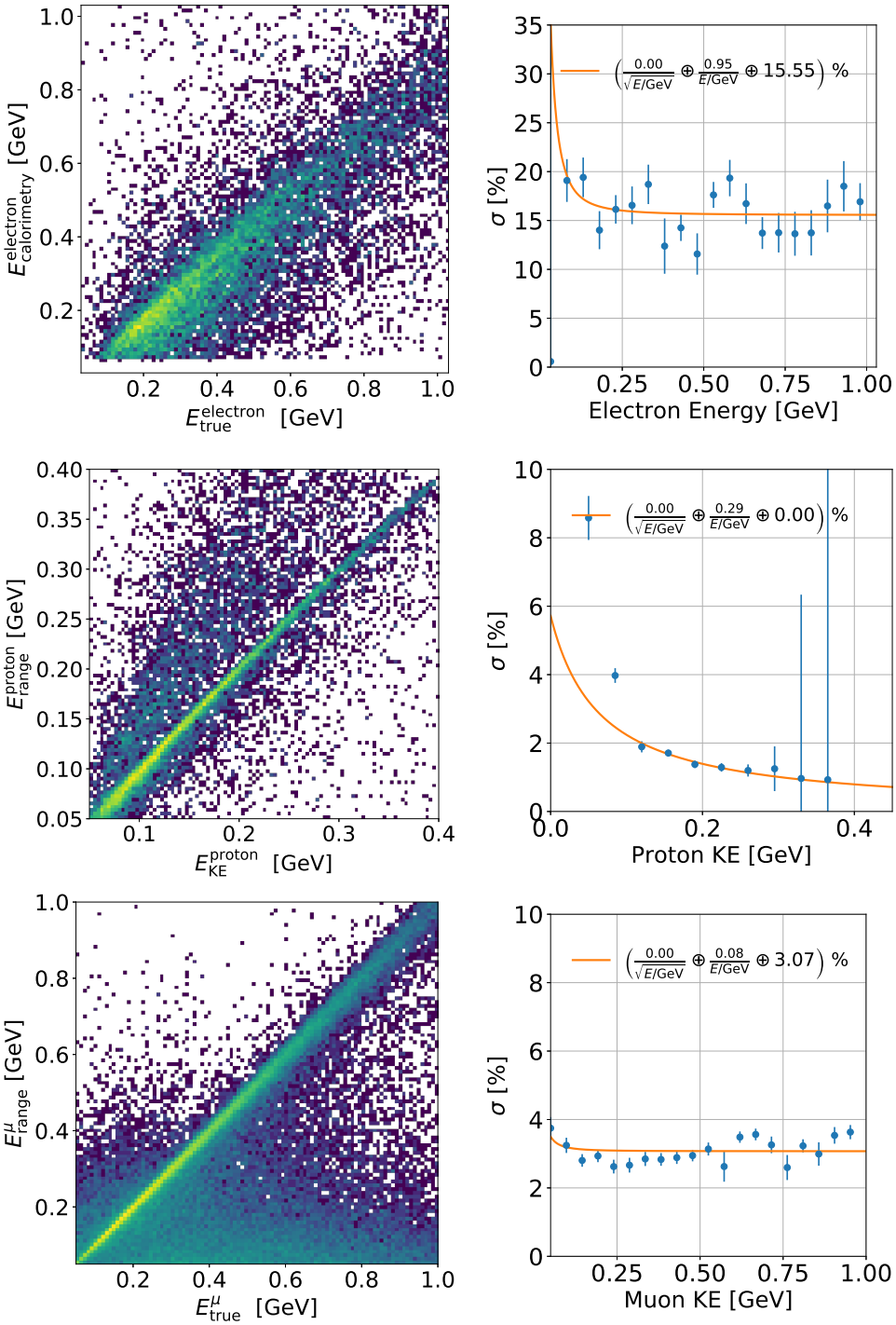

Figure 7.12: Energy resolution for simulated electrons (top), protons (center), and muons (bottom). Left: reconstructed versus true energy resolution (log scale). Right: energy resolution from Gaussian fit to $[E_{\text{reco}} - E_{\text{true}}]/E_{\text{true}}$.

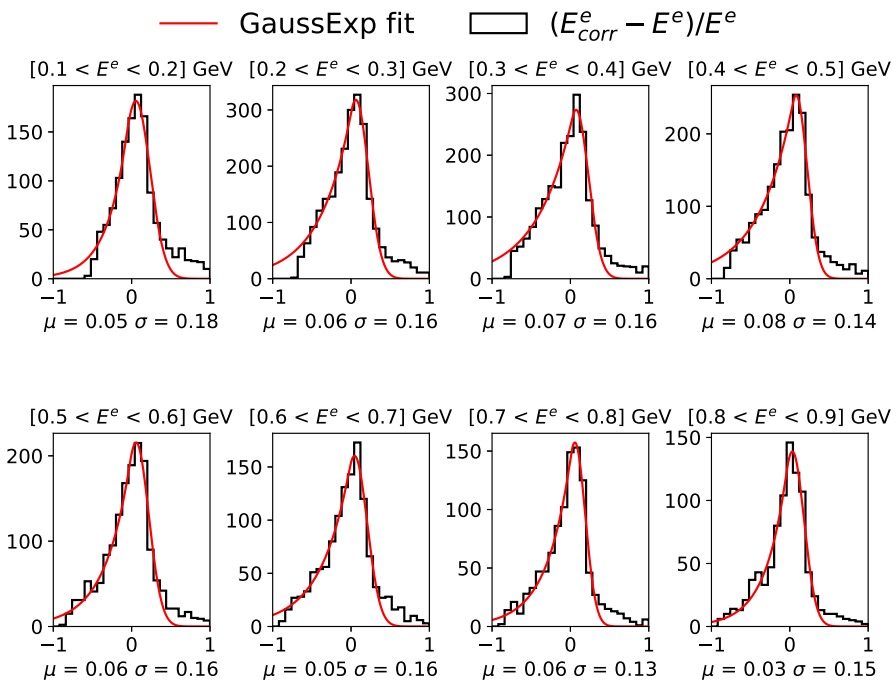

Figure 7.13: Shower energy resolution at various reconstructed energy ranges. A Gaussian plus a one-sided exponential function is fit to each energy distribution with about 3–8% of hits outside of this fit.

thresholding effects. Pandora often fails to correctly cluster an entire shower, leading to missed hits and therefore energy loss. Moreover, shower hits may fall below the energy threshold and are not taken into account for reconstruction. These effects have an expected shower energy loss of 20% [109] and motivate the definition of a corrected shower energy.

A shower energy correction is derived from simulation samples by comparing the true to reconstructed shower energy of electron showers of at least 30 MeV. Figure 7.14a shows that the reconstructed energy is systematically below the simulated energy. A linear fit is then performed on the most probable value in different slices of true energy. Each slice is tuned to account for lower statistics at high energies and provides a reasonable fit to the underlying 2D distribution. This leads to a reconstructed energy definition of $E_{\text{corr}} = E_{\text{calo}}/0.83$ with the results highlighted in Figure 7.14b.

Once the energy for tracks and showers has been calculated, the neutrino interaction energy can be estimated. In this analysis, the reconstructed energy of a neutrino interaction is obtained by combining the visible energy of various reconstructed final-state particles in the interaction.

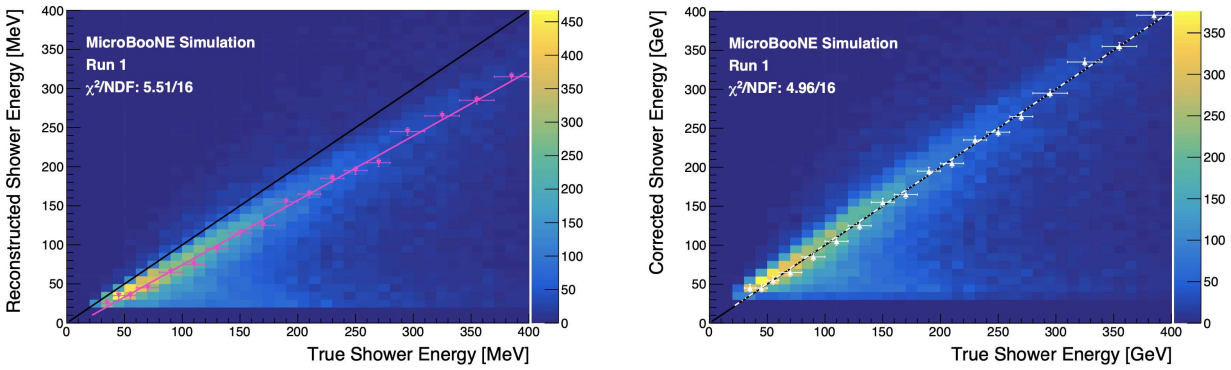

(a) Uncorrected

(b) Corrected

Figure 7.14: (a) 2D distribution of the energy of the reconstructed shower vs. the true energy of the reconstructed showers with at least 30 MeV, taken from a simulated π^0 sample. The points represent the most probable value in each slice of true energy. The slice width (shown by the horizontal error bars) is manually tuned to account for the decreasing statistics at high true energy values. (b) Corrected shower energy vs. true shower energy.

For the ν_e events in $1e0p0\pi$ and $1e\mathrm{N}p0\pi$ channels, the reconstructed energy is defined as:

$$E^{\nu_e}_{\mathrm{reco}} = E^{\mathrm{electron}}_{\mathrm{corr}} + \sum_{\mathrm{tracks}} E^{\mathrm{proton}}_{\mathrm{range}} \tag{7.8}$$

For contained ν_μ interactions, the reconstructed energy is defined as:

$$E^{\nu_\mu}_{\mathrm{reco}} = E^{\mathrm{muon}}_{\mathrm{range}} + \sum_{\mathrm{protons}} E^{\mathrm{proton}}_{\mathrm{range}} + 0.105\ \mathrm{GeV} \tag{7.9}$$

A comparison between the reconstructed and the true neutrino energy can be found in Figure 7.15 for both ν_e and ν_μ. Here, true visible energy is defined as the sum of the lepton energy, pion energy (if present), and proton energy (for all protons above 40 MeV of KE). The comparison shows an accurate reconstruction for most ν_μ events. On the other hand, the ν_e resolution is less accurate, with the smearing dominated by poor shower energy reconstruction.

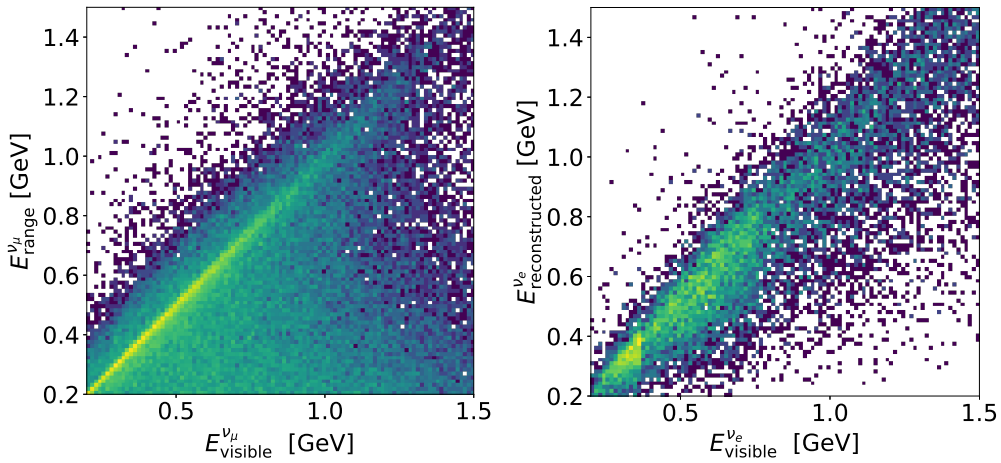

(a) Muon neutrinos.

(b) Electron neutrinos.

Figure 7.15: Log-scale color-maps of reconstructed vs. true energy for ν_μ (a) and ν_e (b). The energy resolution shows good agreement for ν_μ events and some smearing for ν_e events due to poor shower energy reconstruction in some cases.

Chapter 8

Neutrino Selections

This chapter discusses the selection methods and strategies adopted for the eLEE analysis. As discussed in Chapter 6, this analysis is to identify ν_e CC events with the $1e\mathrm{N}p0\pi$ or $1e0p0\pi$ topology and make an inclusive ν_μ measurement. Comparisons of data and prediction for the ν_μ selection provide confidence in the reconstruction tools and refine the predictions of the ν_e CC selections. Then, the full selection chain is presented for both the $1e\mathrm{N}p0\pi$ and $1e0p0\pi$ channels, along with several background data sidebands used for analysis validation. In the end, the final comparisons of the observations and prediction of $1e\mathrm{N}p0\pi$ and $1e0p0\pi$ are used to address whether MicroBooNE observes an excess of low-energy electron neutrinos consistent with the MiniBooNE observation.

This chapter presents both the ν_e and ν_μ selections in detail, including the selection tools used and the selection criteria. In addition, the background sidebands used to validate the consistency of the selection criteria between the data and the prediction will be described. Section 8.1 describes the ν_μ selection. Section 8.2 explains both the ν_e CC selections: the $1e\mathrm{N}p0\pi$ and the $1e0p0\pi$, along with the tools used for making each selection. Finally, Section 8.3 presents several data sidebands that are used to validate analysis tools, calibrations, and energy reconstruction.

8.1 ν_μ Selection

The vast majority of neutrino flux content that arrives at MicroBooNE comes from muon neutrinos, as shown in Figure 5.5a. Obtaining a pure sample of muon neutrinos is key for this analysis to reduce the modeling uncertainties for intrinsic ν_e events and backgrounds, given their common meson parentage and shared ν-Ar interaction modeling.

The expected ν_e rate from the BNB comes with a corresponding set of uncertainties in the estimation. These are associated with detector effects, which affects the reconstruction efficiency, as well as modeling uncertainties in both the ν_e flux and ν-Ar cross section predictions. By having a good handle on the ν_μ rate, one can leverage this information to constrain the flux and ν -Ar cross section uncertainties. The expected flux uncertainties for ν_e are calculated to be $\mathcal{O}(10\%)$ above 800 MeV and increase to 40% at 200 MeV. The lack of ν-Ar cross section measurements makes the uncertainties large for electron neutrino interactions, especially for low energies, due to complex modeling of neutrinos interacting with a heavy target atom such as argon.

In this analysis, the measurement of ν_μ interactions is used to reduce the uncertainty in the measurement of ν_e interactions. This is a data-driven method to constrain the underlying modeling uncertainties that affect both neutrino species. The flux uncertainties are constrained given the fact that muon neutrinos and electron neutrinos intrinsic to the beam are both produced by the decay of common mesons, such as pions and kaons. Furthermore, both neutrinos interact largely through the charged-current interaction mode $\nu_\ell + Ar \rightarrow \ell + X$ and are exploited to further constrain the uncertainties in the ν_e interaction modeling. Figure 8.1 shows the flux correlation matrix for ν_μ (bottom left) and ν_e (top right) interactions obtained from MicroBooNE's adaptation of the BNB simulation developed for MiniBooNE [3]. The red (blue) areas show large (anti)correlation with some quadrants showing strong correlations between both neutrino types. A measurement of muon neutrinos is also used to constrain poorly understood ν-Ar interaction models, specifically in the few-hundred MeV regime that is critical for this analysis. A key goal of this selection is the measurement of low-energy ν_μ interactions to constrain the large uncertainties in low-energy electron neutrinos. Figure 8.2 shows different cross sectional predictions for interacting electron neutrinos and the uncertainty in the cross sections evaluated within the MicroBooNE tune of GENIE-v3 [23].

The rest of this section will focus on the selection of a high-purity and high-statistics sample of muon neutrinos, which will be used to constrain the predictions in the ν_e analysis. This

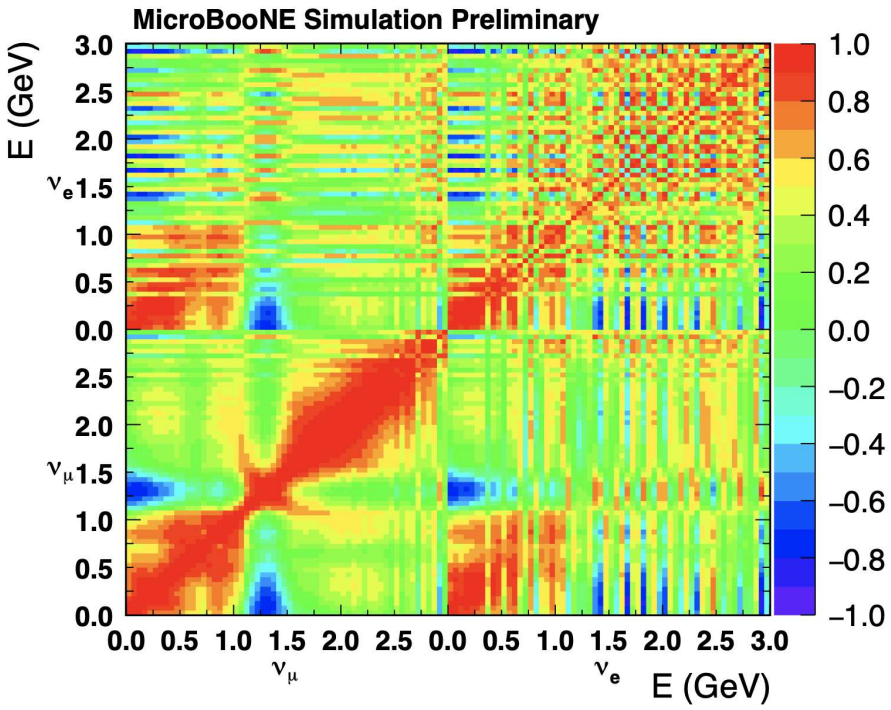

Figure 8.1: Correlation matrix for ν_e and ν_μ flux in true neutrino energy [3].

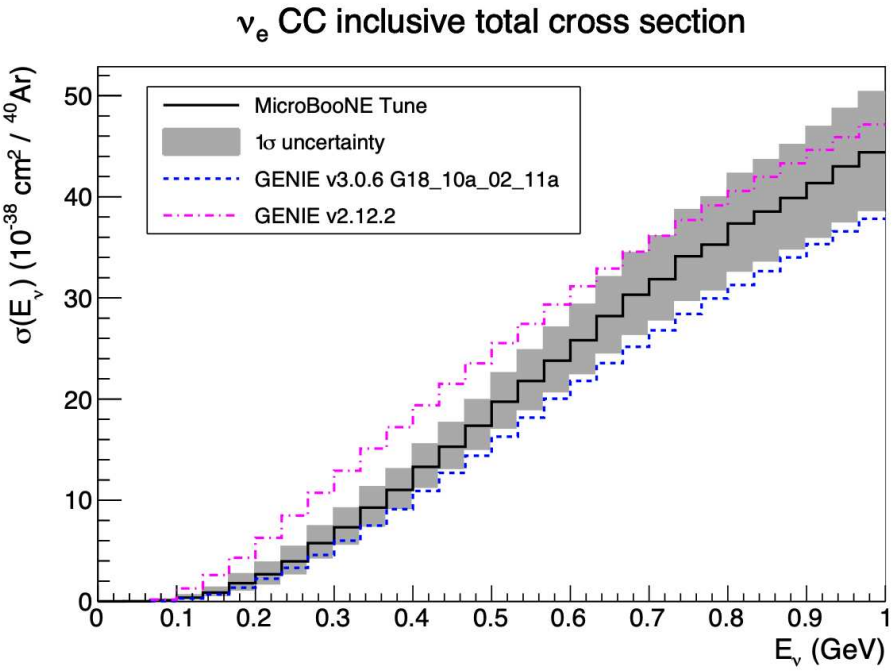

Figure 8.2: Predictions from the "MicroBooNE Tune" for the CC inclusive total cross section for electron neutrinos [23].

selection is a ν_μ CC inclusive selection, allowing for any number of final-state hadrons, with a focus on prioritizing performance in the low-energy region. Furthermore, this selection only uses 2.13×10^{20} POT of data collected after December 2017, when the CRT was available. The candidate event can be identified by the presence of one muon track originating from inside the TPC fiducial volume. Only one track is needed for the selection, but any number of tracks can accompany the muon candidate and are taken into account when calculating the energy of the event. The selection is broken down into two parts. First, an event preselection is applied to primarily filter out cosmic muon activity. Then, a muon selection filter is applied to identify the primary muon in the event. A summary of the variables used for the ν_μ selection is presented in Table 8.1.

Table 8.1: Summary of the definition of the variables used in the ν_μ selection.

	Variable Name	**Description**
Slice	`nslice`	Number of neutrino slices identified by the `SliceID`. Values are 0 or 1.
	`crtveto`	Boolean variable checking if the event passes the CRT veto. Not available for Run 1 and Run 2 data.
	`reco_nu_vtx_sce_{x,y,z}`	Reconstructed neutrino interaction vertex in (x,y,z) coordinates. Spatial space charge corrections are applied.
	`n_tracks_contained`	Number of tracks fully contained in the fiducial volume.
	`_closestNuCosmicDist`	3D distance between the reconstructed neutrino vertex and the closest CRT-tagged cosmic track.
Track	`trk_sce_{start,end}_{x,y,z}`	Reconstructed, space-charge-corrected start/end-points for the tracks.
	`trk_score`	A machine-learned quantity that describes how 'track-like' the reconstructed object is (possible values between 0 and 1).
	`trk_len`	The length of the reconstructed track (in cm).
	`MCS_quality`	Agreement between the muon momentum estimated with the range-based method $P_{\texttt{range}}$ and with the Multiple-Coulomb-Scattering-based method $P_{\texttt{MCS}}$. The variable is defined as $(P_{\texttt{MCS}} - P_{\texttt{range}})/P_{\texttt{range}}$.

8.1.1 Preselection

The preselection filter only uses variables that reflect the event as a whole, but are agnostic to individual tracks. The full set of preselection cuts is listed in Table 8.2 and will be described in this section.

The ν_μ selection starts from the results of the SliceID tool described in the previous chapter. The SliceID tool selects a neutrino event and is used as the primary cosmic rejection filter. The results of the SliceID tool are flavor-agnostic and more cuts are needed to determine the neutrino species. Additional preselection cuts are applied to reduce cosmic and dirt backgrounds and select slices that are more ν_μ-like.

The next set of cuts applied is made on the location of the neutrino vertex. The variable `reco_nu_vtx_sce_{x,y,z}` gives the three-dimensional coordinates of the reconstructed neutrino vertex. Cuts to this variable are then applied to select vertex activity contained in the TPC, which favors ν_μ CC events and disfavors cosmic or dirt-like activity, the latter two originating outside the detector. A cut on the Z coordinate is also applied, which cuts out activity originating in the unresponsive part of the detector (see Section 5.3.2.2). Additionally, the Pandora reconstruction algorithm assesses the extent to which a slice looks like a neutrino interaction in the TPC through the variable `topological_score`, where a lower score is more neutrino-like while a higher score signifies a more cosmic-like event.

The last three variables in the preselection take advantage of the CRT system (see Section 5.4) in MicroBooNE. The `CRT_Veto` and `crthitpe` reflect whether or not the CRT system was triggered in coincidence with the event and how many photoelectrons were recorded by the CRT system, respectively. Furthermore, the distance between the CRT-tagged track and the reconstructed neutrino vertex is calculated in the variable `closestNuCosmicDist`. The CRT cuts remove a significant amount of cosmic activity, which are the primary background for ν_μ CC events, particularly at lower reconstructed energies. The impact of CRT cuts on the selection can be observed in Figure 8.3 with around 64% of cosmic and EXT events being removed.

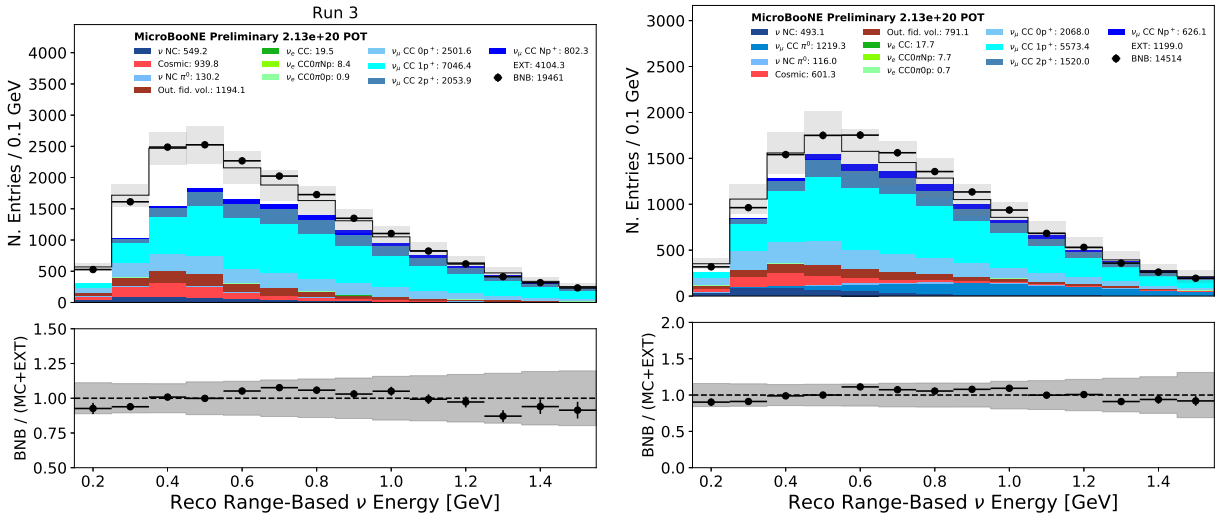

(a) Before CRT cuts.

(b) After CRT cuts.

Figure 8.3: Impact of CRT cuts on muon neutrino selection. Around 64% of events removed belong to the cosmic and EXT categories, indicating a good performance in reducing cosmic backgrounds.

8.1.2 Muon Selection

After preselection, all tracks in the neutrino slice are analyzed to identify individual muon candidates. To be considered a muon candidate, at least one reconstructed track must satisfy the criteria listed in Table 8.3. Several tracks could pass the selection criteria, and in that case, the longest track is taken as the muon candidate. The selection of muons has been tested to correctly tag ~ 94% muons coming from ν_μ CC interactions.

For each reconstructed track analyzed, a series of cuts are applied at the start and end points, requiring the track to be fully contained within the fiducial volume of the detector. The containment of event information is of critical importance when constructing a selection that prioritizes low-energy performance. The variables that contain the three-dimensional start and end point information are `trk_sce_{start,end}_{x,y,z}`. These sets of containment cuts further eliminate cosmic muons and enable the use of range-based energy calculations for the muon. The final cosmic rejection cut is on the `trk_distance` variable, which requires that the starting point of the reconstructed muon be no more than 4 cm from the reconstructed neutrino vertex. This eliminates cosmic muons that happen to be close to the neutrino vertex. To

Table 8.2: Preselection requirements for the ν_μ selection.

Cut goal	Cut definition
Cosmic rejection	nslice = 1
Fiducial volume	`reco_nu_vtx_sce_x` $\in$ [5,251] cm `reco_nu_vtx_sce_y` $\in$ [-110,110] cm `reco_nu_vtx_sce_z` $\in$ [20,986] cm `reco_nu_vtx_sce_z` $\notin$ [675,775] cm
Signal topology	`topological_score` > 0.06
Cosmic rejection (Run3)	`CRT_Veto` != 1 or `crthitpe` < 100 `closestNuCosmicDist` > 5 cm

further enhance muon selection, the variable `track_score` is used to ensure that a more track-like object is selected. For greater fidelity in the PID, the reconstructed track is required to be at least 10 cm in length.

The final cut applied is done on the `MCS_quality` variable, which requires agreement between the muon's range-based and multiple-Coulumb-scattering-based momentum calculations. This cut increases the purity of the selection and the quality of the reconstructed muon neutrinos passing the selection ('broken tracks' would fail this cut for example).

8.1.3 Data Validation

Given the ν_μ CC inclusive selection developed for this analysis, it is important to examine the results in data when compared to prediction. The high statistics for this selection allow for several tests. First, it can serve as a validation for the observation that is consistent with the prediction within the uncertainties evaluated. The agreement can help bring confidence in the model used for the simulation; looking at the reconstructed kinematic variables could prove useful in determining the validity of the neutrino interaction model used to describe the ν_μ CC inclusive signal. Second, it can help validate the common reconstruction tools that are shared with the ν_e CC selection.

The plots in Figures 8.4-8.5 show the comparison between the data and the predicted distributions in the ν_μ CC selection for several variables. The cosmic category is defined as events

Table 8.3: Muon selection requirements for the ν_μ selection.

Cut goal	Cut definition
	ν_μ preselection
Containment	`trk_sce_start_x` ∈ [5,251] cm `trk_sce_start_y` ∈ [-110,110] cm `trk_sce_start_z` ∈ [20,986] cm `trk_sce_end_x` ∈ [5,251] cm `trk_sce_end_y` ∈ [-110,110] cm `trk_sce_end_z` ∈ [20,986] cm
Cosmic rejection	`trk_distance` < 4 cm
Track ID	`trk_llr_pid_score` > 0.2 `trk_score` > 0.8 `trk_length` > 10 cm
Reconstruction quality	-0.5 < `MCS_quality` < 0.5

with at least 80% of the simulated hits in the neutrino slice backtracked to cosmic interactions rather than coming from the neutrino. The shaded gray band represents the systematic uncertainty in the measurement. The selection of ν_μ CC events is associated with a signal purity of 77%. All variables show reasonable agreement within uncertainties, as determined by the χ^2 between data and prediction and the corresponding p-values.

The final reconstructed neutrino energy distribution for the ν_μ selection is shown in Figure 8.4. The observation is around 6% higher than the prediction, well within the 15% normalization uncertainty. This excess is found to be from 400 MeV to about 1 GeV. This difference will be used to inform the final ν_e CC selections using the constraint procedure described in Section 9.6. Several kinematic variables show the performance of the ν_μ CC selection in Figures 8.5, looking at the muon energy (8.5a), and the muon angle (8.5b). Good agreement between data and prediction gives confidence in the neutrino interaction model used for this analysis.

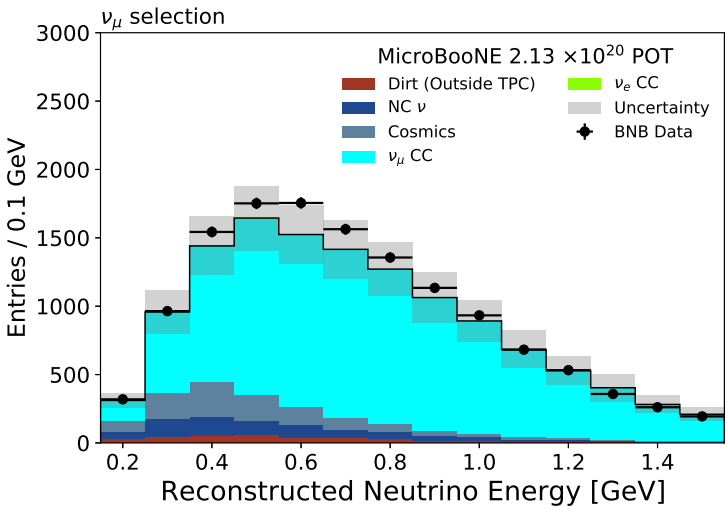

Figure 8.4: Comparison between data and prediction for the reconstructed neutrino energy in the ν_μ CC inclusive selection.

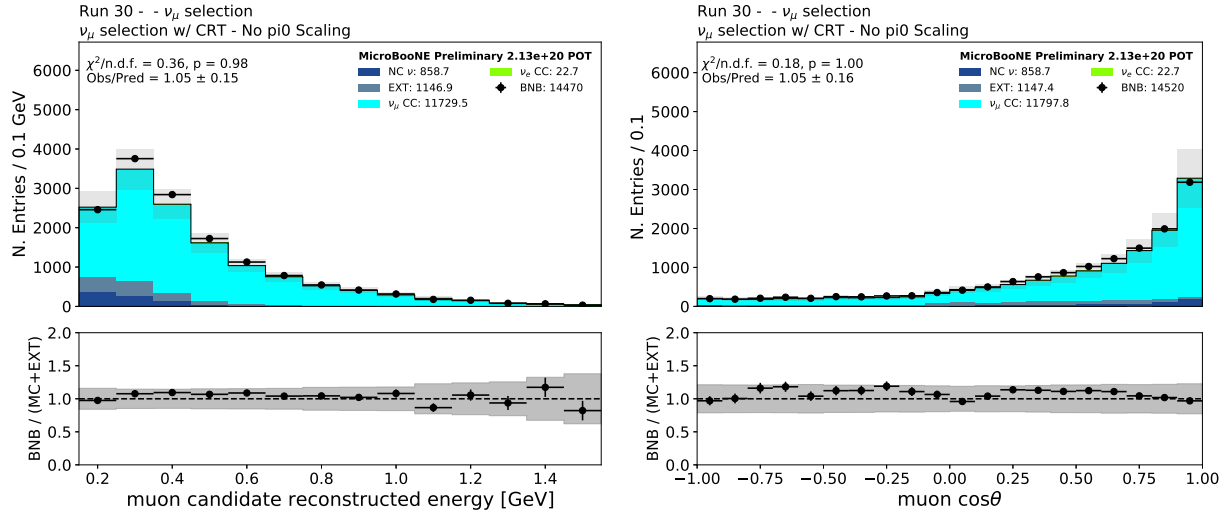

(a) **(b)**

Figure 8.5: Distributions of reconstructed kinematic variables of selected muon neutrino events in the 2.13e20 POT dataset. Overall, good agreement between data and prediction from simulation is observed.

8.2 ν_e Selections

The ν_e CC selection focuses on selecting events that have one electron, any number of protons, and without pions in the final state at low energies. The selection is broken down into two separate selections, targeting events with and without visible protons. The two selections are

the $1e\mathrm{N}p0\pi$ and the $1e0p0\pi$ channels where $N \geq 1$. Protons coming from the simulation are defined as visible if they have a kinetic energy of at least 40 MeV. Both selections combined span the signal definition of electron neutrinos measured by the MiniBooNE detector: events with a single electron, any number of protons, and no pions.

The $1e\mathrm{N}p0\pi$ and $1e0p0\pi$ selections follow the same underlying strategy. First, a set of preselection cuts is applied to identify events that come from ν_e CC interactions by locating at least one shower, followed by a series of geometric cuts that reduce cosmic interactions to first order. After this stage, the $1e\mathrm{N}p0\pi$ and $1e0p0\pi$ selection definitions are split, and different selection requirements known as “loose" cuts are applied to further reduce the backgrounds for each selection. Finally, a set of boosted decision trees (BDT) are trained to further enhance the signal content of each selection.

In Section 8.2.1, the common set of variables used in both selections are defined. Section 8.2.2 gives details of the common set of preselection criteria that the ν_e selections share. Sections 8.2.3 and 8.2.4 discuss the event requirements specific to either selections, variables used for the selections, and the training requirements that went into the BDT training.

8.2.1 Variable Definitions

This section gives an overview of the variables used for the two exclusive ν_e CC selections in the Pandora eLEE analysis. These variables are meant to isolate the characteristics of events with a single electron in the final state. The variables are divided into several categories and use only topological and calorimetric information. The categories are as follows: slice variables, track/shower separation variables, e/γ separation variables and π^0 rejection in the second shower variables. Table 8.4 summarizes all variables used in the ν_e selections with a brief description. Variables that warrant a longer explanation are described below.

Slice variables encompass general features of the reconstructed neutrino event. These variables look at the content of the neutrino slice as a whole, leaving out any calorimetric and topological characteristics of the event. These variables contain information such as the number of showers and tracks fully contained in the fiducial volume, `n_showers_contained` and

n_tracks_contained, respectively. Other important variables are the CosmicIP variables, which characterize the activity of the closest cosmic muon to the reconstructed neutrino vertex, detailing the distance and direction in both the 3D and the individual 2D planes.

The track/shower separation variables target the features of the reconstructed track and shower objects. The variable trkpid is calculated using the LLR-PID method described in Section 7.5, assigning a score from -1 (proton-like) to $+1$ (muon-like) to the longest track in the slice. Other variables examine the topological properties of the reconstructed objects, such as the angle between the leading track and the shower in tksh_angle. Several variables were developed to characterize the topology of the leading shower, such as using a dedicated algorithm to fit the main trunk of the shower to a track and then calculating the fraction of spacepoints that have been successfully fitted to this "track". Furthermore, the length of this "track" can also be used as a variable. Additional variables represent geometric properties of the shower, such as shrmoliereavg, which represents the average angle between the shower's direction and the spacepoints that comprise it. The variable CylFrac2h_1cm describe the fraction of spacepoints in the leading shower that are within 1 cm of the central axis of the shower. Only the second half of the PFParticle is considered for this calculation, where showers are expected to have a lower fraction of spacepoints closer to the central axis compared to tracks. The shrPCA1CMed_5cm variable aims to represent the linearity of the shower. It is calculated by breaking up the leading shower into 5 cm segments and performing a principal component analysis (PCA) on each segment. Then, for each segment, the ratio of the first component eigenvalue and the sum of the eigenvalues is calculated. The median of the ratios is taken. The DeltaRMS2h variable quantifies the spread of the shower along the axis orthogonal to the direction of the shower. This is determined by performing a PCA on the shower spacepoints and calculating the RMS for the second component. Only the second half of the shower is considered. Finally, shrMCSMom characterizes the spread of the leading shower taking into account the separation of each 3D spacepoint from the center of the shower, as well as the length of the shower, and performs a MCS momentum calculation on the shower [65].

The electron/photon separation variables take advantage of the calorimetric information provided by the reconstruction (see Section 7.5). Using the shower track fitting algorithm, these variables use the median dE/dx calculated over different segments of a shower trunk that ranges from [0,2], [1,5], and [0,4] cm. The median dE/dx in the first 2 cm of the shower is represented by the `shr_tkfit_2cm_dedx_{U,V,Y}` variable, which takes advantage of the fact that a photonic shower becomes more MIP-like the further one moves along the shower trunk. The variable `shr_tkfit_gap10_dedx_{U,V,Y}` represents the median dE/dx calculated after 1 cm away from the neutrino vertex, skipping the first centimeter of the shower trunk. This focuses on reducing the amount of proton-induced misreconstruction at the beginning of the shower, which would hamper the ability to distinguish photons from electrons. The last of the calorimetric variables is `shr_tkfit_dedx_max`, where the median dE/dx of the first 4 cm is calculated for the three planes and the maximum is taken as the value. Additionally, there are variables that quantify the distance between the start of the reconstructed leading shower and the neutrino vertex (`shower_vtx_dist`) and the start of the leading track (`tksh_distance`), along with the minimum distance between the leading track and the shower clusters on all wire planes.

A set of variables has been developed to account for Pandora misreconstructing π^0 events. In these cases, one of the photonic showers is correctly identified as belonging to the neutrino slice, but it is not reconstructed as a shower and instead the 2D hits are unclassified. In this analysis, the second shower is defined as the largest cluster of unclassified 2D hits within the neutrino slice. Several variables have been developed characterizing these "lost" showers. First, the number of hits for each plane is stored in the `secondshower_{U,V,Y}_nhit`. The `secondshower_{U,V,Y}_dot` variable stores the dot product between the vector connecting the reconstructed neutrino vertex and the nearest hit within the second shower and the charge-weighted direction of the second shower. Finally, the angle (`anglediff_{U,V,Y}`) and the shortest distance (`secondshower_{U,V,Y}_vtxdist`) between the leading shower and the

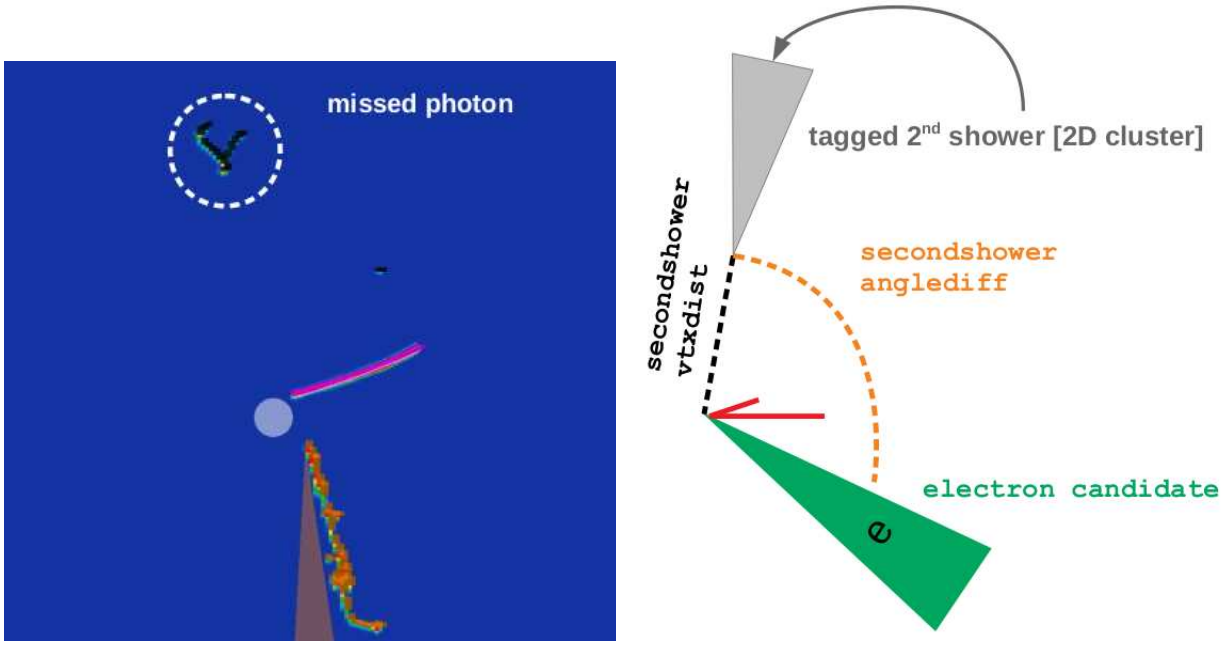

(a) unclustered shower **(b)** second-shower variables

Figure 8.6: Caricature sketch of the second-shower-based π^0 rejection variables. Left: 2D event display of missed second shower photon (black hits) that was not reconstructed in 3D. Right: visual representation of the second shower variables. The gray triangle in the right image represents the black cluster on the left image.

second shower are also calculated. Figure 8.6 shows an event display of a recovered second shower and a visual representation of some of the second shower variables.

8.2.2 The $1e$N$p0\pi$ and $1e0p0\pi$ Preselection

The $1e$N$p0\pi$ and $1e0p0\pi$ selections rely on a common preselection that requires the presence of at least one reconstructed electromagnetic shower of energy above 70 MeV. The energy requirement acts as a Michel electron veto, most of which are produced from cosmic rays or from ν_μ-induced muons. The selection also requires that ν_e interactions be contained within the fiducial volume. This boundary is defined as 10 cm away from the anode/cathode in the drift coordinate, 15 cm from the bottom/top in the vertical coordinate, and 10 cm and 50 cm from the front and end of the TPC in the beam direction, respectively. The distribution of contained tracks and showers are shown in Figure 8.7. Events are then broken down according to their proton content: at least one fully-contained track for the $1e$N$p0\pi$ channel and the absence of

Table 8.4: Summary of the definitions of the variables for the ν_e selection.

	Variable Name	Description
Slice	nslice	Number of neutrino slices identified by the SliceID.
	reco_nu_vtx_sce_{x,y,z}	Reconstructed neutrino interaction vertex in (x,y,z) coordinates.
	n_showers_contained	Number of showers with a starting point within the fiducial volume.
	n_tracks_contained	Number of tracks fully contained in the fiducial volume.
	n_tracks_tot	Total number of tracks in the event; contained or exiting.
	contained_fraction	Hits in PFParticles contained in the fiducial volume over the total number of clustered hits in the slice.
	hits_ratio	Ratio between hits from showers and total number of hits in the slice.
	CosmicIP	Closest distance between shower start and space points associated to tracks flagged as cosmics.
	crtveto	Boolean variable checking if the event passes the CRT veto.
	_closestNuCosmicDist	3D distance between the reconstructed neutrino vertex and the closest CRT-tagged cosmic track.
	slclustfrac	Fraction of hits in the slice that are fully reconstructed to 3D particles.
	shr_trk_sce_{start,end}_y	Start and end point in y of shower when fit as a track.
	nObjHits_{U,V,Y}	Number of hits associated with the object on each plane.
Track/Shower Separation	trkpid	Proton-muon LLR particle identification.
	shr_energy_tot_cali	Sum of the energy of the calibrated showers (in GeV). Used only at preselection as a "Michel veto".
	tksh_angle	Angle between leading shower and longest track directions.
	trkfit	Fraction of the 3D spacepoints successfully fitted with the shower track-fitter algorithm.
	subcluster	Number of isolated 2D segments of charge associated to a reconstructed shower on all three planes.
	shrmoliereavg	Average angle between the shower's direction and its 3D spacepoints.
	shr_trk_len	Length of shower when fit as a track.
	CylFrac2h_1cm	Fraction of spacepoints in a 1 cm cylinder around the second half of the shower.
	shrPCA1CMed_5cm	Median PCA component calculated in 5 cm blocks.
	DeltaRMS2h	RMS of spacepoint distance from shower center in the second half of the shower.
	shrMCSMom	Multiple Coulomb scattering shower momentum.
e/γ Separation	shr_tkfit_gap10_dedx_{U,V,Y}	Median dE/dx computed over [1,5] cm of the shower's trunk.
	shr_tkfit_2cm_dedx_{U,V,Y}	Median dE/dx computed over the first 2 cm of the shower's trunk.
	shr_tkfit_dedx_{U,V,Y}	Median dE/dx computed over the first 4 cm of the shower's trunk.
	shr_tkfit_dedx_max, shr_tkfit_2cm_dedx_max	Median dE/dx on plane with most number of hits in $[0,4],[0,2]$ cm trunk segment.
	shower_vtx_dist	Distance between the shower start and the neutrino vertex.
	tksh_distance	Distance between leading shower and longest track start points in 3D.
	trkshrhitdist2	Minimum distance between leading shower and longest track clusters.
	tk1sh1_angle_alltk	Angle between leading shower and track with most 2D hits.
Second Shower	secondshower_{U,V,Y}_nhit	Number of hits on each plane of the largest cluster associated with the recovered second shower.
	secondshower_{U,V,Y}_dot	Dot product between the vector connecting the vertex to the closest hit in cluster and the charge-weighted cluster direction.
	anglediff_{U,V,Y}	2D angle difference in each plane between the 2nd shower and the 1st shower cluster (cluster direction defined as charge-weighted direction of cluster w.r.t. vertex).
	secondshower_{U,V,Y}_vtxdist	2D distance from vertex for the largest 2D cluster associated with the recovered 2nd shower in each plane.

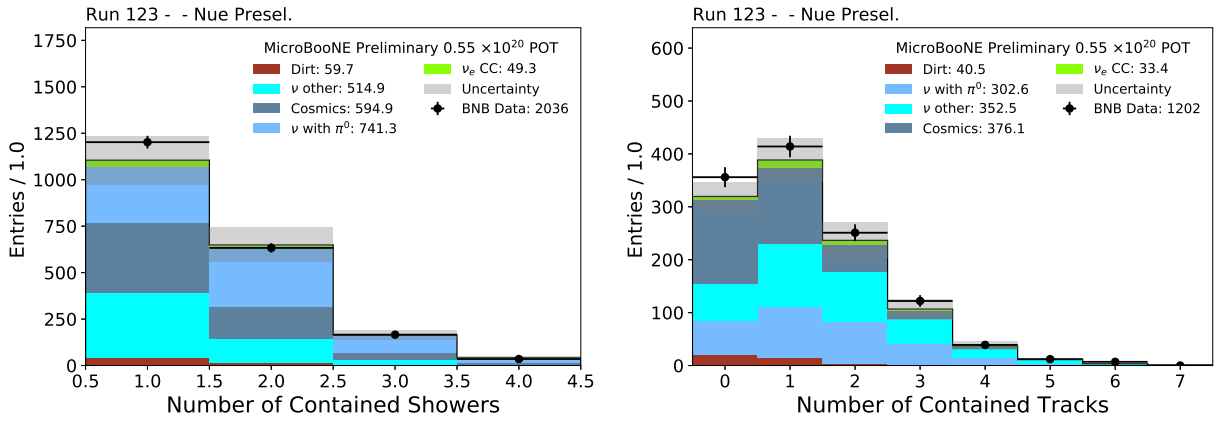

(a) Contained showers

(b) Contained tracks

Figure 8.7: Variables input to the common ν_e $1e\mathrm{N}p0\pi$ and $1e0p0\pi$ preselection.

fully-contained tracks for the $1e0p0\pi$ channel. The list of requirements for each channel preselection is given in Table 8.5. The list of requirements for each channel preselection is given in Table 8.5.

Table 8.5: Preselection requirements for the ν_e CC selection.

Cut goal	Cut definition
Cosmic rejection	nslice = 1
Michel rejection	shr_energy_tot_cali > 0.07 GeV
Signal topology	n_showers_contained > 0 $1e\mathrm{N}p0\pi$: n_tracks_contained > 0 $1e0p0\pi$: n_tracks_contained = 0

8.2.3 The $1e\mathrm{N}p0\pi$ Selection

The $1e\mathrm{N}p0\pi$ channel is most sensitive to the eLEE given the ability to use tracks associated with the neutrino vertex in addition to the electromagnetic shower to select electron neutrinos from backgrounds. Following the preselection, a series of cuts are applied to further reduce background events. This is defined as the “loose" selection. After that, two BDTs are trained with XGBoost [24] and used to obtain a purer selection of ν_e CC events.

After preselection, the main backgrounds dominating the selection are those coming from cosmic activity, ν_μ-induced activity, π^0 decays, and artifacts of the reconstruction. The cuts used to mitigate these backgrounds are listed in Table 8.6. Cosmic activity that is too close to the neutrino interaction vertex is parameterized using the variable `ComicIPAll3D`, which represents the closest distance between the shower start and the spacepoints associated with the tracks marked as cosmic muons. Then, the events are required to have a track PID value that is proton-like value for the main track. The log-likelihood variable, `trkpid`, is used to determine the nature of the track by assigning a value close to -1 for proton-like tracks and values close to +1 to muon-like tracks (see Section 7.5). It is required that the value of `trkpid` be less than 0.02 to eliminate most cosmic events.

Rejection of ν_μ-induced muons is carried out using several variables. First, the ratio between hits from showers and the total number of hits within the neutrino slice must be greater than 0.5 to guarantee a sufficiently large electromagnetic shower. Next, the average angle between the shower's direction and its 3D spacepoints is calculated in `shrmoliereave`, with a requirement for this to be less than 9°. The shower topology is further used for muon discrimination by requiring the shower to have more than four isolated 2D segments of charge associated with the reconstructed shower (`subcluster` > 4), have only a fraction of the 3D spacepoints successfully fitted with the shower track-fitter algorithm (`trkfit` < 0.65), and have this "track" length be less than 300 cm (`shr_trk_len` < 300 cm).

At this stage, the π^0 events are still one of the main backgrounds that hinder the analysis, so several cuts have been implemented. To mitigate the π^0 contribution, the analysis requires that only one reconstructed shower be tagged and contained (`n_showers_contained == 1`). The distance between the leading track and the leading shower 3D start points is calculated and must be short enough to reject showers from pair-producing photons (`tksh_distance` < 6 cm).

Table 8.6: Loose cut requirements for the $1e\mathrm{N}p0\pi$ selection.

Cut goal	Cut definition
Cosmic rejection	CosmicIPAll3D > 10 cm trkpid < 0.02
ν_μ rejection	hits_ratio > 0.5 shrmoliereavg < 9° subcluster > 4 trkfit < 0.65 shr_trk_len < 300 cm
π^0 rejection	n_showers_contained = 1 tksh_distance < 6.0 cm shr_tkfit_nhits_tot > 1 and 0.5 < shr_tkfit_dedx_max < 5.5 MeV/cm
Misreconstruction	tksh_angle > -0.9

The final cut in the loose selection handles partially reconstructed events. The angle between the leading track and the leading shower is calculated, cutting out tracks and showers whose directions are opposite to each other.

8.2.3.1 BDT Selection

After the loose box cuts specified above, events are categorized using two BDTs. The two BDTs are trained using XGBoost to separate the signal from the background: one is trained to target the removal of π^0 backgrounds, and the other targets backgrounds without π^0 events. Both BDTs are trained on the same set of variables and use the same dedicated signal samples of the simulated intrinsic electron neutrinos: one sample with electron neutrinos in the range of $0 < E_{\nu_e} < 400$ MeV and the other with electron neutrinos in the range of $0 < E_{\nu_e} < 800$ MeV. Both BDTs are trained on cosmic events taken from a sample of about 280k events coming from the NuMI EXT data stream. The π^0 samples for BDT training are produced recycling the EXT unbiased events used in the overlay procedure; non-π^0 neutrino-induced background samples are produced with tight filters on truth variables that enhance muon neutrino interactions without neutral pions events that contribute as backgrounds to the analysis. As a result, the relative size of the samples varies significantly, so the event weight in training is enhanced for specific

categories of backgrounds such as ν_μ CC events without pions or EXT and cosmic-dominated events. Training is carried out after requiring `reco_e` < 0.8 and `n_showers_contained` $== 1$ on top of the $1e\mathrm{N}p0\pi$ preselection.

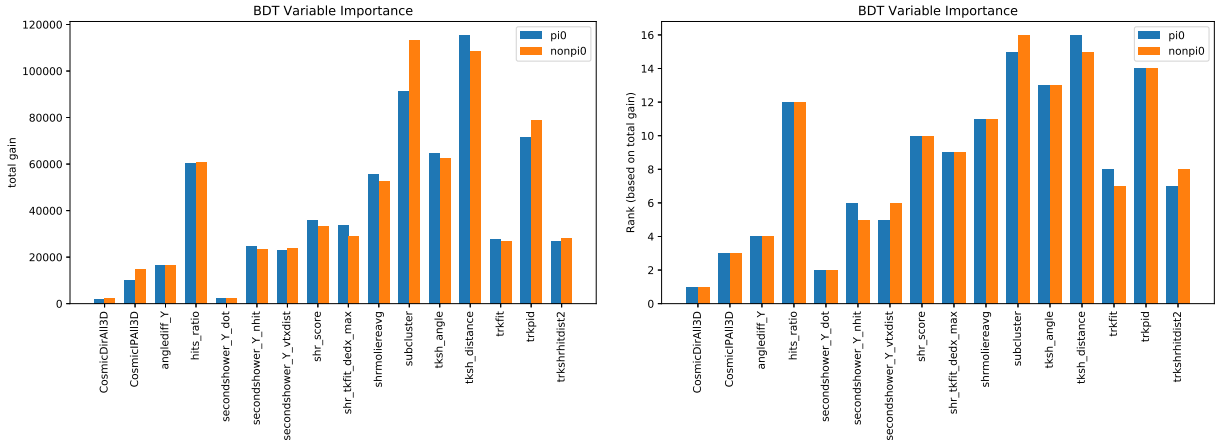

(a) **(b)**

Figure 8.8: BDT variables importance in terms of "total gain". In XGBoost [24], "gain" is the improvement in accuracy brought by a feature to the branches it is on; total gain refers to the sum of the gain across all branches. Left: total gain value. Right: ranking based on the total gain value (highest ranking=15, lowest=1).

The BDT training is able to figure out which variables are most important for each background. Figure 8.8 shows that, while the importance of the training variable is generally very similar in the two BDTs, there are indications that each BDT specializes in its target background; for example, the most discriminating variable is different between the BDTs, being `subcluster` for the non-π^0 BDT and `tksh_distance` for the π^0 BDT.

The BDT responses comparing the prediction to a subset of the whole dataset at the the preselection stage are shown in Figures 8.9 for the π^0 and non-π^0 BDTs, respectively. Figures are divided into the response below and above 0.5 in the right and left panels, respectively. Both BDT plots show a deficit at higher BDT response values given the statistically limited dataset. The BDT selection is done by applying a separate cut to the output of the two BDTs, requiring that the π^0 and non-π^0 responses be greater than 0.67 and 0.70, respectively.

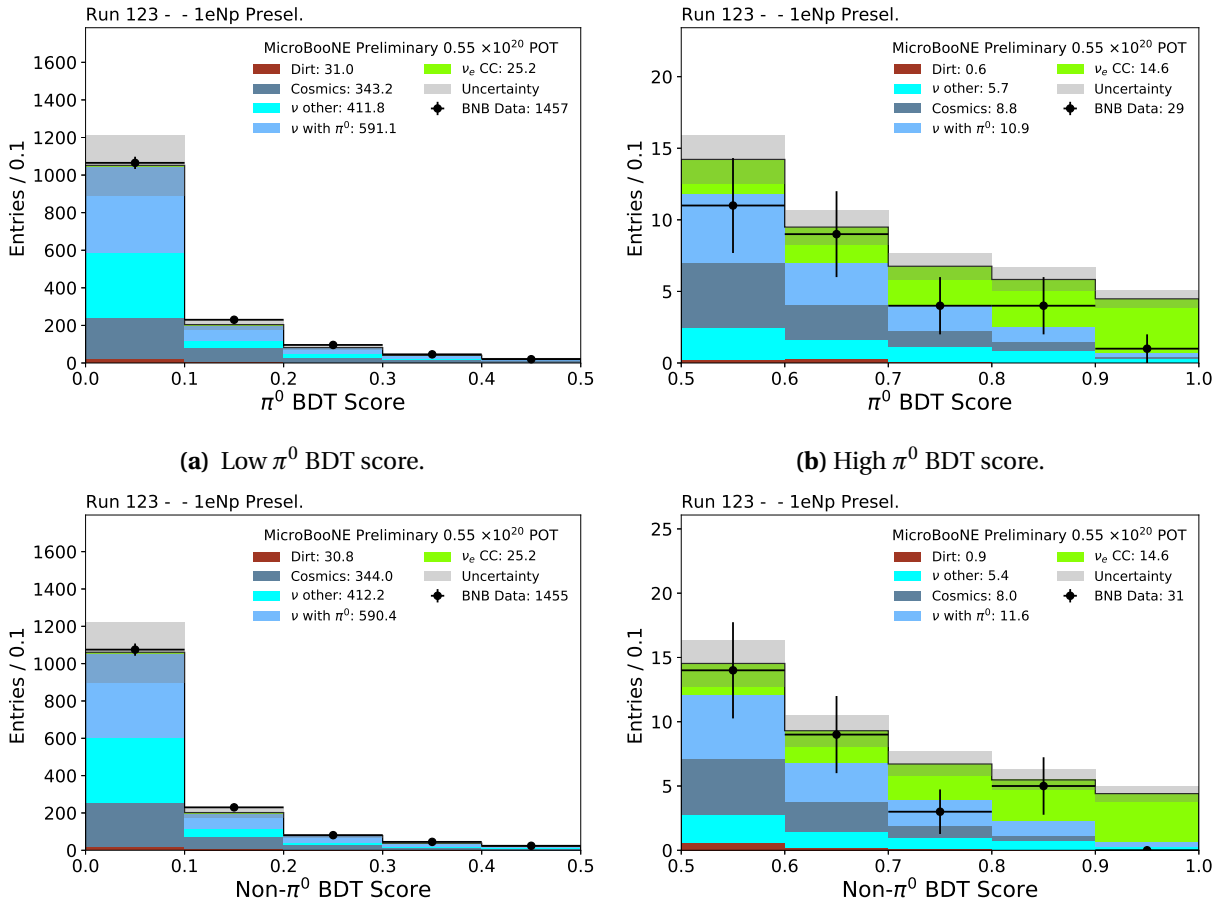

(a) Low π^0 BDT score.

(b) High π^0 BDT score.

(c) Low non-π^0 BDT score.

(d) High non-π^0 BDT score.

Figure 8.9: π^0 and non-π^0 BDT response after $1e\mathrm{N}p0\pi$ preselection. The BDT response is tested using a subset of the whole dataset. A deficit in data is shown for higher values of the BDT response given the statistically limited dataset.

8.2.3.2 Performance and Pre-Unblinding Data Validation

The $1e\mathrm{N}p0\pi$ selection defined in the previous section provides excellent performance in rejecting non-ν_e backgrounds. The predicted reconstructed neutrino energy after the selection of BDT for the entire data set is shown in Figure 8.10 with a numerical breakdown of the selection listed in Table 8.7. The selection has an expected purity of 80% with an efficiency of 15% for true $1e\mathrm{N}p0\pi$ events defined based on the proton energy threshold of 40 MeV. The final selection achieves upwards to 99% rejection of cosmic background and π^0 events relative to the $1e\mathrm{N}p0\pi$ preselection.

Table 8.7: Predicted composition of the $1eNp0\pi$ selected events with unconstrained systematic uncertainties in the reconstructed neutrino energy range 0.01–2.39 GeV for 6.86×10^{20} POT.

Sample	$1eNp0\pi$
ν_e CC $0p0\pi$	0.4 ± 0.1
ν_e CC $Np0\pi$	71.7 ± 10.6
ν_e CC $Xp0\pi$	3.3 ± 0.9
ν_e CC Total	75.4 ± 11.0
ν with π^0	5.1 ± 1.4
ν other	5.5 ± 1.1
Cosmic-rays	0.8 ± 0.5
Total	86.8 ± 11.5

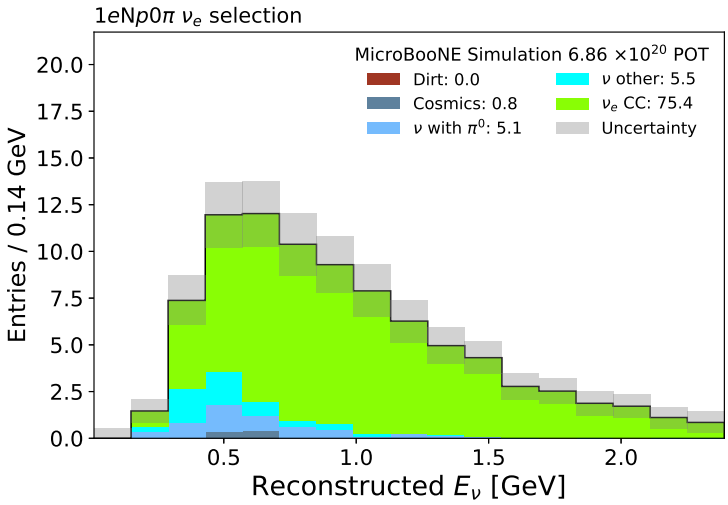

Figure 8.10: Predicted distribution for reconstructed neutrino energies in the $1eNp0\pi$ selection.

Several checks were performed before proceeding to the unblinding of the data of the eLEE region. They include data validation checks using event samples that are similar but insensitive to the eLEE signal. This section will focus on two samples: one where events pass the full $1eNp0\pi$ selection and that have reconstructed energies greater than 0.65 GeV, and another selection where events pass the $1eNp0\pi$ selection except their BDT scores are smaller than those associated with the signal region, < 0.70 and < 0.67 for the π^0 BDT and non-π^0 BDT, respectively. The first sample is called the high-energy sideband and the second sample is called the low-BDT sideband, as described in Chapter 6. Data and simulation comparisons of the reconstructed neutrino energy for these two event samples are shown in Figures 8.11 and 8.12.

In Figure 8.11 there is a notable data deficit in the 0.65 to 0.95 GeV range. This deficit appears to be statistical in nature, given the low number of events per bin. Furthermore, in this region, a goodness-of-fit p-value of 0.277 was measured. This value was obtained by comparing the observed data with the prediction after applying the constraint procedure ν_μ described in Chapter 10. Figure 8.12 shows the low PID selection, where the agreement between the data and the prediction is within the uncertainties. The general agreement between the prediction and the observation is within the systematic and statistical uncertainties in these two event samples. The BDT results, in addition to data sidebands modeling the different backgrounds in the analysis (see Section 8.3), gives validity of the analysis in the regions where there is no expected eLEE signal and supported the move forward to unblinding the full energy range.

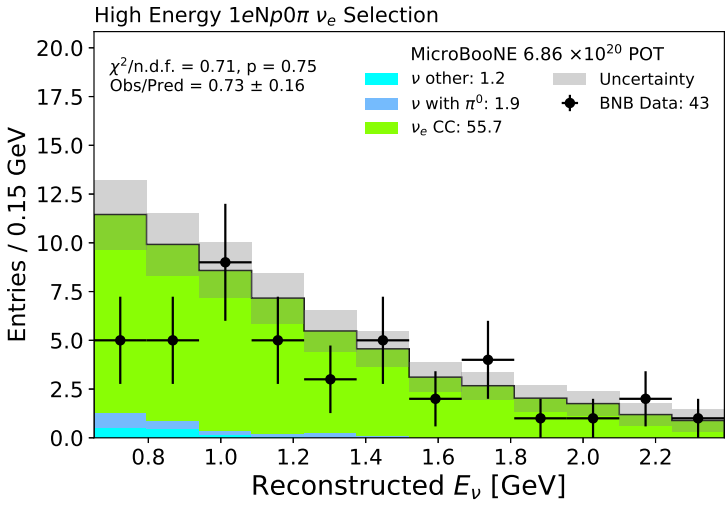

Figure 8.11: Comparison between data and prediction for the high reconstructed neutrino energy sideband (above 0.65 GeV) for the $1e$N$p0\pi$ channel.

8.2.4 The $1e0p0\pi$ Selection

The $1e0p0\pi$ selection is the second signal selection made in this analysis. The topology sought out by this selection is that of a single shower with no visible hadronic production within the MicroBooNE detector. The $1e0p0\pi$ signal complements the $1e$N$p0\pi$ signal: together they form

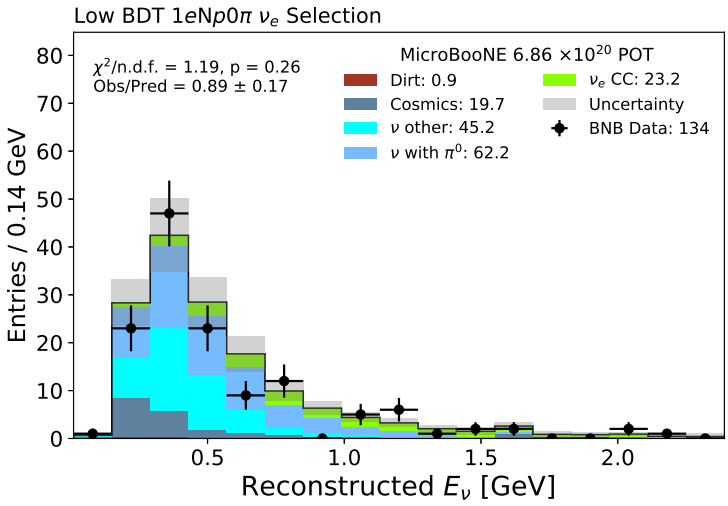

Figure 8.12: Comparison between data and prediction for reconstructed neutrino energy with BDT scores below 0.67 and 0.70 for π^0 and non-π^0 BDTs, respectively, in the $1eNp0\pi$ selection.

the MiniBooNE signal, which is defined as $1eXp0\pi$. As such, the $1e0p0\pi$ topology is sensitive to the eLEE signal, as well as a much wider set of models outside the scope of this analysis [81–83, 110–112].

The $1e0p0\pi$ channel can also be used to constrain uncertainties associated with the $1eNp0\pi$ selection by taking account for correlations between the two channels (see Section 9.6). Uncertainties associated with low-energy protons, such as proton mis-reconstruction or proton multiplicity and kinematics products of neutrino interaction mis-modeling, can be mitigated by this selection.

8.2.4.1 BDT Selection

Similarly to the $1eNp0\pi$ selection, a BDT selection is applied to the $1e0p0\pi$ channel. The BDT is trained on a selection of $1e0p0\pi$ events, which include a set of preselection cuts, plus several additional cuts to focus the training selection on identifying electron neutrinos, summarized in Table 8.8. Similarly, this selection is also trained to optimize performance for low-energy events by including a cut on the reconstructed energy to be below 0.8 GeV.

Table 8.8: Training cut requirements for the $1e0p0\pi$ BDT selection.

Cut goal	Cut definition
	$1e0p0\pi$ Pre-selection
Cosmic rejection	CosmicIPAll3D > 10 cm CosmicDirAll3D > -0.9 and CosmicDirAll3D < 0.9
ν_μ rejection	trkfit < 0.65 shrmoliereavg < 15° subcluster > 4
π^0 rejection	secondshower_Y_nhit < 50 n_showers_contained == 1

The $1e0p0\pi$ BDT training shares several cuts common with the $1eNp0\pi$ selection, specifically the cuts on `CosmicIPAll3D`, `trkfit`, `subcluster`, and `n_showers_contained`. New cuts are added to the training selection to further reduce background components. Cosmic rejection is enhanced by considering reconstructed showers that are anti-aligned with the closest cosmic muon (`CosmicIP3DAll`), targeting Michel decays or highly ionizing cosmic muons. For the rejection of neutral pions, this selection requires a single contained shower, similar to the $1eNp0\pi$ selection. Furthermore, a cut on the second shower variable (`secondshower_Y_nhit`) requires less than 50 hits in the collection plane. Despite the selection reducing the true ν_e CC content by 30%, a large amount of background is removed for the final selection.

Before applying the final cut to the BDT score, a set of cuts is performed on top of the previously defined training cuts. The additional set of cuts is listed in Table 8.9, and together with the training cuts, they are defined as the $1e0p0\pi$ "loose" selection. These cuts were designed to further reduce cosmic rays and ν_μ-induced backgrounds, and were developed after an additional 60% of cosmic data were reprocessed and the far-sideband was unblinded. These cuts make use of the track-fitted shower start and end points in the vertical coordinates (`shr_trk_sce_{start,end}_y`) and keep any events that are within the fiducial volume. Furthermore, it is required that there be no uncontained tracks (`n_tracks_tot`) or, if there is at

least one, that the angle between it and the leading shower (tk1sh1_angle_alltk) be anti-parallel.

Table 8.9: Loose cut requirements for the $1e0p0\pi$ BDT selection.

Cut goal	Cut definition
	$1e0p0\pi$ Training Selection
Cosmic rejection	shr_trk_sce_start_y > -100 cm and shr_trk_sce_start_y < 80 cm shr_trk_sce_end_y > -100 cm and shr_trk_sce_end_y < 100 cm n_tracks_tot == 0 or (n_tracks_tot>0 and tk1sh1_angle_alltk>-0.9)
ν_μ rejection	shr_trk_len < 300 cm

Unlike the $1eNp0\pi$ channel, the $1e0p0\pi$ channel uses only one BDT to reject background events. This BDT classifies events as activity that is a true or is not a true $1e0p0\pi$ or $1eNp0\pi$ ν_e CC interaction. The training used dedicated samples, separate from those used to evaluate the analysis performance and produce the data/simulation comparisons. Similarly to the $1eNp0\pi$ BDTs, this BDT is also trained on dedicated signal samples of simulated intrinsic electron neutrinos in the range of $0 < E_{\nu_e} < 400$ MeV and $0 < E_{\nu_e} < 800$ MeV. Similarly, the π^0 events used for training also have EXT-unbiased events overlayed. Other dedicated truth-filtered ν_μ with no π^0 have also been used to enhance specific background categories that suffer from low statistics in the final predicted selection. Though no dedicated cosmic-ray samples are used for training, a larger training weight is assigned to events that fall into the cosmic category to enhance the BDT background rejection performance.

The BDT for the $1e0p0\pi$ selection is trained using the following variables: shrmoliereavg, shr_score, CosmicIPAll3D, CosmicDirAll3D, subcluster, secondshower_(U,V,Y)_nhit, secondshower_(U,V,Y)_vtxdist, secondshower_(U,V,Y)_dot, anglediff_(U,V,Y), shr_tkfit_2cm_dedx_(U,V,Y), shr_tkfit_gap10_dedx_(U,V,Y), trkfit, shrMCSMom, DeltaRMS2h, shrPCA1CMed_5cm, and CylFrac2h_1cm. More information on the second shower search is included in the BDT, such as the number of hits for each plane, the shortest distance from the shower vertex and the second shower, and the angle between leading and sec-

ond showers. Other variables that further characterize the leading shower are used, such as `shrMCSMom` which uses a multiple Coulomb scattering approach to calculate the shower spread, and the principal component variables are also incorporated into the BDT training. Figure 8.13 shows the relative importance of each of the training variables in the BDT, noting that most of the selection power for the BDT comes from the shower dE/dx variables, as well as the second shower search variables, which provide a valuable handle on π^0 rejection.

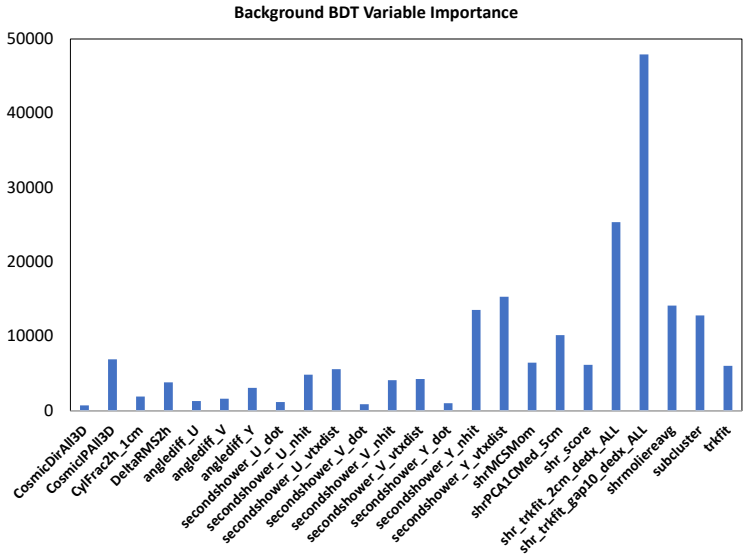

Figure 8.13: Relative importance of each variable of the $1e0p0\pi$ BDT.

The BDT response is shown in Figure 8.14, with the two panels showing the low BDT response in the range of (0-0.5) 8.14a and the high BDT response in the range of (0.5-1) 8.14b after the $1e0p0\pi$ preselection. Overall, the agreement between the data and the simulation is good. The final selection defines signal events as those having a BDT score greater than 0.72.

8.2.4.2 Performance and Pre-Unblinding Data Validation

The predicted reconstructed ν_e energy after the $1e0p0\pi$ BDT selection for the entire data set is shown in Figure 8.15. After the BDT selection is applied the ν_e purity is expected to be 43% with an efficiency of 9% for true $1e0p0\pi$ events. Around 70% of the selected ν_e CC events are expected to be true $1e0p0\pi$ interactions, the rest being mostly $1eNp0\pi$ events at roughly 30%.

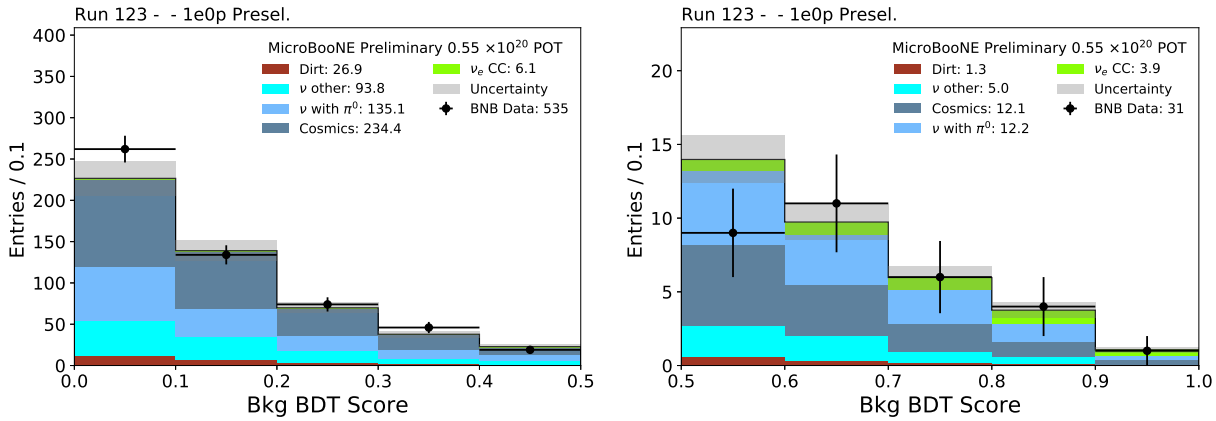

(a) Low BDT response (0-0.5).

(b) High BDT response (0.5-1).

Figure 8.14: BDT response after $1e0p0\pi$ preselection.

Backgrounds after full selection are reduced by 99.7% and 99.8%, relative to the preselection, for π^0 and cosmic ray backgrounds, respectively. Although the π^0 contribution has been significantly reduced, it is still comparable to that of the ν_e CC signal. The lower rate of $1e0p0\pi$ interactions, coupled with limitations of the Pandora reconstruction of single electromagnetic showers, provides a challenge for this selection to properly discriminate backgrounds from signal at low energies. A complete breakdown of the $1e0p0\pi$ selection components is given in Table 8.10.

Table 8.10: Predicted composition of the $1e0p0\pi$ selected events with unconstrained systematic uncertainties in the reconstructed neutrino energy range 0.01–2.39 GeV for 6.86×10^{20} POT.

Sample	$1e0p0\pi$
ν_e CC $0p0\pi$	8.7 ± 3.0
ν_e CC $Np0\pi$	3.8 ± 0.7
ν_e CC $Xp0\pi$	0.3 ± 0.1
ν_e CC Total	12.8 ± 3.4
ν with π^0	8.6 ± 1.9
ν other	3.1 ± 1.1
Cosmic-rays	5.7 ± 1.5
Total	30.1 ± 4.3

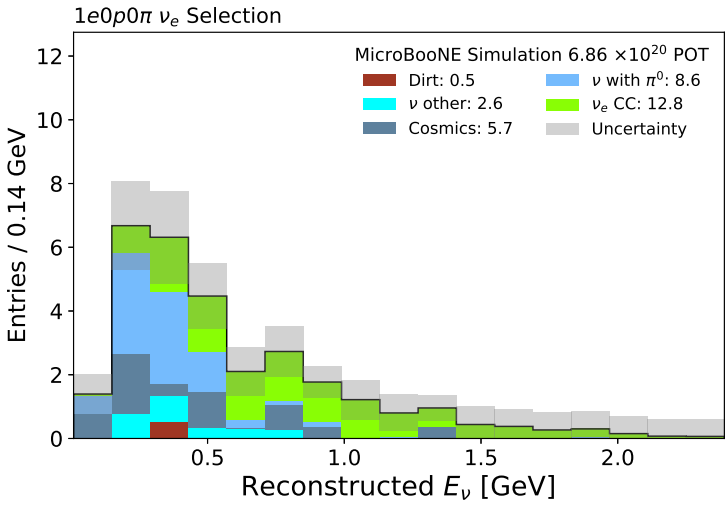

Figure 8.15: Predicted distribution for reconstructed neutrino energies in the $1e0p0\pi$ selection.

In the same fashion as the $1e\text{N}p0\pi$ selection, the $1e0p0\pi$ selection was also vetted with samples insensitive to the eLEE region before data unblinding: one where events pass the full $1e0p0\pi$ selection but events have a reconstructed energy greater than 0.85 GeV, and the other selection where events pass the loose selection but have a BDT score lower than 0.72. Figure 8.16 shows the high-energy sideband; a low number of events make it difficult to gauge the sensitivity of the analysis, but this is due to the cuts geared towards low-energy events. Five events are selected in the high reconstructed energy region; a hand scan reveals that three events are the result of ν_e CC interactions, while the other appear to be cosmic muons. The low BDT selection in Figure 8.17 shows good data/simulation agreement with this background-rich selection.

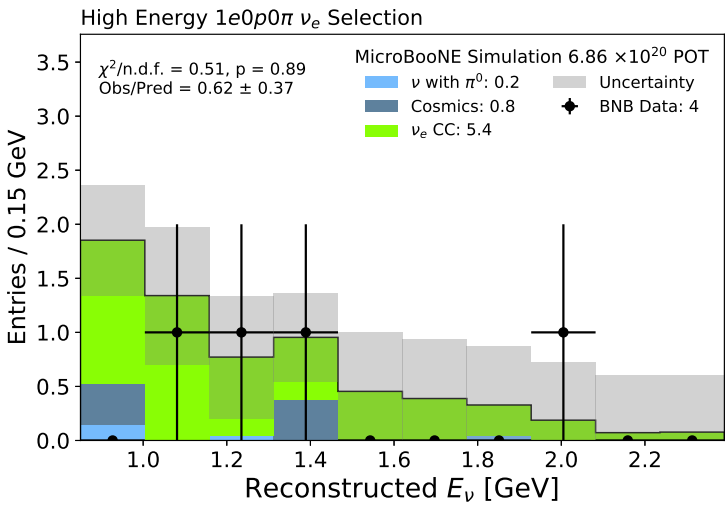

Figure 8.16: Comparison between data and prediction for reconstructed neutrino energy above 0.65 GeV for the $1e0p0\pi$ selection.

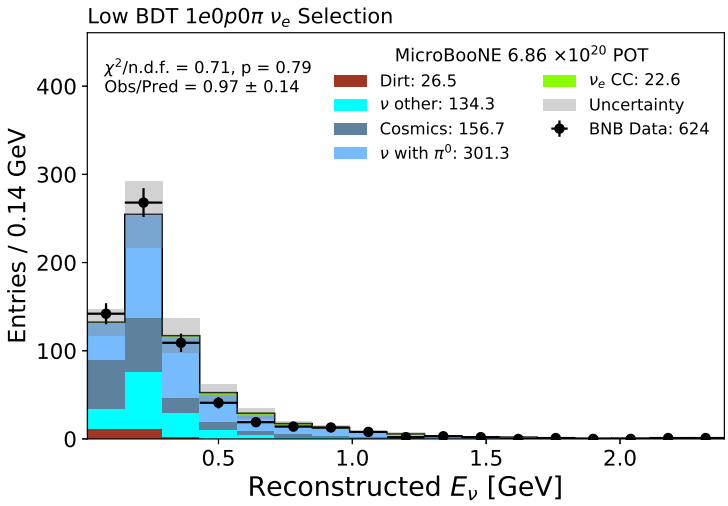

Figure 8.17: Comparison between data and prediction for the reconstructed neutrino energy with BDT scores below 0.72 for background BDT in the $1e0p0\pi$ selection.

8.3 Analysis Validation Data Sidebands

The principal strategy to search for the eLEE that was adopted by MicroBooNE is that of a blind analysis scheme of ν_e CC interactions, where access to the ν_e components of the BNB flux are closed off to the analysis until its end. Relying on this strategy minimizes the risk of bias, but requires extensive validation with the data outside of the eLEE signal region. Several data sidebands are used for the analysis validation: two neutral-pion-rich samples and the NuMI neutrino beam data [113], along with the high-energy and low-BDT sidebands described in the previous section. The rest of this section focuses on describing the π^0 and NuMI sidebands and how they are used to validate the analysis. It should be noted that all validation sidebands presented are non-overlapping to the selection of the ν_e CC signal.

8.3.1 Neutral Pion Sideband

This sideband selects events with a π^0 decaying into two photons in the final state. The study of π^0 events plays an important role for this analysis, as it not only provides a high-statistics sample of low-energy electromagnetic showers (50-300 MeV) that are useful for reconstruction validation, but also serves to characterize this important background to the ν_e signal [107]. Similarly to the ν_e CC selections, this selection was made using a series of cuts using only topological and calorimetric information that targeted the final diphotonic state. The comparison of data and prediction aims to test the reconstruction and calorimetry of the analysis and is presented as area normalized. A flat scaling factor of 0.759 is applied to the CC and NC π^0 events based on the normalization differences found in the π^0 mass distribution in Figure 8.18. This figure shows an area-normalized histogram for the reconstructed π^0 invariant mass, $M_{\gamma\gamma}$, from the decays of neutral pions $\pi^0 \rightarrow \gamma\gamma$. The π^0 selection shows a 1% agreement between data and simulation, and fall within 5% of the nominal π^0 mass of 134.98 MeV/c^2, demonstrating good shower reconstruction and calorimetric performance.

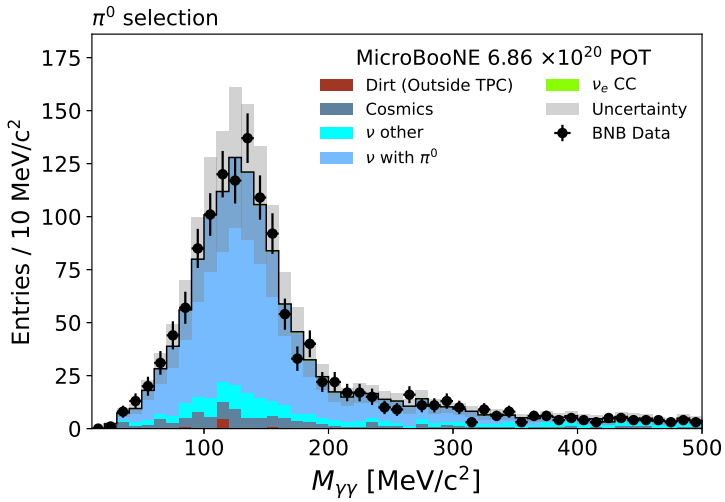

Figure 8.18: Results from the π^0 selection showing the area-normalized distribution of the diphoton mass of the selected candidates. The data and prediction agree within 1% and the peak of the distribution is within 5% of the accepted mass of the π^0 (134.98 MeV/c^2). The selection shows a good calibration on the energy scale for electromagnetic showers.

8.3.2 Two+ Shower Sideband

The two+ shower sideband was developed by applying the ν_e selection but requiring that there be at least two contained reconstructed showers instead of one (`n_showers_contained > 1`). This results in a sideband dominated by neutrino interactions that produce neutral pions. As there is no requirement on the number of tracks contained for this selection, it is useful for checking for agreement between data and prediction for both the $1e\mathrm{N}p0\pi$ and the $1e0p0\pi$ selections. Although a dedicated π^0 selection was developed (previous section 8.3.1), this selection is useful for modeling background events that are close to the eLEE signal defined by the BDT cuts.

The prediction in this sideband shows a high π^0 content, consistent with the π^0 topology given this particle's decay channel $\pi^0 \to \gamma\gamma$. There is a trend to find more predicted π^0 events at higher energies compared to the data, although this trend is covered by the $\mathcal{O}(20\%)$ systematic uncertainty due to pion production in the neutrino interaction model. An example of a variable checked in this sideband is given in Figure 8.19, which shows the distribution of the variable

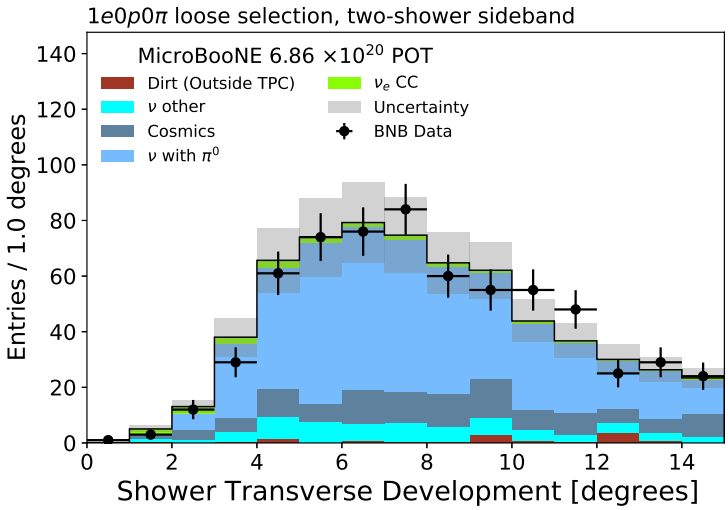

Figure 8.19: The transverse development angle (`showermoliere`) distribution of events passing the $1e0p0\pi$ loose selection, but having more than one shower. Most passing events contain a neutral pion in the final state, and good agreement between data and simulation indicates that this background is well modeled.

`showermoliere`. The events shown here are those that have passed the $1e0p0\pi$ loose selection but with the requirement that more than one shower be present in the event.

8.3.3 NuMI Beam Data

MicroBooNE is not only exposed to the neutrino flux generated by the BNB, but also serves as a target for neutrinos coming from the Neutrinos at the Main Injector (NuMI) beamline [113]. The NuMI beam is a well-understood source of electron neutrinos, and has been used to study ν_e-Ar interactions in ArgoNeuT [114], as well as being used for other MicroBooNE analyses [115, 116]. The NuMI neutrino flux primarily arrives at MicroBooNE at about 27° off the BNB axis, and although the energies of the protons generating the NuMI beamline neutrinos are more energetic (120 GeV protons from the main injector compared to 8 GeV protons from the BNB), the off-axis position makes the neutrino energies comparable between BNB and NuMI. This off-axis nature of the NuMI beamline makes the neutrino energy peak around 1 GeV, with a narrower distribution compared to that of the BNB. Furthermore, the ν_e and $\bar{\nu}_e$ content of the NuMI flux is approximately 5% and is of an order of magnitude higher than that of the intrinsic ν_e prediction in the BNB of around 0.5%. Additionally, the MiniBooNE LEE was only observed

from neutrinos coming from the BNB beamline and no significant excess was seen for NuMI events. These properties, along with the oscillation effects from NuMI neutrinos that are predictably small, make the NuMI data a valuable cross-check for the selection of ν_e events in the full energy spectrum.

The result of applying the full ν_e selection on NuMI data for the $1e\mathrm{N}p0\pi$ and $1e0p0\pi$ selections is presented in Figure 8.20. Both selections are presented with systematic uncertainties derived from the NuMI flux (both hadron production and beamline), GENIE and Geant4 reinteraction systematics along with detector systematics omitted in these plots. Prediction and observation show a good level of agreement with 16 events observed and 16.9 events predicted for the $1e0p0\pi$ selection and 54 events observed with 53 events predicted in the $1e\mathrm{N}p0\pi$ selection.

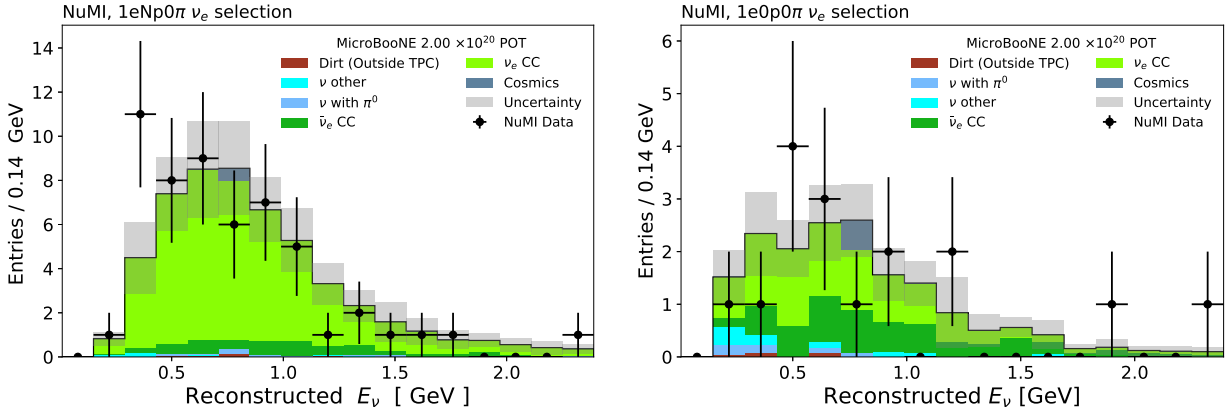

(a) $1e\mathrm{N}p0\pi$ **(b)** $1e0p0\pi$

Figure 8.20: Reconstructed neutrino energy distributions for full selection of events for $1e\mathrm{N}p0\pi$ (8.20a) and $1e0p0\pi$ (8.20b) from the NuMI beam.

Chapter 9

Prediction Uncertainties and Constraint

The predicted energy spectra of the ν_μ and the ν_e selections for this analysis are subject to a range of systematic uncertainties related to different components of the MicroBooNE experiment. The systematic uncertainties are associated with the neutrino beam flux, neutrino-argon interaction cross sections, hadron re-interactions and detector modeling. These systematic uncertainties are calculated for a set of parameters for a given category and give information on the reliability of the prediction and the level of sensitivity of the measurement.

The sources of uncertainty can also be categorized depending on how they are treated within the analysis into re-weightable and non-reweightable parameters. Flux and neutrino interaction uncertainties are are associated with weights and can be applied on an event-by-event basis. Each event can be re-weighted in order to account for the variation a parameter can have on the prediction. Given a parameter, P, it can be varied by the following:

$$P \rightarrow P' \left(1 + x_P \frac{\delta P}{P}\right) \tag{9.1}$$

where δP is the estimated standard deviation of P. The variation of P depends on x_P, which changes the weight of the simulated event. x_P is often referred as a "knob" and varies in the range of $[-1, +1]$. In contrast, non-reweightable parameters, like those belonging to the detector systematic uncertainties, need to be varied individually and require a new set of events whenever its needed to propagate their uncertainties through the analysis. Detector systematic uncertainties are evaluated with a set of dedicated detector variation samples.

This chapter describes the treatment and evaluation of systematic uncertainties, as well as the constraint procedure used in this analysis to reduce the uncertainties. Section 9.1 describes

the covariance matrix formalism. The neutrino beam flux uncertainties are described in Section 9.2, neutrino interaction uncertainties are described in Section 9.3, hadronic re-interaction uncertainties are described in Section 9.4, and detector uncertainties are described in Section 9.5. Lastly, the ν_μ constraint and its application in the analysis are detailed in Section 9.6.

9.1 Covariance Matrix Construction

The eLEE analysis relies on the covariance matrix formalism to evaluate systematic uncertainties. Using the SBNFit framework [117], the fractional covariance matrices are constructed to account for both statistical and systematic uncertainties and to take into account the correlations between different samples in the selections. A covariance matrix for each class of systematic variations is constructed for a given distribution. The full systematic covariance matrix for a distribution is then the sum of the individual covariance matrices calculated for each underlying systematic variation:

$$C^{\text{Syst}} = C^{\text{Flux}} + C^{\text{XSec}} + C^{\text{Detector}} + C^{\text{MCstat}} \tag{9.2}$$

Each covariance matrix, C_{ij}, is calculated using the following equation:

$$C_{ij} = \frac{1}{N}\sum_{k=1}^{N}\left(n_i^k - n_i^{\text{CV}}\right)\left(n_j^k - n_j^{\text{CV}}\right) \tag{9.3}$$

where n^{CV} is the nominal distribution (central value), n^k is a distribution calculated by varying the underlying source of uncertainty within its associated error band, and i, j indicates the bin number. These varied distributions are also referred to as universes, as they represent a slightly tweaked variation about n^{CV}. The covariance matrix is then constructed by considering N separate varied distributions. The full-systematics covariance matrix is then sampled along the diagonal to determine the bin uncertainties of a given distribution. The diagonal components, C_{ii} correspond to σ_{ii}^2 or the square of the error on the i^{th} bin.

9.2 Beam Flux Uncertainties

The flux uncertainties in the BNB have been studied by the MiniBooNE [85] and MicroBooNE [3] collaborations. The dominant source of flux uncertainties comes from the uncertainty in hadron production from proton-beryllium (p-Be) interactions. Hadron production uncertainties affect the rate and spectrum of secondary particles produced by p-Be collisions such as $\pi^{\pm}, K^{\pm}$ and K^0_L. Other subleading sources of uncertainty come from the proton delivery rate, horn current modeling, and secondary hadronic interactions. Both MiniBooNE and MicroBooNE have used a simulation-based procedure to constrain the total flux uncertainty, with the latter obtaining the results shown in Table 9.1. The work in this thesis is focused on the ν_e and ν_μ components of the beam, where the dominant systematic is the production of π^+ at a level of approximately $\mathcal{O}(10\%)$.

Table 9.1: Systematic uncertainties in the calculation of the BNB flux. Table taken from [3].

Systematic	ν_μ [%]	$\bar{\nu}_\mu$ [%]	ν_e [%]	$\bar{\nu}_e$ [%]
Proton delivery	2.0	2.0	2.0	2.0
π^+	11.7	1.0	10.7	0.03
π^-	0.0	11.6	0.0	3.0
K^+	0.2	0.1	2.0	0.1
K^-	0.0	0.4	0.0	3.0
K^0_L	0.0	0.3	2.3	21.4
Other	3.9	6.6	3.2	5.3
Total	12.5	13.5	11.7	22.6

The sources of flux uncertainties considered for this analysis are listed in Table 9.2. The thirteen flux parameters are treated using the many universes method, that is, each source of uncertainty is varied independently by drawing from a Gaussian with width of $\pm 1\sigma$ of their measured uncertainties. Each deviation from the central value is considered as a universe. In this analysis, flux uncertainties are varied simultaneously according to a Gaussian distribution for 1000 universes and are treated as one variation, "flux_all". Figure 9.1 displays the effects of reweighting flux_all variations with respect to the central value on both the $1e\mathrm{N}p0\pi$ and

$1e0p0\pi$ selections. The uncertainty in each bin for a given variation corresponds to the average difference between the central value and each universe.

Table 9.2: List of systematic variations in the flux of the beam.

Parameter Name	Description	Universes
expskin_FluxUnisim	skin-depth electric currents penetrate conductor	–
horncurrent_FluxUnisim	horn current in magnetic focusing horns	–
kminus_PrimaryHadronNormalization	Primary hadron normalization	–
kplus_PrimaryHadronFeynmanScaling	Primary Hadron Feynman Scaling	–
kzero_PrimaryHadronSanfordWang	Primary Hadron Sanford Wang	–
nucleoninexsec_FluxUnisim	nucleon total inelastic cross section on Be	–
nucleonqexsec_FluxUnisim	nucleon total quasi-elastic cross section on Be	–
nucleontotxsec_FluxUnisim	nucleon total cross section on Be	–
piminus_PrimaryHadronSWCentralSplineVariation	Primary Hadron Sanford Wang Central Spline Variation	–
pioninexsec_FluxUnisim	pion total inelastic cross section on Be	–
pionqexsec_FluxUnisim	pion total quasi-elastic cross section on Be	–
piontotxsec_FluxUnisim	pion total cross section on Be	–
piplus_PrimaryHadronSWCentralSplineVariation	Primary Hadron Sanford Wang Central Spline Variation	–
flux_all	13 flux parameters varied randomly and simultaneously according to Gaussian distributions, with 1σ uncertainties	1000

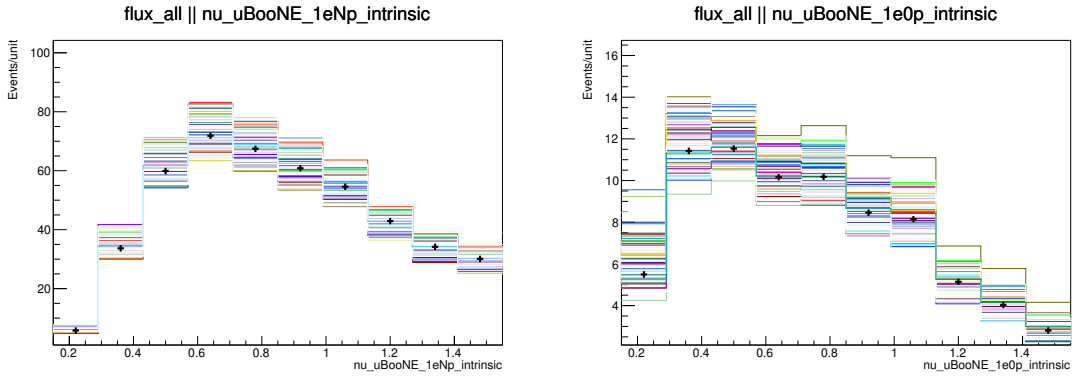

(a) $1e\mathrm{N}p0\pi$ selection

(b) $1e0p0\pi$ selection

Figure 9.1: The effects of the flux_all variations on the intrinsic ν_e subchannel for both the $1e\mathrm{N}p0\pi$ and $1e0p0\pi$ selections. The black crosses indicate the central value, and each colored histogram shows a different universe's reweighting about the central value. The uncertainty magnitude of each bin is calculated by taking the average difference between the central value and each different universe.

The covariance and correlation matrices for the total flux systematic uncertainties on the $1e\mathrm{N}p0\pi$, $1e0p0\pi$ and ν_μ selections are shown in Figure 9.2. The fractional covariance matrix shows a 10% uncertainty on the lowest energy bins (0.15 - 0.29 GeV) for the $1e\mathrm{N}p0\pi$ selection while for the $1e0p0\pi$ selection show the maximum uncertainty of 7% in the 0.43 - 0.57 GeV bin. The correlations between muon neutrinos and electron neutrinos are strongest on the diagonals of each sector, indicating a correlation in true energy that is consistent with expectation given that electron and muon neutrinos of similar energies are products of the same hadronic decay processes.

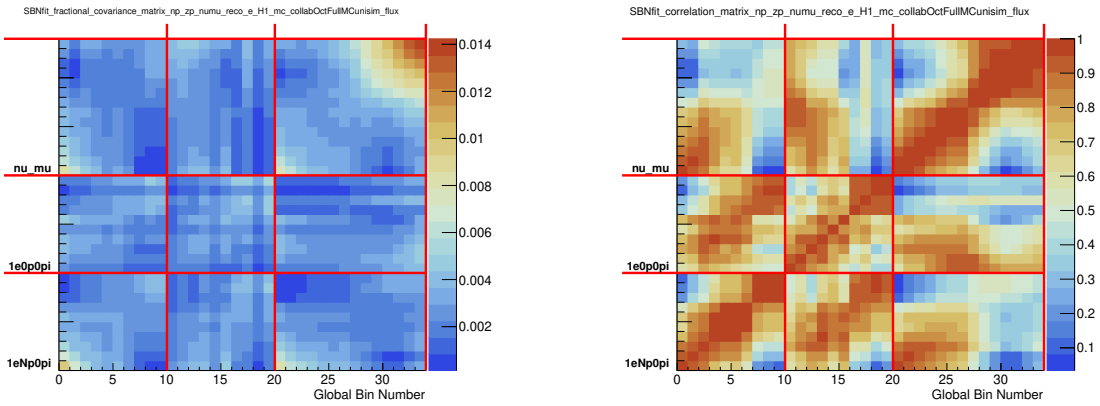

(a) Flux uncertainty fractional covariance matrix.

(b) Flux uncertainty correlation matrix.

Figure 9.2: Flux-only correlation matrix for the combined $1e\mathrm{N}p0\pi$, $1e0p0\pi$, and ν_μ selection as a function of the reconstructed neutrino energy. The global bin number starts from 0.15 to 1.55 GeV, in steps of 0.14 GeV for the $1e\mathrm{N}p0\pi$ and $1e0p0\pi$ selection and in steps of 0.1 GeV for the ν_μ selection.

9.3 Neutrino Cross Section Uncertainties

Neutrino cross-section uncertainties are calculated over a wide variety of parameters from the GENIE event generator. More details on the models used by GENIE to simulate neutrino interactions can be found in Section 7.1.2. A large number of models are used due to the lack of ν-Ar cross section measurements, specially at low neutrino energies $\mathcal{O}(\sim 1\mathrm{GeV})$.

The GENIE reweighting framework is used to propagate uncertainties from parameters to any observables. This is code provided primarily by the GENIE collaboration, together with cus-

tom routines implemented by the MicroBooNE collaboration [86, 93]. The reweighting framework varies “knobs", which are parameters used to model neutrino cross section and final-state interaction uncertainties. Reference [93] documents the GENIE cross section models, central value tunes, and uncertainties used in MicroBooNE analyses.

This analysis considers a total of 54 sources of neutrino interaction uncertainties. Most of these sources are varied through a multisim approach, that is, they are grouped together in a correlated way using a single weight calculator and given the name “All_UBGenie”. Table 9.3 lists the 44 parameters that make up the All_UBGenie knob. The number of variations, or universes, considered for this set of parameters is $N = 500$. The remaining 10 parameters, listed in Table 9.4, are treated through the unisim approach, where each parameter is individually varied. They are either “up” and “down” variations where the model is varied $\pm 1\sigma$ of its given uncertainty, or as “one-sided” variations where there is only one variation to consider. The formation of the covariance matrix for both the up/down and one-sided variations is handled differently. The up/down variations are treated in a similar fashion to those in the multisim approach, only with $N = 2$:

$$C_{ij} = \frac{1}{2}\left[\left(n_i^{\mathrm{CV}} - n_j^{\mathrm{UP}}\right) \times \left(n_i^{\mathrm{CV}} - n_j^{\mathrm{UP}}\right) + \left(n_i^{\mathrm{CV}} - n_j^{\mathrm{DN}}\right) \times \left(n_i^{\mathrm{CV}} - n_j^{\mathrm{DN}}\right)\right]. \tag{9.4}$$

In the case of one-sided variations where $N = 1$, the inclusion in the covariance matrix takes the form:

$$C_{ij} = \left(n_i^{\mathrm{CV}} - n_j^{\mathrm{UP}}\right) \times \left(n_i^{\mathrm{CV}} - n_j^{\mathrm{UP}}\right). \tag{9.5}$$

The resulting fractional covariance and correlation matrices for the $1e\mathrm{N}p0\pi$, $1e0p0\pi$ and ν_μ selections are presented in Figure 9.3 which is estimated to be 20% in average and up to 0% at around 0.15 – 0.25 GeV.

Table 9.3: List of neutrino interaction uncertainties included in All_UBGenie.

GENIE uncertainties	Description
MaCCQE	CCQE axial mass
NormCCMEC	Energy-independent normalization for CCMEC
MaNCEL	Axial mass for NCEL
EtaNCEL	Empirical parameter used to account for sea quark contribution to NCEL form factor
NormNCMEC	Energy-independent normalization for NCMEC
FracPN_CCMEC	Varies fraction of initial nucleon pairs that are pn
FracDelta_CCMEC	Varies relative contribution of Δ diagrams to total MEC cross section
NormCCRES	Energy-independent normalization for CCRES
MaCCRESshape	Shape-only CCRES axial mass
MvCCRESshape	Shape-only CCRES vector mass
NormNCRES	Energy-independent normalization for NCRES
MaNCRESshape	Shape-only NCRES axial mass
MvNCRESshape	Shape-only NCRES vector mass
MaCOHpi	Axial mass for COH π production
R0COHpi	Nuclear radius parameter for COH π production
NonRESBGvpCC1pi	Non-resonant background normalization for νp CC1π
NonRESBGvpCC2pi	Non-resonant background normalization for νp CC2π
NonRESBGvpNC1pi	Non-resonant background normalization for νp NC1π
NonRESBGvpNC2pi	Non-resonant background normalization for νp NC2π
NonRESBGvnCC1pi	Non-resonant background normalization for νn CC1π
NonRESBGvnCC2pi	Non-resonant background normalization for νn CC2π
NonRESBGvnNC1pi	Non-resonant background normalization for νn NC1π
NonRESBGvnNC2pi	Non-resonant background normalization for νn NC2π
NonRESBGvbarpCC1pi	Non-resonant background normalization for $\bar{\nu}$p CC1π
NonRESBGvbarpCC2pi	Non-resonant background normalization for $\bar{\nu}$p CC2π
NonRESBGvbarpNC1pi	Non-resonant background normalization for $\bar{\nu}$p NC1π
NonRESBGvbarpNC2pi	Non-resonant background normalization for $\bar{\nu}$p NC2π
NonRESBGvbarnCC1pi	Non-resonant background normalization for $\bar{\nu}$n CC1π
NonRESBGvbarnCC2pi	Non-resonant background normalization for $\bar{\nu}$n CC2π
NonRESBGvbarnNC1pi	Non-resonant background normalization for $\bar{\nu}$n NC1π
NonRESBGvbarnNC2pi	Non-resonant background normalization for $\bar{\nu}$n NC2π
AhtBY	A_HT higher-twist parameter in the Bodek-Yang model scaling variable xi_w
BhtBY	BHT higher-twist parameter in the Bodek-Yang model scaling variable xi_w
CV1uBY	CV1u valence GRV98 PDF correction parameter in the Bodek-Yang model
CV2uBY	CV2u valence GRV98 PDF correction parameter in the Bodek-Yang model
AGKYxF1pi	Hadronization parameter, applicable to true DIS interactions only
AGKYpT1pi	Hadronization parameter, applicable to true DIS interactions only
MFP_pi	π mean free path
MFP_N	Nucleon mean free path
FrCEx_pi	Fractional cross section for π charge exchange
FrInel_pi	Fractional cross section for π inelastic scattering
FrAbs_pi	Fractional cross section for π absorption
FrCEx_N	Fractional cross section for nucleon charge exchange
FrInel_N	Fractional cross section for nucleon inelastic scattering
FrAbs_N	Fractional cross section for nucleon absorption
RDecBR1gamma	Normalization for $\Delta \rightarrow \gamma$ decays
RDecBR1eta	Normalization for $\Delta \rightarrow \eta$ decays
FrPiProd_pi	Fractional cross section for π^- induced π production
FrPiProd_N	Fractional cross section for nucleon-induced π production

Table 9.4: List of neutrino interaction uncertainties outside of All_UBGenie.

GENIE knobs	Description	Universes
All_UBGenie	44 GENIE knobs are varied randomly and simultaneously according to Gaussian distributions, with 1σ uncertainties	500
RPA_CCQE_UBGenie	Strength of the RPA correction	2
XSecShape_CCMEC_Genie	Changes the CCMEC cross section shape from the Nieves prediction (parameter value = 0) to the shape predicted by GENIE's Empirical MEC model (parameter value = 1)	1
AxFFCCQEshape_UBGenie	Parameterization of the nucleon axial form factor	1
VecFFCCQEshape_UBGenie	Parametrization of the vector form factor model	1
DecayAngMEC_UBGenie	Changes angular distribution of nucleon cluster	1
ThetaDelta2NRad_UBGenie	Interpolates angular distribution for $\Delta \rightarrow N+\gamma$ between isotropic (0) and $\propto \cos^2\theta$ (1)	1
Theta_Delta2Npi_Genie	Interpolates angular distribution for $\Delta \rightarrow N+\pi$ between Rein-Sehgal model (0) and isotropic (1)	1
NormCCCOH_UBGenie	Scaling factor for CC COH π production	2
NormNCCOH_UBGenie	Scaling factor for NC COH π production	2
xsr_scc_Fa3_SCC	Second class currents	10
xsr_scc_Fv3_SCC	Second class currents	10

9.4 Hadronic Re-interaction Uncertainties

This systematic uncertainty is related to hadrons that strongly interact with argon nuclei after leaving the initial nucleus where the neutrino interaction occurred. Re-interactions of protons, π^+, and π^- can impact the event reconstruction by inducing large momentum transfers of re-scattering hadrons. These uncertainties are treated as Geant4-level uncertainties in the argon and hadron cross section. Geant4 truth information for hadron trajectories and propagation through argon is used for event reweighting by the Geant4Reweight framework [118]. The impact on the ν_e CC selections is small with this systematic uncertainty having a larger impact on background events such as CC π^0 and neutral current events with no pions in the final state. Figure 9.4 shows the fractional covariance and correlation matrices for the systematic uncertainty of hadron re-interaction.

9.5 Detector Uncertainties

The detector systematic uncertainties quantify the differences between what the detector measures and what is obtained from simulation. At MicroBooNE, the detector systematic uncer-

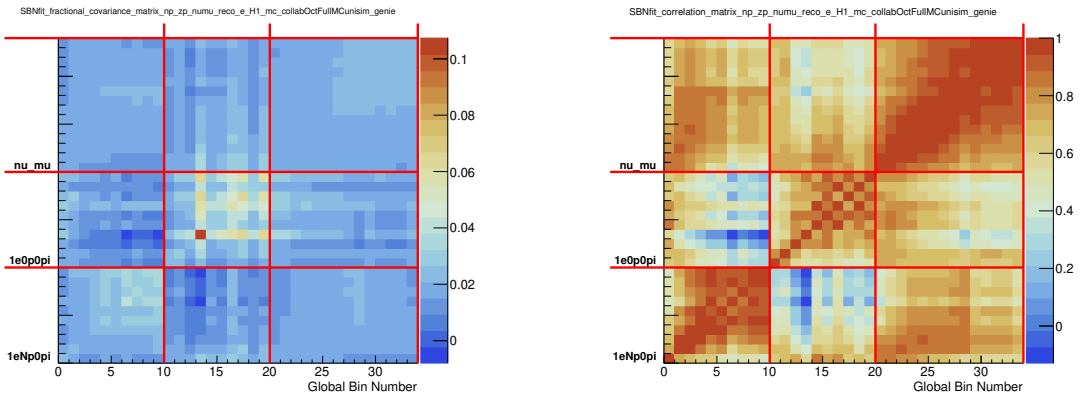

(a) Neutrino cross section fractional covariance matrix **(b)** Neutrino cross section correlation matrix

Figure 9.3: Neutrino-cross-section-only fractional covariance matrix for $1eNp0\pi$ selection. The global bin number starts from 0.15 to 1.55 GeV, in steps of 0.14 GeV for the $1eNp0\pi$ and $1e0p0\pi$ selection and in steps of 0.1 GeV for the ν_μ selection.

tainties are evaluated using dedicated samples, where the detector has been simulated with some deviations in its response. There are nine detector variations and they broadly fall into three categories: wire-modification variations, light-related variations, and other variations dealing with space charge and recombination-specific variations.

Wire modifications deal with variations in the TPC wire waveforms. The uncertainty of wire modification is based on the scaling of the simulation to the data in the detector response and is calculated as a function of the drift direction x, the coordinates (y,z), and the angles θ_{yz} and θ_{xz} of the particle trajectory. This framework was developed by the MicroBooNE collaboration [119] and works by taking the deconvolved waveforms and modifying them to account for the discrepancies in the pulse heights and widths between the data and prediction, producing a ratio that is used to modify each bin of the deconvolved waveform.

The light-related variations are modifications made to the light simulation parameters to estimate the light yield (LY) uncertainties. Three variations are considered for this analysis: first, a uniform LY drop of 25% across the detector to account for the mis-modeling of the overall detector LY. Second, the Rayleigh scattering length in the MicroBooNE simulation is set at 60 cm, however recent measurements have shown this value closer to 100 cm [120]. To ensure

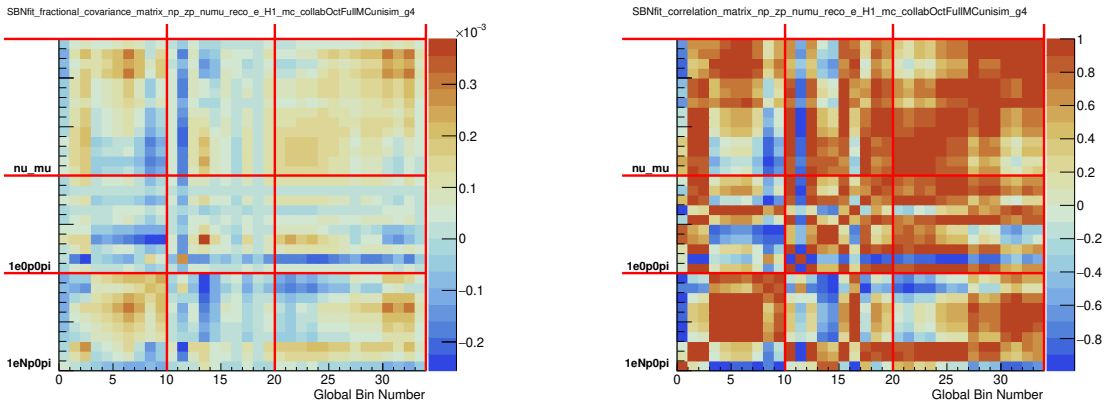

(a) Hadronic re-interaction fractional covariance matrix

(b) Hadronic re-interaction correlation matrix

Figure 9.4: Hadronic re-interaction fractional covariance matrix and correlation matrix for the $1e\mathrm{N}p0\pi$ and $1e0p0\pi$ selection. The global bin number starts from 0.15 GeV to 1.55 GeV, in steps of 0.14 GeV for the $1e\mathrm{N}p0\pi$ and $1e0p0\pi$ selection and in steps of 0.1 GeV for the ν_μ selection.

proper modeling, Rayleigh scattering length is varied to 120 cm in the systematic variation sample. Lastly, the simulation of an 8 meter light attenuation length to account for drift-distance-dependent mis-modeling in light quenching, compared to the flat scaling applied in our simulation and calibration.

The last two variations are on the electric field (E-field) mapping due to space-charge and recombination effects. The space-charge variation sample is calculated by using two data-driven E-field maps, one using cosmic muons [79] and another using the UV laser calibration system installed in the detector [100]. Each map complements the other by covering different regions of the detector where each measurement is strongest: the cosmic muon map is considered more reliable, but it under-performs at the center of the detector for example. Recombination uncertainties are built by varying parameters in the modified Box model that cover the differences between data and simulation observed at high dE/dx for protons.

Detector systematics are evaluated by applying the ν_e CC selections to both the CV simulation and various detector-variation simulations and noting the event count in each bin per variation. These bin-to-bin variations are then used to construct a covariance matrix. An example of how detector systematics are treated can be seen for the WireModX variation, which

Table 9.5: Detector systematics for BDT $1e\mathrm{N}p0\pi$ selection. The final column is the quadrature sum of all systematic variations.

E [GeV]	scale X	scale YZ	angle YZ	angle XZ	Recomb	SCE	LY down	Rayleigh	LY Attn.	Σ
0.15-0.29	0.043	0.067	0.089	0.048	0.011	0.074	0.000	0.010	0.022	0.15
0.29-0.43	0.004	0.085	0.042	0.014	0.074	0.096	0.006	0.007	0.009	0.16
0.43-0.57	0.039	0.020	0.040	0.015	0.037	0.025	0.007	0.002	0.020	0.08
0.57-0.71	0.035	0.011	0.037	0.043	0.010	0.048	0.014	0.002	0.007	0.08
0.71-0.85	0.041	0.044	0.004	0.044	0.057	0.052	0.006	0.002	0.030	0.11
0.85-0.99	0.045	0.000	0.006	0.052	0.030	0.057	0.017	0.003	0.020	0.10
0.99-1.13	0.028	0.006	0.002	0.033	0.006	0.073	0.007	0.000	0.029	0.09
1.13-1.27	0.025	0.032	0.044	0.021	0.068	0.153	0.004	0.000	0.026	0.18
1.27-1.41	0.013	0.007	0.034	0.003	0.060	0.083	0.000	0.010	0.019	0.11
1.41-1.55	0.071	0.039	0.026	0.021	0.008	0.026	0.012	0.012	0.049	0.11

describes the scaling of the simulation in the drift direction x, shown in Figure 9.5. The square roots of the diagonal entries are then taken as the systematic uncertainty associated with the given variation. This is done for each variation, and the final detector systematic uncertainty is evaluated by adding in quadrature all the variations for each bin in each selection. The results for the $1e\mathrm{N}p0\pi$, $1e0p0\pi$ BDT-based selections are shown in Tables 9.5 and 9.6, respectively. Detector systematics are on the order of 10-20%, depending on the energy bin.

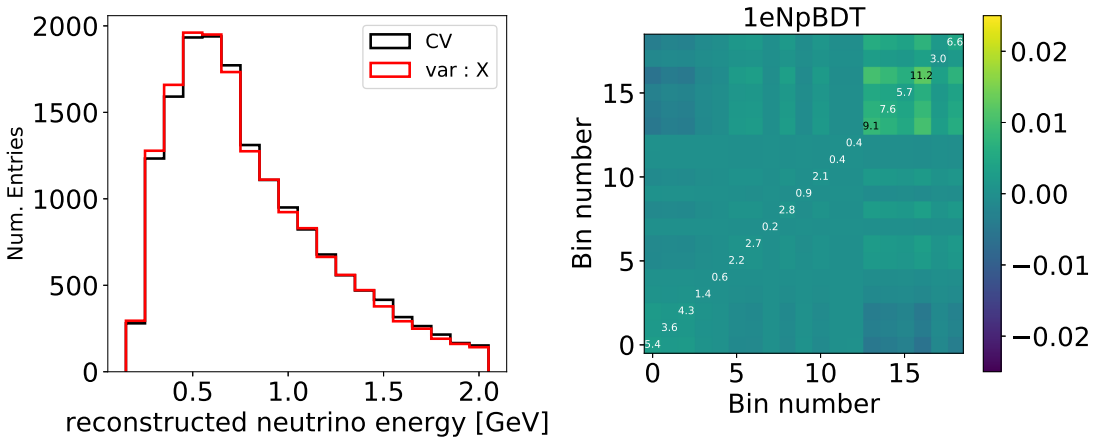

Figure 9.5: Example of the impact of WireModX variation on the $1e\mathrm{N}p0\pi$ BDT selection. The left image shows the comparison of selected events in the central value (black) vs. variation (red) for the $1e\mathrm{N}p0\pi$ selection. The image on the right shows the covariance matrix for this variation with the diagonal entries marked by the square-root of the covariance, representative of each bin's percent uncertainty.

E [GeV]	scale X	scale YZ	angle YZ	angle XZ	Recomb	SCE	LY down	Rayleigh	LY Attn.	Σ
0.15-0.29	0.062	0.014	0.059	0.020	0.085	0.065	0.000	0.005	0.009	0.140
0.29-0.43	0.019	0.016	0.016	0.033	0.025	0.036	0.009	0.007	0.005	0.064
0.43-0.57	0.057	0.007	0.008	0.022	0.017	0.104	0.009	0.009	0.011	0.123
0.57-0.71	0.008	0.018	0.042	0.028	0.017	0.113	0.003	0.009	0.019	0.128
0.71-0.85	0.125	0.041	0.086	0.006	0.046	0.007	0.008	0.008	0.043	0.170
0.85-0.99	0.020	0.027	0.015	0.060	0.126	0.220	0.006	0.014	0.043	0.269
0.99-1.13	0.104	0.026	0.034	0.013	0.076	0.143	0.007	0.016	0.049	0.204
1.13-1.27	0.039	0.031	0.056	0.012	0.062	0.149	0.010	0.000	0.060	0.188
1.27-1.41	0.017	0.033	0.008	0.096	0.111	0.300	0.012	0.000	0.027	0.337
1.41-1.55	0.133	0.019	0.138	0.066	0.078	0.174	0.015	0.043	0.091	0.297

Table 9.6: Detector systematics for BDT $1e0p0\pi$ selection. The final column is the quadrature sum of all systematic variations.

9.6 Application of the ν_μ Constraint

This analysis relies on a well-measured ν_μ CC inclusive selection, described in Section 8.1, to constrain the predicted $1e\mathrm{N}p0\pi$ and $1e0p0\pi$ spectra and their uncertainties. The goal of the constraint procedure is to reduce the systematic uncertainties in the ν_e CC selections, along with updating the central value prediction in order to obtain the best possible prediction with the available information. The constraint relies on measurements of events in a defined sideband, which is the ν_μ CC inclusive measurement in this case, and using this observation to update the ν_e CC prediction and its uncertainty. The procedure relies on the formalism of block matrices or conditional distributions [121]. The concepts described in this section were originally developed by the MiniBooNE collaboration for their ν_e appearance analysis [122].

The constraint procedure follows the results from conditional distributions [121] in which the $1e\mathrm{N}p0\pi$ and $1e0p0\pi$ spectra, along with the inclusive spectra of the ν_μ CC, come from a multivariate normal distribution defined by their joint covariance matrix and predictions. In essence, the ν_e CC predictions are conditioned on the ν_μ CC inclusive data observed. The procedure is described in the following way. The mean number of predicted events for the ν_e selections of the i^{th} bin is defined as $m_i^e = N_i^{e,pred}$ and similarly for the ν_μ selection $m_i^\mu = N_i^{\mu,pred}$. Let X represent the observed data distributions so that the number of observed ν_e events in the i^{th} bin is $X_i^e = N_i^{e,obs}$, and for the ν_μ selection its $X_i^\mu = N_i^{\mu,obs}$. A block matrix is used to

represent the covariance matrix for the joint spectra $X = X^e \oplus X^\mu$ in the following way:

$$\mathrm{cov}(X) = C = \begin{pmatrix} C^{ee} & C^{e\mu} \\ C^{\mu e} & C^{\mu\mu} \end{pmatrix} \tag{9.6}$$

The constrained ν_e prediction is expressed as

$$m^{e,\mathrm{constrained}} = E(X^e | X^\mu = x^\mu) = m^e + C^{e\mu}\left(C^{\mu\mu}\right)^{-1}\left(x^\mu - m^\mu\right), \tag{9.7}$$

and the constrained covariance matrix as:

$$C^{ee,\mathrm{constrained}} = C^{ee} - C^{e\mu}\left(C^{\mu\mu}\right)^{-1} C^{\mu e}. \tag{9.8}$$

The covariance matrix of the ν_μ CC inclusive observation, $C^{\mu\mu}$, must take into account systematic uncertainties in the data and statistical fluctuations to ensure that these effects are not passed onto the constraint procedure. This is achieved by adding the $N^{\mu,pred}$ to the diagonal entries of the $C^{\mu\mu}$ block matrix of Equation 9.6 before the constraint is applied. In contrast, the C^{ee} block has direct uncertainties of the $1e\mathrm{N}p0\pi$ and $1e0p0\pi$ that allow the correct assessment of errors when performing statistical tests.

After the constraint procedure, both the ν_e CC predictions and the associated covariance matrix are updated by effectively incorporating the ν_μ CC observation. Figures 9.6 and 9.7 show the effects of the ν_μ CC constraint on the uncertainties of the $1e\mathrm{N}p0\pi$ and $1e0p0\pi$ ν_e selections, respectively, where a reduction in the uncertainty bands can be seen in the predictions of number of intrinsic ν_e and LEE events. Tables 9.7 and 9.8 show the quantitative impact of the constraint on event prediction uncertainties in different energy bins.

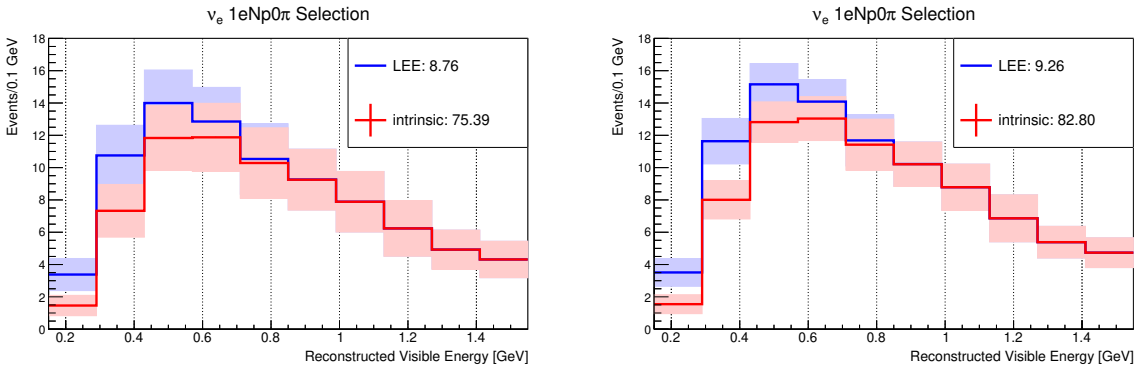

(a) The $1e\mathrm{N}p0\pi$ prediction before the application of constraint.

(b) The $1e\mathrm{N}p0\pi$ prediction after the application of constraint.

Figure 9.6: The final $1e\mathrm{N}p0\pi$ selection scaled to 6.95×10^{20} POT showing the reduction in systematic uncertainties before (left) and after (right) the ν_μ constraint.

Table 9.7: Summary of fractional errors (in percentage) on the sample statistics, flux, cross section, and detector systematics before and after the ν_μ constrain for the $1e\mathrm{N}p0\pi$ BDT selection, assuming no LEE signal.

Energy [GeV]	SampleStat+Flux+GENIE+G4			SampleStat+Flux+GENIE+G4+Det. Syst.		
	Before ν_μ Constraint	After ν_μ Constraint	Reduction [%]	Before ν_μ Constraint	After ν_μ Constraint	Reduction [%]
0.15 - 0.29	41.91	38.59	7.93	43.09	38.03	11.74
0.29 - 0.43	19.29	10.05	47.87	22.28	14.80	33.54
0.43 - 0.57	16.31	7.52	53.89	17.53	10.07	42.54
0.57 - 0.71	16.88	7.61	54.90	18.31	10.74	41.36
0.71 - 0.85	18.63	9.03	51.53	21.21	13.84	34.76
0.85 - 0.99	18.14	9.20	49.25	20.36	13.45	33.94
0.99 - 1.13	22.09	12.34	44.16	23.75	16.29	31.43
1.13 - 1.27	21.51	12.40	42.34	27.64	21.20	23.28
1.27 - 1.41	22.08	14.01	36.56	24.54	18.19	25.87
1.41 - 1.55	23.80	15.08	36.61	26.12	19.48	25.41

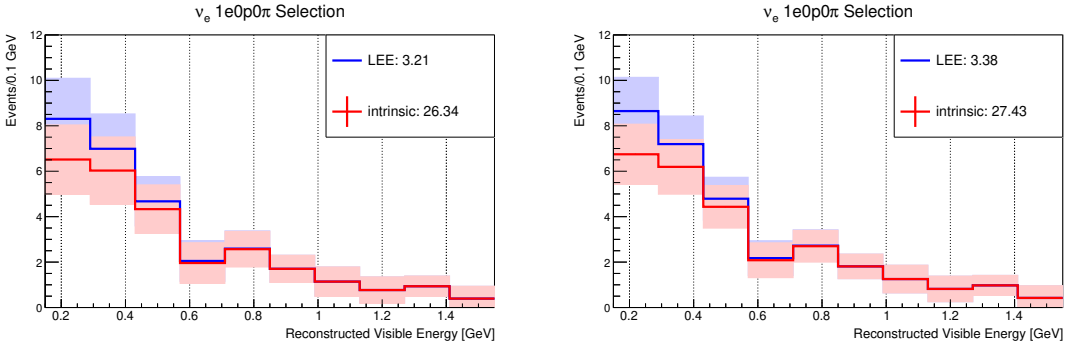

(a) The $1e0p0\pi$ prediction before the application of constraint.

(b) The $1e0p0\pi$ prediction after the application of constraint.

Figure 9.7: The final $1e0p0\pi$ selection scaled to 6.95×10^{20} POT showing the reduction in systematic uncertainties before (left) and after (right) the ν_μ constraint.

Table 9.8: Summary of fractional errors (in percentage) on the sample statistics, flux, cross section, and detector systematics before and after the ν_μ constrain for the $1e0p0\pi$ BDT selection, assuming no LEE signal.

Energy [GeV]	SampleStat+Flux+Genie+G4			SampleStat+Flux+Genie+G4+Det. Syst.		
	Before Constraint	After Constraint	Reduction[%]	Before Constraint	After Constraint	Reduction[%]
0.15 - 0.29	30.58	25.22	17.53	32.70	27.12	17.07
0.29 - 0.43	25.05	19.66	21.50	26.20	20.70	20.98
0.43 - 0.57	32.01	28.09	12.24	33.26	28.29	14.96
0.57 - 0.71	44.69	36.62	18.05	45.74	36.91	19.31
0.71 - 0.85	40.80	35.98	11.81	42.98	35.78	16.76
0.85 - 0.99	38.02	31.04	18.34	44.96	37.64	16.28
0.99 - 1.13	52.91	47.39	10.43	56.70	48.75	14.03
1.13 - 1.27	73.45	69.36	5.57	75.54	68.99	8.68
1.27 - 1.41	72.37	71.43	1.30	79.83	72.95	8.63
1.41 - 1.55	135.12	128.42	4.96	138.35	127.72	7.68

A summary of the systematic uncertainties for this analysis and the constraint procedure is shown in Figure 9.8. The flux, cross section, and detector systematics are represented by the blue, orange, and green histograms, respectively. The sum of all uncertainties are represented by the total uncertainty in the black histogram. The effects of the constraint on the uncertainties are given in gray for the $1e\mathrm{N}p0\pi$ and $1e0p0\pi$ selections. The ν_μ uncertainties are not changed by the constraint. The limited statistics in the higher-energy regions of the $1e0p0\pi$ channel make the uncertainties grow to $\mathcal{O}(100\%)$.

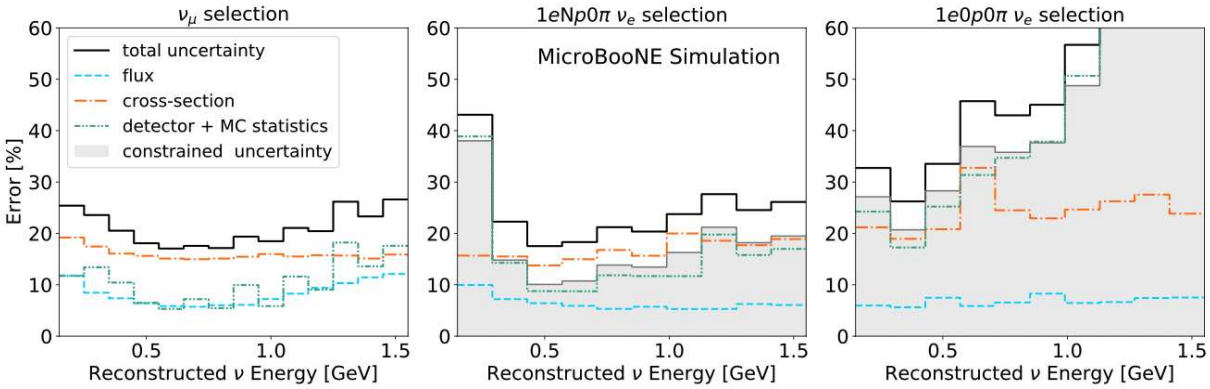

Figure 9.8: Impact of the constraint procedure on the fractional uncertainties for the three channels used in this analysis shown in the 0.15–1.55 GeV energy range used in the final results. The individual unconstrained uncertainty (dashed histograms) contributions coming from flux, cross section, and detector plus simulation statistics are shown in blue, orange, and green, respectively. Detector uncertainties account for both Geant4 re-interaction and detector response modeling uncertainties. The total unconstrained uncertainty is given by the black histogram.

Chapter 10

Results

The main analysis in this thesis was introduced in Chapter 6, which was the search for the low-energy excess observed by MiniBooNE in the MicroBooNE detector specifically looking for charged-current ν_e events without pions in the final state. The two topologies for this search are the $1e\mathrm{N}p0\pi$ and $1e0p0\pi$ channels. In Chapter 7 the steps of transforming raw TPC waveforms into fully reconstructed neutrino events were discussed. Chapter 8 presented the neutrino selection schemes not only for the ν_e channels, but also for the ν_μ constraint selection. Chapter 9 described the systematic uncertainties that were considered in this analysis, along with their treatment in the constraint procedure. This chapter will describe the final steps of this analysis in the statistical tests applied following the unblinding of the signal region.

The chapter sections are as follows: Section 10.1 presents the statistical methods used in this analysis and introduce the test statistic. Section 10.2 describes the final selections as a function of the reconstructed neutrino energies along with describing several key kinematic variables. Sections 10.3, 10.4, and 10.5 discuss the three statistical tests and their results: a goodness-of-fit test, the simple hypothesis test, and the signal strength test, respectively. Finally, Section 10.6, presents the results and compares them with those from the other LEE searches carried out by MicroBooNE.

10.1 Statistical Methods

A series of statistical tests are used in this analysis to compare the the $1e\mathrm{N}p0\pi$ and $1e0p0\pi$ selections with the prediction. Two hypotheses are considered for this analysis: the intrinsic ν_e only hypothesis, in which there is no eLEE contribution and only the intrinsic BNB ν_e CC interactions are present, and the eLEE hypothesis (described in Chapter 6), where there is an

additional ν_e contribution on top of the intrinsic ν_e background. This section will focus on the statistical methods and test statistic used for the quantitative evaluation between the observed data and the two hypotheses presented.

The test statistic used in this analysis is the combined Neyman-Pearson (CNP) χ^2 [84]. This test statistic is a linear combination of Neyman's and Pearson's chi-squares that better approximates a Poisson-likelihood chi-square and has the advantage of following the covariance matrix formalism. Additionally, its known to work better for cases where there are few data events per bin [84], such as those encountered in this analysis. The test statistic χ^2 is defined as

$$\chi^2 = \sum_{i,j=1}^{N} (n_i - m_i)\, C_{ij}^{-1} \left(n_j - m_j\right) \tag{10.1}$$

$$C_{ij} = C_{ij}^{\text{stat CNP}} + C_{ij}^{\text{syst}}, \tag{10.2}$$

where n is the number of observed events, m is the number of predicted events, and i indicates the i-th bin. The covariance matrix, C, incorporates both systematic uncertainties in the prediction with C^{syst}, which was previously defined in Equation 9.2, and statistical uncertainties related to observation in $C^{\text{stat CNP}}$. The error matrix containing information on statistical errors is defined under the CNP χ^2 formalism as:

$$C_{ii}^{\text{stat CNP}} = \begin{cases} \frac{3}{(1/n_i)+(2/m_i)} & n_i > 0 \\ \frac{m_i}{2} & n_i = 0 \end{cases} \tag{10.3}$$

with all statistical uncertainties added to the diagonal of the final covariance matrix. Note that in the CNP χ^2 formalism, the covariance matrix format is a linear combination of the Pearson χ^2 formalism ($C_{ii}^{\text{stat Pearson}} = m_{ii}$) and the Neyman χ^2 formalism ($C_{ii}^{\text{stat Neyman}} = n_{ii}$). Statistical contributions are added to the diagonal of the final covariance matrix before performing any χ^2 calculations. Throughout this work, any mention of χ^2 will refer to the CNP χ^2 described in this section.

To make quantitative statements for any statistical test, the calculated χ^2 must be compared with a probability distribution of the same test statistic under a specific hypothesis. To achieve this, the analysis employs the computation of toy experiments, a method implemented in the SBNFit framework [117]. Each toy experiment can be thought of as a pseudo-observation that is treated as if it were the "real" data. To generate toy experiments, a spectrum is sampled from a multivariate Gaussian distribution defined by the mean predicted spectrum and the covariance matrix for a given hypothesis. This is done by drawing correlated distributions from the systematic covariance matrix. The covariance matrix is run through a Cholesky decomposition routine that breaks down a matrix into the product of a lower triangular matrix and its conjugate transpose. Then, the pseudo-data entries in the toy experiment spectrum are sampled as a Poisson random number around the systematic draw of the predicted spectrum. This yields a set of toy experiments which is used to calculate the test statistic χ^2 distribution. This is done many times under a given hypothesis, and, in the end, the test statistic is calculated for the observed data and compared with the predicted distributions to interpret the results of each of the statistical tests.

10.2 Modeling of Electron Neutrinos

The unblinded data observation for the $1e\mathrm{N}p0\pi$ and $1e0p0\pi$ channels is shown in Figure 10.1, where the data are compared with the prediction after the ν_μ constraint described in Section 9.6. Data for the $1e\mathrm{N}p0\pi$ channel show a total of 64 candidate events observed, compared to the intrinsic ν_e prediction of 86.8 ± 11.5 events. Similarly, the $1e0p0\pi$ channel shows a total of 34 candidate events observed, with 30.1 ± 4.3 events predicted. The event selection for both the $1e\mathrm{N}p0\pi$ and $1e0p0\pi$ selections shown in Figure 10.1 corresponds to the neutrino energy range of 0.0–2.38 GeV.

The $1e\mathrm{N}p0\pi$ selection shows a visible deficit in the data in some of the bins, specifically the 0.28–0.42 GeV bin, the 0.56–0.84 GeV bins, and the 0.98–1.26 GeV bins of the LEE-sensitive region. In general, the energy range 0.15–1.55 GeV, which is the range sensitive to the eLEE, reg-

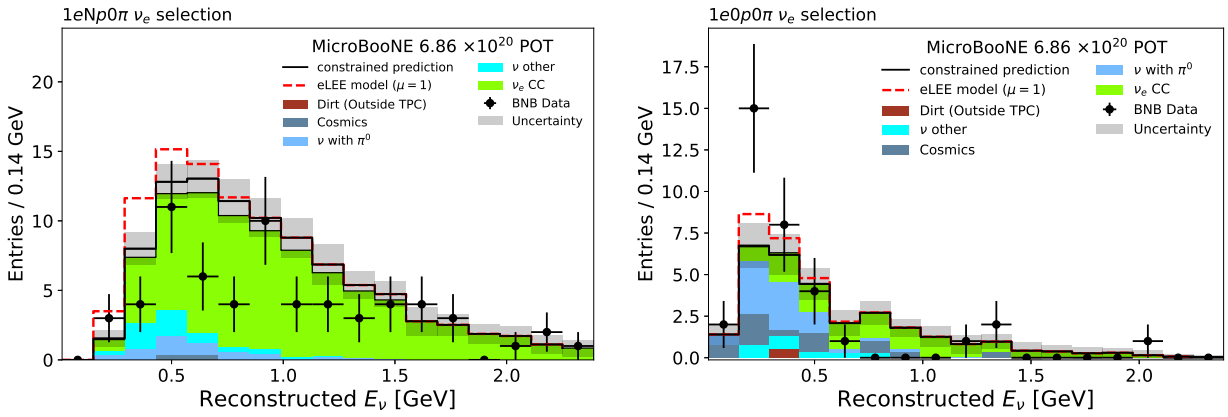

(a) $1e\mathrm{N}p0\pi$ **(b)** $1e0p0\pi$

Figure 10.1: Comparison between the data and the prediction in terms of reconstructed neutrino energy for the final $1e\mathrm{N}p0\pi$ and $1e0p0\pi$ selections. The pre-constrained prediction is shown broken down by the true interaction topology. The constrained prediction and the eLEE model are drawn in thick black lines and dashed red lines, respectively. The systematic uncertainties in the constrained prediction are shown as a shaded band.

isters 53 observed events with a prediction of 78.9 ± 11.6 events; this corresponds to a deficit of 1.7σ. Studying the kinematic variables of the $1e\mathrm{N}p0\pi$ events, this deficit appears to be affecting intermediate proton energies with forward-going showers. This is shown in Figure 10.2, where the final $1e\mathrm{N}p0\pi$ signal region is broken down in terms of the angle (θ) of the reconstructed electron candidate relative to the direction of the beam and the reconstructed kinematic energy of the highest-energy proton in the event.

On the contrary, the $1e0p0\pi$ channel shows good normalization agreement between observation and prediction in the 0.15–1.55 GeV range, with 31 data events observed and 27.8 ± 4.4 events predicted with the simulation underpredicting in the 0.15–0.43 GeV reconstructed neutrino energy range. Figure 10.3 shows the shower angle distributions for both the full reconstructed energy range and events in the 0.15–0.43 GeV range. In Figure 10.3a good agreement is observed between the data and the simulation for the full integrated energy range. Upon further inspection of the 0.15–0.43 GeV energy range, a deficit is observed for forward-going electrons ($\cos(\theta) > 0$) as shown in Figure 10.3b.

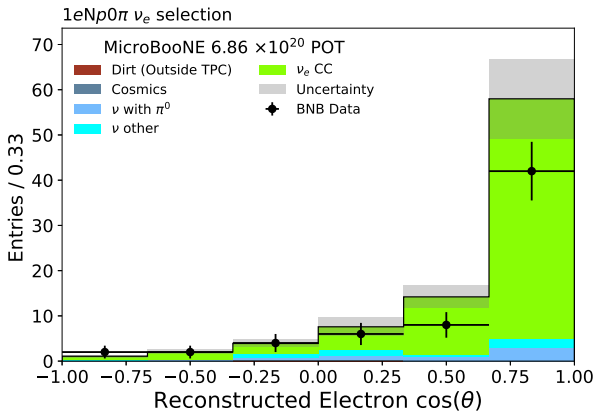

(a) Electron angle relative to beam direction.

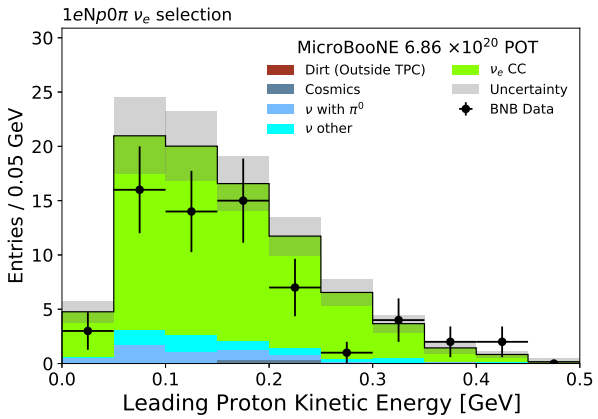

(b) Proton kinetic energy.

Figure 10.2: Selected kinematic distributions for events that pass the $1eNp0\pi$ selection. The expected events and uncertainties are shown as predicted by the intrinsic ν_e-only model.

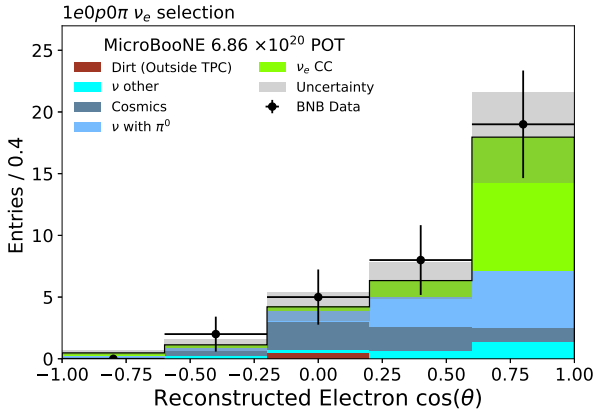

(a) All selected events.

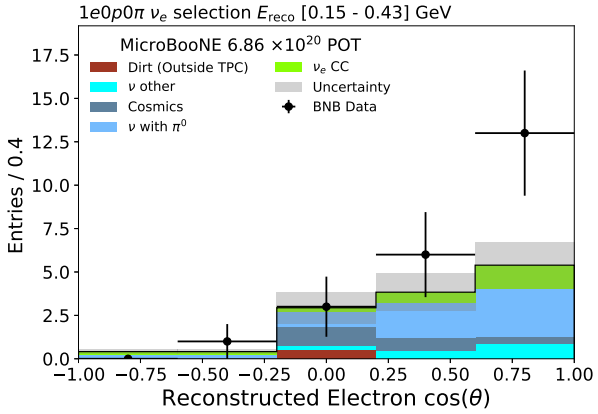

(b) Low-energy selected events from 0.15–0.43 GeV.

Figure 10.3: Selected $1e0p0\pi$ events as a function of the electron angle with respect to the beam. The expected events and uncertainties are shown without the ν_μ constraint applied.

10.3 Goodness-of-Fit Test

The goodness-of-fit (GoF) test is used to describe how well the intrinsic ν_e model fits the observed data. The test statistic used is the χ^2 described in Section 10.1. The GoF test is performed using frequentist calculations that compute the χ^2 metric over draws relying on the full covariance matrix and using the resulting toy experiment distributions to compute a p-value for the measurement obtained with the data. Approximately 10^6 toys are generated to build the χ^2 probability distributions.

For this test, higher values of χ^2 indicate a poorer agreement between observation and prediction. A p-value of the result can be calculated by looking at the probability that the χ^2 sampled from the distribution is greater than the observed value of χ^2. A lower calculated p-value indicates greater tension of the data with the tested model.

The results quantifying the agreement between the intrinsic ν_e model and the observed data in bins of reconstructed neutrino energy are shown in Table 10.1. The data are consistent with the intrinsic ν_e model, in the energy range of 0.15–1.55 GeV, with p-values of 0.182, 0.126 and 0.098, for the $1e\mathrm{N}p0\pi$ channel, $1e0p0\pi$ channel, and combined $1e\mathrm{N}p0\pi$ + $1e0p0\pi$ channels, respectively. Tensions in the model are driven primarily by the data deficit of the $1e\mathrm{N}p0\pi$ channel in the 0.64-0.78 GeV bins and the prediction deficit of the 0.14 GeV bin in the $1e0p0\pi$ selection. In general, the results show that the tension between the data and the intrinsic ν_e model is small for all three channels.

Table 10.1: Summary of χ^2 and p-value results for the goodness-of-fit tests for the intrinsic ν_e model. The p-values are computed with frequentist calculations based on toy experiments.

Channel	χ^2	χ^2/dof	p-value
$1e\mathrm{N}p0\pi$	15.2	1.52	0.182
$1e0p0\pi$	16.3	1.63	0.126
$1e\mathrm{N}p0\pi$ + $1e0p0\pi$	31.50	1.58	0.098

10.4 Simple Hypothesis Test

This is the first of two statistical tests to assess the probability that the eLEE model, introduced in Chapter 6, is consistent with the observed data. The simple hypothesis test provides a method to quantify the preference for observed data in a two-hypothesis scheme. In contrast to the GoF test introduced in the previous section, this test has a direct dependence of the eLEE hypothesis on the test statistic. In this test, the test statistic is $\Delta\chi^2$ and its defined by the following equation:

$$\Delta\chi^2 = \chi^2_{H_0} - \chi^2_{H_1} \tag{10.4}$$

where H_0 refers to the intrinsic ν_e only hypothesis and H_1 refers to the eLEE hypothesis. The test statistic $\chi^2_{H_0}$ is the GoF test statistic calculated for the intrinsic ν_e model and $\chi^2_{H_1}$ is the GoF statistic for the eLEE model. For this test, note that $\Delta\chi^2$ can take negative values. Approximately 10^6 toy experiments are used to generate the $\Delta\chi^2$ distributions according to each hypothesis. When calculating $\Delta\chi^2$ for the data, higher values indicate a preference for hypothesis H_1, while lower values give preference to H_0. Interpreting these results depends on the data $\Delta\chi^2$ and its comparison with the median of each $\Delta\chi^2$ distribution. A p-value is calculated given the fraction of toy experiments above the data $\Delta\chi^2$ for a given hypothesis. The p-value is calculated for hypotheses H_0 and H_1 with small values indicating tension with the tested model.

To gauge the sensitivity of the analysis, the simple hypothesis test can be used to rule out one hypothesis under the assumption that the alternative hypothesis is true. By generating toys under both hypotheses, producing $\Delta\chi^2$ distributions and calculating the median of each distribution, one can calculate the fraction of toys that the median under one hypothesis can be excluded assuming the other is true. The final sensitivities can be summarized as follows.

- The median significance of rejecting H_0 in favor of H_1, assuming that H_1 is true:
  - For the $1e\mathrm{N}p0\pi$ channel alone: p-value = 0.957
  - For the $1e0p0\pi$ channel alone: p-value = 0.759
  - For the combined channels: p-value = 0.968

- The median significance of rejecting H_1 in favor of H_0, assuming that H_0 is true:
  - For the $1e\text{N}p0\pi$ channel alone: p-value = 0.061
  - For the $1e0p0\pi$ channel alone: p-value = 0.249
  - For the combined channels: p-value = 0.049

This first set of results is statistically limited, and the median experiments show a weak ($\sim 1.5\sigma$) ability to separate the eLEE model from the intrinsic ν_e model. A higher median sensitivity is expected for the second wave of results presented by the MicroBooNE collaboration, as it will incorporate the full dataset of the experiment.

The expected sensitivities and the data results are presented in Figure 10.4 and summarized in Table 10.2. The observed $\Delta\chi^2$ between H_0 and H_1 are -3.89, 3.11 and -0.58 for the $1e\text{N}p0\pi$ channel, the $1e0p0\pi$ channel, and the combined channels, respectively. The $1e\text{N}p0\pi$ channel shows that the data have a p-value of 0.285 for the H_0 hypothesis, meaning that 28.5% of the H_0 distribution has a lower value than the observed $\Delta\chi^2$. On the other hand, the p-value for the data and the H_1 distribution is 0.021, which implies that the $1e\text{N}p0\pi$ channel excludes the H_1 hypothesis at the 97.9% confidence level (CL). In the $1e0p0\pi$ channel, the result is not clear. The observation shows that 0.072 of the H_1 distribution and 0.016 of the H_0 distribution are above the observed $\Delta\chi^2$. This indicates a slight preference for the H_1 model. Finally, the combined result is somewhere in the middle of the individual channels. Although it is primarily driven by the more sensitive $1e\text{N}p0\pi$ channel, the preference for the H_0 model is slightly hindered by the preference of the $1e0p0\pi$ channel for the H_1 model.

Table 10.2: Summary of the simple hypothesis tests.

Channel	obs. $\Delta\chi^2$	$\Delta\chi^2 <$ obs. p-value(H_0)	$\Delta\chi^2 <$ obs. p-value(H_1)	Sensitivity p-value(H_0) $\|H_1$	Sensitivity p-value(H_1) $\|H_0$
$1e\text{N}p0\pi$	-3.89	0.285	0.021	0.957	0.061
$1e0p0\pi$	3.11	0.984	0.928	0.759	0.249
$1e\text{N}p0\pi$ +$1e0p0\pi$	-0.58	0.748	0.145	0.968	0.049

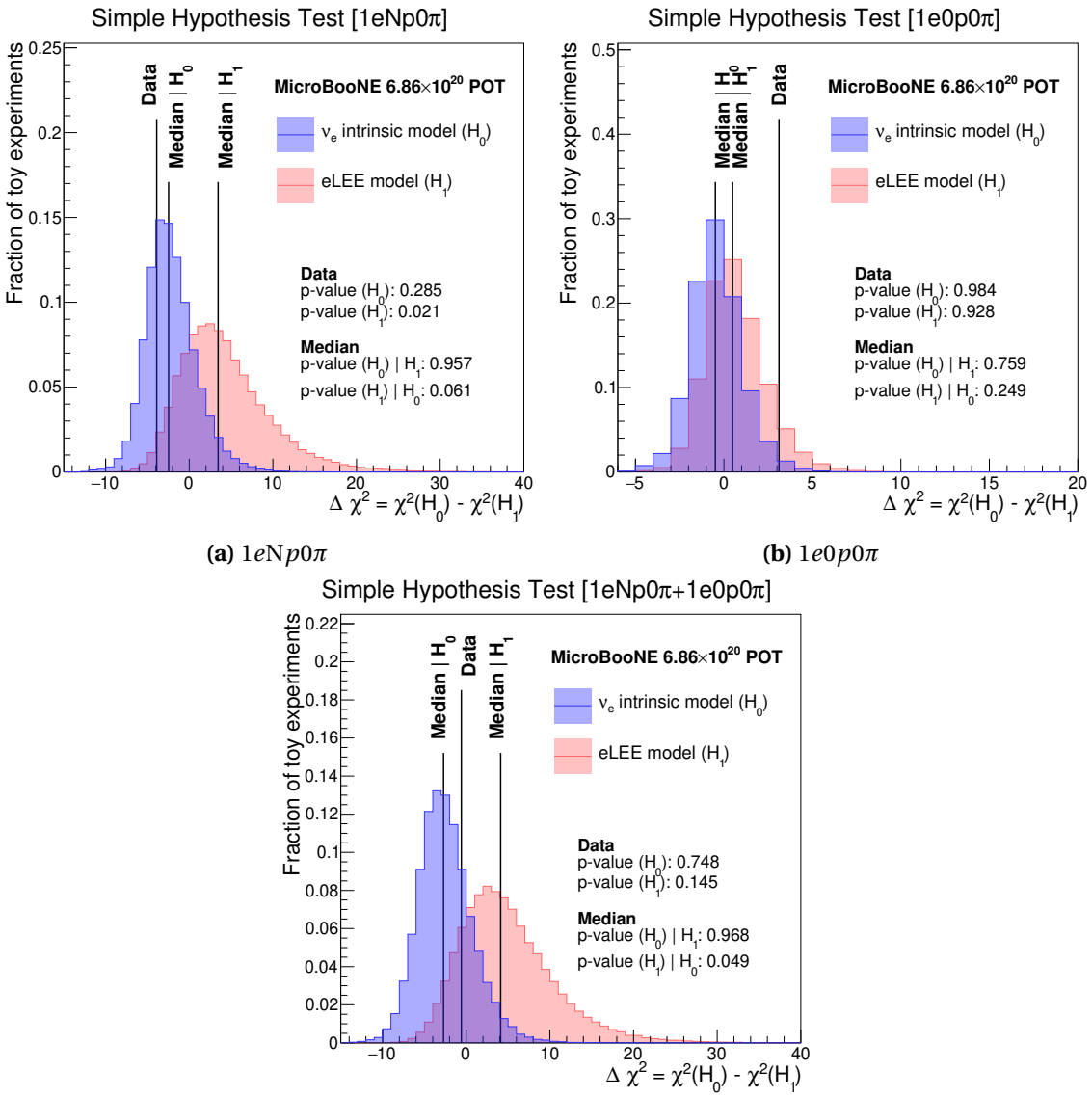

(a) $1e\mathrm{N}p0\pi$ **(b)** $1e0p0\pi$

(c) $1e\mathrm{N}p0\pi$ +$1e0p0\pi$

Figure 10.4: Results for the simple hypothesis test in $1e\mathrm{N}p0\pi$ (a), $1e0p0\pi$ (b), and combined (c) channels comparing each observation with the intrinsic ν_e only and eLEE hypotheses. The blue distribution is the test statistic $\Delta\chi^2$ under the H_0 hypothesis, and the red distribution shows the same for the H_1 hypothesis. The p-values indicate the fraction of toys with $\Delta\chi^2$ smaller than the observation, while the median p-values indicate the sensitivities.

10.5 Signal Strength Fit

The last statistical test performed is that of the signal strength fit, which is a method to find a normalization parameter μ that best fits the observed data in terms of the eLEE event prediction. This test also uses a Feldman-Cousins procedure [123] to calculate the confidence intervals in the measurement of the signal strength. The procedure starts by scaling a signal strength parameter μ relative to the median model so that, for the intrinsic ν_e only model, $\mu = 0$ and for the eLEE model, $\mu = 1$. Note that this range is not limited to two hypotheses, but to a whole spectrum of values. The goal of the fit is to find the signal strength value that minimizes χ^2 between the data and the prediction.

This test is performed on a grid where at each point a true signal strength value μ is enforced and around 10^4 toys are generated. Furthermore, the covariance matrix and the predicted spectrum are updated for the true value of μ at each gridpoint. The metric to define the ordering rule is based on the approximation of the likelihood ratio $R\left(x|\mu\right)$:

$$R\left(x|\mu\right) \sim \Delta\chi^2\left(x|\mu\right) = \chi^2(x,\mu) - \chi^2(x,\mu_{\mathrm{BF}}) \tag{10.5}$$

where μ_{BF} is the value of μ that maximizes the likelihood ratio for a given toy experiment x. At each gridpoint, toy experiments are used to build probability distributions of the $\Delta\chi^2\left(x|\mu\right)$ test statistic for fixed μ.

Subsequently, $\Delta\chi^2\left(\mathrm{data}|\mu\right)$ is calculated using the observed data spectrum and compared in the same vein as 10.5 at each of the gridpoints and the corresponding best-fit value for the signal strength is identified. The value of μ_{BF} that minimizes $\Delta\chi^2\left(x|\mu\right)$ is taken as the result of the fit. The confidence intervals are extracted by sampling the probability distribution of the toys and finding the fraction of $\Delta\chi^2\left(x|\mu\right)$ that is greater than $\Delta\chi^2\left(\mathrm{data}|\mu\right)$. Then a linear interpolation is used at each gridpoint to convert these probabilities into a continuous function $P(\mu)$ over the grid range. Confidence intervals for a given confidence level are then predetermined by probabilities that are greater than a determined confidence level α, such that $P(\mu) \geq \alpha$.

The result of the signal strength test is shown in Figure 10.5, where the black line shows the calculated value of $\Delta\chi^2(\text{data}|\mu)$ as a function of the true signal strength parameter μ; the red and blue dotted lines indicate the 90% CL for μ_{BF} corresponding to the data and the expected sensitivity for $\mu = 0$, respectively. Table 10.3 summarizes the results reported in this section.

An Asimov data set is used to test the expected sensitivity to $\mu = 0$. Unsurprisingly, $\mu_{\text{BF}} = 0$ was found for the $1e\text{N}p0\pi$, $1e0p0\pi$ and combined channels along with an 90% upper limit on μ of 1.16, 3.41 and 1.07, respectively; these values are used to report the sensitivity in constraining μ.

The final selection for the $1e\text{N}p0\pi$ channel yields $\mu_{\text{BF}} = 0$ with values of $\mu > 0.82$ excluded at the 90% CL. The data upper limit CL for the $1e\text{N}p0\pi$ channel is stronger than the expected limits if the intrinsic ν_e only model were true, shown in Figure 10.5a. This is a consequence of the data showing a deficit compared to the nominal ν_e prediction. The $1e0p0\pi$ channel reports $\mu_{\text{BF}} = 4$, with any values outside the range of $\mu \in [1.13, 15.01]$ being excluded at the 90% CL. However, while the $1e0p0\pi$ channel shows a preference for four times the eLEE, the wide range of values within the 90% CL makes it a less sensitive channel to the eLEE model. Finally, μ_{BF} for the combined channel data is 0.36 with $\mu > 1.57$ excluded at the 90% CL.

Table 10.3: Best-fit eLEE model signal strength (μ) and 90% confidence intervals. The sensitivity is quantified by reporting the expected upper limits, assuming $\mu = 0$.

Channel	Data μ_{BF}	Data 90% CL interval on μ	Sensitivity 90% upper limit on μ
$1e\text{N}p0\pi$	0.00	[0.00 , 0.82]	1.16
$1e0p0\pi$	4.00	[1.13 , 15.01]	3.41
$1e\text{N}p0\pi + 1e0p0\pi$	0.36	[0.00 , 1.57]	1.07

10.6 Discussion

To summarize the results, this analysis measured the ν_e content of the BNB in the form of two orthogonal ν_e channels using the MicroBooNE detector to address the MiniBooNE LEE anomaly. The ν_e channels used in this analysis are the $1e\text{N}p0\pi$ channel and the $1e0p0\pi$ chan-

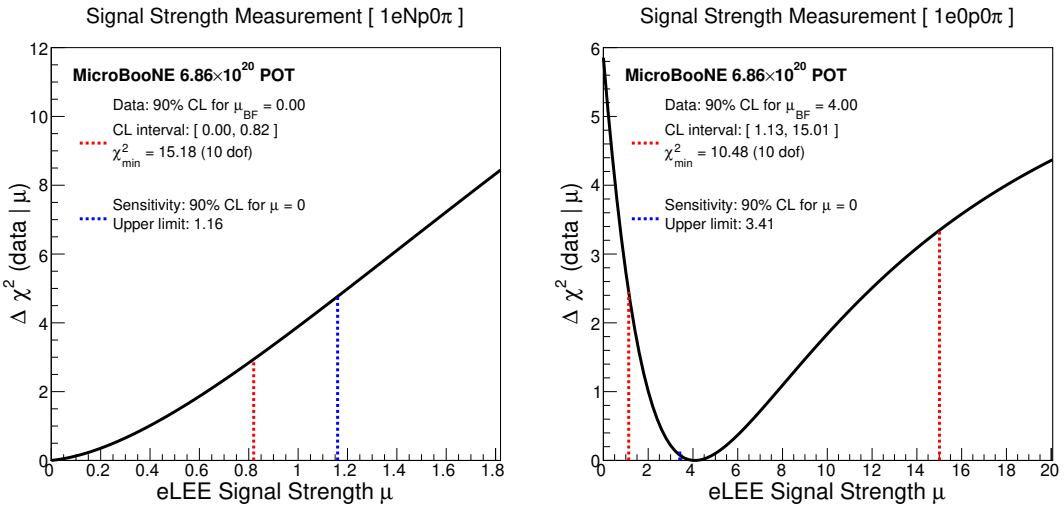

(a) $1eNp0\pi$ **(b)** $1e0p0\pi$

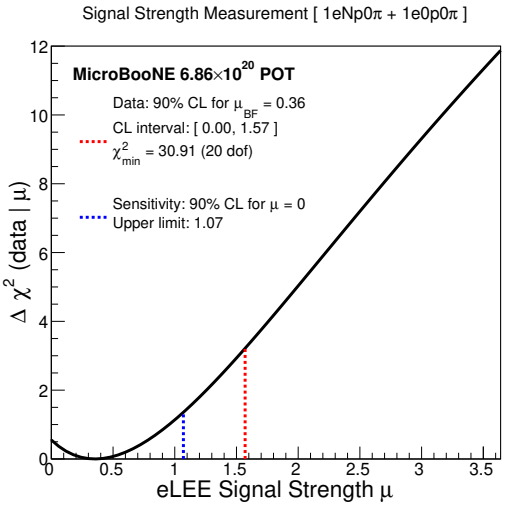

(c) $1eNp0\pi + 1e0p0\pi$

Figure 10.5: Results for the signal strength test in the $1eNp0\pi$ (a), $1e0p0\pi$ (b), and combined (c) channels. The value of $\Delta\chi^2$ as a function of the signal strength is evaluated with respect to the best-fit signal strength value. The observed confidence interval at the 90% confidence level are indicated with vertical lines, as well as the expected upper limit in the case of no signal.

nel. The signal model tested is that of the unfolded MiniBooNE LEE over the true neutrino energy under the assumption that the excess is caused by an anomalous number of true ν_e interactions. The $1e\text{N}p0\pi$ selection shows 64 candidate events with a predicted number of 86 ± 11.5 events for the intrinsic ν_e only hypothesis and the $1e0p0\pi$ channel selection shows 34 candidate events with 30.1 ± 4.3 predicted events. The GoF test showed consistency with the nominal ν_e model with p-values of 9.8%–18.2% in the reconstructed neutrino energy range 0.15–1.55 GeV. The simple hypothesis test disfavored the eLEE model at the 97.9% CL in the $1e\text{N}p0\pi$ channel. The combination of $1e\text{N}p0\pi$ and $1e0p0\pi$ channels does not indicate a strong preference for either of the two hypotheses. Finally, the signal strength fit of the LEE gives a best fit, μ_{BF}, of 0.00, 4.00 and 0.36 for the $1e\text{N}p0\pi$, $1e0p0\pi$ and the combined channels, respectively. Both channels individually reject the eLEE hypothesis at the 90% CL level. The $1e\text{N}p0\pi$ channel drives the analysis sensitivity with higher statistics and a purer selection that shows a preference for the nominal ν_e prediction over the eLEE hypothesis, rejecting any values above $\mu = 0.82$ at the 90% CL. The $1e0p0\pi$ channel is less sensitive and accepts a wide range of values of μ, but has a lower bound of $\mu = 1.13$. The results of this thesis favor the intrinsic ν_e only BNB model and are inconsistent with the measurement of an excess of ν_e interactions in the LEE energy range and overall disfavor an excess of ν_e events for the MiniBooNE LEE.

Beyond the results of this analysis, the MicroBooNE collaboration worked on more measurements of low-energy ν_e interactions. MicroBooNE has reported other LEE results focusing on a ν_e LEE hypothesis for the anomaly reported by MiniBooNE [25] using different channels and reconstruction paradigms. Figure 10.6 shows the ratio of observation to prediction in the LEE energy range for each analysis/channel. The analysis of this thesis covers the $1e\text{N}p0\pi$ and $1e0p0\pi$ channels [18], featured in the center two bins of the plot. The plot also features results from the exclusive charged-current quasi-elastic (CCQE) $1e1p$ selection done using a deep learning approach [124] and the $1eX$ selection using the tomographic reconstruction paradigm known as Wire-Cell [125]. Similar to the case of $1e\text{N}p0\pi$, the CCQE $1e1p$ and inclusive $1eX$ selections also observe a deficit in the data compared to the prediction, indicating an underlying

systematic origin across the different MicroBooNE eLEE analyses. This deficit of events is not seen in the less-sensitive $1e0p0\pi$ channel. Taken together, the three analyses disfavor the eLEE signal model [25]. Moreover, the results of both the $1eNp0\pi$ and $1e0p0\pi$ selections on NuMI data with their associated systematic uncertainties and the sideband studies (see Section 8.3) performed to validate this analysis provide further confidence in the final results presented in this thesis.

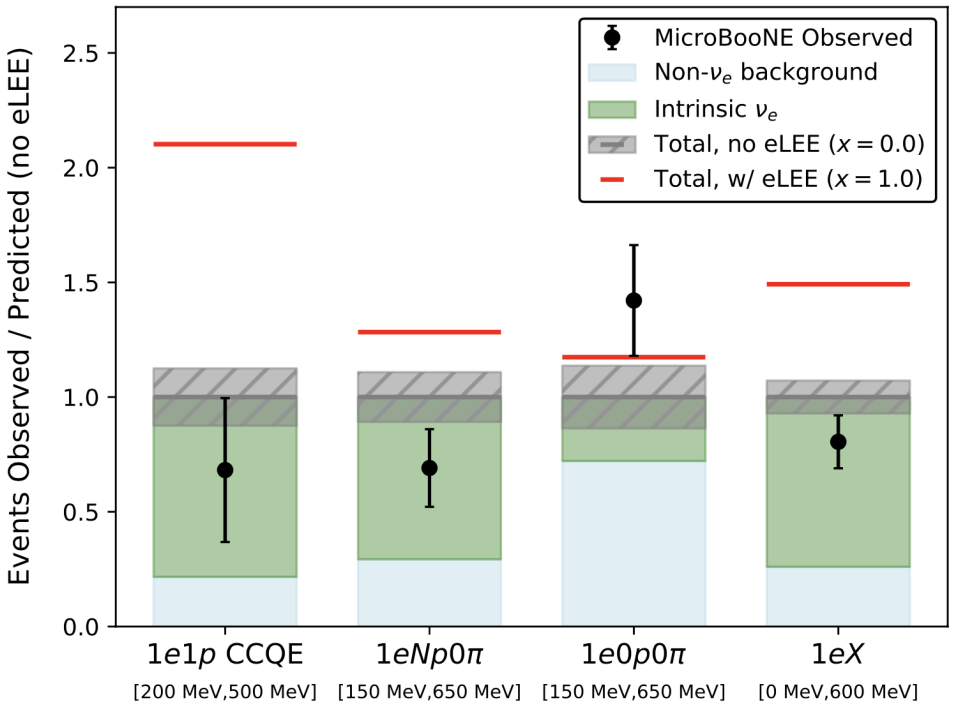

Figure 10.6: Ratio of observed to predicted ν_e CC candidate events for the hypothesis of no eLEE for each LEE analysis' signal energy region. Constrained systematic uncertainties are shown in gray, the intrinsic ν_e content is shown in green, and all non-ν_e backgrounds are shown in light blue. The predicted eLEE signal is colored red [25].

Chapter 11

Conclusions

This thesis presents the main results of MicroBooNE's analysis to address the MiniBooNE low-energy excess (LEE) anomaly by searching for an excess of charged-current (CC) electron neutrino interactions without pions in the final state in 6.67×10^{20} POT of Booster Neutrino Beam (BNB) data taken over a run period of about three years. This is part of a set of analyses that aim to address the LEE using different final-state interactions and reconstruction strategies [18, 25, 124, 125]. This analysis leverages the Pandora multi-algorithmic reconstruction tool set [20] and takes advantage of scintillation light and detailed calorimetric and spatial information from the MicroBooNE TPC in order to make a kinematically agnostic measurement to target CC electron neutrino interactions with the $1e\mathrm{N}p0\pi$ and $1e0p0\pi$ final state topologies. Although the product is a robust measurement across a wide energy range, the final selections and analysis-level choices were tailored to be sensitive to low-energy electron neutrinos, focusing in the sub-GeV energy region, making the analysis sensitive to anomalies similar to those observed by the MiniBooNE experiment. The reconstruction tools used in this analysis were extensively validated using a dedicated ν_μ, NuMI ν_e, π^0 and two+ shower sideband selections. The result of this analysis does not find an excess of electron neutrino candidates in the sub-GeV energy region, and, in fact, a slight deficit is observed compared to the intrinsic ν_e prediction of the BNB. The goodness-of-fit test showed that the data are consistent with the intrinsic ν_e only hypothesis with p-values of 9.8–18.2%. Two additional statistical tests were performed to gauge the preference of data for the intrinsic ν_e only hypothesis or the presence of the LEE that comes from an anomalous number of electron neutrinos in addition to the intrinsic ν_e content from the BNB (eLEE). The first of these tests carried out was the simple hypothesis test, which excluded the eLEE model at the 97.9% confidence level (CL). The second statistical test was the

signal strength fit, which found that an eLEE scaling of the data was $\mu < 1.57$ for the combined $1e\mathrm{N}p0\pi$ + $1e0p0\pi$ channels, with the $1e\mathrm{N}p0\pi$ channel alone leading to an upper bound of $\mu < 0.82$ in the 90% CL. Overall, these results disfavor the assumption that the LEE was mainly due to electron neutrino interactions.

In addition to the analysis presented in this thesis, MicroBooNE also made other analyses looking at different ν_e final-state topologies and using different reconstruction tools [18, 124, 125]. The results of these analyses are summarized in [25], which came to a similar conclusion as the analysis presented in this thesis. In addition to the eLEE analyses, MicroBooNE also explored the hypothesis of a photon excess for the LEE [126]. The photon search looked at neutral current Δ radiative decays with single photons in the final state, which is a Standard Model process predicted to have a branching ratio of $\sim 0.6\%$. The model explored was an enhanced rate of $\Delta \rightarrow N\gamma$ events, where N is a nucleon and γ is a single photon. This enhancement was found to be disfavored as the sole explanation of the MiniBooNE LEE at the 94.8% CL. All four analyses, the three looking for the electron neutrino excess and the one looking for the photon excess, have found no plausible source for the MiniBooNE LEE.

Even though both the photon and electron neutrino explanations for the LEE in MicroBooNE are disfavored, it leaves open the possibility for a sterile neutrino in a $3+1$ model as tenable for certain choice of oscillation parameters and is currently being investigated. Models beyond the Standard Model are also being explored, such as dark sector models where novel particles are created either in the beamline (at the target or via decay of mesons), or directly at the detector by neutrino up-scattering producing signals similar to those producing the LEE [127,128]. MicroBooNE is also part of the Short Baseline Neutrino (SBN) Program [13], which is ramping up its three-LArTPC-detector approach to resolve short baseline neutrino anomalies. The SBN Program is strategically poised to perform sensitive searches for ν_e appearance and ν_μ disappearance in the BNB and shed further insight on the MiniBooNE LEE.

Bibliography

[1] I. Esteban, M. C. Gonzalez-Garcia, M. Maltoni, T. Schwetz, and A. Zhou. “The fate of hints: updated global analysis of three-flavor neutrino oscillations”. *Journal of High Energy Physics*, 2020(9), 2020. vii, 27

[2] A. A. Aguilar-Arevalo et al. (MiniBooNE Collaboration). “Neutrino flux prediction at MiniBooNE”. *Physical Review D*, 79(7), 2009. vii, xi, 56, 58, 59, 60, 66, 67

[3] The MicroBooNE Collaboration. “Booster Neutrino Flux Prediction at MicroBooNE”. *MICROBOONE-NOTE-1031-PUB*, 2018. vii, xiii, 78, 105, 106, 138

[4] J. A. Formaggio and G. P. Zeller. “From eV to GeV: Neutrino cross sections across energy scales”. *Reviews of Modern Physics*, 84(3), 2012. ix, 9

[5] M. Agostini et al. “Comprehensive measurement of pp-chain solar neutrinos”. *Nature*, 562(7728), 2018. ix, 19, 20

[6] T. Kajita. “Atmospheric neutrinos and discovery of neutrino oscillations”. *Proceedings of the Japan Academy Series B: Physical and Biological Sciences*, 86(4), 2010. ix, 20, 21, 22

[7] X. Qian and J. C. Peng. “Physics with reactor neutrinos”. *Reports on Progress in Physics*, 82(3), 2019. ix, 21, 23

[8] P. Gando et al. “White paper: CeLAND - Investigation of the reactor antineutrino anomaly with an intense 144Ce-144Pr antineutrino source in KamLAND". *arXiv:1309.6805*, 2013. ix, 22, 24

[9] T. Katori and J. M. Conrad. “Beyond standard model searches in the MiniBooNE experiment”. *Advances in High Energy Physics*, 2015(1), 2015. ix, 30

[10] S. Kubota, M. Hishida, M. Suzuki, and J. Ruan(Gen). "dynamical behavior of free electrons in the recombination process in liquid argon, krypton, and xenon". *Phys. Rev. B*, 20, 1979. x, 35

[11] R. Acciarri et al. (MicroBooNE Collaboration). "Design and construction of the MicroBooNE detector". *Journal of Instrumentation*, 12(02):P02017–P02017, 2017. x, 37

[12] B. Abi et al. (DUNE Collaboration). "Deep Underground Neutrino Experiment (DUNE), Far Detector Technical Design Report, Volume II: DUNE Physics", 2020. x, 41, 51

[13] R. Acciarri et al. (SBN Collaboration). "A proposal for a three detector short-baseline neutrino oscillation program in the Fermilab Booster Neutrino Beam". *arXiv:1503.01520*, 2015. xi, 59, 167

[14] C. Adams et al. (MicroBooNE Collaboration). "Rejecting cosmic background for exclusive charged current quasi elastic neutrino interaction studies with Liquid Argon TPCs; a case study with the MicroBooNE detector". *European Physical Journal C*, 79(8), 2019. xi, 63

[15] R. Acciarri et al. (MicroBooNE Collaboration). "Noise Characterization and Filtering in the MicroBooNE Liquid Argon TPC". *Journal of Instrumentation*, 12(08):P08003, 2017. xi, xii, 65, 81, 83

[16] C. Adams et al. (MicroBooNE Collaboration). "Design and construction of the MicroBooNE Cosmic Ray Tagger system". *Journal of Instrumentation*, 14(04), 2019. xi, 68

[17] The MicroBooNE Collaboration. "MicroBooNE low-energy excess signal prediction from unfolding MiniBooNE Monte-Carlo and data". *MICROBOONE-NOTE-1043-PUB*, 2018. xi, 73

[18] P. Abratenko et al. (MicroBooNE Collaboration). "Search for an anomalous excess of charged-current ν_e interactions without pions in the final state with the MicroBooNE experiment". *Phys. Rev. D*, 105, 2022. xii, 71, 75, 164, 166, 167

[19] C. Adams et al. (MicroBooNE Collaboration). "Ionization electron signal processing in single phase LArTPCs. Part I. Algorithm Description and quantitative evaluation with MicroBooNE simulation". *Journal of Instrumentation*, 13(7), 2018. xii, 80, 82, 85, 86

[20] R. Acciarri et al. (MicroBooNE Collaboration). "The Pandora multi-algorithm approach to automated pattern recognition of cosmic-ray muon and neutrino events in the MicroBooNE detector". *European Physical Journal C*, 78(1), 2018. xii, 76, 86, 89, 90, 166

[21] C. Adams et al. (MicroBooNE Collaboration). "Calibration of the charge and energy loss per unit length of the MicroBooNE liquid argon time projection chamber using muons and protons". *Journal of Instrumentation*, 15(03):P03022, 2020. xii, 91, 92, 94

[22] P. Abratenko et al. (MicroBooNE Collaboration). "Calorimetric classification of track-like signatures in liquid argon TPCs using MicroBooNE data". *Journal of High Energy Physics*, 2021(12):153, 2021. xii, 95, 96

[23] P. Abratenko et al. (MicroBooNE Collaboration). "New CC0π GENIE model tune for MicroBooNE". *Phys. Rev. D*, 105:072001, 2022. xiii, 105, 106

[24] "XGBoost documentation". xiii, 118, 121

[25] P. Abratenko et al. (MicroBooNE Collaboration). "Search for an Excess of Electron Neutrino Interactions in MicroBooNE Using Multiple Final-State Topologies". *Phys. Rev. Lett.*, 128:241801, 2022. xv, 71, 164, 165, 166, 167

[26] Laurie M. Brown. "The idea of the neutrino". *Physics Today*, 31(9):23–28, 1978. 4

[27] G. Aad et al. "Observation of a new particle in the search for the Standard Model Higgs boson with the ATLAS detector at the LHC". *Physics Letters, Section B: Nuclear, Elementary Particle and High-Energy Physics*, 716(1):1–29, 2012. 5

[28] F. Reines, C. L. Cowan, F. B. Harrison, A. D. McGuire, and H. W. Kruse. "Detection of the free antineutrino". *Physical Review*, 117(1):159–173, 1960. 6

[29] M. Ahmed et al. “Search for the lepton-family-number nonconserving decay $\mu^+ \rightarrow e^+\gamma$”. *Physical Review D*, 65(11):1–31, 2002. 7

[30] M. Aker et al. “Improved Upper Limit on the Neutrino Mass from a Direct Kinematic Method by KATRIN”. *Physical Review Letters*, 123(22):221802, 2019. 7

[31] B. Pontecorvo. “Electron and Muon Neutrinos”. *Zh. Eksp. Teor. Fiz.*, 37:1751–1757, 1959. 9, 23

[32] Raymond Davis. "A review of the homestake solar neutrino experiment". *Progress in Particle and Nuclear Physics*, 32:13–32, 1994. 11

[33] M. Nakahata et al. “Super-Kamiokande”. *Nuclear Physics B - Proceedings Supplements*, 87(1-3):125–134, 2000. 11

[34] Q.R. Ahmad et al. “Direct Evidence for Neutrino Flavor Transformation from Neutral-Current Interactions in the Sudbury Neutrino Observatory”. *Physical Review Letters*, 89(1):1–6, 2002. 11

[35] Andre de Gouvea. “2004 TASI Lectures on Neutrino Physics”. pages 1–62, 2004. 11

[36] B. Pontecorvo. “Neutrino Experiments and the Question of Leptonic-Charge Conservation". *Old and New Problems in Elementary Particles*, 26(5):251–261, 1968. 14

[37] Z. Maki, M. Nakagawa, and S. Sakata. “Remarks on the Unified Model of Elementary Particles”. *Progress of Theoretical Physics*, 28(5):870–880, 1962. 14

[38] J. A. Bagger et al. “Precision electroweak measurements on the Z resonance”. *Physics Reports*, 427(5-6):257–454, 2006. 15

[39] S. Gariazzo, C. Giunti, M. Laveder, Y. F. Li, and E. M. Zavanin. “Light sterile neutrinos”. *Journal of Physics G: Nuclear and Particle Physics*, 43(3), 2016. 15

[40] G. H. Collin, C. A. Argüelles, J. M. Conrad, and M. H. Shaevitz. "Sterile neutrino fits to short baseline data". *Nuclear Physics B*, 908:354–365, 2016. 16

[41] R. L. Workman and Others. Review of Particle Physics. *PTEP*, 2022:083C01, 2022. 18

[42] K Abe et al. "Atmospheric neutrino oscillation analysis with external constraints in Super-Kamiokande I-IV". *Physical Review D*, 97(7):72001, 2018. 21

[43] M. G. Aartsen et al. "Measurement of Atmospheric Neutrino Oscillations at 6-56 GeV with IceCube DeepCore". *Physical Review Letters*, 120(7):71801, 2018. 21

[44] M. G. Aartsen et al. "Measurement of atmospheric tau neutrino appearance with IceCube DeepCore". *Physical Review D*, 99(3):32007, 2019. 21

[45] Patrick Huber. "Determination of antineutrino spectra from nuclear reactors". *Physical Review C - Nuclear Physics*, 84(2):1–16, 2011. 22

[46] Th A. Mueller, D. Lhuillier, M. Fallot, A. Letourneau, S. Cormon, M. Fechner, L. Giot, T. Lasserre, J. Martino, G. Mention, A. Porta, and F. Yermia. "Improved predictions of reactor antineutrino spectra". *Physical Review C - Nuclear Physics*, 83(5):1–17, 2011. 22

[47] G. Mention, M. Fechner, Th Lasserre, Th A. Mueller, D. Lhuillier, M. Cribier, and A. Letourneau. "Reactor antineutrino anomaly". *Physical Review D - Particles, Fields, Gravitation and Cosmology*, 83(7):1–20, 2011. 22

[48] Phys Bev, J Willis, P C Stein, and M Schwartz. J. j. j. 4(6):5–6, 1960. 23

[49] J M Gaillard. "The brookhaven neutrino experiment: Lecture 4". 1963. 23

[50] P. Adamson et al. "Combined analysis of ν_μ disappearance and $\nu_\mu \rightarrow \nu_e$ appearance in MINOS using accelerator and atmospheric neutrinos". *Physical Review Letters*, 112(19):1–6, 2014. 25

[51] I. Esteban, M. C. Gonzalez-Garcia, M. Maltoni, I. Martinez-Soler, and Thomas Schwetz. "Updated fit to three neutrino mixing: exploring the accelerator-reactor complementarity". *Journal of High Energy Physics*, 2017(1), 2017. 26

[52] S. S. Chatterjee and A. Palazzo. "Resolving the NOvA and T2K tension in the presence of Neutrino Non-Standard Interactions". *PoS*, NuFact2021:059, 2022. 26

[53] K. Abe et al. "Physics potential of a long-baseline neutrino oscillation experiment using a J-PARC neutrino beam and Hyper-Kamiokande". *Progress of Theoretical and Experimental Physics*, 2015(5), 2015. 26

[54] The LBNF and Dune Projects. "Long-Baseline Neutrino Facility (LBNF) and Deep Underground Neutrino Experiment (DUNE) Conceptual Design Report Volume 1 : The LBNF and DUNE Projects". 1. 26

[55] K. N. Abazajian et al. "Light Sterile Neutrinos: A White Paper". 2012. 27

[56] A. A. Aguilar-Arevalo et al. (MiniBooNE Collaboration). "Evidence for neutrino oscillations from the observation of $\bar{\nu}_e$ appearance in a $\bar{\nu}_\mu$ beam". *Physical Review D - Particles, Fields, Gravitation and Cosmology*, 64(11):22, 2001. 27

[57] A. A. Aguilar-Arevalo et al. (MiniBooNE Collaboration). "Updated MiniBooNE neutrino oscillation results with increased data and new background studies". *Physical Review D*, 103(5):52002, 2021. 29, 72

[58] A. A. Aguilar-Arevalo et al. (MiniBooNE Collaboration). "Significant Excess of Electronlike Events in the MiniBooNE Short-Baseline Neutrino Experiment". *Physical Review Letters*, 121(22):221801, 2018. 30

[59] A. A. Aguilar-Arevalo et al. (MiniBooNE Collaboration). "Measurement of ν_μ and ν_μ induced neutral current single π^0 production cross sections on mineral oil at $E_\nu \sim 0$ (1 GeV)". *Physical Review D - Particles, Fields, Gravitation and Cosmology*, 81(1):1–14, 2010. 31

[60] Jay N. Marx and David R. Nygren. "The Time Projection Chamber". *Physics Today*, 31N10(1):46–53, 1978. 32

[61] T. Doke, K. Masuda, and E. Shibamura. "Estimation of absolute photon yields in liquid argon and xenon for relativistic (1 MeV) electrons". *Nuclear Instruments and Methods in Physics Research Section A: Accelerators, Spectrometers, Detectors and Associated Equipment*, 291(3):617–620, 1990. 33

[62] O. Bunemann, T. E. Cranshaw, and J. A. Harvey. "Design of Grid Ionization Chambers". *Canadian Journal of Research*, 27a(5):191–206, 1949. 37

[63] B. Abi et al. (DUNE Collaboration). "The Single-Phase ProtoDUNE Technical Design Report". *arXiv:1706.07081*, 2017. 40

[64] R. Acciarri et al. (SBN Program). "A Proposal for a Three Detector Short-Baseline Neutrino Oscillation Program in the Fermilab Booster Neutrino Beam", 2015. 44

[65] B. Baller. "TrajCluster Users Guide". 51, 114

[66] M. Antonello (ICARUS Collaboration) et al. "Experimental observation of an extremely high electron lifetime with the ICARUS-T600 LAr-TPC". *Journal of Instrumentation*, 9(12), 2014. 51

[67] The MicroBooNE Collaboration. "Single differential ν_μ charged-current cross section with the MicroBooNE detector using the Cosmic Ray Tagger". *MICROBOONE-NOTE-1069-PUB*, 2020. 55

[68] P. Abratenko et al. (MicroBooNE Collaboration). "First Measurement of Inclusive Muon Neutrino Charged Current Differential Cross Sections on Argon at $E_\nu \sim 0.8$ GeV with the MicroBooNE Detector". *Phys. Rev. Lett.*, 123:131801, 2019. 55

[69] C Adams et al. "Comparison of ν_μ−Ar multiplicity distributions observed by MicroBooNE to GENIE model predictions". *The European Physical Journal C*, 79(3):248, 2019. 55

[70] P. Abratenko et al. (MicroBooNE Collaboration). "First Measurement of Differential Charged Current Quasielasticlike ν_μ-Argon Scattering Cross Sections with the MicroBooNE Detector". *Phys. Rev. Lett.*, 125:201803, 2020. 55

[71] P. Abratenko et al. (MicroBooNE Collaboration). "Measurement of differential cross sections for ν_μ-Ar charged-current interactions with protons and no pions in the final state with the MicroBooNE detector". *Phys. Rev. D*, 102:112013, 2020. 55

[72] C. Adams et al. (MicroBooNE Collaboration). "First measurement of ν_μ charged-current π^0 production on argon with the MicroBooNE detector". *Phys. Rev. D*, 99:091102, 2019. 55

[73] The MicroBooNE Collaboration. "Selection of charged-current neutrino-induced K^+ production interactions in MicroBooNE". *MICROBOONE-NOTE-1071-PUB*, 2020. 55

[74] The MicroBooNE Collaboration. "Measurement of Low-Q^2 Protons from Neutral Current Events in Argon with MicroBooNE". *MICROBOONE-NOTE-1067-PUB*, 2020. 55

[75] J I Crespo-Anadón on behalf of the MicroBooNE Collaboration. "The MicroBooNE continuous readout stream for detection of supernova neutrinos". *Journal of Physics: Conference Series*, 1312(1):012006, 2019. 56

[76] P. Abratenko et al. (MicroBooNE Collaboration). "Search for heavy neutral leptons decaying into muon-pion pairs in the MicroBooNE detector". *Phys. Rev. D*, 101:052001, 2020. 56

[77] P. Abratenko et al. (MicroBooNE Collaboration). "Search for a Higgs Portal Scalar Decaying to Electron-Positron Pairs in the MicroBooNE Detector". *Phys. Rev. Lett.*, 127:151803, 2021. 56

[78] The MicroBooNE Collaboration. "Study of Reconstructed ^{39}Ar Beta Decays at the MicroBooNE Detector". *MICROBOONE-NOTE-1050-PUB*, 2018. 56

[79] P. Abratenko (MicroBooNE Collaboration) et al. "Measurement of space charge effects in the MicroBooNE LArTPC using cosmic muons". *Journal of Instrumentation*, 15(12):P12037–P12037, 2020. 62, 80, 90, 145

[80] A. A. Aguilar-Arevalo et al. (MiniBooNE Collaboration). "Significant Excess of Electron-like Events in the MiniBooNE Short-Baseline Neutrino Experiment". *Phys. Rev. Lett.*, 121:221801, 2018. 72

[81] Chia-Hung Vincent Chang, Chuan-Ren Chen, Shu-Yu Ho, and Shih-Yen Tseng. "Explaining the MiniBooNE anomalous excess via a leptophilic ALP-sterile neutrino coupling". *Phys. Rev. D*, 104:015030, 2021. 74, 125

[82] Asli Abdullahi, Matheus Hostert, and Silvia Pascoli. "A dark seesaw solution to low energy anomalies: MiniBooNE, the muon (g-2), and BaBar". *Physics Letters B*, 820:136531, 2021. 74, 125

[83] Luis Alvarez-Ruso and Eduardo Saul-Sala. "Radiative decay of heavy neutrinos at MiniBooNE and MicroBooNE", 2017. 74, 125

[84] Xiangpan Ji, Wenqiang Gu, Xin Qian, Hanyu Wei, and Chao Zhang. "Combined Neyman–Pearson chi-square: An improved approximation to the Poisson-likelihood chi-square". *Nuclear Instruments and Methods in Physics Research Section A: Accelerators, Spectrometers, Detectors and Associated Equipment*, 961:163677, 2020. 76, 153

[85] A. A. Aguilar-Arevalo et al. (MiniBooNE Collaboration). "Neutrino flux prediction at MiniBooNE". *Phys. Rev. D*, 79:072002, 2009. 78, 138

[86] C. Andreopoulos, C. Barry, S. Dytman, H. Gallagher, T. Golan, R. Hatcher, G. Perdue, and J. Yarba. "The GENIE Neutrino Monte Carlo Generator: Physics and User Manual". 2015. 78, 141

[87] C. Andreopoulos, A. Bell, D. Bhattacharya, F. Cavanna, J. Dobson, S. Dytman, H. Gallagher, P. Guzowski, R. Hatcher, P. Kehayias, A. Meregaglia, D. Naples, G. Pearce, A. Rubbia,

M. Whalley, and T. Yang. “The GENIE neutrino Monte Carlo generator”. *Nuclear Instruments and Methods in Physics Research Section A: Accelerators, Spectrometers, Detectors and Associated Equipment*, 614(1):87–104, 2010. 78

[88] Alvarez-Ruso et al. (GENIE Collaboration). “Recent highlights from GENIE v3”. *European Physical Journal: Special Topics*, 230(24):4449–4467, 2021. 78

[89] J. Tena-Vidal et al. (GENIE Collaboration). “Neutrino-nucleon cross-section model tuning in GENIE v3”. *Phys. Rev. D*, 104:072009, 2021. 78

[90] J. Nieves, I. Ruiz Simo, and M.J. Vicente Vacas. “The nucleon axial mass and the MiniBooNE quasi-elastic neutrino–nucleus scattering problem”. *Physics Letters B*, 707(1):72–75, 2012. 78

[91] J. Nieves, J. E. Amaro, and M. Valverde. “Inclusive quasielastic charged-current neutrino-nucleus reactions”. *Phys. Rev. C*, 70:055503, 2004. 78, 79

[92] R. Gran, J. Nieves, F. Sanchez, and M. J. Vicente Vacas. “Neutrino-nucleus quasi-elastic and 2p2h interactions up to 10 GeV”. *Phys. Rev. D*, 88:113007, 2013. 78

[93] P. Abratenko et al. (MicroBooNE Collaboration). “New GENIE model tune for MicroBooNE”. *Physical Review D*, 105(7), 2022. 78, 79, 141

[94] R.C. Carrasco and E. Oset. “Interaction of real photons with nuclei from 100 to 500 MeV”. *Nuclear Physics A*, 536(3):445–508, 1992. 78

[95] Ch. Berger and L. M. Sehgal. “Lepton mass effects in single pion production by neutrinos”. *Phys. Rev. D*, 76:113004, 2007. 79

[96] A. Bodek and U.K. Yang. “Modeling deep inelastic cross sections in the few GeV region”. *Nuclear Physics B - Proceedings Supplements*, 112(1):70–76, 2002. 79

[97] S. Agostinelli et al. (GEANT4 Collaboration). "Geant4—a simulation toolkit". *Nuclear Instruments and Methods in Physics Research Section A: Accelerators, Spectrometers, Detectors and Associated Equipment*, 506(3):250–303, 2003. 79

[98] R. Acciarri et al. (MicroBooNE Collaboration). "A study of electron recombination using highly ionizing particles in the ArgoNeuT Liquid Argon TPC". *Journal of Instrumentation*, 8(08):P08005, 2013. 80, 93, 94

[99] M. Mooney. "The MicroBooNE Experiment and the Impact of Space Charge Effects". 2015. 80

[100] C. Adams et al. (MicroBooNE Collaboration). "A method to determine the electric field of liquid argon time projection chambers using a UV laser system and its application in MicroBooNE". *Journal of Instrumentation*, 15(07):P07010–P07010, 2020. 80, 90, 145

[101] P. Abratenko (MicroBooNE Collaboration) et al. "Measurement of the longitudinal diffusion of ionization electrons in the MicroBooNE detector". *Journal of Instrumentation*, 16(09):P09025, 2021. 80

[102] C. Adams et al. (MicroBooNE Collaboration). "Ionization electron signal processing in single phase LArTPCs. Part II. Data/simulation comparison and performance in MicroBooNE". *Journal of Instrumentation*, 13(07):P07007, 2018. 80, 82

[103] P. Abratenko et al. (MicroBooNE Collaboration). "Neutrino event selection in the MicroBooNE liquid argon time projection chamber using Wire-Cell 3D imaging, clustering, and charge-light matching". *Journal of Instrumentation*, 16(06):P06043, 2021. 86

[104] P. Abratenko et al. (MicroBooNE Collaboration). "Wire-cell 3D pattern recognition techniques for neutrino event reconstruction in large LArTPCs: algorithm description and quantitative evaluation with MicroBooNE simulation". *Journal of Instrumentation*, 17(01):P01037, 2022. 86

[105] C. Adams et al. (MicroBooNE Collaboration). "Deep neural network for pixel-level electromagnetic particle identification in the MicroBooNE liquid argon time projection chamber". *Phys. Rev. D*, 99:092001, 2019. 86

[106] D. Caratelli. "Neutrino identification with scintillation light in MicroBooNE". *Journal of Instrumentation*, 15(03):C03023–C03023, 2020. 87

[107] C. Adams et al. (MicroBooNE Collaboration). "Reconstruction and measurement of $\mathcal{O}(100)$ MeV energy electromagnetic activity from $\pi^0 \to \gamma\gamma$ decays in the MicroBooNE LArTPC". *Journal of Instrumentation*, 15(02):P02007–P02007, 2020. 91, 132

[108] The MicroBooNE Collaboration. "Reconstruction Performance Studies with MicroBooNE Data in Support of Summer 2018 Analyses". *MICROBOONE-NOTE-1049-PUB*, 2018. 97

[109] David Caratelli. *"Study of Electromagnetic Interactions in the MicroBooNE Liquid Argon Time Projection Chamber"*. PhD thesis, Columbia U., 2018. 101

[110] Enrico Bertuzzo, Sudip Jana, Pedro A. N. Machado, and Renata Zukanovich Funchal. "Dark Neutrino Portal to Explain MiniBooNE Excess". *Phys. Rev. Lett.*, 121:241801, 2018. 125

[111] Peter Ballett, Silvia Pascoli, and Mark Ross-Lonergan. "$U(1)'$ mediated decays of heavy sterile neutrinos in MiniBooNE". *Phys. Rev. D*, 99:071701, 2019. 125

[112] J. Asaadi, E. Church, R. Guenette, B. J. P. Jones, and A. M. Szelc. "New light Higgs boson and short-baseline neutrino anomalies". *Phys. Rev. D*, 97:075021, 2018. 125

[113] P. Adamson et al. "The NuMI neutrino beam". *Nuclear Instruments and Methods in Physics Research Section A: Accelerators, Spectrometers, Detectors and Associated Equipment*, 806:279–306, 2016. 132, 134

[114] R. Acciarri et al. (ArgoNeuT Collaboration). "First measurement of electron neutrino scattering cross section on argon". *Phys. Rev. D*, 102:011101, 2020. 134

[115] P. Abratenko et al. (MicroBooNE Collaboration). "Measurement of the flux-averaged inclusive charged-current electron neutrino and antineutrino cross section on argon using the NuMI beam and the MicroBooNE detector". *Phys. Rev. D*, 104(5):052002, 2021. 134

[116] P. Abratenko et al. (MicroBooNE Collaboration). "First measurement of inclusive electron-neutrino and antineutrino charged current differential cross sections in charged lepton energy on argon in MicroBooNE". *Phys. Rev. D*, 105:L051102, 2022. 134

[117] D. Cianci and M. Ross-Lonergan. SBNFit. `https://github.com/NevisUB/whipping_star`, 2021. 137, 154

[118] J. Calcutt, C. Thorpe, K. Mahn, and L. Fields. "Geant4Reweight: a framework for evaluating and propagating hadronic interaction uncertainties in Geant4". *Journal of Instrumentation*, 16(08):P08042, 2021. 143

[119] Abratenko et al. (MicroBooNE Collaboration), P. "Novel approach for evaluating detector-related uncertainties in a LArTPC using MicroBooNE data". *Eur. Phys. J. C*, 82(5):454, 2022. 144

[120] M. Babicz, S. Bordoni, A. Fava, U. Kose, M. Nessi, F. Pietropaolo, G.L. Raselli, F. Resnati, M. Rossella, P. Sala, F. Stocker, and A. Zani. "A measurement of the group velocity of scintillation light in liquid argon". *Journal of Instrumentation*, 15(09):P09009, 2020. 144

[121] Morris L. Eaton. *"Multivariate statistics: a vector space approach"*. Wiley, New York, 1983. 147

[122] A. A. Aguilar-Arevalo et al. (MiniBooNE Collaboration). "Search for Electron Neutrino Appearance at the $\Delta m^2 \sim 1$ eV^2 Scale". *Phys. Rev. Lett.*, 98:231801, 2007. 147

[123] G. J. Feldman and R. D. Cousins. "Unified approach to the classical statistical analysis of small signals". *Phys. Rev. D*, 57:3873–3889, 1998. 161

[124] P. Abratenko et al. (MicroBooNE Collaboration). "Search for an anomalous excess of charged-current quasielastic ν_e interactions with the MicroBooNE experiment using Deep-Learning-based reconstruction". *Phys. Rev. D*, 105:112003, 2022. 164, 166, 167

[125] P. Abratenko et al. (MicroBooNE Collaboration). "Search for an anomalous excess of inclusive charged-current ν_e interactions in the MicroBooNE experiment using Wire-Cell reconstruction". *Phys. Rev. D*, 105:112005, 2022. 164, 166, 167

[126] P. Abratenko et al. (MicroBooNE Collaboration). "Search for Neutrino-Induced Neutral-Current Δ Radiative Decay in MicroBooNE and a First Test of the MiniBooNE Low Energy Excess under a Single-Photon Hypothesis". *Phys. Rev. Lett.*, 128:111801, 2022. 167

[127] Carlos A. Argüelles, Matheus Hostert, and Yu-Dai Tsai. "Testing New Physics Explanations of the MiniBooNE Anomaly at Neutrino Scattering Experiments". *Phys. Rev. Lett.*, 123:261801, 2019. 167

[128] Vedran Brdar, Bhaskar Dutta, Wooyoung Jang, Doojin Kim, Ian M. Shoemaker, Zahra Tabrizi, Adrian Thompson, and Jaehoon Yu. "Axionlike Particles at Future Neutrino Experiments: Closing the Cosmological Triangle". *Phys. Rev. Lett.*, 126:201801, 2021. 167